



HAL
open science

Control of the Hierarchical Self-Assembly of Solid Block Copolymer Polyelectrolytes for Electrochemical Energy Storage

Kingsley Aniagbaoso

► **To cite this version:**

Kingsley Aniagbaoso. Control of the Hierarchical Self-Assembly of Solid Block Copolymer Polyelectrolytes for Electrochemical Energy Storage. *Polymers*. Université de Pau et des Pays de l'Adour, 2023. English. NNT: 2023PAUU3052 . tel-04661950

HAL Id: tel-04661950

<https://theses.hal.science/tel-04661950>

Submitted on 25 Jul 2024

HAL is a multi-disciplinary open access archive for the deposit and dissemination of scientific research documents, whether they are published or not. The documents may come from teaching and research institutions in France or abroad, or from public or private research centers.

L'archive ouverte pluridisciplinaire **HAL**, est destinée au dépôt et à la diffusion de documents scientifiques de niveau recherche, publiés ou non, émanant des établissements d'enseignement et de recherche français ou étrangers, des laboratoires publics ou privés.



This project has received funding from the European Union's Horizon 2020 research and innovation programme under the Marie Skłodowska-Curie grant agreement No 860403.

THÈSE

UNIVERSITE DE PAU ET DES PAYS DE L'ADOUR
École doctorale Sciences Exactes et leurs Applications
ED SEA 211

Présentée et soutenue le 14 novembre 2023
par **Kingsley Ikenna ANIAGBAOSO**

pour obtenir le grade de docteur
de l'Université de Pau et des Pays de l'Adour
Spécialité : **Chimie - Physique**

**CONTROLE DE L'AUTO-ASSEMBLAGE HIERARCHIQUE DE
POLYELECTROLYTES SOLIDES A BASE DE COPOLYMERES A BLOCS POUR
LE STOCKAGE D'ENERGIE ELECTROCHIMIQUE**

**CONTROL OF THE HIERARCHICAL SELF-ASSEMBLY OF SOLID BLOCK
COPOLYMER POLYELECTROLYTES FOR ELECTROCHEMICAL ENERGY
STORAGE**

MEMBRES DU JURY

RAPPORTEURS

- Mme. Irune VILLALUENGA
- Mme. Trang PHAN

Emakiker and Ikerbasque Research Fellow/POLYMAT-UPV/EHU, Spain.
Maître de Conférences – HDR/Aix-Marseille Université, France.

EXAMINATEURS

- M. Renaud BOUCHET

Professeur des universités/Grenoble INP, France.

DIRECTEURS

- M. Laurent RUBATAT

Maître de Conférences – HDR/Université de Pau et des Pays de l'Adour, France.

ENCADRANTS

- M. Antoine BOUSQUET
- Mme. Maud SAVE

Maître de Conférences – HDR/Université de Pau et des Pays de l'Adour, France.
Directeur de recherche CNRS/Université de Pau et des Pays de l'Adour, France.









Dedication

For my Mom



ABSTRACT (ENGLISH)

In order to develop novel solid polymer electrolytes to improve safety of lithium-ion battery, star-shaped and linear comb-like block copolymers (BCP) were synthesized to explore the impact of macromolecular architecture on both morphological order and lithium ion transport. These star-shaped BCPEs, containing around 30 wt-% of ion conductive phase, displayed organized nanostructures with reduced tortuosity, increasing ion conductivity eightfold compared to linear counterparts. Non-equilibrium morphologies prepared via photopolymerization-induced microphase separation (PIMS) mediated by either a macromolecular chain transfer agent (macroCTA) or the above-mentioned pre-synthesized BCP, were also investigated. The kinetics of forming these intricate morphologies were assessed through time-resolved SAXS. The solid polymer electrolyte (SPE) derived from PIMS was directly prepared on the lithium metal anode by *in-situ* photopolymerization, as well as on $\text{LiN}_{0.8}\text{M}_{0.1}\text{C}_{0.1}\text{O}_2$ or LiFePO_4 cathode. Assembled half cells exhibited outstanding battery performance attributed to an enhanced electrolyte/electrode interface and the mechanical strength of the SPEs.

RESUME (FRANÇAIS)

Afin de développer de nouveaux électrolytes solides polymère pour améliorer la sécurité des batteries lithium ion, des copolymères à blocs en peigne (BCP) linéaires et en étoile ont été synthétisés pour explorer l'impact de l'architecture macromoléculaire sur l'ordre morphologique et sur le transport ionique. Ces BCP en étoile, contenant environ 30 % en masse de phase conductrice d'ions, ont montré des nanostructures organisées avec une tortuosité réduite, augmentant la conductivité ionique d'un facteur huit par rapport aux homologues linéaires.

Des morphologies hors équilibre induites par la séparation microphasique induite par la photopolymérisation (PIMS), préparées à partir d'un agent de transfert de chaîne macromoléculaire (macroCTA) ou des copolymères à blocs susmentionnés, ont également été étudiées. La cinétique de formation de ces morphologies complexes a été évaluée par SAXS à résolution temporelle. L'électrolyte polymère solide (SPE) issu du procédé PIMS a été directement préparé sur l'anode en lithium métal par photopolymérisation *in-situ*, ainsi que sur les cathodes $\text{LiN}_{0.8}\text{M}_{0.1}\text{C}_{0.1}\text{O}_2$ et LiFePO_4 . Les demi-cellules assemblées ont présenté des performances exceptionnelles attribuées à une interface électrolyte/électrode améliorée et à la résistance mécanique des SPE.



ACKNOWLEDGMENT

Hitherto, God has helped me, and I am deeply grateful.

I extend my heartfelt gratitude to my advisors, Laurent Rubatat, Maud Save, and Antoine Bousquet, for allowing me to find my own path with just the right amount of guidance. If I have seen farther and clearer, it's because you have illuminated my path with your light. Your unwavering support has been instrumental in fostering my growth both as a scientist and as an individual.

I also wish to extend my appreciation to Tim Melender-Bowden and Jan Bintec for their invaluable contributions to my intellectual growth during my time in their laboratories. Your influence has left a lasting mark on my work. I am very grateful to L ena c Madec for giving introductory lessons in battery testing methods.

A special thank you goes to Monika Kr ol and Janne Ruokolainen at Aalto University in Finland for their support in morphological characterization and interpreting my research findings. Your contributions continue to resonate throughout my work. At the same time, I am immensely grateful to the POLY STORAGE European training network for their training and resourceful activities throughout my doctoral research journey.

To the staff and administration at IPREM, I extend my thanks for hosting me over these three years. I want to give special recognition to colleagues at the reception (Daniella and Co.), Celine Cloute, Olivier Gilbert, Abdelouahed Khoukh, Virginie Pellerin, Anthony Laffore and Marie Larregieu for their willingness to help with paperwork and training. I like to take time to acknowledge my work colleagues/friends that have shown me support and camaraderie. Badre, Gregoire, Nabil - thank you for research & coffee discussion. Shout out to Sarah, Marine, Theo, Coste, Oph elie, Alex, Beatrice, Alexis, Benhur, Aranya, Tarik, Christopher, Isaac, Kenza, Adriana, Olivera, Ousman Deborah etc. I appreciate you all.

I owe a debt of gratitude to my Aunties Hadiza Yesufu and Rebecca Ezeh, my Uncles Mustapha Yesufu, Chidi Ezeh, Ifeanyi Ezeh and Chibuike Ezeh. Consistently, you all have been pillars of strength in my life. Your guidance and encouragement have left an indelible mark on my journey. Lastly, my deepest appreciation goes to my parents, Livinus and Florence Aniagbaoso for your boundless patience and unwavering support that has been vital to my growth and development. Mom & Grandma (Paulina), your love and weekly calls has been a cornerstone throughout my postgraduate studies abroad, and I am truly thankful to have your support.



CONTENTS

General Introduction (English)	1
Introduction Generale (Français)	3
Chapter 1: State of the Art on Nanostructured Polymer Electrolytes for Li-Ion Batteries	7
Chapter 2: Improved Solid Electrolyte Conductivity via Macromolecular Self-Assembly: From Linear to Star Comb-Like P(S-Co-BzMA)-B-POEGA Block Copolymer	57
Chapter 3: Block copolymer-derived Nanostructured Solid Polymer Electrolyte based on comb PEO	109
Chapter 4: Photo-Polymerization-Induced Microphase Separation to Design Solid Polymer Electrolyte for Lithium Metal Batteries.	145
General Conclusion (English)	205



GENERAL INTRODUCTION (ENGLISH)

The imperative to maintain a global climate balance goes hand in hand with the demand for clean energy solutions. Renewable energies are environmentally friendly and help to preserve local ecosystems. Lithium batteries offer significant potential for storing energy generated by these renewable yet intermittent systems. However, several challenges must be tackled, including improving safety, achieving high energy density, reducing costs, and enhancing the ability for multiple charge-discharge cycles and extended lifespan.

Block copolymers electrolytes (BCPEs) – a subclass of solid polymer electrolytes (SPEs) is currently being explored to replace traditional liquid electrolytes, thus offering the prospect of safer operations for the next generation of lithium batteries. BCPEs are valued for their combined mechanical and conductive properties. However, the presence of network defects, such as dead ends (discontinuous path), grain boundaries, and post-processing effects, often hampers the ionic conductivity of BCPEs, impeding ion transport and increasing resistance.

The focus of this thesis is to explore novel ways of regulating self-assembly process in BCPEs with the aim of effectively decoupling their mechanical and conductive properties while maintaining efficient ion transport. Our hypothesis is hinged on the fact that reducing defects in the morphology of BCPEs through meticulous design of macromolecular architecture and optimization of fabrication process would tremendously enhance and optimize the performance of BCPEs in batteries.

Chapter 1 sets the stage by first putting together pieces of knowledge on lithium batteries working principles and state-of-the-art of BCPEs. At the same time, this chapter highlights the appeal of PEO-based BCPEs, especially those with comb-like structures, due to their low glass transition temperature (T_g), chain flexibility, and ability to solubilize lithium salts while maintaining electrochemical stability against lithium metal. It underscores the complexity of BCPE architecture and the need to unravel the relationship between structure and properties. Questions regarding the influence of block positional arrangements and arm density in star BCPEs are raised. The chapter acknowledges the challenges in comparing BCPEs with complex architectures with their linear counterparts.

Based on the existing knowledge gaps concerning the morphology of BCPEs and the correlation with performance, chapter 2 presents a method for synthesizing two series of comb-like and 4-arms star comb-like BCPEs through reversible addition fragmentation transfer

(RAFT) polymerization. By comparing stars to linear counterparts, this study offers insights into the correlation between complex macromolecular structures and resulting morphology in BCPEs with comb-like PEO outer blocks. This chapter, focused on controlled synthesis, illuminates the importance of BCPE architecture on tortuosity in relationship with ionic conductivity.

Chapter 3 explores an innovative approach to improve the mechanical and conductive properties of comb-like PEO, diverging from traditional crosslinking methods. It is based on the addition of pre-synthesized BCPs developed in Chapter 2 to the photopolymerization of oligo(ethylene glycol) methyl ether acrylate (OEGA), leading to non-equilibrium morphologies. The relation between the polymer blend morphologies and the solid electrolytes properties are discussed.

Chapter 4 introduces a novel approach, photo-RAFT polymerization induced microphase separation (PIMS), to fabricate flexible solid polymer electrolytes (SPEs) with a disordered yet percolating morphology. This process involves the inclusion of soft phase into hard phase via *in-situ* block copolymer synthesis, offering an alternative to traditional BCPEs. For that purpose, lithium conducting poly(ethylene glycol) methyl ether acrylate-*co*-styrene) P(OEGMA-*co*-Styrene) macromolecular chain transfer agent (macroCTA) are introduced as reactive block in radical photopolymerization of isobornyl acrylate (IBoA). The chapter investigates the structural development of these SPEs with varying compositions of linear and star comb macroCTA via small-angle X-ray scattering (SAXS) experiments. The rapid kinetics of the photo-PIMS process, coupled with its potential for electrode integration, present a promising avenue for SPE development. Demonstrating the feasibility of the approach, the SPEs derived from PIMS were directly applied onto the lithium metal anode, as well as the high-voltage $\text{LiN}_{0.8}\text{M}_{0.1}\text{C}_{0.1}\text{O}_2$ cathode (LiFePO_4 was also employed for performance comparison). Assembled half cells exhibited good battery performance, attributed to an enhanced electrolyte/electrode interface and the mechanical strength of the SPEs.

Overall, this thesis offers valuable insights into the intricate world of BCPEs and their potential to optimize energy storage technologies. These findings would contribute to the development of advanced solid polymer electrolytes for more efficient and reliable lithium metal batteries.

INTRODUCTION GENERALE (FRANÇAIS)

L'impératif de maintenir un équilibre climatique mondial va de pair avec une augmentation de la proportion de solutions énergétiques propres. Les énergies renouvelables sont respectueuses de l'environnement et contribuent à préserver les écosystèmes locaux. Les batteries au lithium offrent un potentiel significatif pour stocker l'énergie générée par ces systèmes intermittents. Cependant, plusieurs défis doivent être relevés, notamment l'amélioration de la sécurité, l'obtention d'une densité énergétique élevée, la réduction des coûts et la stabilité.

Les électrolytes solides à base de copolymères à blocs (BCPEs) sont une sous-catégorie des électrolytes polymères solides (SPEs) et sont actuellement explorés pour remplacer les électrolytes liquides traditionnels et offrir ainsi la perspective d'un fonctionnement plus sûr pour la prochaine génération de batteries au lithium. Les BCPEs sont développées pour leur faculté à combiner propriétés mécaniques et conductrices en un seul matériau. Cependant, la présence de défauts structuraux à l'échelle nanoscopique, tels que des joints de grains et des effets de post-traitement, limite souvent la conductivité ionique des BCPEs.

L'objectif de cette thèse est d'explorer de nouvelles méthodes de contrôle du processus d'auto-assemblage dans les BCPEs dans le but de découpler efficacement leurs propriétés mécaniques et conductrices tout en maintenant un transport ionique efficace. Notre méthodologie repose sur la réduction des défauts dans la morphologie des BCPEs grâce à une conception minutieuse de l'architecture macromoléculaire et du processus de fabrication.

Le chapitre 1 pose les bases bibliographiques en réunissant des connaissances sur les principes de fonctionnement des batteries au lithium et l'état de l'art des BCPEs. Il met en évidence l'attrait des BCPEs à base de PEO, en particulier celles ayant des structures en peigne, en raison de leur faible température de transition vitreuse (T_g), de leur flexibilité de chaîne et de leur capacité à solubiliser les sels de lithium tout en maintenant une stabilité électrochimique face au lithium métallique. Le chapitre souligne la nécessité d'étudier la relation entre la complexité de l'architecture des BCPEs, leur structuration et les propriétés finales. Des questions concernant l'influence des arrangements des blocs et de la densité des branches dans les BCPEs en forme d'étoile sont soulevées. Le chapitre met en évidence les défis liés à la comparaison des architectures complexes avec leurs homologues linéaires.

Afin d'étayer les connaissances existantes concernant la corrélation entre la morphologie des BCPE et leur performance en tant qu'électrolyte solide, le chapitre 2 présente la synthèse de

copolymère à blocs en forme d'étoile à 4 branches avec des blocs PEO en forme de peigne par polymérisation par addition fragmentation réversible (RAFT). Les structures macromoléculaires complexes et la morphologie résultantes dans les BCPEs sont étudiées et comparées à celle de leurs homologues linéaires. Ce chapitre met en lumière l'importance de l'architecture BCPE sur la tortuosité des morphologies en relation avec la conductivité ionique.

Le chapitre 3 explore une approche originale pour améliorer les propriétés mécaniques et conductrices des électrolytes PEO en forme de peigne, s'éloignant des méthodes traditionnelles de réticulation. L'ajout de BCPs, précédemment synthétisés dans le chapitre 2, au processus de photopolymérisation de l'oligo(éthylène glycol) méthyl éther acrylate est étudié. Ceci conduit à des morphologies hors équilibre qui mènent à des modifications des propriétés des BCPEs.

Le chapitre 4 introduit une approche innovante, la microséparation de phase induite par photopolymérisation RAFT (Photo-PIMS), pour fabriquer des électrolytes polymères solides flexibles avec une morphologie désordonnée mais percolante. Ce processus implique l'inclusion de phases conductrices et de phases mécaniquement robustes, offrant une alternative aux BCPEs traditionnels. Le chapitre présente l'évolution structurelle de ces SPEs en fonction du temps grâce à des expériences de diffusion des rayons-X aux petits angles (SAXS) et en faisant varier l'architecture du polymère initial (étoile ou linéaire). Le procédé photo-PIMS, de par la possibilité d'être utilisé in-situ pour la production des batteries et sa cinétique rapide, présente une voie prometteuse pour le développement des SPEs. Démontrant la faisabilité de l'approche, les SPEs obtenus par photo-PIMS ont été directement appliqués sur une anode de lithium métallique, ainsi que sur une cathode $\text{LiN}_{0.8}\text{M}_{0.1}\text{C}_{0.1}\text{O}_2$ (LiFePO_4 a également été utilisé pour la comparaison des performances). Les demi-cellules assemblées ont montré de bonnes performances, attribuées à une interface électrolyte/électrode améliorée et à la tenue mécanique des SPEs.

Les résultats de ce travail de thèse permettent d'apporter de nouvelles connaissances sur BCPEs à l'équilibre et hors équilibre et mettent en avant leur potentiel à optimiser les technologies de stockage d'énergie. Ces résultats contribueront au développement d'électrolytes polymères solides de dernière génération pour des batteries au lithium plus efficaces et fiables.





Chapter 1

State of the Art on Nanostructured Polymer Electrolytes for Li-Ion Batteries



Synopsis

This chapter starts with a recapitulation on the need to adopt clean and renewable technologies as a way to alleviate carbon footprint of the energy sector. With major focus on Lithium ion batteries as one of the foremost electrochemical energy storage devices, I have briefly discussed the working principles of such secondary batteries, as well as the challenges of solid-state battery development.

In the following sections, I will present the perspective on nanostructured block copolymer electrolytes that results from equilibrium and non-equilibrium assembly obtained via different fabrication methods. The aim is to provide the reader with a more comprehensive and in-depth understanding of morphologies generated through these different fabrication methods, the key influencing parameters and the correlation of generated morphology to electrolyte properties.

Furthermore, it is expected that this will inform the reader on the state-of-the-art strategies for designing robust electrolytes with decoupled mechanical and conductive properties.

Table of Content

1	Introduction	11
2	Li-ion Battery	14
2.1	How does it work	14
2.2	Different types of Electrolytes.....	17
2.2.1	Liquid Electrolytes	17
2.2.2	Polymer electrolytes	19
3	Block Copolymers as Solid Polymer Electrolytes.....	24
3.1	Dual-Ion Block Copolymer Electrolyte Based on Comb PEO	25
3.2	Self-Assembly of Block Copolymer Electrolytes (BCPEs).....	26
3.2.1	Influence of salt-doping on the morphology of BCPEs.....	28
3.2.2	Influence of BCPE Architecture	29
3.3	Conductivity of Block Copolymer Electrolytes.....	31
4	Polymerization Induced Microphase Separation (PIMS)	34
4.1	What is PIMS?.....	34
4.2	PIMS SPE for battery	35
5	Conclusion.....	42
6	References	43

1 INTRODUCTION

Climate change is one of the most pressing issues facing our planet today.¹ The burning of fossil fuels, such as coal, oil, and natural gas, is the primary cause of greenhouse gas emissions, which are contributing to the warming of the earth's atmosphere and the resulting changes in weather patterns, sea levels, and ecosystems.

According to the UN Department of Economic and Social Affairs (UNDESA) and the French Institute for Demographic Studies (INED), the world's population is estimated to hit approximately 10 billion marks by 2050 and the planet will have to sustain over 11 billion people by the end of the 21st century. As a result, demands for energy would skyrocket amidst depleting fossil fuel resources. Moreover, the actions against climate change necessitates the wider adoption of sustainable energy solutions to supplant well-established fossil fuel-based solutions.¹ To provide energy for the future and secure our planet, the shift towards renewable energy represents the only viable and best solution.

Renewable energies are produced from natural, sustainable sources such as the sun, wind, water, and geothermal heat. These sources are abundant, clean, and do not produce any emissions that contribute to climate change. In contrast, fossil fuels are a finite resource that not only contribute to climate change but also deplete natural resources. By transitioning to renewable energy, we can reduce our dependence on fossil fuels, decrease greenhouse gas emissions, and help to mitigate the effects of climate change.

Despite the many benefits of renewable energy, there are still some challenges that need to be overcome. One of the main challenges is that renewable energy sources are not yet cost-competitive with fossil fuels – the infrastructures have a high initial cost of installation and maintenance. However, as the technology prospects improve and economies of scale are achieved, the cost of renewable energy is expected to decrease. Additionally, governments can provide financial incentives and subsidies to support the development and switch to renewable energy.

Another challenge is the intermittency of the energy sources. Solar and wind energy, for example, are dependent on weather conditions, which means that the energy production is not constant and predictable. For the emergence of a new energy economy, it is imperative to tackle

these challenges – optimization of renewable energy systems, integration of renewable energy (large-scale solar and wind farms) into the existing energy grids as well as the development of new and efficient low-cost energy storage systems to store the energy produced by renewable sources for later use.²

Energy storage systems can be classified into several categories, including mechanical, chemical, thermal, and Electrochemical storage.³ Mechanical energy storage systems include pumped hydroelectric storage, in which water is pumped uphill to a reservoir during periods of low demand and then released downhill through a turbine to generate electricity during periods of high demand, flywheels⁴, which store energy in a rotating mass. Compressed air energy storage is another example of a mechanical storage system, in which air is compressed and stored in an underground cavern or repurposed natural gas storage facility, and then released to drive a turbine and generate electricity.⁵ Thermal energy storage systems include sensible heat storage, in which heat is stored in a material with a high heat capacity, and latent heat storage, in which heat is stored in a material that undergoes a phase change, such as melting or freezing.⁶ One example of a thermal energy storage system is a molten salt thermal energy storage system, in which a mixture of salts is heated during periods of low demand and then used to generate electricity during periods of high demand by passing through a heat exchanger to produce steam and drive a turbine. Electrochemical energy storage systems (EESS) convert chemical reactions into electrical energy.⁷ They include capacitors, super capacitors, batteries and fuels cells. **Figure 1** shows the Ragone plot roughly describing the power vs energy densities* that can be accessed from these EESS.

* Power or Energy density is a measure of how much power or energy respectively, that can be produced by a battery of a given size and weight.

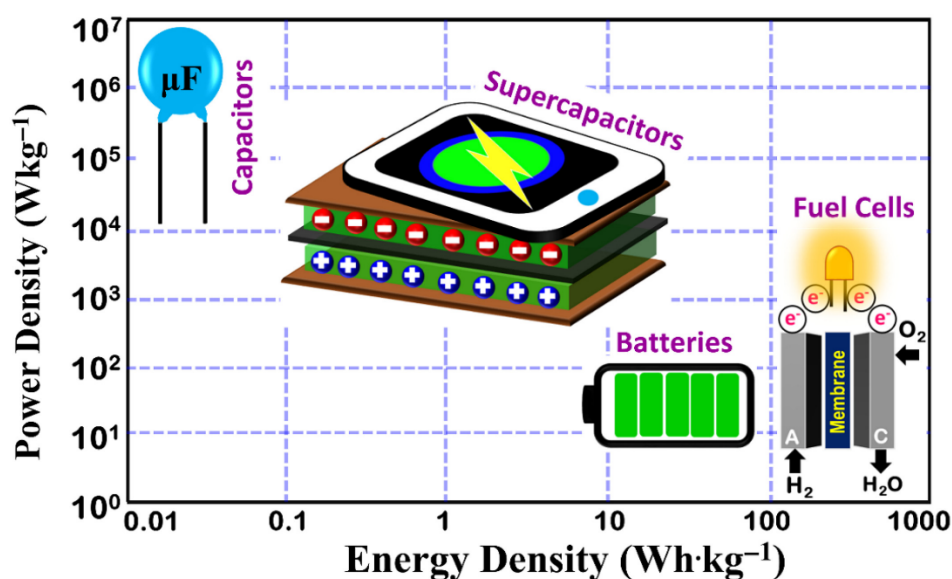


Figure 1. Ragone plot showing the typical energy density (Wh kg^{-1}) and power density (W kg^{-1}) range of electrochemical energy storage systems: fuel cells, batteries, supercapacitors, and conventional capacitors. Taken from literature.⁸

Batteries are relatively easy to install and maintain, and are becoming increasingly affordable as technology improves. However, the lifespan of batteries is limited, and they can be expensive to replace. Batteries come in many different forms, including lead-acid batteries, lithium-ion batteries, redox flow batteries to mention but a few. The type of chemical reactions that occur in a battery depend on the specific materials used in the electrodes and electrolyte. Lithium-ion batteries are the most widely used type of battery for energy storage because they have a high energy density, long life cycle, and low self-discharge rate.⁹ Apart from optimization of the energy storage capabilities, one of the most critical challenges in the advancement of lithium batteries is the unsustainable and unethical acquisition of mineral resources.¹⁰ This obstacle continues to hinder their widespread integration into the energy grid and have accelerated the investigation of alkali metal ion batteries as in Sodium ion (Na^+) and Potassium ion (K^+) batteries, or multi-valent metal ion as in Magnesium ion (Mg^{2+}), Calcium ion (Ca^{2+}), Zinc ion (Zn^{2+}) and Aluminum ion (Al^{3+}) batteries.¹¹ These so-called post-lithium-ion battery technology offer advantages like relative greater abundance, lower costs, and sustainable supply chain, offer a promising opportunity to tackle resource concerns effectively. However, replacing Li-ions with Na-, Mg-, or Al-ions requires deep revision and re-exploration of the cathode and electrolyte materials and electrochemistry of such batteries.¹²

2 LI-ION BATTERY

2.1 HOW DOES IT WORK

In the last three decades, lithium battery technology has dominated the global battery market¹³ making it the foremost researched rechargeable battery system owing to their capacity to deliver high energy density of $\sim 272 \text{ Wh kg}^{-1}$ compared to Sodium ion and Potassium ion batteries with density of 231 Wh kg^{-1} and 218 Wh kg^{-1} respectively.¹⁴ Lithium ion batteries (LIBs) consists of two electrodes having different potentials and separated by an ionically conductive material called an electrolyte as shown in Figure 2. The electrodes can be externally connected via a device circuit which allows the spontaneous flow of electron from the more negative to the more positive potential while ions are exchanged between electrodes through the electrolyte to maintain charge balance. The continuous flow of electrons, known as electric current (I), over a period leads to the build-up of charges within the electrode. The quantity of these accumulated charges in milli ampere hour (mAh) can be determined using equation 1.

$$Q = \sum e^- = I \times t \quad 1$$

LIBs are regarded as secondary batteries because voltage can be applied in the opposite direction to reverse the process thus recharging the battery.^{15,16} A typical anode of LIB is made of graphite, while the cathode is made of a lithium-containing compound such as lithium cobalt oxide (LiCoO_2), lithium manganese oxide (LiMn_2O_4) or lithium iron phosphate (LiFePO_4), to mention a few. The electrolyte is classically a liquid or gel that conducts lithium ions between the anode and cathode, and the separator is a material that prevents the anode and cathode from coming into direct contact with each other.

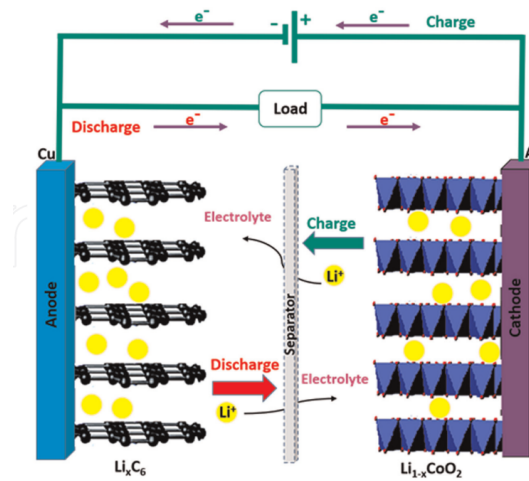
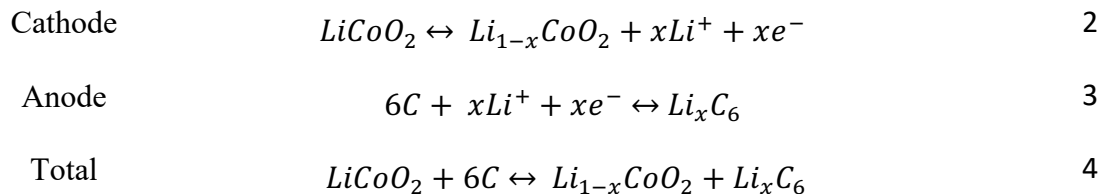


Figure 2. Schematic representation of principle of operation of lithium battery. The illustration shows the discharging process, where the electrons move from the negative anode to the positive cathode while powering a device. At the same time, lithium-ions are moving from the electrolyte to the cathode to create a charge balance. During charging, the reverse process occurs. Redrawn from literature.¹⁷

Typical redox reactions occurring at the cathode (in this case LiCoO_2) and anode (in this case graphite) are as follows:¹⁸



The cell voltage (ΔE)[†] of LIBs varies depending on the specific materials used in the electrodes and the electrolyte. The energy capacity (in Wh)[‡] of LIBs can be calculated from equation 5.

$$\text{Energy capacity} = Q \times \Delta E \quad 5$$

Recent efforts to optimize energy capacity of LIBs have led to the development of conversion-based[§] electrodes like silicon anodes¹⁹, sulphur cathodes in lithium-sulphur batteries²⁰, and O-redox cathodes in lithium-air batteries²¹. This is because they provide a higher specific capacity

[†] Cell voltage of a lithium-ion battery refers to the electric potential difference between the positive and negative electrodes within a single cell of the battery.

[‡] Energy capacity refers to the maximum attainable capacity of a cell, regardless of size, chemistry, age, etc.

[§] Conversion-based electrodes refer to one where lithiation/delithiation goes through a different mechanism known as "alloying" or "conversion".

compared to the intercalation-based^{**} ones like graphite, LiCoO₂, LiFePO₄ etc (refer to **Figure 3**).^{14, 22}

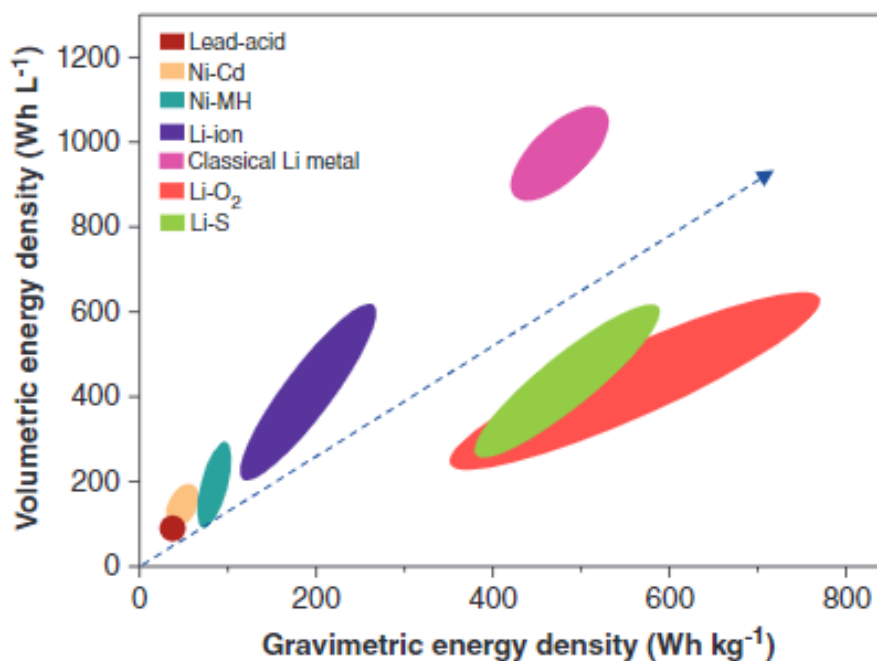


Figure 3. Gravimetric energy density vs volumetric energy density plot of various types of rechargeable batteries: Lead acid, Nickel-cadmium (Ni-Cd), Nickel-metal hydride (Ni-MH), Lithium ion (Li-ion), Lithium metal (Li-metal), Lithium-oxygen (Li-O₂), and Lithium-sulphur (Li-S) batteries. Taken from literature.²³

Lithium metal batteries (LMBs) is another promising variant of the lithium rechargeable battery technology wherein lithium metal completely replaces the anode commonly used in LIBs.^{24, 25} Lithium metal is very light (0.53 g cm⁻³) and has an extremely low redox potential versus standard hydrogen electrode (-3.04 V), thus can facilitate a large operating voltage when paired with essentially any cathode.²⁶ The theoretical capacity of a metallic Li anode is often touted as 3842 mAh g⁻¹, but it's crucial to clarify that this value represents the capacity of lithium as a charge carrier, not the Li anode itself.¹⁴ To fulfil the potential of the Li anode, it is crucial to achieve fully reversible lithiation/delithiation during battery cycling. When this condition is met, the mass of Li in the anode precisely matches the amount needed to fully lithiate the cathode material, resulting in a so-called negative to positive (N : P) capacity ratio

^{**} Intercalation-based electrodes refer to one where lithium ions are inserted between the layers of graphite during charging and discharging.

of 1:1.²⁶ Excess of Li metal is often utilized to compensate for irreversibly ion losses during battery cycling and achieve a high cycle life for the battery. Therefore, the capacity 3842 mAh g^{-1} is rarely achieved because the entire anode cannot be completely utilized during discharge.

Despite the relatively higher capacity reported for Li metal batteries, it is not safe to use due to its high chemical reactivity that results to multiple issues such as rough electrodeposition of lithium ions, uncontrolled parasitic side reactions with the liquid electrolyte and dendrite-induced short circuits.^{27, 28} Overcoming all these challenges is crucial to harnessing the potential benefits of LMBs.

2.2 DIFFERENT TYPES OF ELECTROLYTES

2.2.1 Liquid Electrolytes

The most common liquid electrolyte (LE) used in lithium batteries is a non-aqueous lithium salt solution such as lithium hexafluorophosphate (LiPF_6) salt dissolved in organic carbonates like ethylene carbonate (EC), dimethyl carbonate (DMC), propylene carbonate (PC), diethyl carbonate (DEC), ethyl methyl carbonate (EMC), etc.²⁹ A common characteristics of these organic solvents is their strong ability to coordinate with lithium salt and they are differentiated by their unique properties like: dielectric constant (ϵ), viscosity, electrochemical stability particularly against the cathode and anode during cell operation, operating temperature range, and thermal flash point.²⁹ During the operation of LIBs, a solid electrolyte interphase (SEI) layer forms on the surface of the electrodes, due to side reactions with the liquid electrolyte. The solid electrolyte interphase (SEI) is a protective layer that develops on the electrodes of a Li-ion battery, primarily during the initial cycles. Once formed, the SEI layer acts as a barrier, preventing excessive chemical reactions between the electrodes and the electrolyte. This protective allows selective lithium ion migration while preventing further electrolyte degradation.

The presence of a stable SEI layer is crucial to ensuring efficient battery operation, but controlling its formation and growth can prove challenging due to its complex mechanisms of formation involving competitive pathways occurring on time scales ranging from picoseconds³⁰ to days.^{31, 32} The common practice of combining appropriate lithium salts with

carbonate solvents in different proportions aims to leverage their distinct properties and optimize overall formation and performance of SEI has become increasingly popular.³¹

For instance, Zhang *et al.*³³ compared the ionic properties of different combination of electrolytes of LiClO₄, LiBF₄, and LiPF₆ salts in PC and 1:1 EC/DMC. LiClO₄ exhibits high ionic conductivity (5.6 mS cm⁻¹ in PC, 8.4 mS cm⁻¹ in EC/DMC) and has the advantage of potentially forming less resistive SEI layers compared to LiPF₆ and LiBF₄, as it avoids LiF decomposition. However, it suffers from thermal instability, reacting with solvents at elevated temperatures and being explosive. On the other hand, LiBF₄ offers better thermal stability and is less sensitive to moisture than LiPF₆. However, its adoption in the industry is limited due to lower ion conductivity (3.4 mS cm⁻¹ in PC, 4.9 mS cm⁻¹ in EC/DMC), approximately 40% lower than LiPF₆ (5.8 mS cm⁻¹ in PC, 10.7 mS cm⁻¹ in EC/DMC), and the high resistance of SEI formation from the LiBF₄ electrolyte. Occasionally incorporating small amount of electrolyte additive can help improve the stability of the SEI layer.³⁴⁻³⁶

Organic fluoro-solvents are considered highly promising electrolyte solvents for high voltage stability, surpassing carbonate solvents.³⁷ A report by Zhang *et al.*³⁸ showed that the substitution of EMC with fluorinated ethyl methyl carbonate (F-EMC) and EC with fluorinated cyclic carbonate (F-AEC) greatly improved the voltage limits of the electrolyte. This is because fluorinated molecules possess higher oxidation potentials, attributed to the potent electron-withdrawing effect of the fluorine atom.

For safety reasons, when LEs are used in LIBs, a separator is needed to prevent the electrodes from coming into contact and causing a short circuit. Though the separator increases internal cell resistance, which also takes up valuable space inside within the battery, optimizing the separator design in LIBs can impact several battery performance parameters, including cycle life, energy and power density, and safety.³⁹ LIBs are designed to vent automatically under busy conditions, due to drastic increase in internal cell pressure caused by overheating. The inability of the cell to vent under extreme pressure could lead to a pressure build up and subsequent explosion.^{35, 40} Also, if the liquid electrolyte escapes during venting into a searing external cell environment, it can inflame. The reason is that this type of electrolytes are extremely flammable thus necessitating the redesign of battery casing to prevent electrolyte leakage.⁴¹ Also, dissolution of cathode material in liquid electrolytes is an existing problem

responsible for quick aging and capacity fading of LIBs.⁴² Given these safety and performance concerns, polymer electrolytes (PEs) have been investigated as potential replacement for LEs.^{34, 43-45}

2.2.2 Polymer electrolytes

Non-volatility and nonflammability property of higher molar mass polymers make them ideal and safer for use as electrolytes.^{41, 45} They have good processability and flexibility that can easily be applied to battery manufacturing process. PEs often comprises of polymers fortified with an appropriate lithium salt and in some cases, solvents, and fillers, capable of transporting charged species such as ions or protons across the molecular matrix.

Among the polymers, ones containing strongly electronegative atoms like Oxygen, Nitrogen, Fluorine, and Chlorine on the backbone are of interest because they can interact with the metal cations of metallic salts to form salt-polymer complexes.⁴⁵ Furthermore, segmental motion of the chains (both inter- and intra-chain motion), facilitates the movement of complexed Li^+ ions through the bulk of amorphous polymeric electrolytes, as depicted in Figure 4.⁴⁶ In 1975, P.V Wright first reported the complexation of poly(ethylene oxide) (PEO) with alkali salts with conductivities near $10^{-2} \text{ S cm}^{-1}$ when the melting temperature ($66 - 75 \text{ }^\circ\text{C}$) of the polymer was exceeded.⁴⁷ Later in 1978, M.A Armand demonstrated their application as electrolytes for batteries.⁴⁸ Since then, other polymers like Poly(oligo ethylene oxide methacrylate) (POEGMA), Poly(oligo ethylene oxide acrylate) (POEGA), poly(trimethylene carbonate) (PTMC), polyethylene carbonate (PEC), polycaprolactone (PCL), Polyketone (PK), poly(vinylidene fluoride-hexafluoropropylene) (PVdF-HFP), poly(vinyl chloride) (PVC), poly(acrylonitrile) (PAN), poly(acrylic acid) (PAA), poly(ethyl methacrylate) (PEMA), to mention a few have also been investigated in this context.^{46, 49-54}

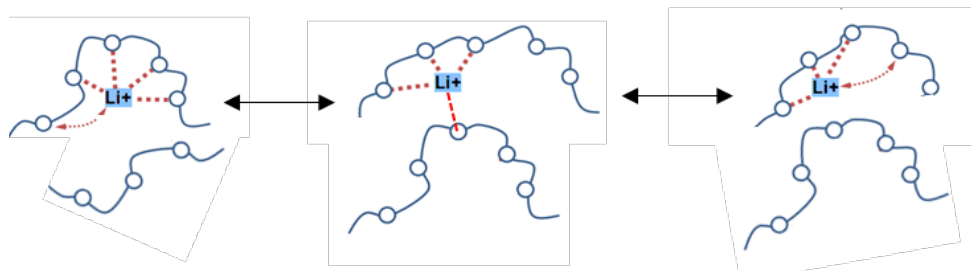


Figure 4. Illustration of assisted mobility of Li^+ ion by segmental chain motion, inter- and intra-chain ion-hopping between coordinating sites in polyethylene oxide-based polymer. Redrawn from literature.⁴⁶

PEO is essentially a semi-crystalline polymer which exhibits a dominant amorphous phase with activated chain segments (above $T_g \approx -41^\circ$) beneficial for ionic transport. However, at low operating temperatures, the formation of crystalline domains results in low ionic conductivities.^{27, 55} To repress crystallinity and increase the percentage of the amorphous phase of PEO, it is important to break up the symmetry of long-range order to improve polymer chain dynamics.⁵⁶ Various strategies have been employed to achieve this, such as the addition of non-volatile plasticizer⁵⁷⁻⁶¹ or nanofiller,^{62, 63} polymer blends,⁶⁴⁻⁶⁷ grafting short ethylene oxide (EO) oligomers onto polymer backbones, cross-linking PEO based polymers,⁶⁸⁻⁷² or synthesizing block copolymers⁷³⁻⁷⁹. In line with these strategies, completely amorphous electrolytes with even higher conductivities can be produced for very high salt concentrations where the materials could rather be considered a polymer-in-salt electrolytes (PISE) than a salt-in-polymer electrolytes.⁴⁶

Incorporating inorganic fillers into PEs can significantly boost mechanical performance as well. This approach offers a dual advantage: firstly, it effectively enhances the overall ionic conductivity by hindering polymer crystallization. Secondly, it preserves the exceptional flexibility and malleability of the polymer base.⁸⁰ Recent findings suggest that incorporating fillers promotes stable interfaces between electrodes and electrolytes through even dispersion of ceramic particles.^{80, 81} In this context, the PEs are termed composite polymer electrolytes (CPEs). Inorganic fillers utilized in CPEs can be categorized as either passive or active. The term "passive" refers to ceramic fillers without Li^+ , such as Al_2O_3 ^{82, 83}, SiO_2 ⁸⁴, TiO_2 ⁸⁵, ZnO ⁸⁶ and ZrO_2 ⁸⁷. Conversely, the term "active" describes ceramic fillers containing Li^+ , including,

$\text{Li}_{1+x}\text{Al}_x\text{Ge}_{2-x}(\text{PO}_4)_3$ (LAGP)⁸⁸, Li_3N ^{89, 90}, $\text{Li}_7\text{La}_3\text{Zr}_2\text{O}_{12}$ (LLZO)⁹¹⁻⁹³, $\text{Li}_{1+x}\text{Al}_x\text{Ti}_{2-x}(\text{PO}_4)_3$ (LATP)^{94, 95}, $\text{Li}_{3x}\text{La}_{2/3-x}\text{TiO}_3$ (LLTO)⁹⁶, LiAlO_2 ^{97, 98}, among others.

A significant concern that has hindered the competitiveness of PEs when compared to LEs is their inadequate interfacial contact with electrodes and limited ionic conductivity at room temperature (RT). The latter problem could be linked to the crystalline characteristics and constrained molecular mobility within the polymer matrices in this temperature range. In this regard, PEs could be formulated to contain significant amount of solvent trapped within the polymer matrix. This is considered as gel polymer electrolyte (GPE) and ionic transport is facilitated by a combination of solvent flux and segmental motion thus providing it with quite good conductivity at RT.⁹⁹ However, these types of electrolytes have similar flammability poor mechanical integrity and find use in applications in which mechanical strength is not crucial. There are several literatures that offer more details on GPE, herein, the review by Zhu *et al.*¹⁰⁰ is recommended.

Regarding the practical implementation of PEs in lithium-ion batteries (LIBs), several attributes are necessary to attain optimal performance. Among these, a crucial requirement is achieving high ionic conductivity at RT. Typically, LEs containing lithium salts can achieve an ionic conductivity ranging from 1 mS cm^{-1} to 10 mS cm^{-1} , while solid polymer electrolytes (PEs) strive for a minimum ionic conductivity of 0.1 mS cm^{-1} at RT, a goal that often presents challenges in most instances.¹⁰¹ Additionally, a high Li^+ transference number (t_+) is desirable, indicating a significant Li^+ mobility ($\text{m}^2 \text{V}^{-1}\text{s}^{-1}$) compared to other ions. t_+ is essentially a comparison of the relative mobilities of cations and anions (μ_+ and μ_- respectively). For a simple dual-ion salt in a PE, the cation transference number, t_+ is calculated as follows:⁴⁶

$$t_+ = \frac{\mu_+}{\mu_+ + \mu_-} \quad 6$$

Since ion diffusion D ($\text{m}^2 \text{s}^{-1}$), and ion mobility μ , have a proportional relationship as established by Einstein's equation,¹⁰² it is sufficient to rewrite equation 6 in diffusion terms.

$$t_+ = \frac{D_+}{D_+ + D_-} \quad 7$$

Therefore, by leveraging self-diffusion coefficients determined from pulsed field gradient NMR, one can calculate the value of t_+ for PEs with ionic salt that are NMR-active. Nonetheless, a more accessible way to measure the value of t_+ is the method combining direct current (dc) polarization and impedance spectroscopy, known as the ac/dc method, as suggested by Bruce *et al.*¹⁰³ Such experiment is performed on a symmetric Li|PE|Li cell to obviate erroneous contributions due to ion concentration gradients. The cell is subjected to a relatively small dc polarization (~ 10 mV) for a couple of hours, which creates an electric field across the PE. This causes the migration of charged ions within the electrolyte. By gauging the current decay from the start (I_0 = initial current) to the end of experiment (I_{ss} = steady state current), as well as the impedance response before (R_0 = initial internal resistance) and after (R_{ss} = initial internal at steady state), the contribution of each ion to the total current can be determined according to equation 8.

$$t_+ = \frac{I_{ss}(\Delta V - I_0 R_0)}{I_0(\Delta V - I_{ss} R_{ss})} \quad 8$$

When the t_{Li^+} is low, there is significant local polarization that leads to uneven deposition of cations.^{104, 105} This condition detrimentally affects the cycle life and power density of the battery. Furthermore, anions are not utilized at the electrodes; their accumulation over time can potentially lead to their decomposition, causing detrimental effects on the cell.¹⁰⁶ Generally, PEO-based PEs exhibit a t_{Li^+} value below 0.5 (see **Figure 5**), indicating greater mobility of anions than lithium ions.¹⁰⁷

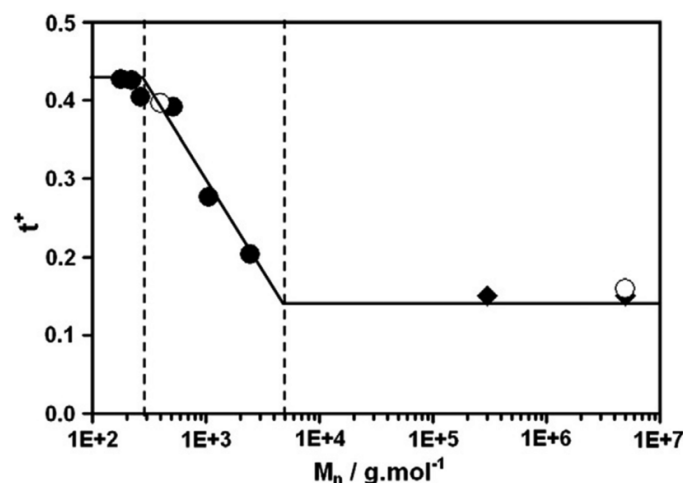


Figure 5. Evolution of the Li^+ transference number (t_{Li^+}) with molar mass of PEO electrolyte. Taken from Literature¹⁰⁸.

A t_{Li^+} approaching 1 will effectively reduce concentration polarization in electrolytes during the charge/discharge cycle. This, in turn, leads to the potential for achieving higher energy densities.¹⁰⁹ One viable method for achieving restricted anion mobility involves anchoring the anion to the polymer backbone, thereby establishing what is known as a single-ion conducting polymer electrolyte.¹¹⁰

Another crucial requirement is that the PEs must exhibit an adequate electrochemical stability window (ESW), which signifies the disparity between the electrolyte's oxidation and reduction potentials. In order for batteries to exhibit desirable charge and discharge performance, the PEs need to operate within a designated voltage range of the electrodes.¹¹¹ For instance, the oxidation and reduction potential of the PE must be up to 5 V and - 0.5V, respectively to ensure minimal degradation during the course of battery operation.¹¹²

Lastly, the polymer electrolytes should exhibit robust mechanical strength to effectively inhibit the growth of lithium dendrites and be suitable for large-scale manufacturing processes. According to the prediction by Newman and Monroe, the strength (in terms of storage moduli) needed to suppress Li-dendrite growth is at about $G' > 1 \text{ GPa}$ ¹¹³ which is by far out of reach for soft PEO/salt electrolytes. Designing mechanical robust PEs poses a big challenge because mechanical properties and ionic conductivity exists in a duality, efforts to optimize either one of the properties would trade off the other.^{114, 115} Therefore, it is necessary to decouple the mechanical properties of polymer electrolyte membranes from the ionic conductivity. One approach to achieve this is to create phase-separated polymer electrolytes – where one of the

phases conducts ions and the other enhances the mechanical rigidity of the heterogeneous polymer electrolyte. Hitherto, strategies like self-assembly of pre-formed block copolymer²⁷ or more recently in-situ block copolymer self-assembly by polymerization-induced microphase separation processes (PIMS)¹¹⁶ have been reported to generate such nanostructured electrolytes.

3 BLOCK COPOLYMERS AS SOLID POLYMER ELECTROLYTES

One of the many approaches that have been explored to increase percentage of amorphous phase in PEO electrolytes with the aim of increasing ion conductivity and mechanical performance is blending PEO with other polymers to combine their unique properties⁶⁴⁻⁶⁷ or covalently bonding a second distinct block of polymer to PEO.^{27, 28} Some polymers are immiscible due to the repulsive interaction between mixed components and this is exacerbated by high degree of polymerization, N .¹¹⁷ As a result, a macroscopic phase separation can occur, leading to distinct regions with bulk properties similar to those of pure polymers. This can be a major drawback for blend electrolytes.¹¹⁸ To circumvent the risk of macroscopic electrolyte failure and to enhance synergistic performance, it becomes essential to reduce phase separation to the nano-scale. This is why the use of block copolymers becomes particularly intriguing, as they offer the potential to achieve this goal.

Block copolymers (BCPs) consist of two or more chemically homogeneous polymers joined together by covalent bonds. The net repulsion between the immiscible blocks induces microphase-separation and self-assembly processes that give rise to ordered morphologies with periodically spaced nanoscopic domains.^{78, 119}

To utilize BCPs as electrolytes for lithium batteries, two primary strategies are employed to incorporate lithium ions into the ionic-conductive block based on PEO. One approach involves doping BCPs with suitable lithium salts, as seen in dual-ion block copolymer electrolytes (Dual-ion BCPEs).¹²⁰⁻¹²³ Alternatively, only the anions can be immobilized on one of the blocks, resulting in single-ion block copolymer electrolytes (Single-ion BCPEs)¹²⁴⁻¹²⁶ (see Figure 6 for illustration).

inducing microphase separation were utilized, resulting in concurrent enhancements in the mechanical properties of the system. Meanwhile, other stiff high- T_g block, such as poly(4-vinylpyridine)¹³¹, poly(lauryl methacrylate)¹²¹, poly(methyl methacrylate)^{72, 132}, poly(benzyl methacrylate)⁷³ among others have been explored to impart dimensional stability to the material to BCPEs.

Niitani *et al.*¹³³ investigated the properties of a BCPE consisting of polystyrene-*b*-poly((ethylene glycol) methyl ether methacrylate)-*b*-polystyrene (PS-POEGMA-PS) doped with LiClO₄ (EO: Li=20). The study focused on comparing two contrasting characteristics, stress at break (in MPa) and ionic conductivity (in S cm⁻¹), at RT, while varying the weight fraction of POEGMA. Figure 7 displays the evolution of these properties. At RT, the maximum ionic conductivity of 10⁻⁴ S.cm⁻¹ is achieved when the POEGMA content is at least 80%. The stress at break declines significantly with an increase in the proportion of the conductive block, dropping from 58 MPa (10% POEGMA) to 3 MPa (75% POEGMA).

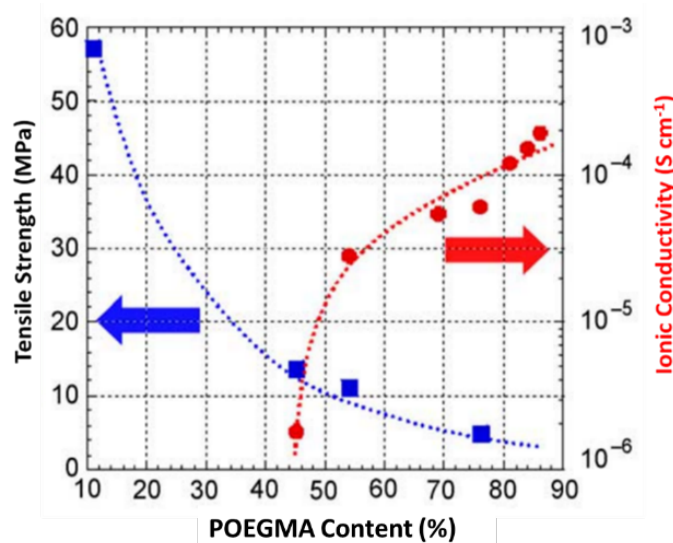


Figure 7. Effects of POEGMA content of PS-*b*-POEGMA-*b*-PS BCP on ionic conductivity and film strength.¹³³ (Copyright 2005. Elsevier B.V.)

3.2 SELF-ASSEMBLY OF BLOCK COPOLYMER ELECTROLYTES (BCPEs)

Flory-Huggins theory explains the basis for the thermodynamics of polymer mixing and there are several literatures that offer more details on this theory.¹³⁴⁻¹³⁶ For brevity, we will highlight only the essential theoretical construction needed to explain this work. The interaction energies

between the components in the block copolymer can be characterized with the Flory-Huggins interaction parameter “ χ ”, given as.

$$\chi_{AB} = \left(\frac{Z}{kT} \right) \left[\varepsilon_{AB} - \frac{1}{2} (\varepsilon_{AA} + \varepsilon_{BB}) \right] \quad 9$$

In equation 9, χ_{AB} and ε_{AB} describes respectively the interaction parameter and interaction energy between polymer A and B. Z represents the coordination number, i.e., the number of nearest neighbors per repeat unit in the lattice. When there is a net attraction between the polymer pairs, $\chi_{AB} < 0$. On the other hand, a positive χ_{AB} represents an effective repulsion between the polymer pairs.

Block copolymers (BCPs) self-assembly into well-defined morphologies is mainly driven by the balance between enthalpic and entropic contribution in the system. The free energy of mixing for a block copolymer is given as,

$$\Delta F_{mix} = kT \left[\frac{\phi}{N_A} \ln \phi + \frac{(1-\phi)}{N_B} \ln(1-\phi) + \phi \chi_{AB} (1-\phi) \right] \quad 10$$

The first two logarithmic terms are entropic contribution of the Helmholtz free energy of mixing while the third term is enthalpic contribution which depends on the interaction parameter. For a given volume fraction of each polymer block (Φ), the enthalpy of the system will scale as χ_{AB} and entropy as $1/N$. Therefore, the product χN is a relevant parameter used to describe BCP phase segregation behaviour and has been estimated to have an inverse temperature dependence.⁷⁵ By merely adjusting Φ , N , block chemistry, as well as macromolecular architecture, unique self-assembled morphologies such as spheres (SPH), cylinders (CYL), gyroids (GYR), and lamellae (LAM) can be obtained. Self-consistent mean-field phase diagram of di-block copolymer (di-BCP) is shown in **Figure 8**.

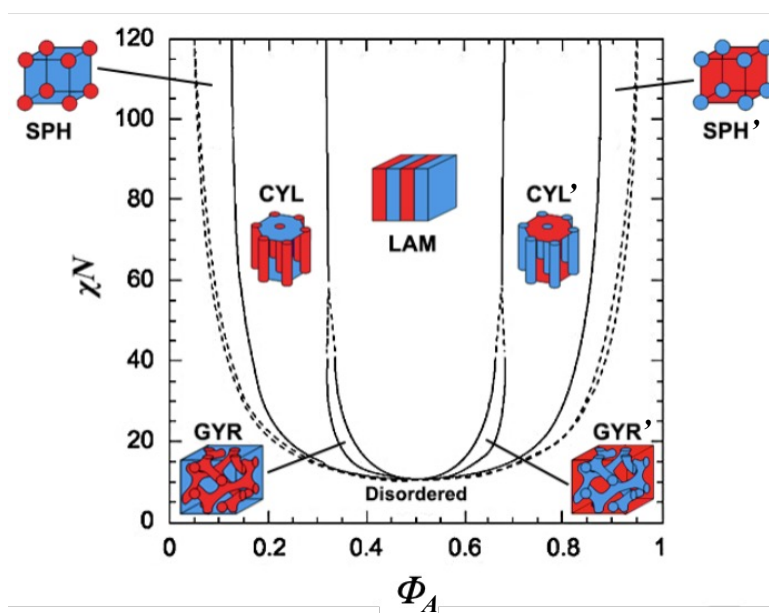


Figure 8. Self-consistent mean-field phase diagram of diblock copolymer, Hofman *et al.*¹³⁷

The phase behaviour of block copolymer can be described by three regions with reference to the segregation strength (χN): the strong segregation limit (SSL) for $\chi N > 100$, weak segregation limit (WSL) for $\chi N < 10$ (entropy dominates) and right between it is the intermediate segregation regime (ISR) for $10 < \chi N < 100$.⁷⁵ At some point when $\chi N \approx 10$, the system is in a transition state and the temperature of occurrence is described to be order-disorder transition temperature (T_{ODT}). A typical di-BCP system exhibit a symmetric phase behaviour, i.e., for similar χN values, the equilibrium phases at Φ_A and $1 - \Phi_A$ exhibit the same structure, but with an inverted arrangement.¹³⁷

3.2.1 Influence of salt-doping on the morphology of BCPEs

In dual-ion conducting BCPEs wherein neutral BCPs is doped with suitable lithium salt, ion conduction is facilitated by the local solvation of cations and anions. The local ion solvation drastically increases the incompatibility between both blocks of BCP often described by the effective Flory-Huggins parameter χ_{eff} .¹³⁸⁻¹⁴⁰ Experimental observations have revealed that salt-doping of BCPs can create ion-induced morphological variation,¹⁴¹ and increased domain spacing.^{79, 142, 143} The magnitude of these doping effects has a strong relationship with salt concentration in the solvating block. While some works have reported a linear scaling of χ_{eff} with salt concentration,¹⁴³ calculations of χ_{eff} from scattering data⁷⁵ imply that the relationship of χ_{eff} with salt concentration is indeed nonlinear, especially at higher salt concentrations.

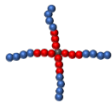
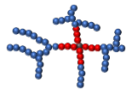
Furthermore, the full range of phase behaviour caused by the addition of ions in BCPs cannot be captured solely by a single effective parameter χ_{eff}^{144} but by defining also a fitting parameter – the ionic solvation radius.¹⁴⁰ In some case, where ion solvation of the salt is affected by both blocks, the copolymer system would not be amenable to phase separation, therefore it would remain in a mixed state.¹³²

3.2.2 Influence of BCPE Architecture

The use of advanced synthetic techniques has allowed for the design of BCPEs with complex architectures, providing new opportunities to take advantage of their unique morphologies. Numerous BCP chemistries and diverse macromolecular architectures have been investigated for their potential as electrolytes, as depicted in **Table 1**.

Table 1. Brief overview of notable BCPE architectures explored as electrolytes. Ion conducting blocks (blue) contain mainly PEO or comb-PEO while the associating block (red) represent a varied range of high- T_g polymers

Conducting block	Hard block	Architecture	Schematic	ref
Poly[oligo(oxyethylene) methacrylate]	Poly(lauryl methacrylate)	di-block		121
Poly(vinylbenzylmethoxy Poly(ethyleneoxide)ether)	Polystyrene			145
Poly(ethylene oxide)	Polystyrene			74, 77
Poly((ethylene glycol)	Polystyrene	tri-block copolymer		146, 147
Poly((ethylene glycol) methyl ether methacrylate)	Polystyrene			133
Poly (oligo ethylene glycol) methyl ether methacrylate)	Poly(benzyl methacrylate)			73
Poly(ethylene glycol) methyl ether methacrylate)	Poly(methyl methacrylate)			72
Poly(ethylene oxide)	Poly(acryloisobutyl polyhedral oligomeric silsesquioxane)			148
Poly((ethylene glycol)	Polystyrene	miktoarm		149
Poly((ethylene glycol) methyl ether methacrylate)	Polystyrene	tapered block copolymer		150
Poly(ethylene glycol) methyl ether methacrylate)	Polystyrene	inverse tapered block copolymer		150, 151

Poly((ethylene glycol) methyl ether methacrylate)	Polystyrene	star block copolymer		152
Poly[methoxy-poly(ethylene glycol) methacrylate]	Poly1[(4-cyano-4'-biphenyl) oxy] decatyl methacrylate			153
Poly-(methoxy-poly(ethylene glycol) methacrylate)	Poly[(4-cyano-4'-biphenyl) oxy] decatyl methacrylate			154
Poly(ethylene glycol) methyl ether methacrylate	Polystyrene	hyper-branched block copolymer		155

AB di-block is the simplest type of BCPs, making its symmetric phase diagram (except for BCPs with highly polydisperse molar masses¹⁵⁶) from SCFT (self-consistent field theory) a fundamental basis for understanding the phase behaviour of BCPs. However, incorporating a third component or a different macromolecular chain architecture in BCPs makes it challenging to create a SCFT phase diagram. This is because the covalent connection of blocks can impact self-assembly due to changes in translational and configurational entropy.¹¹⁹ Fortunately, thanks to the efforts of materials theorists, SCFT phase diagrams are now available for ABA triblocks,^{157, 158} multiblocks,¹⁵⁹ diblock-arm stars,¹⁶⁰ triblock-arm stars,¹⁶¹ miktoarm stars,^{161, 162} branched diblocks,^{163, 164} and multigraft combs¹⁶⁵. Although the topology of the phase diagrams remains relatively unaffected by differences in architecture, the phase boundaries can shift significantly with composition.¹⁶⁶

Six-arm diblock star PS-*b*-POEGMA BCP with discotic liquid crystal core have been reported to exhibit ionic conductivities that are eightfold greater than those of the corresponding linear BCPE. This enhancement is attributed to the increased flexibility of their arms and the long-range molecular orientation by combining the advantages of star architecture and liquid crystals.¹⁵² Lee *et al.*¹⁴⁹ showed that three-arm PEO connected to a PS block in a miktoarm BCP configuration simultaneously increased conductivity and modulus compared to their linear analogue. They explained that such miktoarm arrangement promoted long-range narrow lamellar morphology due to densification of the chains, thus enhancing ion-chain dynamics. In a recent study by Chakraborty *et al.*¹⁴⁸ it was found that arranging PEO chains in a triblock copolymer configuration with poly(acryloisobutyl polyhedral oligomeric silsesquioxane) as the external block effectively hinders plastic deformation.

3.3 CONDUCTIVITY OF BLOCK COPOLYMER ELECTROLYTES.

When lithium ions move from one electrode to the other, the transport is governed at two levels: intragrain and intergrain transport. Intragrain transport refers to the conduction that occurs within the boundaries of individual grains, while intergrain transport relates to the connectivity of conducting pathways across these grain boundaries.^{44, 167} Therefore, the morphology and grain alignment (see illustration in **Figure 9**) play a crucial role in determining the ionic conductivity (in-plane or through-plane), represented by σ . This principle also applies to properties associated with the other phase in BCPE, such as mechanical strength.

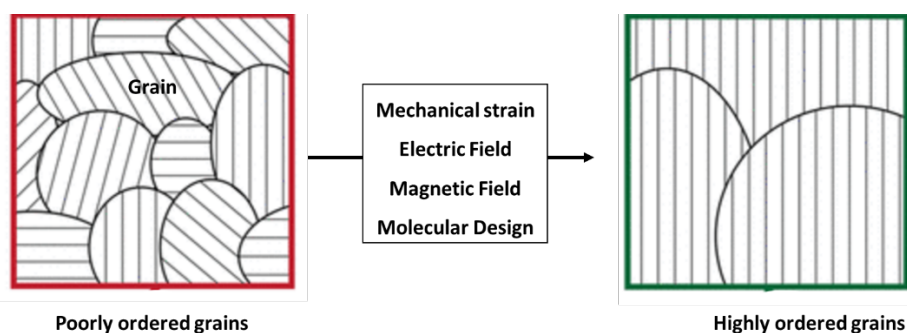


Figure 9. Illustration of methods for grain enlargement and alignment in BCPs.

Ideally, the conductivity of the BCPE (σ) is expected to increase with the conductivity of the pure conducting phase (σ_0) and the volume fraction of the conducting phase (Φ_c). However, other factors such as the tortuosity factor (τ) and morphological factor (f) can also impact conductivity. τ represents the ratio of the effective path length required for ion transport to the thickness of the electrolyte and f describes the global grain alignment in the direction of the electric field. Initially, Sax and Ottino developed a widely adopted model based on effective medium theory to calculate f in the context of diffusion of small molecules in randomly oriented morphologies relevant to block copolymer materials.¹⁶⁸ This model is widely used to predict conductivity in block copolymer materials (see equation 11).⁴⁴

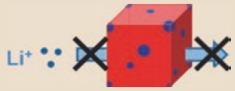
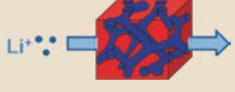
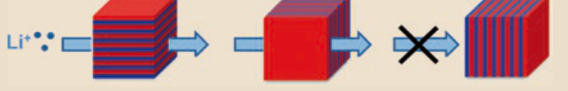
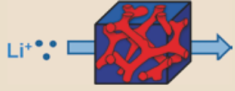
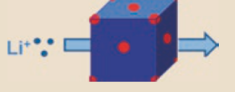
$$\sigma = \frac{f}{\tau} \phi_c \sigma_0 \quad 11$$

Where σ_0 is the conductivity of the pure conductive phase of the BCPE. Values of f and τ^{-1} for various morphologies were reported in Table 2.⁴⁴ However, it is important to note that the values reported therein reflect an ideal case of perfect global alignment of grains with respect to the x, y, and z directions of a cartesian coordinate system. In real systems, a couple of factors

causes BCPEs to deviate from the effective medium theory. Factors such as i) dead zone effects – reduced segmental motion and decreased ion solvation at interface between the conducting non-conducting phases,^{146, 169, 170} ii) grain boundary effects – lack of alignment at boundary between two grains (characteristic size $\sim 10 - 100$ nm),^{171, 172} iii) electrolyte processing effects – unfavourable re-orientation of ion-conducting pathways,^{172, 173} could depress the effective mobility of ions. Altogether, these effects emphasize the importance of retaining long-range ordering as well as 3D continuity of conducting pathways. Bouchet *et al.*¹⁴⁶ reported on the existence of a ‘dead zone’, excluded from ionic transport, at the PS/PEO interface of PS-*b*-PEO-*b*-PS triblock copolymer. The thickness of this zone was experimentally determined to include about 4–5 EO units (ca 1.6 nm).

Traditional methods using mechanical handling,¹⁷⁴⁻¹⁷⁶ electrical,^{177, 178} and magnetic field¹⁷⁹⁻¹⁸² have been explored to enforce grain alignment of BCPs with decent level of successes. In the same vein, bottom-up approaches like macromolecular engineering of block components have demonstrated similar successes. For example, tapered BCPEs (refer to **Table 1**) and BCP/Homopolymer blend electrolytes have been utilized to overcome dead zone effects as well as to promote bi-continuous 3D structures with higher ionic conductivities and mechanical performance.^{150, 183-185} Lamellar morphologies of star BCPEs have also shown to exhibit higher ionic conductivities compared to their linear analogues^{152, 186} which is reportedly connected to the long-range ordering of the ionic paths that transcends grain dimensions.

Table 2. Morphology and Tortuosity factors for transport in ion-conducting block copolymers with specified morphology. Taken from literature ⁴⁴

Morphology		f	τ^{-1}
Conducting Spheres		0	1
Conducting Cylinders		1/3	1
Conducting Minor Gyroid		1	1/2
Lamellae		2/3	1
Conducting Gyroid Matrix		1	4/5
Cylinders in Conducting Matrix		1	$\frac{1}{2 - \phi_c}$
Spheres in Conducting Matrix		1	$\frac{2}{3 - \phi_c}$

4 POLYMERIZATION INDUCED MICROPHASE SEPARATION (PIMS)

The prevailing literature on BCPEs has primarily focused on influencing the equilibrium states of these materials using diverse approaches. These strategies encompass adjustments in molecular design, blocking chemistry, degrees of polymerization (N), and blocking ratios, among others.

Typical BCPEs lack long-ranged continuity except ones featuring gyroid morphology. The gyroid morphologies are typically limited by a specific range of block volume fractions in which they occur.¹⁸⁷ Moreover, typical BCPEs require cumbersome processing steps prior to final integration in batteries, and may be amenable to post-processing effects that may originally impact morphology. To this end, investigation into new processes to create nanostructures that feature two co-continuous, percolating domains are critically required. In recent times, there has been an endeavour to engineer SPEs that mirror the bi-continuous gyroid morphologies observed in BCPEs by polymerization-induced micro-phase separation (PIMS).

4.1 WHAT IS PIMS?

PIMS refers to the fact that the in-situ synthesis of block copolymer in bulk is associated with simultaneous self-assembly; as growing of second block is concomitant to self-assembly, the phase separation is induced by polymerization (see **Figure 10**).¹⁸⁸ The specific nature of the phase separation induced by this process depends on factors such as the reaction kinetics, the thermodynamics of the system, and the starting composition of the material. By understanding and controlling these factors, researchers can manipulate the phase behaviour of materials and develop new materials with desired properties.

In 1996, Hellmann *et al.* first reported on the evolution of phase patterns during radical polymerization of styrene containing dissolved polybutadiene (PB).¹⁸⁹ The reaction led, intermediately, to blends of yet ungrafted PB, of the homopolymer PS, and of graft copolymers PB-g-S varying in the number of PS grafts per PB chain, effectively prompting phase separation and subsequent phase inversion at distinct stages of the process. Later, Motokawa's group provided valuable insights into the dynamic behaviour of poly(methyl methacrylate)-

block-polystyrene (PMMA-*b*-PS) block copolymers during synthesis and sheds light on the formation of various microstructures, contributing to a deeper understanding of microphase separation phenomena.^{190, 191} A sequence of transformation was observed, starting from a homogeneous solution, progressing to a disordered state, then forming a Lamellar (LAM) structure, further transforming into a Hexagonally Packed Cylinders (HEX) configuration, and finally achieving a Body-Centered Cubic (BCC) arrangement through chain extension polymerization of styrene from the end of PMMA macromolecular chain transfer agent (macroCTA. A macroCTA is a reactive block synthesized by reversible deactivation radical polymerization (RDRP), most often by reversible addition fragmentation transfer polymerization (RAFT), exhibiting chain end functionality able to chain extend the polymerization of a second monomer by RAFT polymerization.

PIMS has attracted significant attention in recent years since the following the work of Hillmyer *et al.*¹⁹² due to its potential for creating advanced materials with tailored properties. It has been explored for various applications, including nanoporous membranes,¹⁹³⁻¹⁹⁹ biomedical membranes,²⁰⁰ and energy storage devices.^{116, 201-207}

4.2 PIMS SPE FOR BATTERY

Till date, investigations have documented the fabrication of solid polymer electrolytes (SPEs) using the Polymerization-induced micro-phase separation (PIMS) technique, utilizing initiators of radical polymerization that are triggered by either thermal decomposition (thermal-RAFT)^{116, 201-205} or photon activation (photo-RAFT)^{206, 207} as shown in Table 3. The fabrication protocol for solid polymer electrolyte necessitates a meticulous choice of chemistry to achieve specific performance properties. A common trend in these studies is the utilization of PEO polymers (PEO-TTC) with reactive trithiocarbonate chain end (TTC) as macroCTAs. The PEO nanophase exhibits a strong ionic affinity towards ionic salts.

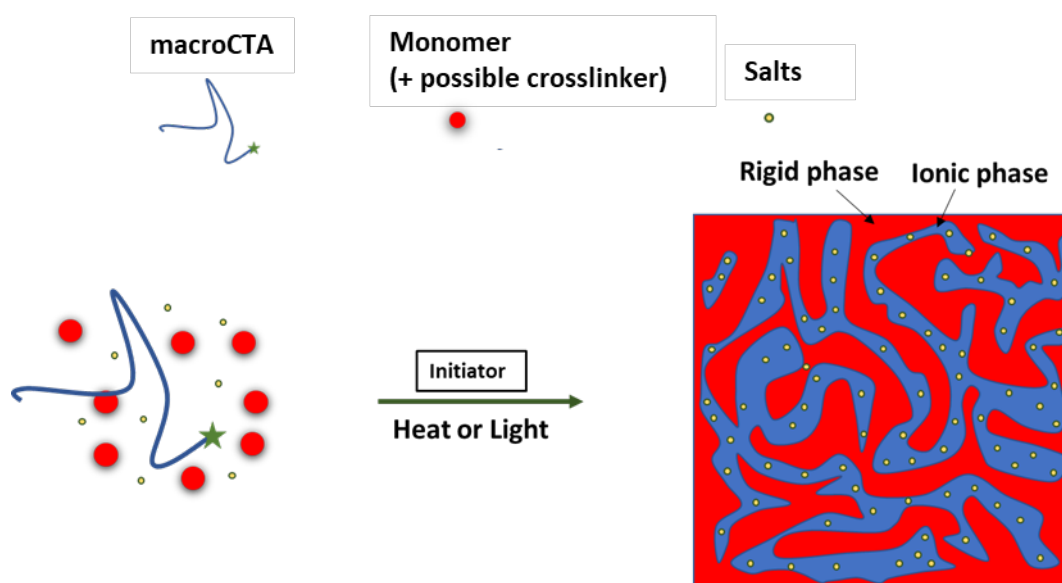


Figure 10. Scheme for SPE fabrication by PIMS mediated by a macroCTA.

The work by Hillmyer and Lodge serves as an early exemplar, elucidating the application of PIMS for SPE design through RAFT polymerization initiated by a thermally activated benzoyl peroxide initiator.¹¹⁶ Initiating with a precisely calculated blend of styrene/divinyl benzene monomers, 1-butyl-3-methylimidazolium bis(trifluoromethylsulfonyl)imide (BMITFSI) ionic liquids (IL), lithium bis(trifluoromethanesulfonyl)imide (LiTFSI), and PEO-TTC (depicted in **Figure 10**), they effectively achieved the formation of a dual-phase network after polymerizing for at least 20 h at 120 °C. The network consisted of a crosslinked polystyrene rigid phase alongside an ion-conductive PEO/ionic moieties phase (IL/LiTFSI) following the execution of the PIMS procedure. Through the use of hydroiodic acid for chemical etching of the PEO phase, the inherent 3-D interconnected structures of cross-linked polystyrene (PS) within the SPE resulting from the PIMS process can be unveiled (Figure 11b). It is noteworthy that the conducting domains consisting of PEO are primarily continuous, allowing for ionic conductivity to approach its theoretical maximum. Moreover, minor adjustments in the cross-link density of the PS phase by adding divinyl benzene crosslinker (DVB) does not impact the conductivity of the material, because mechanical and transport properties are decoupled via microphase separation. Finally, the PIMS SPEs demonstrated exceptional mechanical stability at high temperatures ($G' \geq 10^8$ Pa at $T \leq 200$ °C, Figure 11d) in comparison to linear PEO-*b*-PS electrolytes ($G' = 10^8$ Pa at $T = 90$ °C)²⁰⁸, which experience a significant decrease in elastic

modulus beyond 100 °C. This was attributed to the crosslinked nature of the electrolytes which helps it remain solid at elevated temperature, where the conductivity is maximized.

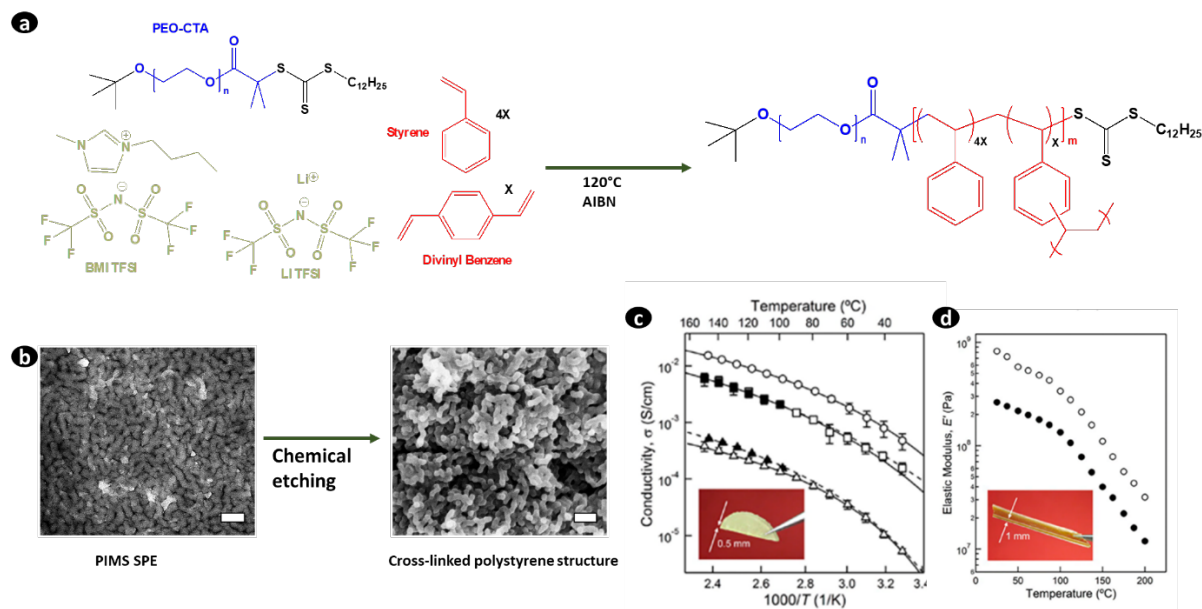


Figure 11. a) Reaction scheme used to prepare polymerization induced microphase separation solid polymer electrolytes (PIMS SPEs) b) The morphology of the PIMS-fabricated SPE sample, utilizing PEO-CTA with a molecular weight of 28 kg mol $^{-1}$ and 21 vol% BMITFSI, examined prior to etching (TEM) and after etching (SEM) of the PEO and BMITFSI components using a 57 wt% aqueous hydroiodic acid solution. c) Ionic conductivity as a function of temperature for PIMS SPEs prepared with 5 kg mol $^{-1}$ PEO-CTA (CTA = chain transfer agent). Open symbols: Samples prepared with BMITFSI. Filled symbols: Samples prepared with a 1 M mixture of LiTFSI in BMITFSI. Overall salt concentrations are 5 (Δ), 7 (\blacktriangle), 21 (\square and \blacksquare), and 40 vol % (\circ). d) Temperature-dependent linear elastic response of PIMS SPEs prepared with 28 kg mol $^{-1}$ PEO-CTA and no ionic liquid (\circ) and with 21 vol % BMITFSI (\bullet) (Adapted from the work of Schulze *et al.*¹¹⁶).

Table 3. A summary of PIMS SPEs investigated to date.

MacroCTA	Matrix	Ionic Component	Method	σ /Scm ⁻¹	G'/Pa	Year	Comment	Ref
PEO-TTC	S/DVB	BMITFSI /LiTFSI	Thermal-RAFT	1.7×10^{-4} @ 30°C	1×10^9	2014	Electrolyte for lithium batteries	Schulze <i>et al.</i> ¹¹⁶
PEO-TTC	S/DVB	BMITFSI	Thermal-RAFT	N/A	1×10^9	2015	Mechanistic study	McIntosh <i>et al.</i> ²⁰²
PEO-TTC	S/DVB	[HEIm][TFSI] Protic IL	Thermal-RAFT	3.0×10^{-4} @ 40°C	5×10^7	2016	Electrolyte for fuel cells	Chopade <i>et al.</i> ²⁰³
PEO-TTC	S/DVB	SN/LiTFSI	Thermal-RAFT	2.0×10^{-3}	3×10^8	2017	Electrolyte for lithium-ion batteries	Chopade <i>et al.</i> ²⁰⁴
PEO-TTC	IBOA/TMPTA	BMITFSI	Photo-RAFT	3.0×10^{-4}	2×10^8	2022	Practical demonstration in supercapacitor	Lee <i>et al.</i> ²⁰⁶
PEO-TTC	S/DVB /Acetonitrile	POM	Thermal-RAFT	4.0×10^{-4} @ 50°C	n/a	2022	Electrolyte for fuel cells and lithium-ion batteries	Liu <i>et al.</i> ²⁰⁵
POEGMA-TTC (linear)	IBoA/TMPTA	BMITFSI	Photo-RAFT	1.2×10^{-4}	2×10^8	2023	Practical demonstration in supercapacitor	Melodia <i>et al.</i> ²⁰⁷

Abbreviations:

S: Styrene, DVB: Divinyl Benzene, IBoA: Isobonyl Acrylate, TMPTA: Trimethylolpropane triacrylate, PC: Propylene carbonate, BMITFSI: 1-Butyl-3-methylimidazolium bis(trifluoromethylsulfonyl)imide. SN: Succinonitrile, POM: Polyoxometalates.

N/A: not applicable.

A mechanistic study on how this nanoscale morphology is formed in such thermal-RAFT PIMS process was presented by McIntosh *et al.*²⁰² They performed a series of *in-situ*, time-resolved experiments – small-angle X-ray scattering, conductivity, rheology, and polymerization kinetic – to monitor the electrolyte evolution from a macroscopically homogeneous liquid to a microphase-separated solid (**Figure 12**).

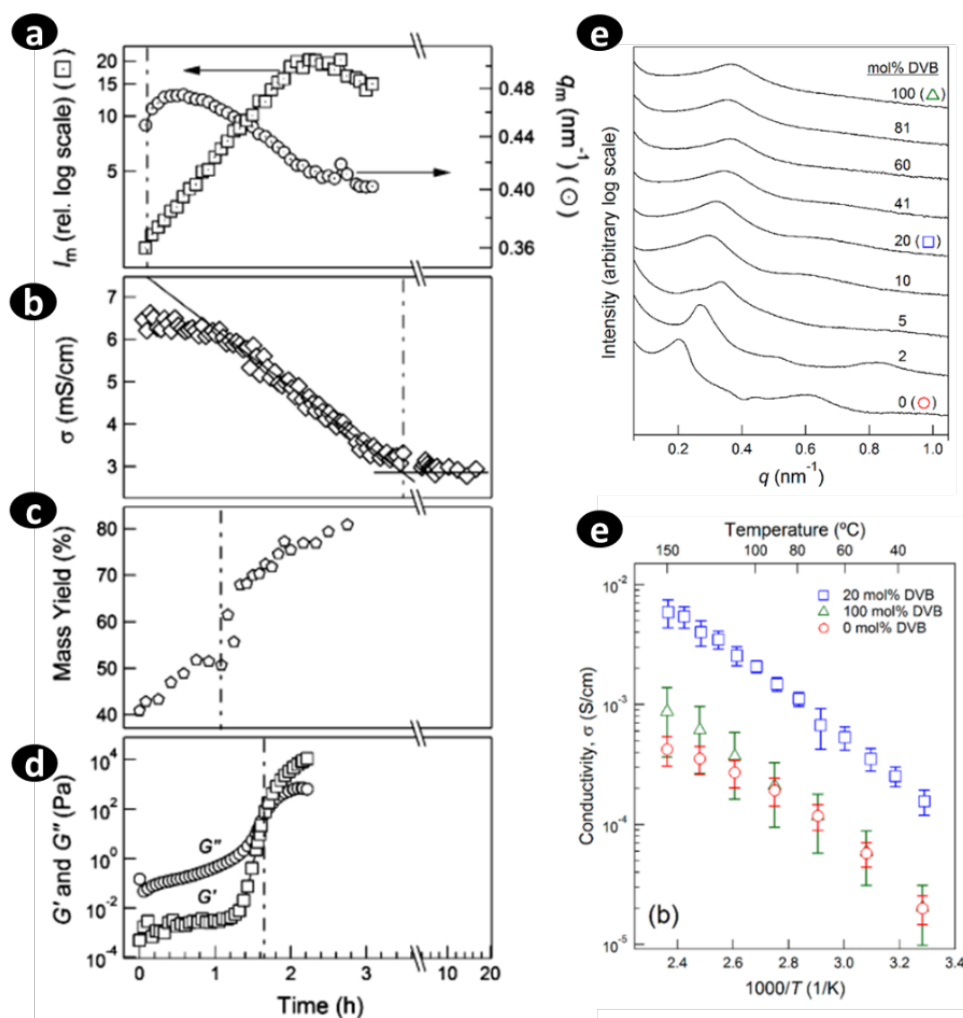


Figure 12. Comparison of a) SAXS, b) conductivity, c) mass yield, and d) rheology *in-situ* experiments for a sample prepared with 21 vol % BMITFSI. I_m is the maximum scattered intensity of the structure factor peak at wave vector q_m . The solid black lines in panel b) were used to determine time at which conductivity plateaus. The dash-dot lines indicate the characteristic time scale associated with each experiment. e) SAXS data for samples prepared with 5 kg/mol PEO-CTA, 21 vol % BMITFSI, and S/DVB, with varying concentration of DVB. Note that the radical initiator AIBN was not used in the preparation of these samples. Reduced cross-linker content leads to materials exhibiting Bragg-like diffraction and long-range order. e) Temperature-dependent conductivity as a function of DVB concentration. Error bars represent one standard deviation based on three or more samples. (Taken from the work of McIntosh *et al.*²⁰²).

These time-resolved experiments revealed that at $t \approx 1$ h, discrete flocs of cross-linked polymers are formed. The local viscosity and elastic modulus increased continuously until it reaches the apparent gel point at $t \approx 1.7$ h. At this point, the growing block polymer already formed well-defined domains and the individual chains would not be able to rearrange after gelation. This suggested that the interconnection of the network was a direct result of chemical cross-linking the diblock polymer before the order-disorder transition (ODT) preceded by strong isotropic concentration fluctuations. This conclusion was validated by analysing the scattering pattern of samples with varying mole fractions of the cross-linking agent (DVB) in the monomer mixture. The observations revealed that reducing crosslinker leads to better defined morphology.

In the same polymeric system, Chopade *et al.*²⁰³ replaced the ionic species of BMITFSI with [HEIm][TFSI] protic ionic liquid. The goal was to strategically adapt the PIMS approach to fabricate SPEs suited for fuel cells. Following this, their investigations ventured into incorporating succinonitrile (SN) as a plasticizer and LiTFSI salt as the chosen ionic specie.²⁰⁴ This methodology transformed the conducting pathways based on PEO into a fully amorphous structure, thereby enabling facile ion transport. This led to a conductivity of approximately 0.35 mS/cm and an elastic modulus of around 0.3 GPa at a temperature of 30°C.

In a ground-breaking study, Lee *et al.* demonstrated the fabrication of 3D printed nanostructured electrolytes specifically designed for symmetric carbon supercapacitors (Figure 13a and Figure 13b).²⁰⁶ They implemented photo-RAFT for PEO-TTC chain extension with isobornyl acrylate (IBoA) and trimethylpropane triacrylate (TMPTA) monomers, within a mixture of BMITFSI IL. This process rapidly generated a second bi-continuous phase of poly(isobornyl acrylate-*stat*-trimethylpropane triacrylate) (P(IBoA-*stat*-TMPTA)) within minutes (Figure 13c), leveraging the fast kinetics associated with photopolymerization processes. The resulting solid polymer electrolyte (SPE) exhibited good electromechanical properties, including a high shear modulus ($G' > 10^8$ Pa) and an impressive conductivity of 3×10^{-4} S cm⁻¹ at RT (22°C), as shown in Figure 13d and Figure 13e respectively. It is perhaps important to note that conductivity reported is due to BMI⁺ and TFSI⁻ ions. The utilization of photo-PIMS offers distinct advantages over thermal-PIMS processes in terms of design flexibility, fabrication time, scalability, and direct industrial application. Subsequently, Melodia *et al.* expanded the possibilities for SPE development by employing non-crystalline

POEGMA-TTC in lieu of semi-crystalline PEO-TTC to enhance macromolecular chain dynamics at RT.²⁰⁷

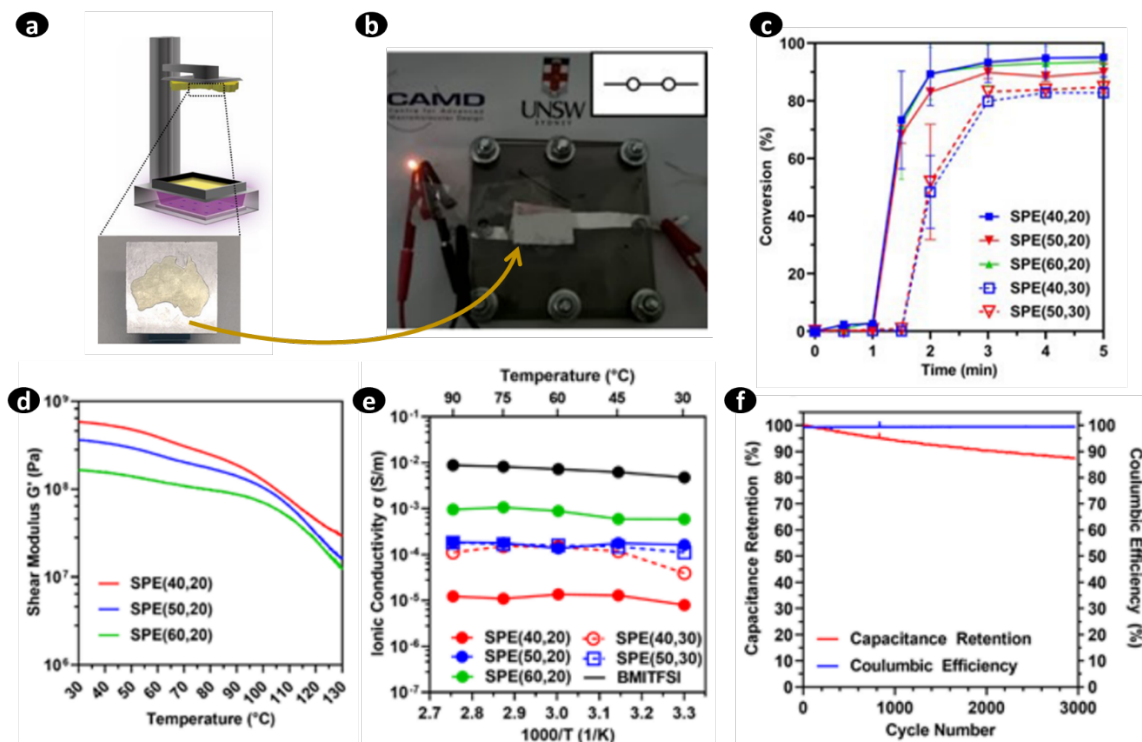


Figure 13. a) 3D printing process used to fabricate SPE(60,20) into an Australia-shaped geometry, total build stage width is 60 mm b) Powering an LED using the assembled 3D printed SPE supercapacitor c) Vinyl bond conversion vs time during exposure to violet light ($\lambda_{\text{max}} = 405 \text{ nm}$, $I_0 = 2.06 \text{ mW cm}^{-2}$) for each SPE formulation d) storage modulus (G') with increasing temperature for SPEs with $r_{\text{PEO}} = 20$ and varied BMITFSI IL content e) ionic conductivities as a function of temperature f) capacitance retention of a symmetric carbon supercapacitor with the SPE(60,20) electrolyte. (Taken from the work of Lee *et al.*²⁰⁶).

5 CONCLUSION

As previously mentioned, PEO-based BCPEs have garnered significant attention due to their typical advantages such as a low T_g , chain flexibility, effective dissociation of lithium salt and electrochemical stability against lithium-metal. Notably, there has been a growing focus on comb PEO systems as they exhibit diminished crystallinity in contrast to their linear PEO counterparts.

Existing literature regarding BCPEs provides substantial evidence that altering the architecture of these copolymers can profoundly influence their eventual morphology, mechanical traits, and even conductivity. Nevertheless, a multitude of questions regarding the intricate interplay between complex architectures and BCPE properties still linger. Inquiries such as the potential influence of block positional arrangements (both outer and inner blocking) of the conducting phase within these architectures, as well as the consequences of arm density on the characteristics of star BCPEs, remain unresolved, to name just a few. Meanwhile, accurate comparison of architectures with their linear analogues can pose a slight challenge because of the intricacies of the synthetic approach for macromolecules with such complex architecture.

The main objective of the present PhD thesis is to unravel ways of regulating self-assembly in BCPEs which major focus on the relationship between structure-property block copolymer templates.

6 REFERENCES

1. ÓhAiseadha, C.; Quinn, G.; Connolly, R.; Connolly, M.; Soon, W., Energy and Climate Policy—An Evaluation of Global Climate Change Expenditure 2011–2018. *Energies* **2020**, *13* (18).
2. Stram, B. N., Key challenges to expanding renewable energy. *Energy Policy* **2016**, *96*, 728-734.
3. Michael, S.; Franz, B., Definition and Classification of Energy Storage Systems. In *Handbook of Energy Storage*, Stadler ed.; Stadler, Ed. Springer-Verlag GmbH Germany, Heidelberg, 2019.
4. Pullen, K. R., 11 - Flywheel energy storage. In *Storing Energy (Second Edition)*, Letcher, T. M., Ed. Elsevier: 2022; pp 207-242.
5. Ingo, S.; Franz, B.; Marcus, B.; Eduard, H.; Daniel, W., Mechanical Energy Storage. In *Handbook of Energy Storage*, Stadler ed.; Stadler, Ed. Springer-Verlag GmbH Germany, Heidelberg, 2019.
6. Ingo, S.; Andreas, H.; Thomas, B., Thermal Energy Storage. In *Handbook of Energy Storage*, Stadler ed.; Stadler, Ed. Springer-Verlag GmbH Germany, Heidelberg, 2019.
7. Michael, S.; Franz, B.; Fritz, C.; Fabian, E.; Christian, v. O.; Daniel, T.; Martin, T., Chemical Energy Storage. In *Handbook of Energy Storage*, Stadler ed.; Stadler, Ed. Springer-Verlag GmbH Germany, Heidelberg, 2019.
8. Dutta, A.; Mitra, S.; Basak, M.; Banerjee, T., A comprehensive review on batteries and supercapacitors: Development and challenges since their inception. *Energy Storage* **2023**, *5* (1), e339.
9. Xie, J.; Lu, Y.-C., A retrospective on lithium-ion batteries. *Nature Communications* **2020**, *11* (1), 2499.
10. Grey, C. P.; Hall, D. S., Prospects for lithium-ion batteries and beyond—a 2030 vision. *Nature Communications* **2020**, *11* (1), 6279.
11. Tian, Y.; Zeng, G.; Rutt, A.; Shi, T.; Kim, H.; Wang, J.; Koettgen, J.; Sun, Y.; Ouyang, B.; Chen, T.; Lun, Z.; Rong, Z.; Persson, K.; Ceder, G., Promises and Challenges of Next-Generation “Beyond Li-ion” Batteries for Electric Vehicles and Grid Decarbonization. *Chemical Reviews* **2021**, *121* (3), 1623-1669.
12. Walter, M.; Kovalenko, M. V.; Kravchyk, K. V., Challenges and benefits of post-lithium-ion batteries. *New Journal of Chemistry* **2020**, *44* (5), 1677-1683.
13. Blomgren, G. E., The Development and Future of Lithium Ion Batteries. *Journal of The Electrochemical Society* **2016**, *164* (1), A5019-A5025.
14. Eftekhari, A., On the Theoretical Capacity/Energy of Lithium Batteries and Their Counterparts. *ACS Sustainable Chemistry & Engineering* **2019**, *7* (4), 3684-3687.
15. Nishi, Y., Lithium ion secondary batteries; past 10 years and the future. *J. Power Sources* **2001**, *100* (1), 101-106.
16. Karuppasamy, K.; Reddy, P. A.; Srinivas, G.; Sharma, R.; Tewari, A.; Kumar, G. H.; Gupta, D., An efficient way to achieve high ionic conductivity and electrochemical stability of safer nonaflate anion-based ionic liquid gel polymer electrolytes (ILGPEs) for rechargeable lithium ion batteries. *Journal of Solid State Electrochemistry* **2017**, *21* (4), 1145-1155.
17. Chatterjee, K.; Sridhar, M. K.; Kumar Singh, A.; Kumar Sahu, K., Application of Ionic Liquids in Rechargeable Li-Ion Batteries: A Comprehensive Guide to Design, Synthesis and Computational Aspects. **2023**.

18. Jow, T. R.; Delp, S. A.; Allen, J. L.; Jones, J.-P.; Smart, M. C., Factors Limiting Li⁺ Charge Transfer Kinetics in Li-Ion Batteries. *Journal of The Electrochemical Society* **2018**, *165* (2), A361.
19. Lee, J.; Oh, G.; Jung, H.-Y.; Hwang, J.-Y., Silicon Anode: A Perspective on Fast Charging Lithium-Ion Battery. *Inorganics* **2023**, *11* (5), 182.
20. Li, Y.; Shapter, J. G.; Cheng, H.; Xu, G.; Gao, G., Recent progress in sulfur cathodes for application to lithium–sulfur batteries. *Particuology* **2021**, *58*, 1-15.
21. House, R. A.; Marie, J.-J.; Pérez-Osorio, M. A.; Rees, G. J.; Boivin, E.; Bruce, P. G., The role of O₂ in O-redox cathodes for Li-ion batteries. *Nature Energy* **2021**, *6* (8), 781-789.
22. Yao, R.; Jun-sheng, F.; Yong-zhu, F., Recent strategies for improving the performances of rechargeable lithium batteries with sulfur- and oxygen-based conversion cathodes. *Recent strategies for improving the performances of rechargeable lithium batteries with sulfur- and oxygen-based conversion cathodes* **2023**, *3* (2), 300015.
23. Liang, Y.; Zhao, C. Z.; Yuan, H.; Chen, Y.; Zhang, W.; Huang, J. Q.; Yu, D.; Liu, Y.; Titirici, M. M.; Chueh, Y. L.; Yu, H.; Zhang, Q., A review of rechargeable batteries for portable electronic devices. *InfoMat* **2019**, *1* (1), 6-32.
24. Armand, M.; Tarascon, J. M., Building better batteries. *Nature* **2008**, *451* (7179), 652-657.
25. Tarascon, J. M.; Armand, M., Issues and challenges facing rechargeable lithium batteries. *Nature* **2001**, *414* (6861), 359-367.
26. Zheng, J.; Kim, M. S.; Tu, Z.; Choudhury, S.; Tang, T.; Archer, L. A., Regulating electrodeposition morphology of lithium: towards commercially relevant secondary Li metal batteries. *Chemical Society Reviews* **2020**, *49* (9), 2701-2750.
27. Phan, T. N. T.; Issa, S.; Gigmès, D., Poly(ethylene oxide)-Based Block Copolymer Electrolytes for Lithium Metal Batteries. *Polymer International* **2019**, *68* (1), 7-13.
28. Hallinan, D. T.; Mullin, S. A.; Stone, G. M.; Balsara, N. P., Lithium Metal Stability in Batteries with Block Copolymer Electrolytes. *Journal of The Electrochemical Society* **2013**, *160* (3), A464-A470.
29. Xu, K., Nonaqueous Liquid Electrolytes for Lithium-Based Rechargeable Batteries. *Chemical Reviews* **2004**, *104* (10), 4303-4418.
30. Leung, K., Two-Electron Reduction of Ethylene Carbonate: A Quantum Chemistry Re-Examination of Mechanisms. *ECS Meeting Abstracts* **2013**, *MA2013-01* (5), 342.
31. An, S. J.; Li, J.; Daniel, C.; Mohanty, D.; Nagpure, S.; Wood, D. L., The state of understanding of the lithium-ion-battery graphite solid electrolyte interphase (SEI) and its relationship to formation cycling. *Carbon* **2016**, *105*, 52-76.
32. Heiskanen, S. K.; Kim, J.; Lucht, B. L., Generation and Evolution of the Solid Electrolyte Interphase of Lithium-Ion Batteries. *Joule* **2019**, *3* (10), 2322-2333.
33. Zhang, S. S.; Xu, K.; Jow, T. R., EIS study on the formation of solid electrolyte interface in Li-ion battery. *Electrochimica Acta* **2006**, *51* (8), 1636-1640.
34. Armand, M. B., Polymer Electrolytes. *Annual Review of Materials Science* **1986**, *16* (1), 245-261.
35. Meng, F.; Zhu, S.; Gao, J.; Zhang, F.; Li, D., Effect of electrolyte additives on the performance of lithium-ion batteries. *Ionics* **2021**, *27* (9), 3821-3827.
36. Park, S.; Jeong, S. Y.; Lee, T. K.; Park, M. W.; Lim, H. Y.; Sung, J.; Cho, J.; Kwak, S. K.; Hong, S. Y.; Choi, N.-S., Replacing conventional battery electrolyte additives

with dioxolone derivatives for high-energy-density lithium-ion batteries. *Nature Communications* **2021**, *12* (1), 838.

37. Croy, J. R.; Abouimrane, A.; Zhang, Z., Next-generation lithium-ion batteries: The promise of near-term advancements. *MRS Bulletin* **2014**, *39* (5), 407-415.
38. Zhang, Z.; Hu, L.; Wu, H.; Weng, W.; Koh, M.; Redfern, P. C.; Curtiss, L. A.; Amine, K., Fluorinated electrolytes for 5 V lithium-ion battery chemistry. *Energy & Environmental Science* **2013**, *6* (6), 1806-1810.
39. Luiso, S.; Fedkiw, P., Lithium-ion battery separators: Recent developments and state of art. *Current Opinion in Electrochemistry* **2020**, *20*, 99-107.
40. Flamme, B.; Rodriguez Garcia, G.; Weil, M.; Haddad, M.; Phansavath, P.; Ratovelomanana-Vidal, V.; Chagnes, A., Guidelines to design organic electrolytes for lithium-ion batteries: environmental impact, physicochemical and electrochemical properties. *Green Chemistry* **2017**, *19* (8), 1828-1849.
41. Hallinan, D. T.; Balsara, N. P., Polymer Electrolytes. *Annual Review of Materials Research* **2013**, *43*, 503-525.
42. Wohlfahrt-Mehrens, M.; Vogler, C.; Garche, J., Aging mechanisms of lithium cathode materials. *J. Power Sources* **2004**, *127* (1), 58-64.
43. Li, Q.; Chen, J.; Fan, L.; Kong, X.; Lu, Y., Progress in electrolytes for rechargeable Li-based batteries and beyond. *Green Energy & Environment* **2016**, *1* (1), 18-42.
44. Hallinan, D. T.; Villaluenga, I.; Balsara, N. P., Polymer and Composite Electrolytes. *MRS Bulletin* **2018**, *43* (10), 759-767.
45. Kotobuki, M., Polymer Electrolytes. *Polymer Electrolytes: Characterization Techniques and Energy Applications* **2020**, 1-22.
46. Brandell, D.; Hernandez, G.; Mindemark, J., *Polymer-based Solid State Batteries*. De Gruyter: Uppsala University, Sweden, 2021.
47. Wright, P. V., Electrical conductivity in ionic complexes of poly(ethylene oxide). *British Polymer Journal* **1975**, *7* (5), 319-327.
48. Armand, M. B.; Duclot, M. Electrochemical generators for producing current and new materials for their manufacture. U.S. Patent 4303748A, 12 January 1978, 1981.
49. Li, Y.; Liu, M.; Duan, S.; Liu, Z.; Hou, S.; Tian, X.; Cao, G.; Jin, H., A High-Voltage Hybrid Solid Electrolyte Based on Polycaprolactone for High-Performance all-Solid-State Flexible Lithium Batteries. *ACS Applied Energy Materials* **2021**, *4* (3), 2318-2326.
50. Yang, M.; Zhao, B.; Li, J.; Li, S.; Zhang, G.; Liu, S.; Cui, Y.; Liu, H., Modified Poly(vinylidene fluoride-co-hexafluoropropylene) Polymer Electrolyte for Enhanced Stability and Polymer Degradation Inhibition toward the Li Metal Anode. *ACS Applied Energy Materials* **2022**, *5* (7), 9049-9057.
51. Wang, S. H.; Kuo, P. L.; Hsieh, C. T.; Teng, H., Design of poly(acrylonitrile)-based gel electrolytes for high-performance lithium ion batteries. *ACS Appl Mater Interfaces* **2014**, *6* (21), 19360-70.
52. Zhang, X.; Xu, B.-Q.; Lin, Y.-H.; Shen, Y.; Li, L.; Nan, C.-W., Effects of Li_{6.75}La₃Zr_{1.75}Ta_{0.25}O₁₂ on Chemical and Electrochemical Properties of Polyacrylonitrile-based Solid Electrolytes. *Solid State Ion.* **2018**, *327*, 32-38.
53. Kimura, K.; Tominaga, Y., Understanding Electrochemical Stability and Lithium Ion-Dominant Transport in Concentrated Poly(ethylene carbonate) Electrolyte. *ChemElectroChem* **2018**, *5* (24), 4008-4014.

54. Mindemark, J.; Lacey, M. J.; Bowden, T.; Brandell, D., Beyond PEO—Alternative host materials for Li⁺-conducting solid polymer electrolytes. *Progress in Polymer Science* **2018**, *81*, 114-143.
55. Gavelin, P.; Ostrovskii, D.; Adebahr, J.; Jannasch, P.; Wesslen, B., Amphiphilic polymer gel electrolytes. II. Influence of the ethylene oxide side-chain length on the gel properties. *Journal of Polymer Science Part B: Polymer Physics* **2001**, *39* (13), 1519-1524.
56. Xue, Z.; He, D.; Xie, X., Poly(ethylene oxide)-Based Electrolytes for Lithium-ion Batteries. *Journal of Materials Chemistry A* **2015**, *3* (38), 19218-19253.
57. Bandara, L. R. A. K.; Dissanayake, M. A. K. L.; Mellander, B. E., Ionic conductivity of plasticized(PEO)-LiCF₃SO₃ electrolytes. *Electrochimica Acta* **1998**, *43* (10), 1447-1451.
58. Cao, J.; He, R.; Kyu, T., Fire retardant, superionic solid state polymer electrolyte membranes for lithium ion batteries. *Current Opinion in Chemical Engineering* **2017**, *15*, 68-75.
59. Kim, Y.-T.; Smotkin, E. S., The effect of plasticizers on transport and electrochemical properties of PEO-based electrolytes for lithium rechargeable batteries. *Solid State Ion.* **2002**, *149* (1), 29-37.
60. Qian, X.; Gu, N.; Cheng, Z.; Yang, X.; Wang, E.; Dong, S., Plasticizer effect on the ionic conductivity of PEO-based polymer electrolyte. *Materials Chemistry and Physics* **2002**, *74* (1), 98-103.
61. Kumar, Y.; Hashmi, S. A.; Pandey, G. P., Lithium ion transport and ion polymer interaction in PEO based polymer electrolyte plasticized with ionic liquid. *Solid State Ion.* **2011**, *201*, 73-80.
62. Fergus, J. W., Ceramic and polymeric solid electrolytes for lithium-ion batteries. *J. Power Sources* **2010**, *195*, 4554.
63. Srivastava, S.; Schaefer, J. L.; Yang, Z.; Tu, Z.; Archer, L. A., 25th anniversary article: polymer-particle composites: phase stability and applications in electrochemical energy storage. *Adv Mater* **2014**, *26* (2), 201-34.
64. Wen, Z.; Itoh, T.; Ichikawa, Y.; Kubo, M.; Yamamoto, O., Blend-based polymer electrolytes of poly(ethylene oxide) and hyperbranched poly[bis(triethylene glycol)benzoate] with terminal acetyl groups. *Solid State Ion.* **2000**, *134* (3), 281-289.
65. Aoki, T.; Konno, A.; Fujinami, T., Lithium ion conductivity of blend polymer electrolytes based on borate polymers containing fluoroalkane dicarboxylate and poly(ethylene oxide). *Electrochimica Acta* **2004**, *50* (2), 301-304.
66. Park, C. H.; Sun, Y.-K.; Kim, D.-W., Blended polymer electrolytes based on poly(lithium 4-styrene sulfonate) for the rechargeable lithium polymer batteries. *Electrochimica Acta* **2004**, *50* (2), 375-378.
67. Brandell, D.; Kasemägi, H.; Tamm, T.; Aabloo, A., Molecular dynamics modeling the Li-PolystyreneTFSI/PEO blend. *Solid State Ion.* **2014**, *262*, 769-773.
68. Magistris, A.; Singh, K., PEO-based polymer electrolytes. *Polymer International* **1992**, *28* (4), 277-280.
69. Liang, Y.-H.; Wang, C.-C.; Chen, C.-Y., Synthesis and characterization of a new network polymer electrolyte containing polyether in the main chains and side chains. *European Polymer Journal* **2008**, *44* (7), 2376-2384.
70. Murata, K.; Izuchi, S.; Yoshihisa, Y., An overview of the research and development of solid polymer electrolyte batteries. *Electrochimica Acta* **2000**, *45* (8), 1501-1508.
71. Butzelaar, A. J.; Röring, P.; Mach, T. P.; Hoffmann, M.; Jeschull, F.; Wilhelm, M.; Winter, M.; Brunklau, G.; Théato, P., Styrene-Based Poly(ethylene oxide) Side-Chain

- Block Copolymers as Solid Polymer Electrolytes for High-Voltage Lithium-Metal Batteries. *ACS Applied Materials & Interfaces* **2021**, *13* (33), 39257-39270.
72. Bergman, M.; Bergfelt, A.; Sun, B.; Bowden, T.; Brandell, D.; Johansson, P., Graft Copolymer Electrolytes for High Temperature Li-battery Applications, Using Poly(methyl methacrylate) Grafted Poly(ethylene glycol)methyl Ether Methacrylate and Lithium bis(trifluoromethanesulfonimide). *Electrochimica Acta* **2015**, *175*, 96-103.
73. Bergfelt, A.; Rubatat, L.; Brandell, D.; Bowden, T., Poly(benzyl methacrylate)-poly (oligo ethylene glycol) Methyl Ether Methacrylate Triblock-copolymers as Solid Electrolyte for Lithium Batteries. *Solid State Ion.* **2018**, *321*, 55-61.
74. Chintapalli, M.; Le, T. N. P.; Venkatesan, N. R.; Mackay, N. G.; Rojas, A. A.; Thelen, J. L.; Chen, X. C.; Devaux, D.; Balsara, N. P., Structure and Ionic Conductivity of Polystyrene-block-poly(ethylene oxide) Electrolytes in the High Salt Concentration Limit. *Macromolecules* **2016**, *49* (5), 1770-1780.
75. Teran, A. A.; Balsara, N. P., Thermodynamics of Block Copolymers with and without Salt. *The Journal of Physical Chemistry B* **2014**, *118* (1), 4-17.
76. Zhang, Z.-K.; Ding, S.-P.; Zhou, Y.-T.; Ye, Z.; Wang, R.-Y.; Du, B.-Y.; Xu, J.-T., Influence of Salt Doping on the Entropy-Driven Lower Disorder-to-Order Transition Behavior of Poly(ethylene oxide)-b-Poly(4-vinylpyridine). *Macromolecular Chemistry and Physics* **2021**, *222* (24), 2100303.
77. Chintapalli, M.; Chen, X. C.; Thelen, J. L.; Teran, A. A.; Wang, X.; Garetz, B. A.; Balsara, N. P., Effect of Grain Size on the Ionic Conductivity of a Block Copolymer Electrolyte. *Macromolecules* **2014**, *47* (15), 5424-5431.
78. Bates, F. S.; Fredrickson, G. H., Block Copolymers—Designer Soft Materials. In *Physics Today*, American Institute of Physics: 1999; Vol. 52.
79. Loo, W. S.; Galluzzo, M. D.; Li, X.; Maslyn, J. A.; Oh, H. J.; Mongcopa, K. I.; Zhu, C.; Wang, A. A.; Wang, X.; Garetz, B. A.; Balsara, N. P., Phase Behavior of Mixtures of Block Copolymers and a Lithium Salt. *The Journal of Physical Chemistry B* **2018**, *122* (33), 8065-8074.
80. Yu, X.; Manthiram, A., A review of composite polymer-ceramic electrolytes for lithium batteries. *Energy Storage Materials* **2021**, *34*, 282-300.
81. Fan, W.; Li, N.-W.; Zhang, X.; Zhao, S.; Cao, R.; Yin, Y.; Xing, Y.; Wang, J.; Guo, Y.-G.; Li, C., A Dual-Salt Gel Polymer Electrolyte with 3D Cross-Linked Polymer Network for Dendrite-Free Lithium Metal Batteries. *Advanced Science* **2018**, *5* (9), 1800559.
82. Lim, Y.-J.; An, Y.-H.; Jo, N.-J., Polystyrene-Al₂O₃ composite solid polymer electrolyte for lithium secondary battery. *Nanoscale Research Letters* **2012**, *7* (1), 19.
83. Suthanthiraraj, S. A.; Sheeba, D. J., Structural investigation on PEO-based polymer electrolytes dispersed with Al₂O₃ nanoparticles. *Ionics* **2007**, *13* (6), 447-450.
84. Gondaliya, N.; Kanchan, D. K.; Sharma, P.; Pant, M.; Jayswal, M. S., Dielectric And Conductivity In Silver-Poly (ethylene oxide) Solid Polymer Electrolytes Dispersed With SiO₂ Nanoparticles. *AIP Conference Proceedings* **2010**, *1313* (1), 112-114.
85. Croce, F.; Appetecchi, G. B.; Persi, L.; Scrosati, B., Nanocomposite Polymer Electrolytes for Lithium Batteries. *Nature* **1998**, *394* (6692), 456-458.
86. Xiong, H.-M.; Wang, Z.-D.; Xie, D.-P.; Cheng, L.; Xia, Y.-Y., Stable polymer electrolytes based on polyether-grafted ZnO nanoparticles for all-solid-state lithium batteries. *Journal of Materials Chemistry* **2006**, *16* (14), 1345-1349.
87. Guo, X.; Yuan, R.-Z., On the grain boundaries of ZrO₂-based solid electrolyte. *Solid State Ion.* **1995**, *80* (1), 159-166.

88. Meesala, Y.; Chen, C.-Y.; Jena, A.; Liao, Y.-K.; Hu, S.-F.; Chang, H.; Liu, R.-S., All-Solid-State Li-Ion Battery Using $\text{Li}_{1.5}\text{Al}_{0.5}\text{Ge}_{1.5}(\text{PO}_4)_3$ As Electrolyte Without Polymer Interfacial Adhesion. *The Journal of Physical Chemistry C* **2018**, *122* (26), 14383-14389.
89. Yang, J.; Jia, Y.; Yao, Z., Study on the lithium solid electrolytes of $\text{Li}_3\text{N}-\text{Li}_3\text{Bi}-\text{LiCl}$ ternary system — $2\text{Li}_3\text{Bi} \cdot 3\text{LiCl}$ lithium solid electrolyte. *Solid State Ion.* **1997**, *96* (3), 215-218.
90. Kitahama, K.; Furukawa, Y.; Kawai, S.; Nakamura, O., Synthesis and NMR study of solid electrolytes in the system $\text{Li}_3\text{N}-\text{LiCl}$. *Solid State Ion.* **1981**, *3-4*, 335-339.
91. Wang, A.-N.; Nonemacher, J. F.; Yan, G.; Finsterbusch, M.; Malzbender, J.; Krüger, M., Mechanical properties of the solid electrolyte Al-substituted $\text{Li}_7\text{La}_3\text{Zr}_2\text{O}_{12}$ (LLZO) by utilizing micro-pillar indentation splitting test. *Journal of the European Ceramic Society* **2018**, *38* (9), 3201-3209.
92. Li, J.; Zhu, K.; Yao, Z.; Qian, G.; Zhang, J.; Yan, K.; Wang, J., A promising composite solid electrolyte incorporating LLZO into PEO/PVDF matrix for all-solid-state lithium-ion batteries. *Ionics* **2020**, *26* (3), 1101-1108.
93. Yu, S.; Schmidt, R. D.; Garcia-Mendez, R.; Herbert, E.; Dudney, N. J.; Wolfenstine, J. B.; Sakamoto, J.; Siegel, D. J., Elastic Properties of the Solid Electrolyte $\text{Li}_7\text{La}_3\text{Zr}_2\text{O}_{12}$ (LLZO). *Chemistry of Materials* **2016**, *28* (1), 197-206.
94. Liu, L.; Chu, L.; Jiang, B.; Li, M., $\text{Li}_{1.4}\text{Al}_{0.4}\text{Ti}_{1.6}(\text{PO}_4)_3$ nanoparticle-reinforced solid polymer electrolytes for all-solid-state lithium batteries. *Solid State Ion.* **2019**, *331*, 89-95.
95. Yu, S.; Schmohl, S.; Liu, Z.; Hoffmeyer, M.; Schön, N.; Hausen, F.; Tempel, H.; Kungl, H.; Wiemhöfer, H. D.; Eichel, R. A., Insights into a layered hybrid solid electrolyte and its application in long lifespan high-voltage all-solid-state lithium batteries. *Journal of Materials Chemistry A* **2019**, *7* (8), 3882-3894.
96. Liu, W.; Lee, S. W.; Lin, D.; Shi, F.; Wang, S.; Sendek, A. D.; Cui, Y., Enhancing ionic conductivity in composite polymer electrolytes with well-aligned ceramic nanowires. *Nature Energy* **2017**, *2* (5), 17035.
97. Zhang, N.; He, J.; Han, W.; Wang, Y., Composite solid electrolyte PEO/SN/ LiAlO_2 for a solid-state lithium battery. *Journal of Materials Science* **2019**, *54* (13), 9603-9612.
98. Villarreal, I.; Morales, E.; Acosta, J. L., Ionic conductivity and spectroscopic characterisation of γ - LiAlO_2 -filled polymer electrolytes. *Die Angewandte Makromolekulare Chemie* **1999**, *266* (1), 24-29.
99. Feuillade, G.; Perche, P., Ion-conductive macromolecular gels and membranes for solid lithium cells. *Journal of Applied Electrochemistry* **1975**, *5* (1), 63-69.
100. Zhu, M.; Wu, J.; Wang, Y.; Song, M.; Long, L.; Siyal, S. H.; Yang, X.; Sui, G., Recent advances in gel polymer electrolyte for high-performance lithium batteries. *Journal of Energy Chemistry* **2019**, *37*, 126-142.
101. Bocharova, V.; Sokolov, A. P., Perspectives for Polymer Electrolytes: A View from Fundamentals of Ionic Conductivity. *Macromolecules* **2020**, *53* (11), 4141-4157.
102. Pang, M.-C.; Marinescu, M.; Wang, H.; Offer, G., Mechanical behaviour of inorganic solid-state batteries: can we model the ionic mobility in the electrolyte with Nernst–Einstein's relation? *Physical Chemistry Chemical Physics* **2021**, *23* (48), 27159-27170.
103. Bruce, P. G.; Evans, J.; Vincent, C. A., Conductivity and transference number measurements on polymer electrolytes. *Solid State Ion.* **1988**, *28-30*, 918-922.

104. Zhao, Q.; Liu, X.; Stalin, S.; Archer, L., In-Built Polymer-in-Solvent and Solvent-in-Polymer Electrolytes for High-Voltage Lithium Metal Batteries. *Cell Reports Physical Science* **2020**, *1* (8), 100146.
105. Ding, P.; Lin, Z.; Guo, X.; Wu, L.; Wang, Y.; Guo, H.; Li, L.; Yu, H., Polymer electrolytes and interfaces in solid-state lithium metal batteries. *Materials Today* **2021**, *51*, 449-474.
106. Xi, G.; Xiao, M.; Wang, S.; Han, D.; Li, Y.; Meng, Y., Polymer-Based Solid Electrolytes: Material Selection, Design, and Application. *Advanced Functional Materials* **2021**, *31* (9), 2007598.
107. Porcarelli, L.; Shaplov, A. S.; Bella, F.; Nair, J. R.; Mecerreyes, D.; Gerbaldi, C., Single-Ion Conducting Polymer Electrolytes for Lithium Metal Polymer Batteries that Operate at Ambient Temperature. *ACS Energy Letters* **2016**, *1* (4), 678-682.
108. Devaux, D.; Bouchet, R.; Glé, D.; Denoyel, R., Mechanism of ion transport in PEO/LiTFSI complexes: Effect of temperature, molecular weight and end groups. *Solid State Ion.* **2012**, *227*, 119-127.
109. Yuan, H.; Luan, J.; Yang, Z.; Zhang, J.; Wu, Y.; Lu, Z.; Liu, H., Single Lithium-Ion Conducting Solid Polymer Electrolyte with Superior Electrochemical Stability and Interfacial Compatibility for Solid-State Lithium Metal Batteries. *ACS Applied Materials & Interfaces* **2020**, *12* (6), 7249-7256.
110. Qin, B.; Liu, Z.; Zheng, J.; Hu, P.; Ding, G.; Zhang, C.; Zhao, J.; Kong, D.; Cui, G., Single-ion dominantly conducting polyborates towards high performance electrolytes in lithium batteries. *Journal of Materials Chemistry A* **2015**, *3* (15), 7773-7779.
111. Marchiori, C. F. N.; Carvalho, R. P.; Ebadi, M.; Brandell, D.; Araujo, C. M., Understanding the Electrochemical Stability Window of Polymer Electrolytes in Solid-State Batteries from Atomic-Scale Modeling: The Role of Li-Ion Salts. *Chemistry of Materials* **2020**, *32* (17), 7237-7246.
112. Chen, L.; Venkatram, S.; Kim, C.; Batra, R.; Chandrasekaran, A.; Ramprasad, R., Electrochemical Stability Window of Polymeric Electrolytes. *Chemistry of Materials* **2019**, *31* (12), 4598-4604.
113. Monroe, C.; Newman, J., The Impact of Elastic Deformation on Deposition Kinetics at Lithium/Polymer Interfaces. *Journal of The Electrochemical Society* **2005**, *152* (2), A396.
114. Snyder, J. F.; Carter, R. H.; Wetzel, E. D., Electrochemical and Mechanical Behavior in Mechanically Robust Solid Polymer Electrolytes for Use in Multifunctional Structural Batteries. *Chemistry of Materials* **2007**, *19* (15), 3793-3801.
115. Willgert, M.; Kjell, M. H.; Jacques, E.; Behm, M.; Lindbergh, G.; Johansson, M., Photoinduced free radical polymerization of thermoset lithium battery electrolytes. *European Polymer Journal* **2011**, *47* (12), 2372-2378.
116. Schulze, M. W.; McIntosh, L. D.; Hillmyer, M. A.; Lodge, T. P., High-modulus, High-conductivity Nanostructured Polymer Electrolyte Membranes via Polymerization-induced Phase Separation. *Nano Lett* **2014**, *14* (1), 122-6.
117. Shukutani, T.; Myojo, T.; Nakanishi, H.; Norisuye, T.; Tran-Cong-Miyata, Q., Tricontinuous Morphology of Ternary Polymer Blends Driven by Photopolymerization: Reaction and Phase Separation Kinetics. *Macromolecules* **2014**, *47* (13), 4380-4386.
118. Blatt, M. P.; Hallinan, D. T., Jr., Polymer Blend Electrolytes for Batteries and Beyond. *Industrial & Engineering Chemistry Research* **2021**, *60* (48), 17303-17327.
119. Bates, F. S.; Fredrickson, G. H., Block Copolymer Thermodynamics: Theory and Experiment. *Annual Review of Physical Chemistry* **1990**, *41* (1), 525-557.

120. Giles, J. R. M.; Gray, F. M.; MacCallum, J. R.; Vincent, C. A., Synthesis and characterization of ABA block copolymer-based polymer electrolytes. *Polymer* **1987**, *28* (11), 1977-1981.
121. Soo, P. P.; Huang, B.; Jang, Y. I.; Chiang, Y. M.; Sadoway, D. R.; Mayes, A. M., Rubbery Block Copolymer Electrolytes for Solid-State Rechargeable Lithium Batteries. *Journal of The Electrochemical Society* **1999**, *146* (1), 32-37.
122. Ruzette, A.-V. r. G.; Soo, P. P.; Sadoway, D. R.; Mayes, A. M., Melt-Formable Block Copolymer Electrolytes for Lithium Rechargeable Batteries. *Journal of The Electrochemical Society* **2001**, *148* (6), 537 - 543.
123. Young, W.-S.; Kuan, W.-F.; Epps, I., Thomas H., Block Copolymer Electrolytes for Rechargeable Lithium Batteries. *Journal of Polymer Science Part B: Polymer Physics* **2014**, *52* (1), 1-16.
124. Porcarelli, L.; Aboudzadeh, M. A.; Rubatat, L.; Nair, J. R.; Shaplov, A. S.; Gerbaldi, C.; Mecerreyes, D., Single-ion triblock copolymer electrolytes based on poly(ethylene oxide) and methacrylic sulfonamide blocks for lithium metal batteries. *J. Power Sources* **2017**, *364*, 191-199.
125. Zhang, H.; Li, C.; Piszcz, M.; Coya, E.; Rojo, T.; Rodriguez-Martinez, L. M.; Armand, M.; Zhou, Z., Single lithium-ion conducting solid polymer electrolytes: advances and perspectives. *Chemical Society Reviews* **2017**, *46* (3), 797-815.
126. Zhu, Y. S.; Gao, X. W.; Wang, X. J.; Hou, Y. Y.; Liu, L. L.; Wu, Y. P., A single-ion polymer electrolyte based on boronate for lithium ion batteries. *Electrochemistry Communications* **2012**, *22*, 29-32.
127. Butzelaar, A. J.; Liu, K. L.; Röring, P.; Brunklaus, G.; Winter, M.; Theato, P., A Systematic Study of Vinyl Ether-Based Poly(Ethylene Oxide) Side-Chain Polymer Electrolytes. *ACS Applied Polymer Materials* **2021**, *3* (3), 1573-1582.
128. Nagajothi, A. J.; Kannan, R.; Rajashabala, S., Electrochemical performance of plasticized PEO-LiTf complex-based composite gel polymer electrolytes with the addition of barium titanate. *Ionics* **2018**, *24* (5), 1407-1414.
129. Wang, W.; Fang, Z.; Zhao, M.; Peng, Y.; Zhang, J.; Guan, S., Solid polymer electrolytes based on the composite of PEO-LiFSI and organic ionic plastic crystal. *Chemical Physics Letters* **2020**, *747*, 137335.
130. Maurel, A.; Armand, M.; Grugeon, S.; Fleutot, B.; Davoisne, C.; Tortajada, H.; Courty, M.; Panier, S.; Dupont, L., Poly(Ethylene Oxide)-LiTFSI Solid Polymer Electrolyte Filaments for Fused Deposition Modeling Three-Dimensional Printing. *Journal of The Electrochemical Society* **2020**, *167* (7), 070536.
131. Li, J.; Khan, I. M., MIXED (ELECTRONIC AND IONIC) CONDUCTIVE SOLID POLYMER MATRIX .1. SYNTHESIS AND PROPERTIES OF POLY(2,5,8,11,14,17,20,23-OCTAOXAPENTACOSYL METHACRYLATE)-BLOCK-POLY(4-VINYLPYRIDINE). *Makromolekulare Chemie-Macromolecular Chemistry and Physics* **1991**, *192* (12), 3043-3050.
132. Bergfelt, A.; Rubatat, L.; Mogensen, R.; Brandell, D.; Bowden, T., D(8)-poly(methyl methacrylate)-poly (oligo ethylene glycol) Methyl Ether Methacrylate Tri-block-copolymer Electrolytes: Morphology, Conductivity and Battery Performance. *Polymer* **2017**, *131*, 234-242.
133. Niitani, T.; Shimada, M.; Kawamura, K.; Kanamura, K., Characteristics of new-type solid polymer electrolyte controlling nano-structure. *J. Power Sources* **2005**, *146* (1), 386-390.

134. Cloitre, M. *MATERIAUX POLYMERES STRUCTURES : Mélanges, alliages, copolymères à blocs* ESPCI - Paris Tech, Paris, 2001.
135. Rubinstein, M.; Colby, R. H., Thermodynamics of mixing. In *Polymer physics*, Oxford University Press: Oxford, 2004; p 440.
136. Strobl, G. R., *The Physics of Polymers : Concepts for Understanding Their Structures and Behavior*. Springer: Verlag Berlin Heidelberg, 2007; p XIV, 518.
137. Hofman, A. H.; ten Brinke, G.; Loos, K., Hierarchical structure formation in supramolecular comb-shaped block copolymers. *Polymer* **2016**, *107*, 343-356.
138. Gartner, T. E.; Morris, M. A.; Shelton, C. K.; Dura, J. A.; Epps, T. H., Quantifying Lithium Salt and Polymer Density Distributions in Nanostructured Ion-Conducting Block Polymers. *Macromolecules* **2018**, *51* (5), 1917-1926.
139. Wang, J.-Y.; Chen, W.; Russell, T. P., Ion-Complexation-Induced Changes in the Interaction Parameter and the Chain Conformation of PS-*b*-PMMA Copolymers. *Macromolecules* **2008**, *41* (13), 4904-4907.
140. Hou, K. J.; Loo, W. S.; Balsara, N. P.; Qin, J., Comparing Experimental Phase Behavior of Ion-Doped Block Copolymers with Theoretical Predictions Based on Selective Ion Solvation. *Macromolecules* **2020**, *53* (10), 3956-3966.
141. Epps, T. H.; Bailey, T. S.; Pham, H. D.; Bates, F. S., Phase Behavior of Lithium Perchlorate-Doped Poly(styrene-*b*-isoprene-*b*-ethylene oxide) Triblock Copolymers. *Chemistry of Materials* **2002**, *14* (4), 1706-1714.
142. Gunkel, I.; Thurn-Albrecht, T., Thermodynamic and Structural Changes in Ion-Containing Symmetric Diblock Copolymers: A Small-Angle X-ray Scattering Study. *Macromolecules* **2012**, *45* (1), 283-291.
143. Nakamura, I.; Wang, Z.-G., Salt-doped Block Copolymers: Ion Distribution, Domain Spacing and Effective χ Parameter. *Soft Matter* **2012**, *8* (36), 9356-9367.
144. Hou, K. J.; Qin, J., Solvation and Entropic Regimes in Ion-Containing Block Copolymers. *Macromolecules* **2018**, *51* (19), 7463-7475.
145. Butzelaar, A. J.; Röring, P.; Hoffmann, M.; Atik, J.; Paillard, E.; Wilhelm, M.; Winter, M.; Brunklaus, G.; Theato, P., Advanced Block Copolymer Design for Polymer Electrolytes: Prospects of Microphase Separation. *Macromolecules* **2021**, *54* (23), 11101-11112.
146. Bouchet, R.; Phan, T. N. T.; Beaudoin, E.; Devaux, D.; Davidson, P.; Bertin, D.; Denoyel, R., Charge Transport in Nanostructured PS-PEO-PS Triblock Copolymer Electrolytes. *Macromolecules* **2014**, *47* (8), 2659-2665.
147. Beaudoin, E.; Phan, T. N. T.; Robinet, M.; Denoyel, R.; Davidson, P.; Bertin, D.; Bouchet, R., Effect of Interfaces on the Melting of PEO Confined in Triblock PS-*b*-PEO-*b*-PS Copolymers. *Langmuir* **2013**, *29* (34), 10874-10880.
148. Chakraborty, S.; Sethi, G. K.; Frenck, L.; Ho, A. S.; Villaluenga, I.; Wantanabe, H.; Balsara, N. P., Effect of Yield Stress on Stability of Block Copolymer Electrolytes against Lithium Metal Electrodes. *ACS Applied Energy Materials* **2022**, *5* (1), 852-861.
149. Lee, D.; Jung, H. Y.; Park, M. J., Solid-State Polymer Electrolytes Based on AB₃-Type Miktoarm Star Copolymers. *ACS Macro Letters* **2018**, *7* (8), 1046-1050.
150. Kuan, W.-F.; Remy, R.; Mackay, M. E.; Epps, I. I. I. T. H., Controlled ionic conductivity via tapered block polymer electrolytes. *RSC Adv.* **2015**, *5* (17), 12597-12604.
151. Ketkar, P. M.; Epps, T. H., Nanostructured Block Polymer Electrolytes: Tailoring Self-Assembly to Unlock the Potential in Lithium-Ion Batteries. *Accounts of Chemical Research* **2021**, *54* (23), 4342-4353.

152. Wang, S.; Wang, A.; Yang, C.; Gao, R.; Liu, X.; Chen, J.; Wang, Z.; Zeng, Q.; Liu, X.; Zhou, H.; Zhang, L., Six-arm Star Polymer Based on Discotic Liquid Crystal as High Performance All-solid-state Polymer Electrolyte for Lithium-ion Batteries. *J. Power Sources* **2018**, *395*, 137-147.
153. Tong, Y.; Chen, L.; He, X.; Chen, Y., Free Mesogen Assisted Assembly of the Star-shaped Liquid-crystalline Copolymer/Polyethylene Oxide Solid Electrolytes for Lithium Ion Batteries. *Electrochimica Acta* **2014**, *118*, 33-40.
154. Tong, Y.; Chen, L.; He, X.; Chen, Y., Sequential effect and enhanced conductivity of star-shaped diblock liquid-crystalline copolymers for solid electrolytes. *J. Power Sources* **2014**, *247*, 786-793.
155. Niitani, T.; Amaike, M.; Nakano, H.; Dokko, K.; Kanamura, K., Star-Shaped Polymer Electrolyte with Microphase Separation Structure for All-Solid-State Lithium Batteries. *Journal of The Electrochemical Society* **2009**, *156*, 577 - 583.
156. Lynd, N. A.; Meuler, A. J.; Hillmyer, M. A., Polydispersity and block copolymer self-assembly. *Progress in Polymer Science* **2008**, *33* (9), 875-893.
157. Matsen, M. W.; Thompson, R. B., Equilibrium behavior of symmetric ABA triblock copolymer melts. *The Journal of Chemical Physics* **1999**, *111* (15), 7139-7146.
158. Matsen, M. W., Equilibrium behavior of asymmetric ABA triblock copolymer melts. *The Journal of Chemical Physics* **2000**, *113* (13), 5539-5544.
159. Matsen, M. W.; Schick, M., Stable and Unstable Phases of a Linear Multiblock Copolymer Melt. *Macromolecules* **1994**, *27* (24), 7157-7163.
160. Matsen, M. W.; Schick, M., Microphase Separation in Starblock Copolymer Melts. *Macromolecules* **1994**, *27* (23), 6761-6767.
161. Lynd, N. A.; Oyerokun, F. T.; O'Donoghue, D. L.; Handlin, D. L., Jr.; Fredrickson, G. H., Design of Soft and Strong Thermoplastic Elastomers Based on Nonlinear Block Copolymer Architectures Using Self-Consistent-Field Theory. *Macromolecules* **2010**, *43* (7), 3479-3486.
162. Grason, G. M.; Kamien, R. D., Interfaces in Diblocks: A Study of Miktoarm Star Copolymers. *Macromolecules* **2004**, *37* (19), 7371-7380.
163. Grason, G. M.; Didonna, B. A.; Kamien, R. D., Geometric Theory of Diblock Copolymer Phases. *Physical Review Letters* **2003**, *91* (5).
164. Grason, G. M.; Kamien, R. D., Self-consistent field theory of multiply branched block copolymer melts. *Physical Review E* **2005**, *71* (5), 051801.
165. Wang, L.; Zhang, L.; Lin, J., Microphase separation in multigraft copolymer melts studied by random-phase approximation and self-consistent field theory. *The Journal of Chemical Physics* **2008**, *129* (11), 114905.
166. Matsen, M. W., Effect of Architecture on the Phase Behavior of AB-Type Block Copolymer Melts. *Macromolecules* **2012**, *45* (4), 2161-2165.
167. Glynos, E.; Pantazidis, C.; Sakellariou, G., Designing All-Polymer Nanostructured Solid Electrolytes: Advances and Prospects. *ACS Omega* **2020**, *5* (6), 2531-2540.
168. Sax, J.; Ottino, J. M., Modeling of transport of small molecules in polymer blends - application of effective medium theory. *Polymer Engineering and Science* **1983**, *23* (3), 165-176.
169. Devaux, D.; Glé, D.; Phan, T. N. T.; Gignes, D.; Giroud, E.; Deschamps, M.; Denoyel, R.; Bouchet, R., Optimization of Block Copolymer Electrolytes for Lithium Metal Batteries. *Chemistry of Materials* **2015**, *27* (13), 4682-4692.

170. Molinari, N.; Mailoa, J. P.; Kozinsky, B., Effect of Salt Concentration on Ion Clustering and Transport in Polymer Solid Electrolytes: A Molecular Dynamics Study of PEO–LiTFSI. *Chemistry of Materials* **2018**, *30* (18), 6298-6306.
171. Kambe, Y.; Arges, C. G.; Patel, S.; Stoykovish, M. P.; Nealey, P. F., Ion Conduction in Microphase-Separated Block Copolymer Electrolytes. *The Electrochemical Society Interface* **2017**, *26* (1), 61-67.
172. Young, W.-S.; Epps, T. H., Ionic Conductivities of Block Copolymer Electrolytes with Various Conducting Pathways: Sample Preparation and Processing Considerations. *Macromolecules* **2012**, *45* (11), 4689-4697.
173. Coote, J. P.; Kinsey, T.; Street, D. P.; Kilbey, S. M., II; Sangoro, J. R.; Stein, G. E., Surface-Induced Ordering Depresses Through-Film Ionic Conductivity in Lamellar Block Copolymer Electrolytes. *ACS Macro Letters* **2020**, *9* (4), 565-570.
174. Angelescu, D. E.; Waller, J. H.; Adamson, D. H.; Deshpande, P.; Chou, S. Y.; Register, R. A.; Chaikin, P. M., Macroscopic Orientation of Block Copolymer Cylinders in Single-Layer Films by Shearing. *Advanced Materials* **2004**, *16* (19), 1736-1740.
175. Fredrickson, G. H., Steady shear alignment of block copolymers near the isotropic–lamellar transition. *Journal of Rheology* **1994**, *38* (4), 1045-1067.
176. Albalak, R. J.; Thomas, E. L., Roll-Casting of block copolymers and of block copolymer-homopolymer blends. *Journal of Polymer Science Part B: Polymer Physics* **1994**, *32* (2), 341-350.
177. Park, M. J.; Balsara, N. P., Anisotropic Proton Conduction in Aligned Block Copolymer Electrolyte Membranes at Equilibrium with Humid Air. *Macromolecules* **2010**, *43* (1), 292-298.
178. Lee, J.-Y.; Lee, J.-H.; Ryu, S.; Yun, S.-H.; Moon, S.-H., Electrically aligned ion channels in cation exchange membranes and their polarized conductivity. *Journal of Membrane Science* **2015**, *478*, 19-24.
179. Majewski, P. W.; Gopinadhan, M.; Jang, W.-S.; Lutkenhaus, J. L.; Osuji, C. O., Anisotropic Ionic Conductivity in Block Copolymer Membranes by Magnetic Field Alignment. *Journal of the American Chemical Society* **2010**, *132* (49), 17516-17522.
180. Majewski, P. W.; Gopinadhan, M.; Osuji, C. O., Understanding anisotropic transport in self-assembled membranes and maximizing ionic conductivity by microstructure alignment. *Soft Matter* **2013**, *9* (29), 7106-7116.
181. Majewski, P. W.; Gopinadhan, M.; Osuji, C. O., Magnetic field alignment of block copolymers and polymer nanocomposites: Scalable microstructure control in functional soft materials. *Journal of Polymer Science Part B: Polymer Physics* **2012**, *50* (1), 2-8.
182. Rokhlenko, Y.; Gopinadhan, M.; Osuji, C. O.; Zhang, K.; O'Hern, C. S.; Larson, S. R.; Gopalan, P.; Majewski, P. W.; Yager, K. G., Magnetic Alignment of Block Copolymer Microdomains by Intrinsic Chain Anisotropy. *Physical Review Letters* **2015**, *115* (25).
183. Morris, M. A.; Sung, S. H.; Ketkar, P. M.; Dura, J. A.; Nieuwendaal, R. C.; Epps, T. H., III, Enhanced Conductivity via Homopolymer-Rich Pathways in Block Polymer-Blended Electrolytes. *Macromolecules* **2019**, *52* (24), 9682-9692.
184. Kuan, W.-F.; Reed, E. H.; Nguyen, N. A.; Mackay, M. E.; Epps, T. H., Using tapered interfaces to manipulate nanoscale morphologies in ion-doped block polymers. *MRS Communications* **2015**, *5* (2), 251-256.
185. Zhang, H.; Riggelman, R. A., Percolation of co-continuous domains in tapered copolymer networks. *Molecular Systems Design & Engineering* **2023**, *8* (1), 115-122.

186. Xie, H.-q.; Xie, D.; Liu, J., Solid Polymer Electrolyte Complexes of Polyoxyethylene-Containing Star-Shaped Block Copolymers and Copolymers with Uniform Grafts. *Polymer-plastics Technology and Engineering* **1989**, *28*, 355-369.
187. Bates, F. S., Network Phases in Block Copolymer Melts. *MRS Bulletin* **2005**, *30* (7), 525-532.
188. Lequeieu, J.; Magenau, A. J. D., Reaction-induced Phase Transitions with Block Copolymers in Solution and Bulk. *Polymer Chemistry* **2021**, *12* (1), 12-28.
189. Fischer, M.; Hellmann, G. P., On the Evolution of Phase Patterns during the High-Impact-Modified Polystyrene Process. *Macromolecules* **1996**, *29* (7), 2498-2509.
190. Motokawa, R.; Iida, Y.; Zhao, Y.; Hashimoto, T.; Koizumi, S., Living Polymerization Induced Macro- and Microdomain Investigated by Focusing Ultra-small-angle Neutron Scattering. *Polymer Journal* **2007**, *39* (12), 1312-1318.
191. Motokawa, R.; Taniguchi, T.; Kumada, T.; Iida, Y.; Aoyagi, S.; Sasaki, Y.; Kohri, M.; Kishikawa, K., Photonic Crystals Fabricated by Block Copolymerization-Induced Microphase Separation. *Macromolecules* **2016**, *49* (16), 6041-6049.
192. Seo, M.; Hillmyer, M. A., Reticulated nanoporous polymers by controlled polymerization-induced microphase separation. *Science* **2012**, *336* (6087), 1422-5.
193. Lee, J.; Seo, M., Downsizing of Block Polymer-Templated Nanopores to One Nanometer via Hyper-Cross-Linking of High χ -Low N Precursors. *ACS Nano* **2021**, *15* (5), 9154-9166.
194. Oh, J.; Seo, M., Photoinitiated Polymerization-Induced Microphase Separation for the Preparation of Nanoporous Polymer Films. *ACS Macro Letters* **2015**, *4* (11), 1244-1248.
195. Park, J.; Kim, K.; Seo, M., Hyper-cross-linked polymers with controlled multiscale porosity via polymerization-induced microphase separation within high internal phase emulsion. *Chemical Communications* **2018**, *54* (57), 7908-7911.
196. Saba, S. A.; Lee, B.; Hillmyer, M. A., Tricontinuous Nanostructured Polymers via Polymerization-Induced Microphase Separation. *ACS Macro Letters* **2017**, *6* (11), 1232-1236.
197. Saba, S. A.; Mousavi, M. P. S.; Bühlmann, P.; Hillmyer, M. A., Hierarchically Porous Polymer Monoliths by Combining Controlled Macro- and Microphase Separation. *Journal of the American Chemical Society* **2015**, *137* (28), 8896-8899.
198. Seo, M.; Murphy, C. J.; Hillmyer, M. A., One-Step Synthesis of Cross-Linked Block Polymer Precursor to a Nanoporous Thermoset. *ACS Macro Letters* **2013**, *2* (7), 617-620.
199. Oh, J.; Kim, B.; Lee, S.; Kim, S.-H.; Seo, M., Semipermeable Microcapsules with a Block-Polymer-Templated Nanoporous Membrane. *Chemistry of Materials* **2018**, *30* (1), 273-279.
200. Xie, Y.; Hillmyer, M. A., Nanostructured Polymer Monoliths for Biomedical Delivery Applications. *ACS Applied Bio Materials* **2020**, *3* (5), 3236-3247.
201. Khurana, R.; Schaefer, J. L.; Archer, L. A.; Coates, G. W., Suppression of Lithium Dendrite Growth Using Cross-Linked Polyethylene/Poly(ethylene oxide) Electrolytes: A New Approach for Practical Lithium-Metal Polymer Batteries. *Journal of the American Chemical Society* **2014**, *136* (20), 7395-7402.
202. McIntosh, L. D.; Schulze, M. W.; Irwin, M. T.; Hillmyer, M. A.; Lodge, T. P., Evolution of Morphology, Modulus, and Conductivity in Polymer Electrolytes Prepared via Polymerization-Induced Phase Separation. *Macromolecules* **2015**, *48* (5), 1418-1428.

203. Chopade, S. A.; So, S.; Hillmyer, M. A.; Lodge, T. P., Anhydrous Proton Conducting Polymer Electrolyte Membranes via Polymerization-Induced Microphase Separation. *ACS Applied Materials & Interfaces* **2016**, *8* (9), 6200-6210.
204. Chopade, S. A.; Au, J. G.; Li, Z.; Schmidt, P. W.; Hillmyer, M. A.; Lodge, T. P., Robust Polymer Electrolyte Membranes with High Ambient-Temperature Lithium-Ion Conductivity via Polymerization-Induced Microphase Separation. *ACS Applied Materials & Interfaces* **2017**, *9* (17), 14561-14565.
205. Liu, L.; Wu, Z.; Zheng, Z.; Zhou, Q.; Chen, K.; Yin, P., Polymerization-induced microphase separation of polymer-polyoxometalate nanocomposites for anhydrous solid state electrolytes. *Chinese Chemical Letters* **2022**, *33* (9), 4326-4330.
206. Lee, K.; Shang, Y.; Bobrin, V.; Kuchel, R.; Kundu, D.; Corrigan, N.; Boyer, C., 3D Printing Nanostructured Solid Polymer Electrolytes with High Modulus and Conductivity. *Advanced Materials* **2022**, *n/a* (n/a), 2204816.
207. Melodia, D.; Bhadra, A.; Lee, K.; Kuchel, R.; Kundu, D.; Corrigan, N.; Boyer, C., 3D Printed Solid Polymer Electrolytes with Bicontinuous Nanoscopic Domains for Ionic Liquid Conduction and Energy Storage. *Small* **2023**, *n/a* (n/a), 2206639.
208. Singh, M.; Odusanya, O.; Wilmes, G. M.; Eitouni, H. B.; Gomez, E. D.; Patel, A. J.; Chen, V. L.; Park, M. J.; Fragouli, P.; Iatrou, H.; Hadjichristidis, N.; Cookson, D.; Balsara, N. P., Effect of Molecular Weight on the Mechanical and Electrical Properties of Block Copolymer Electrolytes. *Macromolecules* **2007**, *40* (13), 4578-4585.



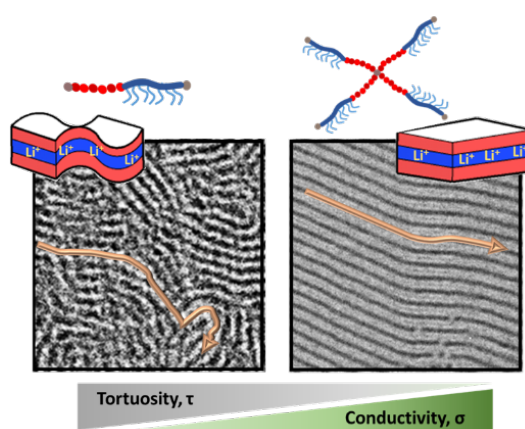
Chapter 2

Improved Solid Electrolyte Conductivity Via Macromolecular Self-Assembly: From Linear to Star Comb-Like P(S-*co*-BzMA)-*b*-POEGA Block Copolymer



Synopsis

Star block copolymer electrolytes with lithium ion conducting phase are investigated in the present work to assess the influence of this complex architecture compared to the linear one, on both, bulk morphology and ionic conductivity. For that purpose, the controlled synthesis of a series of poly(styrene-co-benzyl methacrylate)-*b*-poly[oligo(ethylene glycol) methyl ether acrylate] (P(S-co-BzMA)-*b*-POEGA) block copolymers (BCPs) by RAFT polymerization was performed from either a monofunctional or a tetrafunctional chain transfer agent (CTA) containing trithiocarbonate groups. We emphasized how a small amount of styrene (6 mol-%) improved drastically the control of the RAFT polymerization of benzyl methacrylate mediated by the tetrafunctional CTA. Transmission electron microscopy (TEM) and small angle X-ray scattering (SAXS) demonstrated a clear segregation of the BCPs in the presence of lithium salt. Interestingly, the star BCPs gave rise to highly ordered lamellar structures compared to the linear analogue. Consequently, the reduced lamellae tortuosity of self-assembled star BCPs improved the lithium conductivity by more than 8 times at 30°C for ~30 wt-% of POEGA conductive phase.



The morphological characterization by SAXS and TEM was carried out in collaboration with Monika Król and Janne Ruokolainen at Aalto University in Finland.

Table of Contents

1	Introduction	62
2	Synthesis and Characterization of Block copolymers	65
2.1	P(S- <i>co</i> -BzMA) Macromolecular Chain Transfer Agent.....	65
2.2	Characterization of star architecture.....	72
2.3	P(S- <i>co</i> -BzMA)- <i>b</i> -POEGA Block copolymers.....	74
3	Conductivity versus morphology.....	76
4	Conclusion.....	85
5	Supporting Information	85
5.1	Materials	85
5.2	Synthesis of linear and star macro-CTA of P(S- <i>co</i> -BzMA).....	86
5.3	NMR analysis for monomer conversion.....	86
5.3.1	The Extended Kelen-Tüdös (e-KT) method.....	90
5.4	Synthesis of linear and star P(S- <i>co</i> -BzMA)- <i>b</i> -POEGA block copolymer.....	91
5.5	Size Exclusion Chromatography (SEC).	92
5.6	Synthesis of P(S- <i>co</i> -BzMA)- <i>b</i> -POEGA block copolymer.	94
5.7	Preparation of Block Copolymer Electrolytes (BCPEs) films.	97
5.8	Differential Scanning Calorimetry (DSC).	99
5.9	Electrochemical Impedance Spectroscopy (EIS).....	100
5.10	Small Angle X-ray Scattering (SAXS).	100
5.11	Transmission Electron Microscopy (TEM).	102
5.12	Rheology measurements	104
6	References	105

1 Introduction

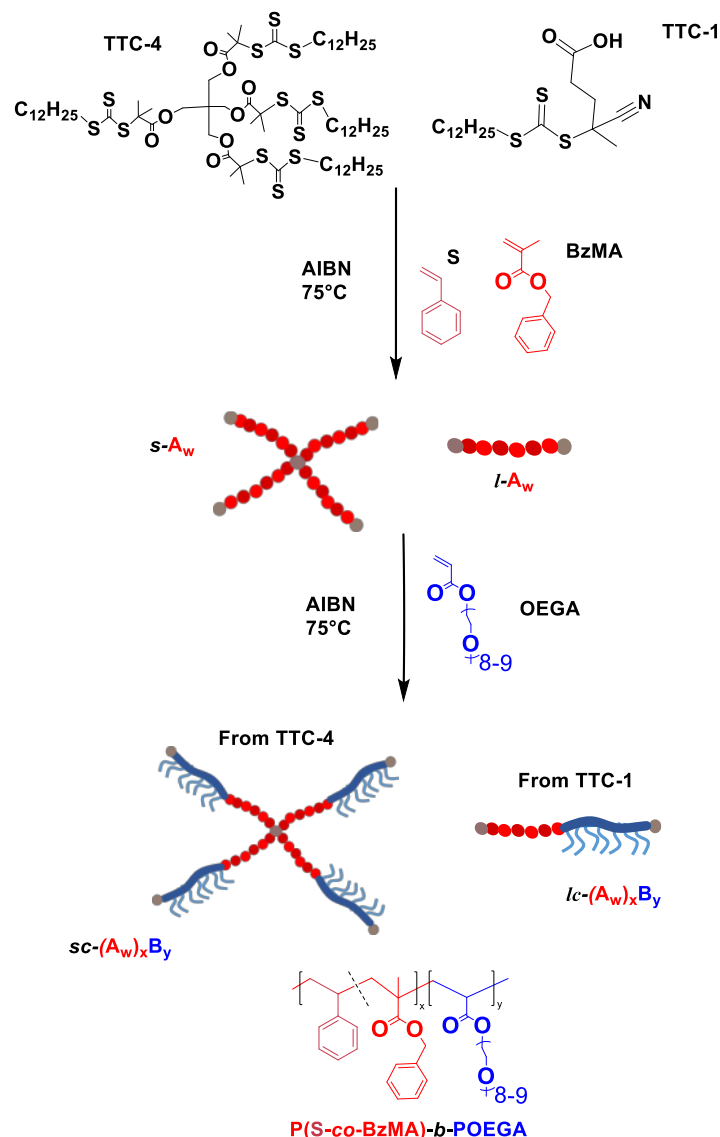
Lithium ion batteries have gained increasing interest over the years as mobile energy storage for electric vehicles (EVs), personal electronic devices, etc.¹ Development of low cost, high energy density and safe batteries have been the core of many research endeavours since the last three decades. Indeed, organic solvent based liquid electrolytes, classically used in commercialized lithium ion batteries, constitute a hazard due to leakage and flammability. To tackle that issue, solid polymer electrolytes (SPEs) with tunable mechanical properties are considered.² The most commonly investigated polymer is the low glass transition temperature (T_g) and semi-crystalline poly(ethylene oxide) (PEO).³ However, its lithium ion conductivity remains low compared to liquid electrolytes. Improved ion transport can be achieved at temperatures above melting temperature, activated by an increased macromolecular segmental motion⁴ and a reduced crystallinity.⁵ Lower PEO crystallinity can be realized at room temperature by breaking up the long-range macromolecular symmetry. This can be achieved by either utilizing PEO with comb or star macromolecular architectures or incorporating inorganic nanoparticles.⁵⁻⁷ Comb-like architecture can be obtained by polymerization of oligo(ethylene glycol (meth)acrylate) (OEGA or OEGMA) macromonomer to provide polymer backbone grafted with short pendant ethylene oxide (EO) oligomers.⁸ Star-shaped PEO has also demonstrated a reduced degree of crystallinity and melting temperature (T_m) compared to the linear PEO.⁶ That is resulting from the globular structure in a star-shaped polymer which hinders arm packing for crystallization.⁹ Nevertheless, the loss of crystallinity induces a loss of mechanical properties. In this context, the use of block copolymer electrolyte (BCPE) has been considered in order to achieve a compromise between mechanical and ion transport properties.¹⁰ Indeed, BCPEs containing at least one Li^+ -conductive polymer block and one high- T_g block are expected to simultaneously exhibit good levels of ionic conductivity and mechanical strength. Major studies throughout the years focused on linear BCPE systems based on PEO, especially the polystyrene-*block*-poly(ethylene oxide) (PS-*b*-PEO) copolymers where ionic conductivity, mechanical properties and microphase separation have been extensively studied.¹¹⁻¹⁸ Devaux *et al.* showed that lowering both melting temperature (T_m) and degree of crystallinity via the comb-like architecture of POEGMA-*b*-PS block copolymer improve lithium conductivity compared to the linear PEO-*b*-PS.¹⁹ The influence of side chain length and graft density was studied by Butzelaar *et al.*²⁰ They demonstrated for a library of polymers featuring different PEO side-chain lengths a drastic reduction in PEO crystallinity by 98% for

11 side EO units and by 39% for 54 side EO units in comparison to pure PEO.²⁰ Regarding the high- T_g block, PS is largely used but other high- T_g blocks have been studied. For instance, BCP of poly(methyl methacrylate) (PMMA) and POEGMA were reported by Ruzette *et al.* where they demonstrated that microphase separation can be induced in a controlled manner by the incorporation of lithium salt.²¹ Such BCPEs showed higher conductivity than the statistical analogue copolymers.²¹ Later, triblock copolymer based on poly(benzyl methacrylate) (PBzMA) and POEGMA (EO = 9) were synthesized as BCPE; this study also revealed that the phase separation of BCP is triggered by the addition of lithium bis(trifluoromethane)-sulfonylimide (LiTFSI) salt.²²

Star BCP have attracted increasing attention in various applications due to the compact and stabilizing steric structure, which may lead to peculiar morphological and rheological properties.^{23, 24} Few reports have described the use of star BCP as solid electrolytes in lithium ion batteries,²⁵⁻²⁹ but only two studies have compared the performances with their linear analogues in details. In the first study, a miktoarm BCPE consisting of 3-arms PEO connected to a PS block was shown to promote long-range narrow lamellar morphologies with high conductivities whereas the linear analogue showed swirly broader lamellar morphology with lower ionic conductivities.²⁵ In the other study, six-arms star PS-*b*-POEGMA BCP with a discotic liquid crystal core reportedly exhibit longer range ordered morphology and ionic conductivity 8 times higher than that of the corresponding linear BCPE; however, the presence of the discotic liquid crystal core in the star copolymer hinders an accurate comparison.²⁶

The interest of the present work is to combine star architecture with comb-like character of POEGA in order to investigate the effect of such architecture on morphology and on lithium ion conductivity of the self-assembled BCPEs. For that purpose, we first undertook the synthesis of linear and star high- T_g first block by reversible addition fragmentation transfer (RAFT) polymerization via a core-first approach (Scheme 1). Two different chain transfer agents (CTA), either monofunctional or tetrafunctional, were used to copolymerize benzyl methacrylate (BzMA) with increasing fraction of styrene (S) to achieve the best control of polymerization. The second block of poly(oligo(ethylene glycol) methyl ether acrylate) (POEGA) was then synthesized by chain extension of the linear or star P(S-*co*-BzMA) macromolecular chain transfer agent (macroCTA) to produce the desired BCPEs. Finally, solid electrolytes were prepared by mixing the BCPEs with lithium

bis(trifluoromethanesulfonyl)imide (LiTFSI) salt to investigate their morphology by SAXS and TEM in relationship with their ionic conductivity.



Scheme 1. Schematic illustration of the synthesis route to synthesize $lc-(A_w)_x B_y$ and $sc-(A_w)_x B_y$ block copolymers (BCP) by RAFT polymerization using either TTC-1 monofunctional CTA or TTC-4 tetrafunctional CTA. The A block corresponds to the P(S-co-BzMA) block and B block to POEGA. The subscripts w represents the weight fraction of the BzMA compared to S in the macro-CTA, the subscripts x and y correspond respectively to the weight fractions of P(S-co-BzMA) hard block and POEGA soft block in the AB block copolymer. The prefix $lc-$ and $sc-$ depicts the linear comb-like or star comb-like architecture.

2 Synthesis and Characterization of Block copolymers

2.1 P(S-co-BzMA) Macromolecular Chain Transfer Agent

In the present work, RAFT polymerization of benzyl methacrylate (BzMA) was first carried out via two different chain transfer agents (CTA), either the monofunctional trithiocarbonate (TTC-1) or the tetrafunctional trithiocarbonate (TTC-4) in order to produce linear or star polymers (Scheme 1). Both CTA are non-symmetrical trithiocarbonate exhibiting identical stabilizing Z-group ($-\text{CH}_2(\text{CH}_2)_{10}\text{CH}_3$) but different R-initiating groups (Scheme 1). The tetrafunctional CTA contains the R group in the core to preserve the star architecture whatever the degree of livingness (Scheme 1). The polymerization was performed in bulk with constant initial $[\text{CTA}]/[\text{AIBN}]$ ratio and constant value of AIBN concentration across all synthesis (Table 1). Number-average molar mass (M_n) and dispersity (D) of samples taken during polymerization were determined using SEC-MALLS and plotted as a function of the overall weight monomer conversion (Figure 2). By using the TTC-1 monofunctional CTA, a linear evolution of M_n versus conversion is observed on Figure 2(left), for BzMA homopolymerization but the values are slightly higher compared to theoretical ones ($M_{n,\text{SEC-MALLS}}/M_{n,\text{theo}} \sim 1.15$ for PBzMA). Such discrepancy between experimental and theoretical M_n is even more pronounced on Figure 2(right) when RAFT polymerization is carried out with the TTC-4 tetrafunctional CTA ($M_{n,\text{SEC-MALLS}}/M_{n,\text{theo}} \sim 1.57$ for PBzMA), along with higher dispersity values. This cannot be ascribed to bias in SEC measurement as M_n were determined by MALLS and not relative to any standard calibration. As previously reported in the literature, this trend is characteristic of a low chain transfer constant ($C_{\text{tr}} = k_{\text{ex}}/k_{\text{p}}$) in RAFT polymerization.³⁰ The leaving R group plays a role on the exchange rate and especially the fragmentation step. Note that both CTAs display two different R groups: $(\text{C}(\text{CN})(\text{CH}_3)\text{CH}_2\text{CH}_2\text{COOH})$ for TTC-1 monofunctional CTA and $(-\text{C}(\text{CH}_3)_2\text{CO}_2\text{CH}_2-)$ for TTC-4 tetrafunctional CTA. Based on profiles reported in reference³⁰, one can conclude from Figure 2 that BzMA RAFT polymerization mediated with TTC-1 is associated with C_{tr} above 1 while C_{tr} is probably far below 1 for TTC-4.

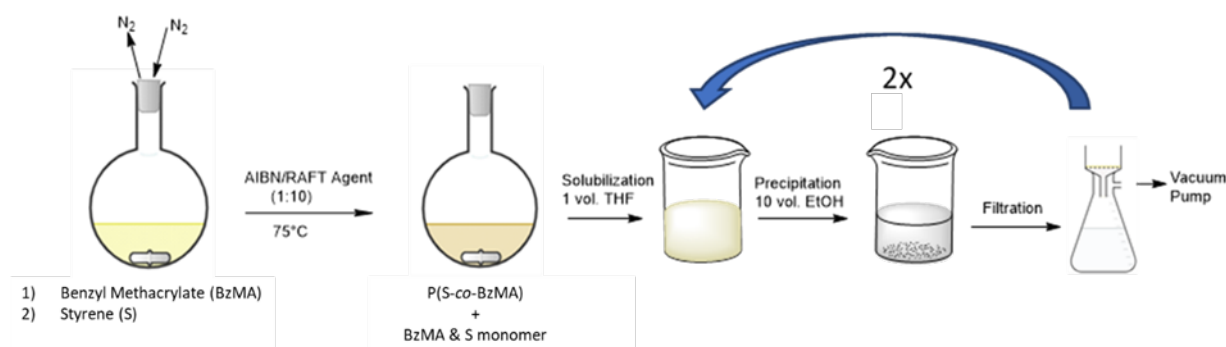


Figure 1. Schematic description of synthetic process for the macroCTA.

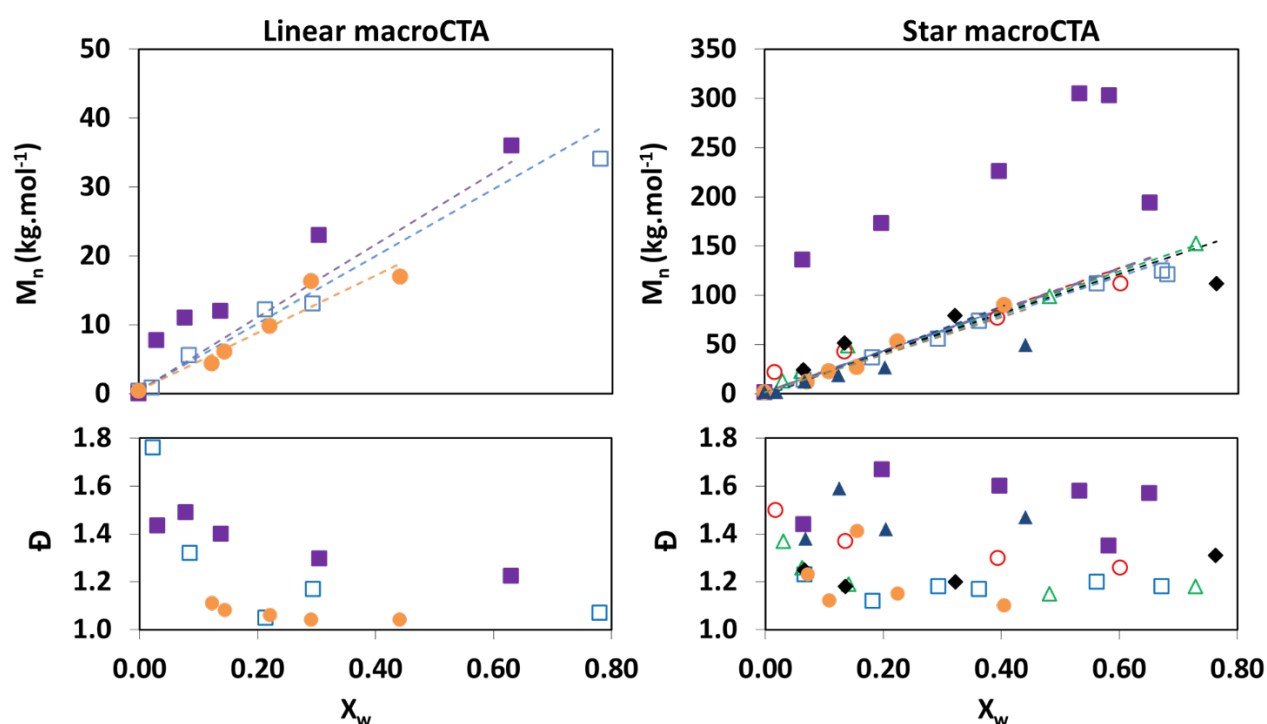


Figure 2. Evolution of $M_{n,MALLS}$ and dispersity of P(S-co-BzMA) copolymers versus the overall monomer weight conversion (X_w , see Eq S4) for various initial molar fractions in BzMA: \bullet $f_{BzMA,0}=0$, \blacktriangle $f_{BzMA,0}=0.19$, \square $f_{BzMA,0}=0.38$, \blacklozenge $f_{BzMA,0}=0.50$, \triangle $f_{BzMA,0}=0.75$, \circ $f_{BzMA,0}=0.94$, \blacksquare $f_{BzMA,0}=1$. (Left) Theoretical trend is represented with dotted lines (Eq S14) are represented with dotted lines (Table 1).

In order to favor fragmentation of the initial CTA, we decided to introduce styrene as comonomer since styrenic monomers are less stabilized compared to the *R*-group of TTC-4. Monomer feed molar composition was varied from 1 to 0 in BzMA to synthesize a series of P(S-co-BzMA) statistical copolymers and PS homopolymer from both TTC-1 and TTC-4 CTAs. Table 1 shows a summary of the compositions of the initial monomer feed ($f_{BzMA,0}$) and of final purified copolymer (F_{BzMA}) together with values of molar mass and dispersity of the copolymers. Figure 2 shows that by adding as little as 6 mol% of styrene in the feed monomer

composition ($f_{BzMA} = 0.94$), the experimental $M_{n,SEC-MALLS}$ values of star copolymers match perfectly with theoretical values and dispersity values are reduced to 1.3. Thus, the introduction of low fraction of styrene induces an increase of C_{tr} value, thus enabling to control the synthesis of star copolymers based on PBzMA. It should be noted that the M_n values of the series of P(S-co-BzMA) copolymers and PS homopolymer perfectly match the theoretical M_n values by using both monofunctional and tetrafunctional CTAs (Figure 2 left).

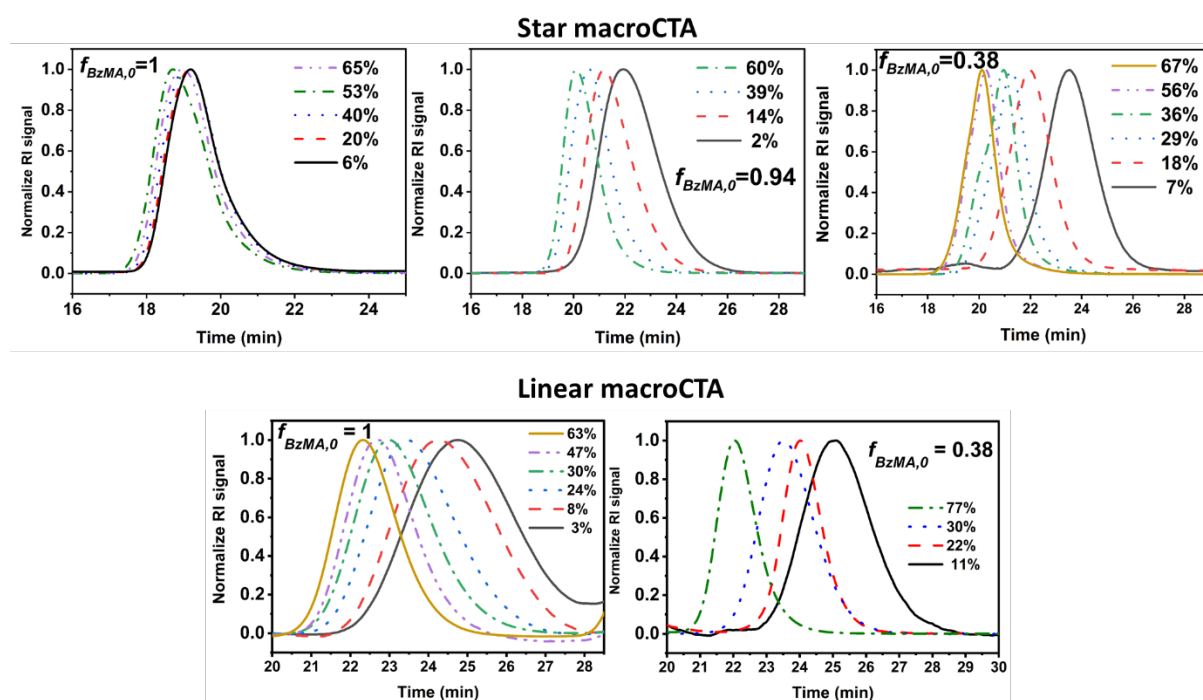


Figure 3. Evolution of the size exclusion chromatogram (RI trace) with monomer conversion for star (up) and linear (down) copolymers at different feed ratios.

The SEC chromatograms depicted in Figure 3 show monomodal traces for linear and star P(S-co-BzMA) copolymers synthesized at different monomer feed ratios ($f_{BzMA,0}$ from 1 to 0.38), as well as for linear PBzMA homopolymer. The shift of SEC traces towards lower elution volume upon increasing monomer conversion together with linear evolution of M_n confirms control of RAFT polymerization. On the other hand, the lower shift of SEC traces of star PBzMA (Figure 3) is in accordance with low C_{tr} value of the tetrafunctional CTA towards methacrylate monomers, as discussed above. The semilogarithmic kinetic plot of the overall monomer conversion versus time is linear for each monomer feed composition (Figure 4) and for both mono and tetrafunctional CTAs. This means that there is a constant number of propagating radicals in the systems. As the fraction of BzMA in monomer feed ($f_{BzMA,0}$) decreases, the apparent average rate constant of copolymerization ($\langle k_p \rangle [P^\bullet]$) is significantly

decreased. The value of the average rate constant of copolymerization ($\langle k_p \rangle$) depends on two criteria:³¹ values of reactivity ratios and values of individual rate constant of homopolymerization (k_p (S) = 87 L mol⁻¹ s⁻¹ and k_p (BzMA) = 390 L mol⁻¹ s⁻¹ at 25°C according to reference (see Figure S16).³²

Table 1. Final Composition and Macromolecular Features of the P(S-*co*-BzMA) macro-CTA Synthesized by RAFT Copolymerization in Bulk

CTA	$f_{BzMA,0}^a$	$\frac{[M]_0}{[TTC]_0}^b$	t (h)	X_w^c (%)	W_{BzMA}^d	$M_{n,theo}^e$ (kg.mol ⁻¹)	$M_{n,MALLS}^f$ (kg.mol ⁻¹)	\bar{D}_{MALLS}	macroCTA ^g
TTTC-4	1.00	300:1	3.0	65	1.00	138	217	1.51	<i>s</i> -A _{1.0}
	0.94	300:1	3.0	60	0.98	128	123	1.25	<i>s</i> -A _{0.98}
	0.74	325:1	7.5	73	0.86	151	152	1.15	<i>s</i> -A _{0.86}
	0.51	350:1	22	76	0.71	155	134	1.25	<i>s</i> -A _{0.71}
	0.38	375:1	31.5	68	0.62	135	122	1.30	<i>s</i> -A _{0.62}
	0.21	350:1	49.0	57	0.43	113	80	1.39	<i>s</i> -A _{0.43}
	0	500:1	96.0	52	0	110	122	1.20	<i>s</i> -A ₀
TTTC-1	1.00	300:1	3	62	1.00	33	38	1.10	<i>l</i> -A _{1.0}
	0.38	300:1	27	76	0.59	31	28	1.06	<i>l</i> -A _{0.59}
	0	440:1	95	52	0	25	22	1.04	<i>l</i> -A ₀

^a $f_{BzMA,0}$ is the molar fraction of BzMA in the initial monomer feed (See Eq S5 in SI).

^b $[TTC]_0$ is the concentration in trithiocarbonate functions, $[TTC]_0 = [TTC-1]_0 = 4 \times [TTC-4]_0$ and $[M]_0 = [S+BzMA]_0$. $[AIBN]_0 = 1.98$ mmol.L⁻¹, $[TTC]_0/[AIBN]_0 = 10$.

^c Overall weight conversion of both S and BzMA monomers (Eq. S4 in SI).

^d W_{BzMA} (See Eq S12 in SI) is the weight fraction of BzMA in the copolymer after purification determined from $F_{BzMA,\gamma}$ molar fraction measured by ¹H NMR (See Eq S11 in SI).

^e $M_{n,theo}$ is calculated from Eq S15 in SI

^f M_n values obtained from the SEC analysis with RI/MALLS detectors (see determination of dn/dc values for each copolymer in Table S4)

^g *s*- and *l*- represents the star and linear P(S-*co*-BzMA) copolymers respectively, and the subscript is the weight fraction of BzMA (W_{BzMA}) in the purified macroCTA.

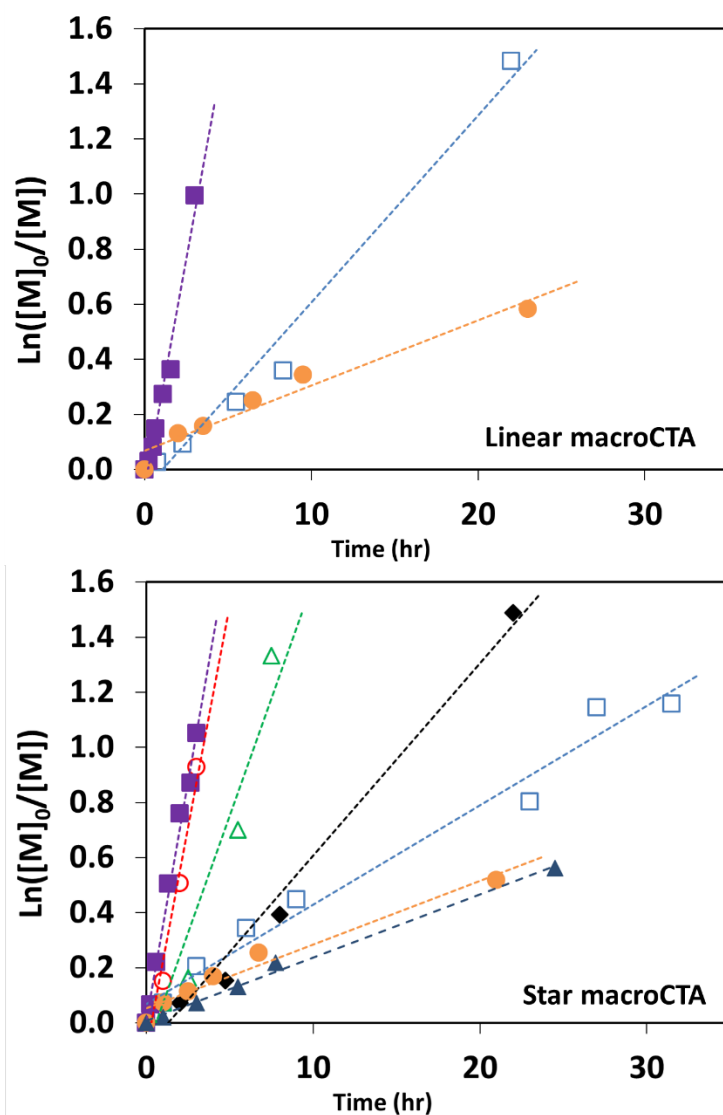


Figure 4. Semi-logarithmic plots of overall molar monomer conversion (X_m) versus time for RAFT copolymerization of S and BzMA from either TTC-1 (top) or TTC-4 (bottom) CTA at different monomer feed ratios (**Table 1**): ● $f_{BzMA,0} = 0$, ▲ $f_{BzMA,0} = 0.2$, □ $f_{BzMA,0} = 0.38$, ◆ $f_{BzMA,0} = 0.50$, △ $f_{BzMA,0} = 0.75$, ○ $f_{BzMA,0} = 0.94$, ■ $f_{BzMA,0} = 1$. Dotted lines are linear fits.

Two sets of values for reactivity ratio of styrene and BzMA are reported in the literature: $r_S = 0.46 \pm 0.02$, $r_{BzMA} = 0.52 \pm 0.08$,³³ and $r_S = 0.27 \pm 0.14$, $r_{BzMA} = 0.86 \pm 0.36$ for nitroxide-mediated polymerization (NMP).³⁴ In the present work, we determined reactivity ratio of S/BzMA with extended Kelen-Tüdös (e-KT) method (see Figure S18 and equations in supporting information). We considered the composition of the purified copolymers ($F_{BzMA,\gamma}$, Eq S11) which was measured by ¹H NMR in CD₂Cl₂ for better accuracy compared to measurements in CDCl₃ as signal of CHCl₃ overlaps with aromatic protons (Table S1). Data of Figure S18 provided values of reactivity ratios of $r_S = 0.70 \pm 0.20$ and $r_{BzMA} = 0.67 \pm 0.09$. In order to assess the distribution of comonomer along the polymer chain of macroCTA, the

experimental fraction in BzMA in the monomer feed (f_{BzMA} , Eq S6) was monitored with time and plotted over the overall molar monomer conversion (X_m , Eq S3) (**Figure 5**). Such data could be fitted with Skeist equation as another method of determination of the reactivity ratios but in the present case the number of experimental points was too low for an accurate fitting. **Figure 5** shows a quasi-constant fraction of BzMA comonomer during RAFT copolymerization in the absence of significant drift in monomer composition at least for monomer conversion below 80 % applied in the present work. As polymer chains are supposed to grow simultaneously in RAFT polymerization for sufficiently high value of C_{tr} , the homogeneous distribution of both monomers along the copolymer chain is expected to be similar for all chains. In addition, it is interesting to note that the plots of theoretical f_{BzMA} (dotted lines in **Figure 5**), calculated from reactivity ratios determined by the extended Kelen-Tüdös method in the present work ($r_S = 0.70 \pm 0.20$ and $r_{BzMA} = 0.67 \pm 0.09$), fit well with experimental data. On the other hand, a higher deviation between fitted plots and experimental data is observed for f_{BzMA} below 0.5 when applying values of reactivity ratio of $r_S = 0.27 \pm 0.14$, $r_{BzMA} = 0.86 \pm 0.36$ from literature³⁴ (see Figure S17).

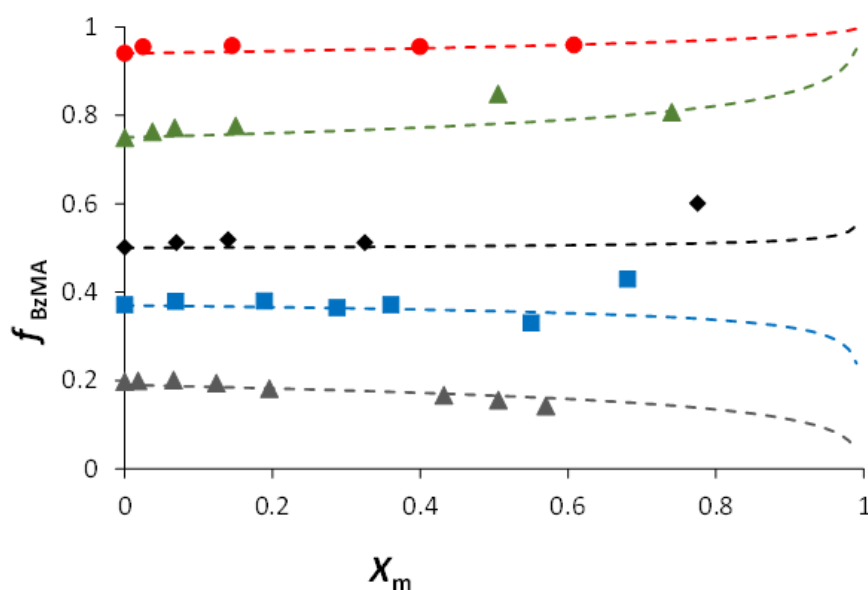


Figure 5. Evolution of BzMA fraction in monomer feed with X_m conversion. \blacktriangle $f_{BzMA,0} = 0.19$, \blacksquare $f_{BzMA,0} = 0.38$, \blacklozenge $f_{BzMA,0} = 0.50$, \blacktriangle $f_{BzMA,0} = 0.75$, \bullet $f_{BzMA,0} = 0.94$. The dotted line corresponds to the fit of f_{BzMA} versus conversion calculated from Eq S8 by using reactivity ratios of present work ($r_S = 0.70 \pm 0.20$ and $r_{BzMA} = 0.66 \pm 0.09$).

In order to confirm the synthesis of statistical copolymers, the T_g evolution of the star macroCTAs vs. $f_{BzMA,0}$ was investigated by DSC. The series of P(BzMA-co-S) copolymers (**Figure 6**) exhibited indeed a single glass transition temperature (T_g) peak appearing between

T_g values of both homopolymers ($T_{g,PBzMA} = 63^\circ\text{C}$, $T_{g,PS} = 100^\circ\text{C}$). The T_g increased with decreasing weight fraction of BzMA (W_{BzMA}) in agreement with theoretical ($T_{g,theo}$) calculations from the Fox-Flory equation (Eq 1, see Figure 7) as expected for statistical copolymers.

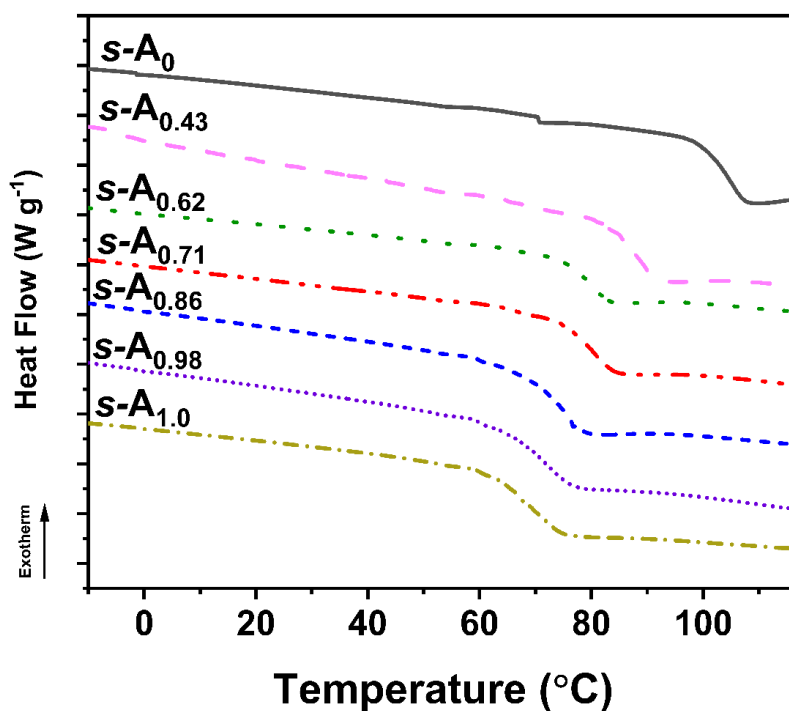


Figure 6. Glass transition temperature (T_g) of star P(S-co-BzMA) copolymer with increasing content of styrene.

$$\frac{1}{T_{g,theo}} = \frac{W_{BzMA}}{T_{g,BzMA}} + \frac{W_{styrene}}{T_{g,styrene}} \quad 1$$

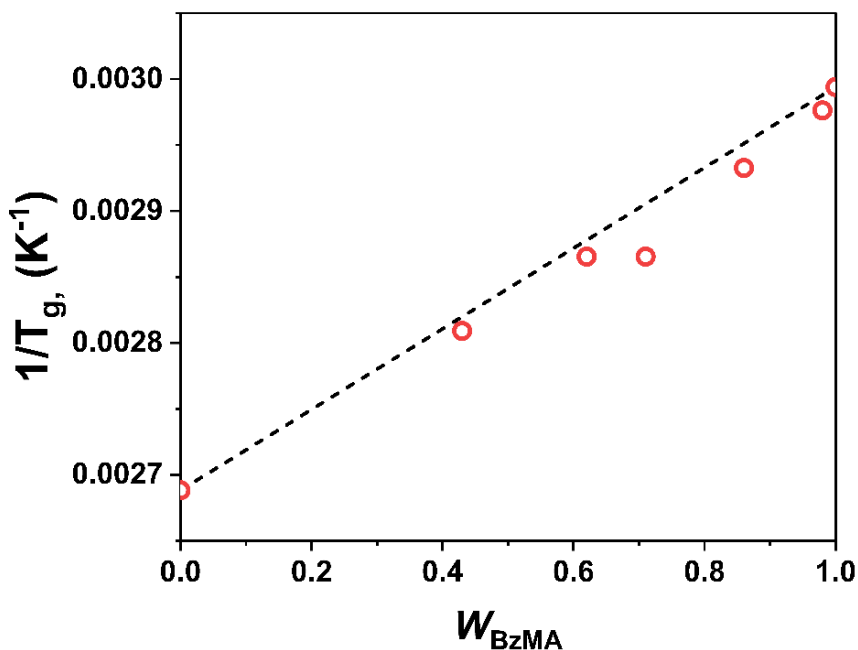


Figure 7. Plot of the weight fraction of BzMA of star macroCTA versus experimental T_g (\circ). The dotted line corresponds to the theoretical T_g calculated from Eq 1.

2.2 Characterization of star architecture.

Based on the work of Zimm and Stockmayer,³⁵ the number of arms, f , for star polymers with monodispersed arm length can be determined from the contraction factor, g , defined in Eq 2 and Eq 3.

$$g = \frac{3f - 2}{f^2} \quad 2$$

$$g = \left[\frac{([\eta]_s)}{([\eta]_l)_M} \right]^{1/\varepsilon} \quad 3$$

$[\eta]_s$ and $[\eta]_l$ represents the intrinsic viscosities of the star and linear polymer respectively, at the same molar mass M , and ε is known as the viscosity shielding ratio which describes the draining behaviour of the polymer in solution.³⁶ The ε value were reported to generally fall in the range of 0.5 to 1.5.³⁵ The branched structure of star PS synthesized by RAFT polymerization from TTC-4 CTA ($s\text{-A}_0$ in Table 1) was assessed from the determination of the contraction factor by comparison with linear standard PS samples (see experimental part). Kinetic samples taken at different intervals during synthesis of the star PS were analysed by

SEC with an online viscosimeter. The logarithmic plot of intrinsic viscosity against molar mass ($\text{Log } [\eta]$ vs $\text{Log } M$) were plotted for each chromatogram as depicted in Figure 8.

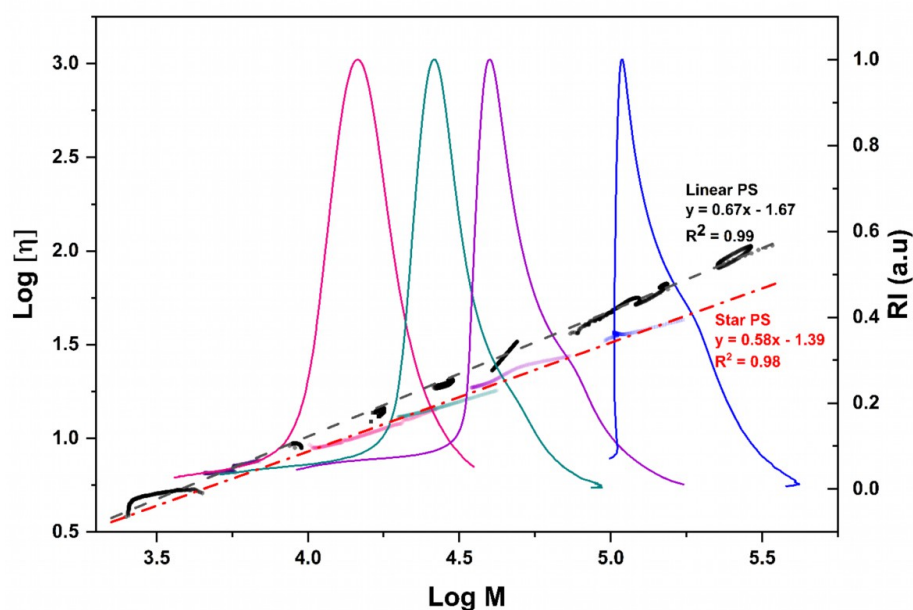


Figure 8. Mark-houwink-sakurada plot for star PS, s-A₀, at different monomer conversion with molar mass range 13.7 – 128.7 kg.mol⁻¹ (coloured traces/symbols and red linear regression) overlaid with the chromatogram from RI detector to indicate eluting population. Linear PS standards, commercially available for Polystyrene Standard Service PSS supplier (synthesized by anionic polymerization) with molar mass in the range 2.9 – 290 kg.mol⁻¹ were used as a basis for comparison (black symbol and black linear regression).

The linear regression of the experimental values provided an average value of the Mark-Houwink-Sakurada exponent ($[\eta] = KM^\alpha$) equal to $\alpha_{s-PS} = 0.58$ for star PS and $\alpha_{l-PS} = 0.67$ for linear PS. This is related to a lower hydrodynamic volume ($V_h \sim [\eta]M$) occupied by star polymer due to their higher compaction compared with linear polymers of the same molar mass. Therefore, lower α value of star PS confirms the branched character of the polymers synthesized from TTC-4 CTA. For each slices of $\text{Log } M$, the quadratic equation that results from Eq 2 and Eq 3 was solved for values of ε equal to either 0.5, 1.0 or 1.5 in order to plot the value of number of arms f as a function of molar mass (Figure 9). Whatever the chosen ε value, f is above 2, which indicates that PS synthesized from TTC-4 are not analogous to linear PS. For the intermediate $\varepsilon = 1$ value, f ranges between 2.8 and 3.8 (Fig S9). Consequently, in the further part of the work, the macroCTA synthesized from TTC-4 CTA will be considered as star polymers and the ones synthesized from TTC-1 CTA as linear polymers (see Scheme 1 and Table 1).

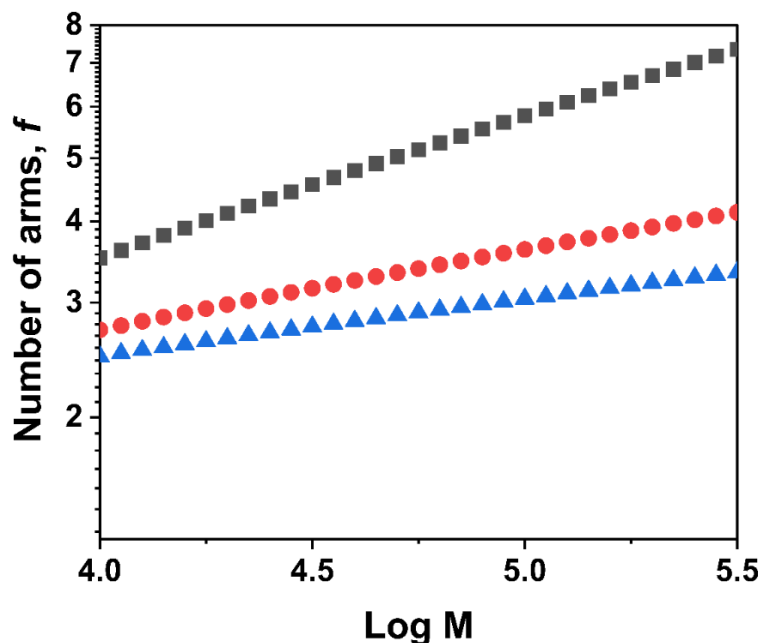


Figure 9. Graph showing the calculated number of arms, f versus molar mass (M) of star PS, s -A₀. Shielding ratio ϵ of 0.5 (■), 1 (●) and 1.5 (▲) have been overlaid to show influence of the parameter on the calculated number of arms.

2.3 P(S-*co*-BzMA)-*b*-POEGA Block copolymers.

Block copolymers (BCP) consisting of a hard block of statistical copolymer of styrene and benzyl methacrylate, and a soft ion-conductive block of poly(oligo(ethylene glycol) methyl ether acrylate) (POEGA) were synthesized by chain extension of linear and star first blocks described in the previous part (see Table 2). RAFT polymerization of OEGA was performed in bulk using P(S-*co*-BzMA) as macro-CTA and AIBN as initiator (Scheme 1). This protocol implies a good solubility of the macro-CTA in OEGA. This is the interest of PBzMA or P(S-*co*-BzMA) copolymers which are soluble in OEGA while solubilisation of PS in OEGA requires the addition of 1,4-dioxane solvent (see experimental part 5.3.1). ¹H NMR of both s -A_{0.62} star precursor and associated sc -(A_{0.62})_{0.80}B_{0.20} star comb-like block copolymer is displayed in **Figure 10**. The weight fraction of POEGA in BCP was derived from molar fraction of POEGA calculated from the ¹H NMR integrals (see Eq S19, Table 2). Interestingly, DOSY NMR of sc -(A_{0.62})_{0.80}B_{0.20} block copolymer displays only one diffusion coefficient correlated with ¹H NMR signals of both P(S-*co*-BzMA) and POEGA moieties (**Figure 10**). This confirms the successful preparation of block copolymers, which was corroborated by the shift of SEC traces towards higher values of Log M between initial macroCTA and final BCP

from both linear and star precursors (Figure S20 - Figure S23). However, it should be noted that upon targeting intermediate OEGA conversion from star P(S-*co*-BzMA) macroCTA in bulk with high initial ratio of [OEGA]/[macroCTA], the final polymer was not soluble (gel-like) and could not be accurately analyzed by SEC (*sc*-(A_{0.62})_{0.23}B_{0.77} sample in Table 2). This can be explained by star–star coupling by radical-radical combination reactions producing high molar mass hyper-branched structures, as previously reported for R-core mediated RAFT polymerization.³⁷

Table 2. Features of the AB Linear Comb-like and Star Comb-like Diblock Copolymers Synthesized from the macro-CTA reported in Table 1

macroCTA	$\frac{[\text{OEGA}]_0}{[\text{macroCTA}]_0}$	Conv. (%)	W_{POEGA}^a	$M_{n,\text{theo}}^b$ (kg·mol ⁻¹)	$M_{n,\text{MALLS}}$ (kg·mol ⁻¹)	$\mathcal{D}_{\text{MALLS}}$	BCP ^c
<i>l</i> -A ₀	102	77 ^e	0.68	59	41	1.20	<i>lc</i> -(A ₀) _{0.32} B _{0.68}
<i>l</i> -A _{0.59}	41	94 ^e	0.29	48	41	1.10	<i>lc</i> -(A _{0.59}) _{0.71} B _{0.29}
<i>s</i> -A _{0.62}	1525	54	0.77	530	<i>n.a.</i> ^d	<i>n.a.</i> ^d	<i>sc</i> -(A _{0.62}) _{0.23} B _{0.77}
<i>s</i> -A _{0.62}	175	98 ^e	0.27	219	414	1.31	<i>sc</i> -(A _{0.62}) _{0.73} B _{0.27}
<i>s</i> -A _{0.62}	1525	13	0.20	153	155	1.22	<i>sc</i> -(A _{0.62}) _{0.80} B _{0.20}
<i>s</i> -A _{0.43}	1523	4	0.16	95	109	1.31	<i>sc</i> -(A _{0.43}) _{0.84} B _{0.16}

^a W_{POEGA} is the weight fraction of POEGA in the block copolymer after purification, as determined from the molar fraction calculated from ¹H NMR spectra (see Eq. S19).

^b Theoretical molar mass determined from Eq. S16.

^c *s*- and *l*- represents the star and linear polymers respectively.

^d The SEC analysis was not applicable as the solubility of samples was too low and refractive index signal at very low intensity to be reliable.

^e Experiment performed in solution (1:1 v/v 1,4 dioxane:OEGA).

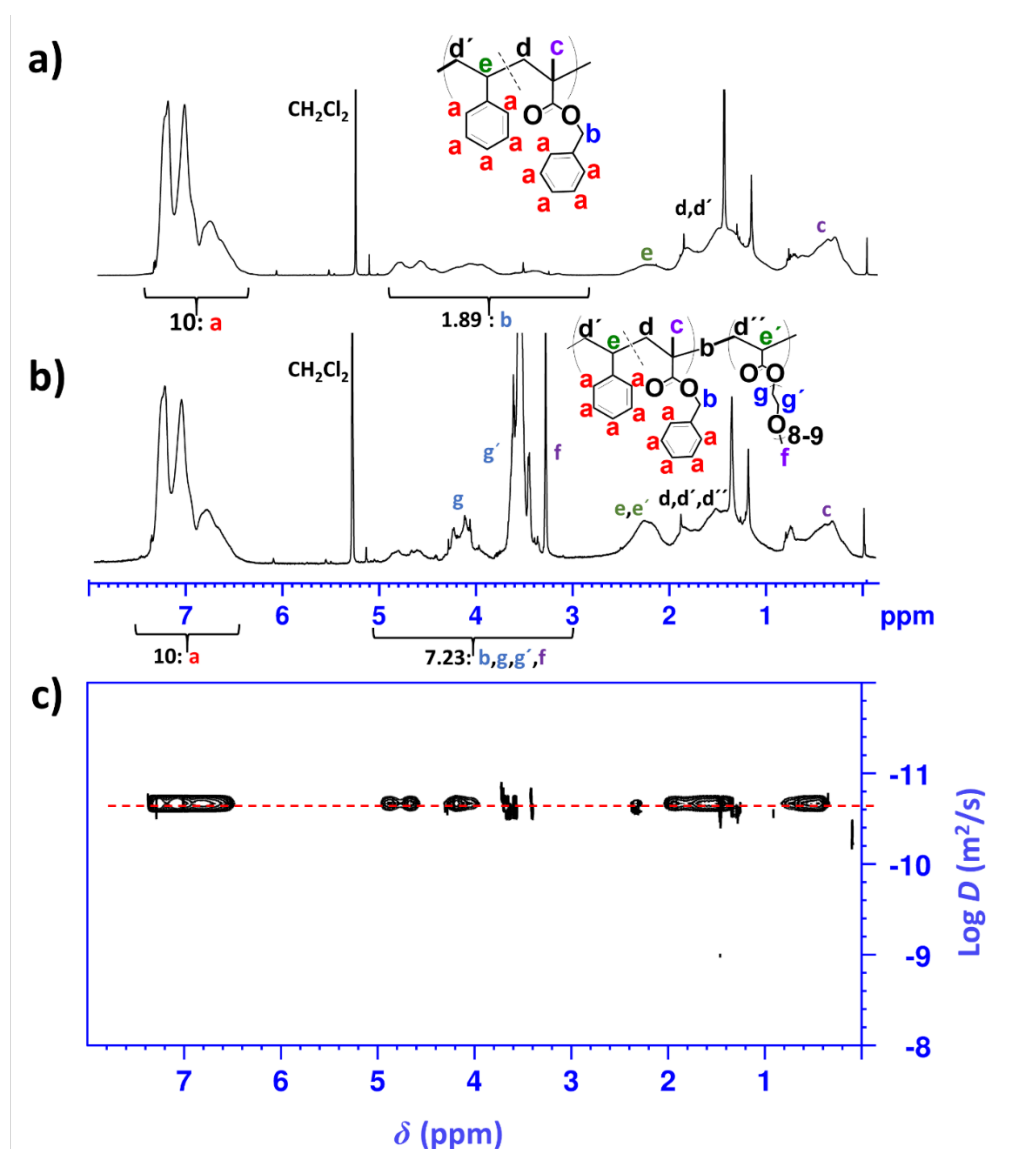


Figure 10. ^1H NMR spectra of a) $s\text{-A}_{0.62}$ and b) $sc\text{-}(\text{A}_{0.62})_{0.80}\text{B}_{0.20}$ in CD_2Cl_2 ($[\text{polymer}] = 10 \text{ mg}\cdot\text{mL}^{-1}$). Numbers correspond to the integrals of signals. c) DOSY NMR Spectrum: diffusion coefficient (D) versus chemical shift (δ) of $sc\text{-}(\text{A}_{0.62})_{0.80}\text{B}_{0.20}$.

3 Conductivity versus morphology.

The temperature-dependent ion conductivities which is a critical parameter for application in solid state batteries, was evaluated by EIS measurements. Conductivity versus temperature curves are shown in Figure 11. As expected, in all samples, conductivity decreased with decreasing temperature due to a reduced segmental chain mobility at lower temperatures. Another observable trend was that conductivity increased with increasing volume fraction of the POEGA conducting phase, ϕ_c (see inset graph in Figure 11, Table S4). The conductivity of

sc-(A_{0.43})_{0.84}B_{0.16} copolymer was significantly lower, probably due to a weakly percolating POEGA conducting phase with such low ϕ_c .

The conductivity data versus temperature were fitted with either the Vogel-Fulcher-Tammann (VFT) or the Arrhenius models, thus pointing out different ion transport mechanisms. The VFT model depicts a coupling between the polymer chain segmental motion and the ion transport that scales with temperature.³⁸ Its expression is

$$\sigma = \sigma_0 \exp\left(-\frac{B}{R(T-T_0)}\right), \quad 1$$

where B is the pseudo activation energy for ion transport, σ_0 is a prefactor related to the number of charge carriers present in the electrolyte, R is the gas constant, and T_0 is the Vogel temperature. T_0 is a reference temperature at which the configurational entropy of the polymer matrix becomes zero and is empirically related to the polymer T_g . On the other hand, the Arrhenius model is associated to a Grotthuss mechanism of ion transport.³⁹ The corresponding expression is

$$\sigma = \sigma_0 \exp\left(-\frac{E_a}{RT}\right), \quad 2$$

with E_a being the activation energy, which differs from the VFT pseudo-activation energy. The model selection was based on the shape of the conductivity curves on the Arrhenius plot, as described hereafter. Data collected on the BCPEs with the larger POEGA blocks (cf. Table 2), i.e. sc-(A_{0.62})_{0.23}B_{0.77}, sc-(A_{0.62})_{0.73}B_{0.27}, sc-(A_{0.62})_{0.80}B_{0.20}, and lc-(A₀)_{0.32}B_{0.68}, were fitted with the VFT model to account for the curvature on the Arrhenius plot, thus indicating a significant role of the POEGA segmental motion on the ion transport. The values of T_0 (in °C) are presented in Table S3 together with the corresponding conductive block T_g measured by DSC. The T_0 ranges between 40 and 60 °C below the T_g which agrees with the empirical value of 50 °C reported in the literature.³⁸ The two BCPEs with shorter POEGA blocks (cf. Table 2), i.e., sc-(A_{0.43})_{0.84}B_{0.16} and lc-(A_{0.59})_{0.71}B_{0.29} do not exhibit evident curvatures, then the Arrhenius model was used to fit the data. Considering those two samples, linear and star comb-like BCPEs, one can expect that POEGA segmental motion is limited due the reduced block molar masses which remain anchored to the high T_g domains. Since the morphology of the self-assembled BCPEs is known to play a role in ion conductivity, the bulk morphologies of the BCPE films were investigated using SAXS and TEM.

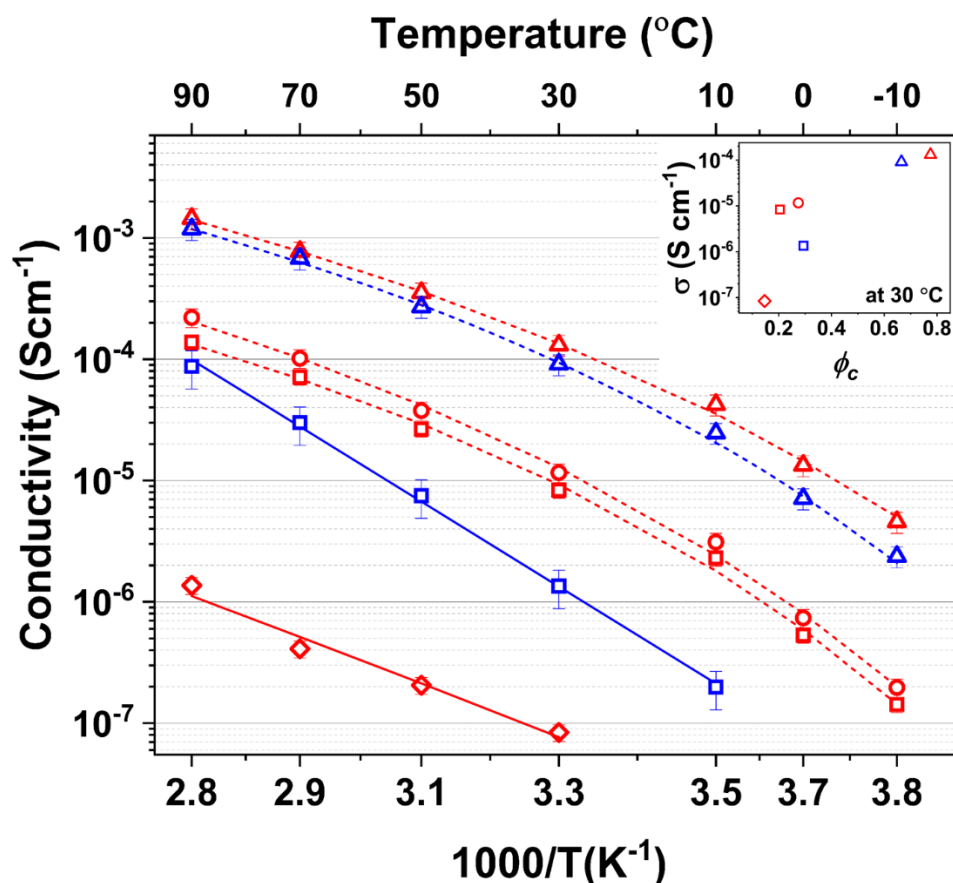


Figure 11. Temperature-dependent ionic conductivity derived from the EIS measurements of BCPEs: (Δ) $sc-(A_{0.62})_{0.23}B_{0.77}$, (\circ) $sc-(A_{0.62})_{0.73}B_{0.27}$, (\square) $sc-(A_{0.62})_{0.80}B_{0.20}$, (\diamond) $sc-(A_{0.43})_{0.84}B_{0.16}$, (Δ) $lc-(A_0)_{0.32}B_{0.68}$, (\square) $lc-(A_{0.59})_{0.71}B_{0.29}$. Solid lines represent Arrhenius fits and the dashed lines represent VFT fits. Inset graph shows plot of σ versus ϕ_c of conducting phase for star comb-like (red) and linear comb-like (blue) BCPEs.

SAXS profiles were collected for linear and star comb-like BCPs for temperatures ranging from 25 to 100 °C. Linear BCPs show no structural peak (exemplified with sample $lc-(A_{0.59})_{0.71}B_{0.29}$ in Figure S26a), while star BCPEs show a broad single peak (exemplified with sample $sc-(A_{0.62})_{0.80}B_{0.20}$ in Figure S27a) thus indicating poor phase separation of the BCPs. After blending the BCP with LiTFSI salt (at ratio $[EO]/[Li]=15$), low intensity structural peaks were observed at 25 °C indicating phase separation of the individual blocks. Upon annealing at 100 °C, slightly shifted higher intensity structural peaks could be observed indicating stronger phase separation. Several reports have indicated that addition of lithium salt increases the effective Flory–Huggins interaction parameter (χ_{eff}) between the polymer blocks as well as the stiffness of the chains comprising the ion-conducting domain.⁴⁰⁻⁴² In order to follow any possible phase transition that may be associated with temperature-dependent changes, *in-situ* SAXS measurements were performed while cooling stepwise to 30 °C (see Figure S26b and

Figure S27b). However, there was no drastic re-definition of the structural patterns thus signifying that the samples retain their morphologies after annealing.

The following structural characterization was performed on BCPEs, after a temperature annealing at 100 °C, by SAXS (Figure 12) and bright field TEM (Figure 13). For star comb-like series, the scattering profiles of $sc-(A_{0.62})_{0.73}B_{0.27}$ and $sc-(A_{0.62})_{0.80}B_{0.20}$ BCPEs (Figure 12a) show primary peaks at $q^* \approx 0.15 \text{ nm}^{-1}$ and $q^* \approx 0.16 \text{ nm}^{-1}$ respectively with higher order peaks positioned at $2q^*$, $3q^*$, $4q^*$ and $5q^*$ which are signatures of lamellar microstructure (LAM). The characteristic LAM periods were calculated from $d = 2\pi / q^*$ and given as $d = 41 \text{ nm}$ and 39 nm respectively. In case of $sc-(A_{0.43})_{0.84}B_{0.16}$, low intensity and broad structural peaks at q^* , $2q^*$, $3q^*$ indicates also a LAM pattern, with $d = 58 \text{ nm}$. TEM pictures collected on those three samples confirm the SAXS findings, displaying evident LAM morphologies (Figure 13b-d). Nevertheless, TEM images bring additional information on the quality of the ordering. Indeed, samples $sc-(A_{0.62})_{0.73}B_{0.27}$ and $sc-(A_{0.62})_{0.80}B_{0.20}$ feature long-range LAM ordering. On the other hand, $sc-(A_{0.43})_{0.84}B_{0.16}$ BCPE ordering is limited and punctuated with inverted hexagonal cylinders (HEX') phases (see arrow markers in Figure 13d). This later feature might act as dead ends thus impeding ion transport. The scattering curve collected on sample $sc-(A_{0.62})_{0.23}B_{0.77}$ (Figure 12a) shows a broad primary peak, $q^* \approx 0.14 \text{ nm}^{-1}$ and secondary peak at $\sqrt{7} q^*$. The secondary peak indicates that the morphology is not LAM and the TEM image (Figure 13a) shows evident spherical objects dispersed in the POEGA conducting phase. A characteristic sphere-to-sphere distance, $d = 45 \text{ nm}$ is estimated from the Bragg relation $d = 2\pi / q^*$.

For the linear comb-like BCPE series, the TEM image collected on sample $lc-(A_0)_{0.32}B_{0.68}$ (Figure 13e) shows an evident HEX morphology with a majority POEGA conducting phase. This is confirmed by SAXS (Figure 12b) with structural peaks positioned at $q^* \approx 0.17 \text{ nm}^{-1}$, $2q^*$, $\sqrt{7}q^*$ and $\sqrt{13}q^*$. A cylinder-to-cylinder distance $d = 43 \text{ nm}$ is calculated with $d = 4\pi / \sqrt{3}q^*$. The SAXS profile measured on sample $lc-(A_{0.59})_{0.71}B_{0.29}$ (Figure 12b) displays peaks at $q^* \approx 0.18 \text{ nm}^{-1}$, $2q^*$, $3q^*$, and $4q^*$ indicative of a LAM morphology with $d = 35 \text{ nm}$. This is also in agreement with the TEM image (Figure 13f) exhibiting swirly short-range ordered lamella.

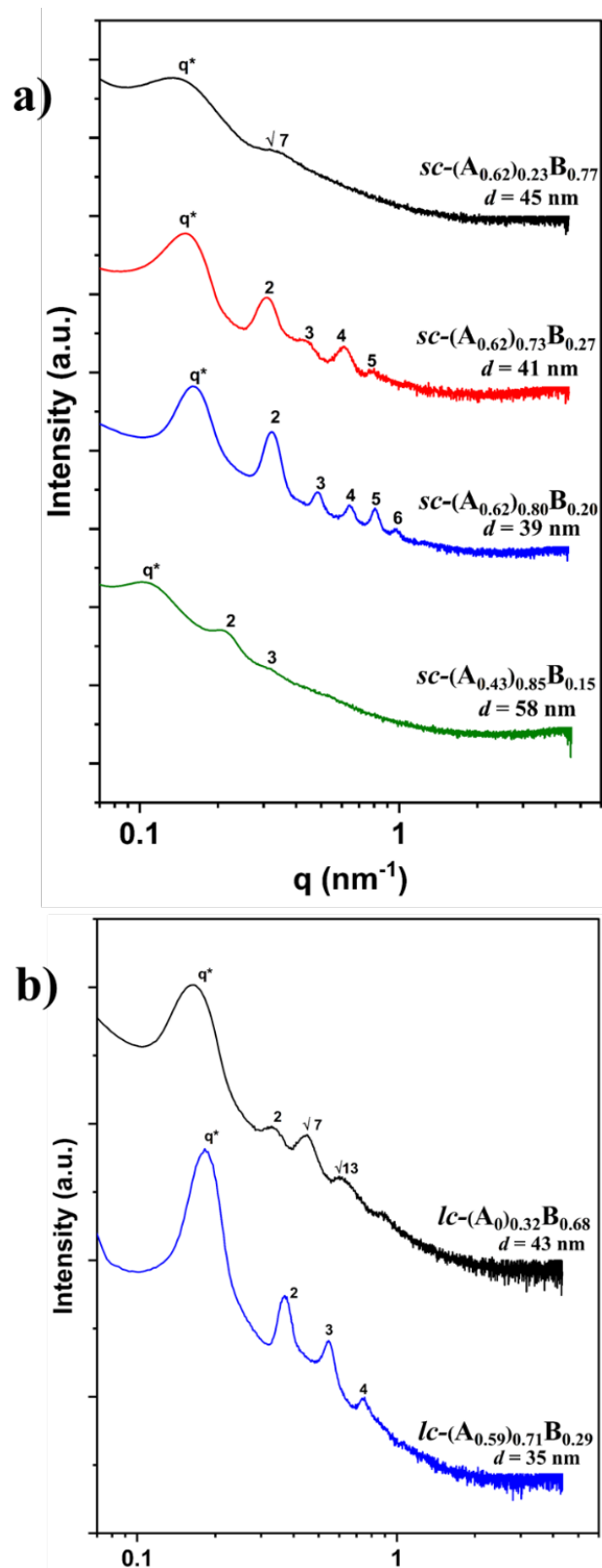


Figure 12. SAXS profiles of BCPEs at 30 °C after cooling. a) star comb-like BCPE b) linear comb-like BCPE.

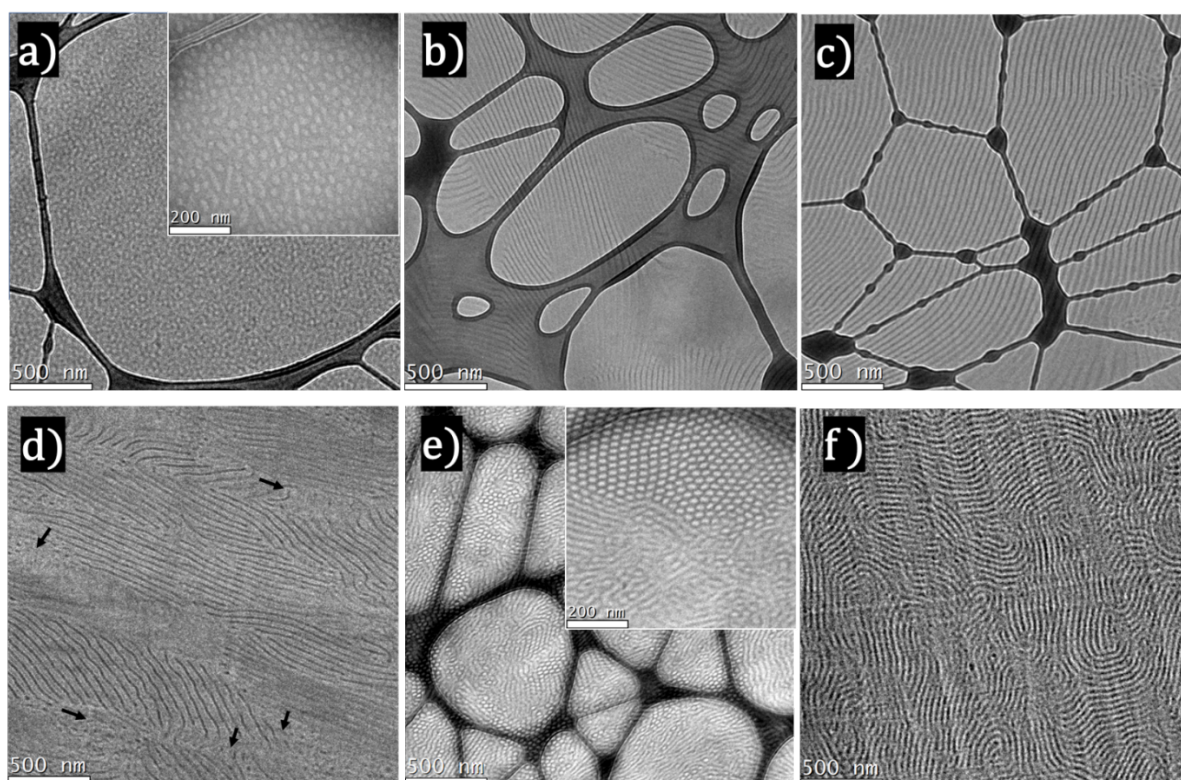


Figure 13. TEM images for annealed star comb-like BCPE (Top) and linear comb-like BCPEs (bottom) prepared by mixing LiTFSI and BCP with varying ratio of final conducting volume fraction of POEGA/LiTFSI conducting phase (ϕ_c). a) $sc-(A_{0.62})_{0.23}B_{0.77}$, $\phi_c = 0.78$ (Sphere), b) $sc-(A_{0.62})_{0.73}B_{0.27}$, $\phi_c = 0.27$ (LAM), c) $sc-(A_{0.62})_{0.80}B_{0.20}$, $\phi_c = 0.20$ (LAM), d) $sc-(A_{0.43})_{0.84}B_{0.16}$, $\phi_c = 0.15$ (LAM and HEX'), e) $lc-(A_0)_{0.32}B_{0.68}$, and f) $lc-(A_{0.59})_{0.71}B_{0.29}$, $\phi_c = 0.68$ (HEX) and $\phi_c = 0.29$ (LAM) respectively. Black arrows show regions of hexagonal cylinders (HEX') with POEGA minority phase.

Despite a rather similar composition the star BCPEs $sc-(A_{0.62})_{0.73}B_{0.27}$ and $sc-(A_{0.62})_{0.80}B_{0.20}$ and the linear $lc-(A_{0.59})_{0.71}B_{0.29}$ display a stark difference. The star BCPEs exhibit straight and long-range LAM morphologies (Figure 13b and Figure 13c), resulting from dense self-assembly of multiple arms of the star BCPE. Similar results have been reported for miktoarm star PS-*b*-(PEO)₃ BC by Lee *et al.*²⁵ Consequently, this reduced tortuosity leads to a higher ionic conductivity compared to the linear $lc-(A_{0.59})_{0.71}B_{0.29}$ BCPE. To further depict the influence of morphologies on ionic conductivity, we assumed that (i) the overall mobility of ions in the electrolytes is facilitated by the segmental motion of the EO side chains and hence conductivity can be correlated to ϕ_c as discussed previously; (ii) the POEGA phase in the BCPEs considered separately presents all the same ionic conductivity, σ_0 at a specific salt concentration. Based on these assumptions, σ , the BCPE conductivity, can be define as¹⁴

$$\sigma = \frac{f}{\tau} \phi_c \sigma_0, \quad 3$$

where τ is a local tortuosity factor, *i.e.*, the ratio of the effective pathway required for ion transport through the electrolyte thickness, and f is a morphological factor to quantify the global grain alignment in the direction of the electric field. Values of $f\tau^{-1}$ for LAM, HEX and BCC (spheres) morphologies have been reported in literature based on effective medium theory (see First, POEGA conductivity values, σ_0 was evaluated at 30 °C via Eq 3 by using the experimentally measured conductivity, σ , of *sc*-(A_{0.62})_{0.23}B_{0.77} and *lc*-(A₀)_{0.32}B_{0.68} and the theoretical values of $f\tau^{-1}$ of sphere and HEX morphologies as reported in **Table 3**. *sc*-(A_{0.62})_{0.23}B_{0.77} and *lc*-(A₀)_{0.32}B_{0.68} samples were chosen as references because the observed morphologies (spheres and HEX respectively) feature continuous POEGA conducting majority phases. Also, Balsara and coworkers have shown that the conductivity models fit better the experimental values at higher ϕ_c .¹⁴ POEGA conductivity values, σ_0 of 1.87×10^{-4} and 2.05×10^{-4} S.cm⁻¹ were obtained respectively from *sc*-(A_{0.62})_{0.23}B_{0.77} (spheres) and *lc*-(A₀)_{0.32}B_{0.68} (HEX). Both values are relatively close thus reinforcing the previous assumptions. Also, as expected, this indicates that star and linear architectures do not significantly impact the ion conductivity of the majority POEGA phase, when POEGA is the BCP outer blocks. Hereafter, the σ_0 average value of 1.96×10^{-4} S.cm⁻¹ at 30 °C will be used. We note in passing the storage moduli of *sc*-(A_{0.62})_{0.23}B_{0.77} and *lc*-(A₀)_{0.32}B_{0.68} were very close ~1 MPa at room temperature (Figure S31 and Figure S32).

Table 3).⁴³

First, POEGA conductivity values, σ_0 was evaluated at 30 °C via Eq 3 by using the experimentally measured conductivity, σ , of *sc*-(A_{0.62})_{0.23}B_{0.77} and *lc*-(A₀)_{0.32}B_{0.68} and the theoretical values of $f\tau^{-1}$ of sphere and HEX morphologies as reported in **Table 3**. *sc*-(A_{0.62})_{0.23}B_{0.77} and *lc*-(A₀)_{0.32}B_{0.68} samples were chosen as references because the observed morphologies (spheres and HEX respectively) feature continuous POEGA conducting majority phases. Also, Balsara and coworkers have shown that the conductivity models fit better the experimental values at higher ϕ_c .¹⁴ POEGA conductivity values, σ_0 of 1.87×10^{-4} and 2.05×10^{-4} S.cm⁻¹ were obtained respectively from *sc*-(A_{0.62})_{0.23}B_{0.77} (spheres) and *lc*-(A₀)_{0.32}B_{0.68} (HEX). Both values are relatively close thus reinforcing the previous assumptions. Also, as expected, this indicates that star and linear architectures do not significantly impact the ion

conductivity of the majority POEGA phase, when POEGA is the BCP outer blocks. Hereafter, the σ_0 average value of 1.96×10^{-4} S.cm⁻¹ at 30 °C will be used. We note in passing the storage moduli of *sc*-(A_{0.62})_{0.23}B_{0.77} and *lc*-(A₀)_{0.32}B_{0.68} were very close ~1 MPa at room temperature (Figure S31 and Figure S32).

Table 3. Morphology Factor, f , and Tortuosity, τ , for the morphologies of interest⁴³

Morphology	f	τ
LAM	2/3	1
HEX	1	$(2-\phi_c)$
BCC	1	$(3-\phi_c)/2$

In order to evaluate the influence of the nanometer morphology, the conductivity of each BCPEs, σ , were normalized by $\phi_c \sigma_0$, which theoretically equals to $f\tau^{-1}$, representative of a given model morphology following Eq 3 and First, POEGA conductivity values, σ_0 was evaluated at 30 °C via Eq 3 by using the experimentally measured conductivity, σ , of *sc*-(A_{0.62})_{0.23}B_{0.77} and *lc*-(A₀)_{0.32}B_{0.68} and the theoretical values of $f\tau^{-1}$ of sphere and HEX morphologies as reported in **Table 3**. *sc*-(A_{0.62})_{0.23}B_{0.77} and *lc*-(A₀)_{0.32}B_{0.68} samples were chosen as references because the observed morphologies (spheres and HEX respectively) feature continuous POEGA conducting majority phases. Also, Balsara and coworkers have shown that the conductivity models fit better the experimental values at higher ϕ_c .¹⁴ POEGA conductivity values, σ_0 of 1.87×10^{-4} and 2.05×10^{-4} S.cm⁻¹ were obtained respectively from *sc*-(A_{0.62})_{0.23}B_{0.77} (spheres) and *lc*-(A₀)_{0.32}B_{0.68} (HEX). Both values are relatively close thus reinforcing the previous assumptions. Also, as expected, this indicates that star and linear architectures do not significantly impact the ion conductivity of the majority POEGA phase, when POEGA is the BCP outer blocks. Hereafter, the σ_0 average value of 1.96×10^{-4} S.cm⁻¹ at 30 °C will be used. We note in passing the storage moduli of *sc*-(A_{0.62})_{0.23}B_{0.77} and *lc*-(A₀)_{0.32}B_{0.68} were very close ~1 MPa at room temperature (Figure S31 and Figure S32).

Table 3. All the experimental values of $f\tau^{-1}$ are displayed in Figure 14, in addition, for comparison, the theoretical value of $f\tau^{-1} = 2/3$, for LAM, is plotted as short dashed line (black) across the ϕ_c region where LAM phases were observed. In Figure 14, experimental $f\tau^{-1}$ of *sc*-(A_{0.62})_{0.73}B_{0.27}, *sc*-(A_{0.62})_{0.80}B_{0.20} and *lc*-(A_{0.59})_{0.71}B_{0.29} are significantly lower than the theoretical 2/3. An explanation for those deviations is that defects, such as grain boundaries

and lamellar fluctuations, constitute extra tortuosity, thus $\tau > 1$.^{25, 44} Tortuosity factors, τ , can be then evaluated from the experimental σ and Eq 3, considering $f = 2/3$. Values of $\tau = 3.2, 3.1$ and 28.2 are obtained respectively for star ($sc-(A_{0.62})_{0.73}B_{0.27}$, $sc-(A_{0.62})_{0.80}B_{0.20}$) and linear ($lc-(A_{0.59})_{0.71}B_{0.29}$) BCPEs. The larger values found for the linear BCPE can be explained by the swirly lamellar observed by TEM (see Figure 13f). Indeed, star BCPEs encompasses unique macromolecular self-organization that affect the structural range and connectivity of ordered grains so that the ionic pathway is less tortuous than the linear ones.

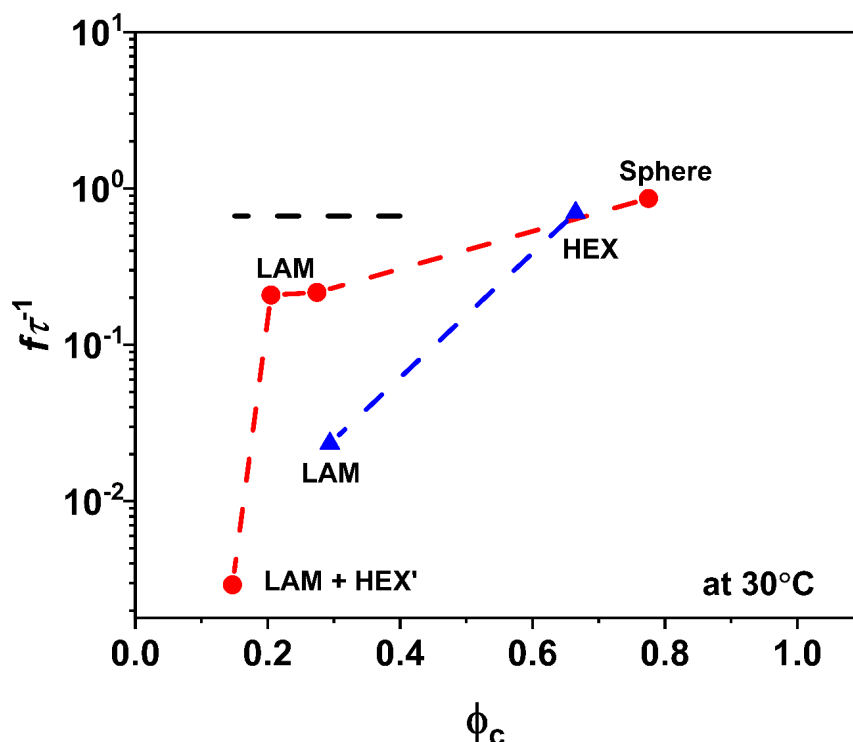


Figure 14. Normalized Conductivity ($\sigma/(\phi_c \sigma_0) = f\tau^{-1}$) at 30°C as a function of ϕ_c for star (●) and linear (▲) BCPEs. The solid black line (---) corresponds to theoretical values $f\tau^{-1}$ for lamellar in First, POEGA conductivity values, σ_0 was evaluated at 30 °C via Eq 3 by using the experimentally measured conductivity, σ , of $sc-(A_{0.62})_{0.23}B_{0.77}$ and $lc-(A_0)_{0.32}B_{0.68}$ and the theoretical values of $f\tau^{-1}$ of sphere and HEX morphologies as reported in Table 3. $sc-(A_{0.62})_{0.23}B_{0.77}$ and $lc-(A_0)_{0.32}B_{0.68}$ samples were chosen as references because the observed morphologies (spheres and HEX respectively) feature continuous POEGA conducting majority phases. Also, Balsara and coworkers have shown that the conductivity models fit better the experimental values at higher ϕ_c .¹⁴ POEGA conductivity values, σ_0 of 1.87×10^{-4} and 2.05×10^{-4} S.cm⁻¹ were obtained respectively from $sc-(A_{0.62})_{0.23}B_{0.77}$ (spheres) and $lc-(A_0)_{0.32}B_{0.68}$ (HEX). Both values are relatively close thus reinforcing the previous assumptions. Also, as expected, this indicates that star and linear architectures do not significantly impact the ion conductivity of the majority POEGA phase, when POEGA is the BCP outer blocks. Hereafter, the σ_0 average value of 1.96×10^{-4} S.cm⁻¹ at 30 °C will be used. We note in passing the storage moduli of $sc-(A_{0.62})_{0.23}B_{0.77}$ and $lc-(A_0)_{0.32}B_{0.68}$ were very close ~ 1 MPa at room temperature (Figure S31 and Figure S32).

Table 3.

4 Conclusion

Two series of P(S-*co*-BzMA)-*b*-POEGA block copolymers of comb-like star and linear architecture were successfully synthesized by RAFT polymerization. The addition of a small amount of styrene (minimum 6%) was needed to control BzMA polymerization mediated by the tetrafunctional chain transfer agent. S and BzMA comonomers were homogeneously distributed along the polymer chain for a wide range of monomer feed ratios ($f_{\text{BzMA},0}$ from 0 to 0.94) to produce statistical star copolymers with tunable properties. Mark-Houwink-Sakurada plot and determination of the g contraction factor confirmed the star-like architecture of the PS macroCTA. The block's phase segregation was induced by addition of lithium salt and lamellar, hexagonal cylinder and sphere phases have been observed by TEM and SAXS. As expected, the conductivity increased with the volume fraction of POEGA/LiTFSI conducting phase, however a strong dependence on the self-assembled morphologies is observed. Focussing on the quality of the lamellar morphology produced by star and linear BCPEs a correlation can be done between the generated tortuosity and ionic conductivity. Indeed, the star comb-like BCPs with ~30 wt-% of POEGA/LiTFSI conductive phase gave rise to highly ordered lamellar structures compared to the swirly lamellae of linear analogue. Consequently, the reduced lamellae tortuosity of self-assembled star comb-like BCPs improved the lithium conductivity by more than 8 times at 30°C.

5 Supporting Information

5.1 Materials

Benzyl Methacrylate (BzMA, Sigma-Aldrich, 96%) was passed through a silica gel column to remove monomethyl ether hydroquinone inhibitor. Styrene (S, Sigma-Aldrich, 99%⁺), Azobis(isobutyronitrile) (AIBN, Sigma-Aldrich, 98%), Oligo(ethylene glycol) methyl ether acrylate (OEGA, DP_n = 8-9, average M_n = 480 g.mol⁻¹, Sigma-Aldrich) were used as purchased. Pentaerythritol tetrakis[2-(dodecylthiocarbonothioylthio)-2-methylpropionate (tetrafunctional chain transfer agent named TTC-4, Sigma-Aldrich, 97%), 4-cyano 4-[(dodecylsulfanylthiocarbonyl)-sulfanyl]-pentanoic acid (monofunctional chain transfer agent named TTC-1, Sigma-Aldrich, 97%), Lithium bis(trifluoromethanesulfonyl)imide (LiTFSI,

Sigma-Aldrich, 99%⁺ anhydrous), Tetrahydrofuran (THF, Sigma-Aldrich, 99%⁺), Ethanol (EtOH, VWR, 96%⁺), linear PS standards (Polymer Standards Service GmbH).

5.2 Synthesis of linear and star macro-CTA of P(S-*co*-BzMA)

Polymerizations were performed with a total of 8 g of monomers, varying the initial molar fractions of BzMA and S from $f_{\text{BzMA},0} = 0$ to 1 as described in Table 1. In a typical experiment, *s*-A_{0.62} for synthesis of star macro-CTA, AIBN (2.5 mg, 1.63×10^{-2} mmol, 0.1 eq), TTC-4 (61.0 mg, 4.07×10^{-2} mmol TTC-4 = 1.63×10^{-1} mmol of trithiocarbonate TTC function, 1 eq), BzMA (4.00 g, 2.27×10^{-2} mol, 139 eq), and S (4.00 g, 3.85×10^{-2} mol, 236 eq) were mixed in a 25 mL round bottom flask and sealed with a septum. The reactant mixture was degassed with nitrogen bubbling for 20 min in an ice bath. A sample was withdrawn under nitrogen at time $t = 0$ for kinetic. The round bottom flask was placed into an oil bath at previously heated to 75 °C to start the reaction. Kinetic samples were collected at regular intervals under nitrogen flow for NMR and SEC analysis. The reaction was stopped at $t = 31.5$ h by cooling down in an ice-water bath and by introduction of oxygen in the crude mixture. Purification was done by addition of 1 vol. equivalence of THF to solubilize the crude mixture and precipitation into 10 vol. equivalence of EtOH at room temperature. Purification was performed twice to ensure complete removal of unreacted monomer and precipitated polymers were recovered via vacuum filtration and dried under vacuum for 72 h. Individual conversions of monomers (x_{BzMA} and x_{S}) were calculated from ¹H NMR spectra (see Eq S1, Eq S2 and Figure S15). The equations for the calculation of the overall molar (X_{m}) and weight (X_{w}) conversion in both S and BzMA monomers are detailed in Supporting Information along with the calculations of the fractions of BzMA units in the P(S-*co*-BzMA) copolymer.

5.3 NMR analysis for monomer conversion

NMR spectra were recorded using a Bruker 400 MHz spectrometer at 25 °C with 32 scans and a time delay D1 of 5 seconds. ¹H NMR measurements were performed at frequencies of 400 MHz. DOSY NMR spectra were recorded at 30 °C with 6000 scans and a time delay D1 of 2 seconds. Deuterated chloroform (CDCl₃) and deuterated dichloromethane (CD₂Cl₂) were used as solvent respectively for crude and purified polymer. All products were dissolved with concentrations between 10 and 20 mg/mL.

Individual conversions of monomers (x_{BzMA} and x_S) were calculated from 1H NMR spectra using the aromatic group (copolymer and monomers) in BzMA and S as internal standard, Eq. S1 and Eq S2 respectively.

$$x_{BzMA} = 1 - \frac{[I_{1H, BzMA(5.6ppm)}]_t / [I_{1H, IS (7.5 - 6.4ppm)} - I_{1H, S(5.8ppm)}]_t}{[I_{1H, BzMA(5.6ppm)}]_0 / [I_{1H, IS (7.5 - 6.4ppm)} - I_{1H, S(5.8ppm)}]_0} \quad S1$$

$$x_S = 1 - \frac{[I_{1H, S(5.8ppm)}]_t / [I_{1H, IS (7.5 - 6.4ppm)} - I_{1H, S(5.8ppm)}]_t}{[I_{1H, BzMA(5.6ppm)}]_0 / [I_{1H, IS (7.5 - 6.4ppm)} - I_{1H, S(5.8ppm)}]_0} \quad S2$$

$I_{1H, BzMA(5.6ppm)}$ corresponds to the integral of one vinyl proton of BzMA at 5.6 ppm, $I_{1H, IS (7.5 - 6.4ppm)}$ corresponds to the integral of all 5 polymeric protons and 6 monomeric protons of the aromatic groups of BzMA and S plus 1 vinyl proton of S, $I_{1H, S(5.8ppm)}$ corresponds to the integral of one vinyl proton of S (5.8 ppm, 1H). it is important to say that the NMR of the kinetics were performed in $CDCl_3$ (7.25 ppm) and contributes $\approx 5\%$ error to the calculation.

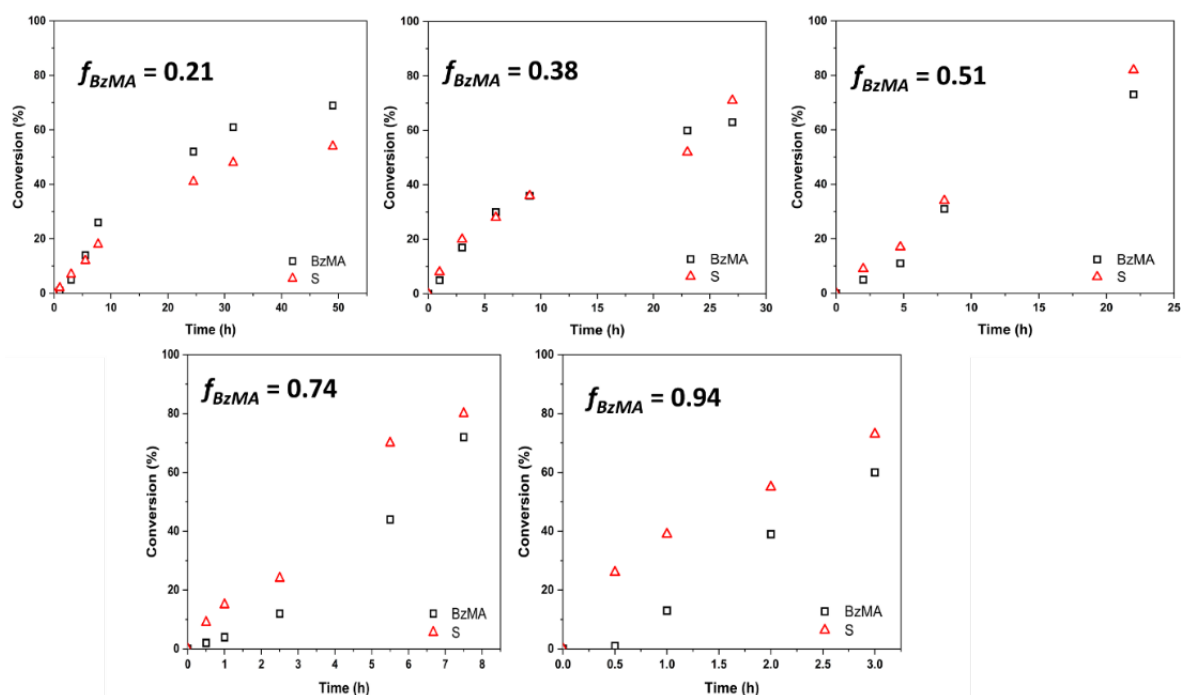


Figure S15. Individual molar conversion of benzyl methacrylate and styrene over time during RAFT polymerization.

The final overall molar and weight conversions (X_m and X_w respectively) were calculated from the individual monomer conversions according to Eq S3 and Eq. S4 (n_0 and m_0 respectively corresponds to the initial number of moles and the initial mass of each monomer).

$$X_m = \frac{(x_{BzMA} \times n_{0,BzMA}) + (x_S \times n_{0,S})}{(n_{0,BzMA} + n_{0,S})} \quad \text{S3}$$

$$X_w = \frac{(x_{BzMA} \times m_{0,BzMA}) + (x_S \times m_{0,S})}{(m_{0,BzMA} + m_{0,S})} \quad \text{S4}$$

The initial molar fraction corresponds to the initial number of moles from the mass of each monomer (see Eq S5).

$$f_{BzMA,0} = \frac{(m_{0,BzMA}/M_{BzMA})}{(m_{0,BzMA}/M_{BzMA}) + (m_{0,S}/M_S)} \quad \text{S5}$$

The experimental fraction of BzMA (f_{BzMA}) in the monomer feed at time, t was calculated from Eq S6.

$$f_{BzMA} = \frac{I_{1H, BzMA}(5.6ppm)}{(I_{1H, S}(5.8ppm) + I_{1H, BzMA}(5.6ppm))} \quad \text{S6}$$

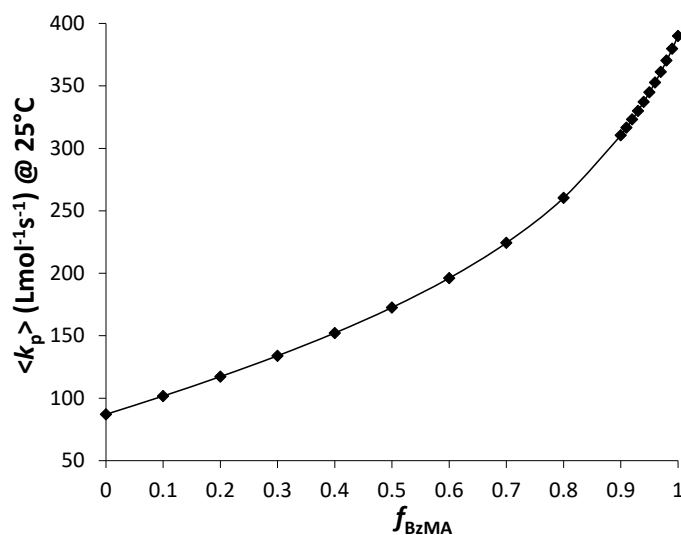


Figure S16. Estimation of the average rate constant of copolymerization ($\langle k_p \rangle$) at 25°C for styrene and benzyl methacrylate radical copolymerization based on Eq S7.

$$\langle k_p \rangle = \frac{r_{BzMA} f_{BzMA}^2 + 2f_{BzMA} f_S + r_S f_S^2}{r_{BzMA} \frac{f_{BzMA}}{k_{p,BzMA}} + r_S \frac{f_S}{k_{p,S}}} \quad S7$$

In Figure 3 and Figure S17, the theoretical values of f_{BzMA} are calculated step-by-step from Eq S8.

$$f_{BzMA,x} = \frac{f_{BzMA,x-dx} - F_{BzMA, theo} \cdot dx}{(f_{BzMA,x-dx} - F_{BzMA, theo} \cdot dx) + (f_{S,x-dx} - F_S \cdot dx)} \quad S8$$

With x the monomer conversion and dx as the change in monomer conversion (dx set at 0.1) and by using Lewis-Mayo equation (Eq S9) for determination of $F_{BzMA, theo}$.

$$F_{BzMA, theo} = \frac{r_{BzMA} \times f_{BzMA}^2 + f_{BzMA} \times f_S}{r_{BzMA} \times f_{BzMA}^2 + 2 \times f_{BzMA} \times f_S + r_S \times f_S^2} \quad S9$$

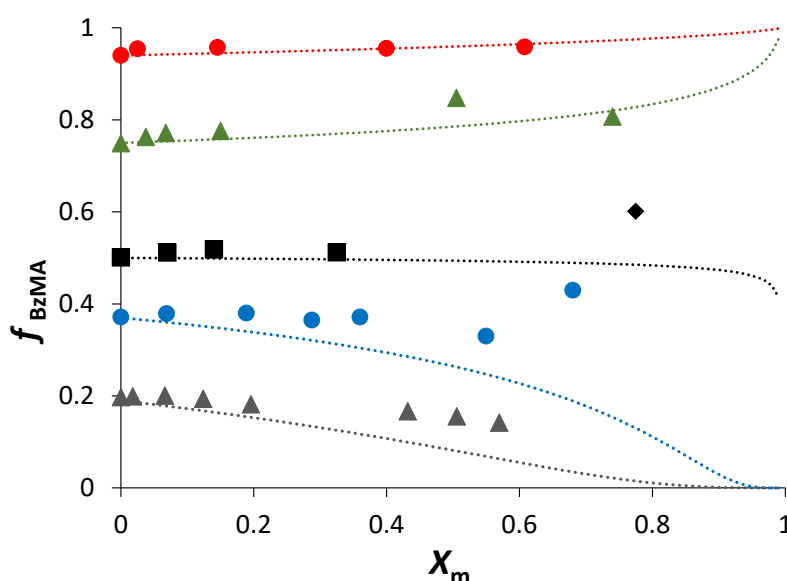


Figure S17. Evolution of BzMA fraction in monomer feed with X_m conversion. \blacktriangle $f_{BzMA,0} = 0.19$, \blacksquare $f_{BzMA,0} = 0.38$, \blacklozenge $f_{BzMA,0} = 0.50$, \blacktriangle $f_{BzMA,0} = 0.75$, \bullet $f_{BzMA,0} = 0.94$. The dotted line corresponds to the fit of f_{BzMA} versus conversion calculated from Eq S8 by using reactivity ratios of reference ³⁴ ($r_S = 0.27 \pm 0.14$, $r_{BzMA} = 0.86 \pm 0.36$).

The molar fraction of the BzMA monomer incorporated into the copolymer ($F_{BzMA,\beta}$) was calculated from the individual monomer conversions (x_{BzMA} and x_S) and the initial number of moles of monomer ($n_{0,BzMA}$ and $n_{0,S}$), according to Eq S10.

$$F_{BzMA,\beta} = \frac{x_{BzMA} \times n_{0,BzMA}}{x_{BzMA} \times n_{0,BzMA} + x_S \times n_{0,S}} \quad S10$$

The molar fraction of BzMA in the copolymer after purification ($F_{BzMA,\alpha}$ and $F_{BzMA,\gamma}$) was calculated from ^1H NMR in CDCl_3 and CD_2Cl_2 respectively is given by Eq S11. The integral of the peak from 5 ppm to 3 ppm corresponds to 2 protons of PBzMA in the copolymer and the integral of the peak from 7.5 ppm to 6.4 ppm corresponds to the 5 protons of benzyl group of PBzMA and PS. CDCl_3 constitutes an error of $\pm 5\%$ owing to the presence of hydrogen peak at 7.26 ppm.

$$F_{BzMA,\gamma} = \frac{I_{1H,PBzMA} \text{ units}}{[I_{1H,PBzMA} \text{ units} + I_{1H,PS} \text{ units}]} \quad S11$$

The weight fraction of BzMA in the copolymer (W_{BzMA}) was obtained from Eq S12, considering the molar fraction of the BzMA monomer ($F_{BzMA,\gamma}$) in the purified copolymer measured in CD_2Cl_2 and the molar masses of each monomer ($M_{BzMA} = 176 \text{ g.mol}^{-1}$ and $M_S = 104 \text{ g.mol}^{-1}$).

$$W_{BzMA,\gamma} = \frac{(F_{BzMA,\gamma} \times M_{BzMA})}{(F_{BzMA,\gamma} \times M_{BzMA}) + ((1 - F_{BzMA,\gamma}) \times M_S)} \quad S12$$

5.3.1 The Extended Kelen-Tüdös (e-KT) method

The copolymer composition (F_{BzMA}) of the purified polymer was determined in CD_2Cl_2 . The reactivity ratios are estimated through linear regression of the experimental data fitted by the relationship of equation S13.

$$\eta = \left[r_{BzMA} + \left(\frac{r_S}{\alpha} \right) \right] \times \zeta - \frac{r_S}{\alpha} \quad S13$$

Where $\zeta = \frac{G}{(\alpha+F)}$, $\zeta = \frac{F}{(\alpha+F)}$, with $\alpha = (F_{min} \times F_{max})^{1/2}$,

$$G = \frac{(F_{BzMA}/F_S)^{-1}}{z} \text{ and } F = \frac{(F_{BzMA}/F_S)}{z^2} \text{ where } z = \frac{\ln(1-x_{BzMA})}{\ln(1-x_S)}$$

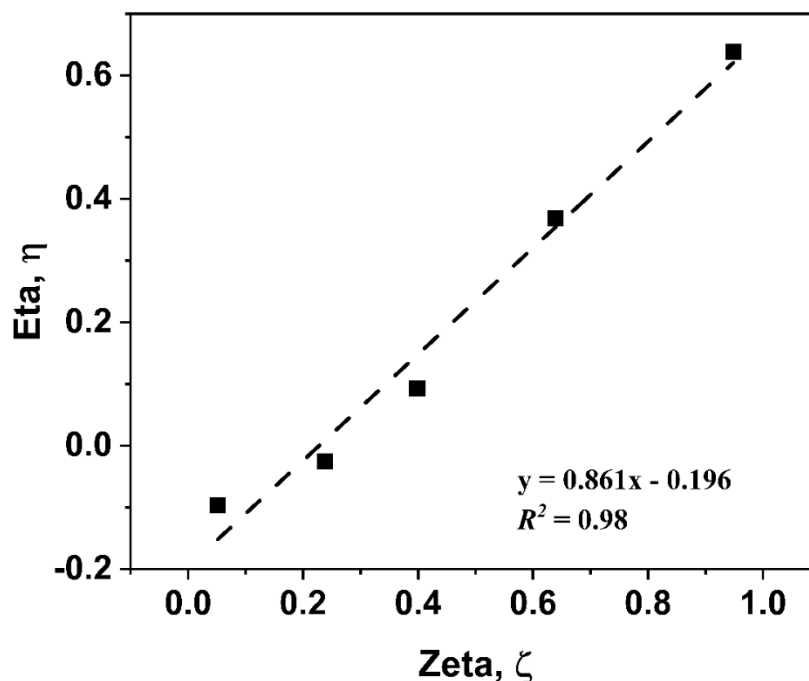


Figure S18. Plot of Eta, η vs Zeta, ζ from Eq S13.

5.4 Synthesis of linear and star P(S-co-BzMA)-b-POEGA block copolymer

MacroCTA of P(S-co-BzMA) previously synthesized were used for the bulk RAFT polymerization of OEGA using AIBN as initiator (Table 2). In a typical experiment *sc*-(A_{0.62})_{0.80}B_{0.20}, (0.9 mg, 5.57×10^{-3} mmol), macroCTA: *s*-A_{0.62} (1.7 g, $M_n = 122 \text{ kg}\cdot\text{mol}^{-1}$, 1.39×10^{-2} mmol = 5.57×10^{-2} mmol TTC), and OEGA (10.2 g, 21.3 mmol) were inserted in a 25 mL round bottom flask and sealed with a septum. The reactant mixture was left to stand for 50 min under stirring conditions. In the case of PS macroCTA, the polymerization was performed in a solution mixture of OEGA and 1,4-dioxane (1/1, v/v) due to insolubility of PS in OEGA. The reaction mixture was degassed with nitrogen bubbling for 30 min in an ice bath. A sample was withdrawn under nitrogen at time $t = 0$. The round bottom flask was placed into an oil bath at previously heated 75 °C to start the reaction. The reaction was stopped at $t = 50$ min for *sc*-(A_{0.62})_{0.80}B_{0.20} (or up to 2 h for *sc*-(A_{0.62})_{0.23}B_{0.77}) by cooling down in an ice-water bath and by introduction of oxygen in the crude mixture. Note that synthesis of *sc*-(A_{0.62})_{0.73}B_{0.27} was performed with 50 vol-% of 1,4-Dioxane based on OEGA to enable the decrease of the initial OEGA content while enabling solubilisation of macroCTA. Purification was done by addition of 5 vol. equivalence of THF to solubilize the crude mixture and dialyzed over distilled water using 50kDa regenerated cellulose membrane. Dialysis was carried out over 6-water cycles to

ensure complete removal of unreacted OEGA monomer and dialyzed sample is lyophilized. Conversion of OEGA was determined from Eq S17 by taking the integral of one aromatic proton (7.5 – 6.4 ppm) of P(BzMA-co-S) first block as internal standard.

5.5 Size Exclusion Chromatography (SEC).

Measurements were performed on a bank of 4 Shodex columns (KF801, KF8025, KF804 and KF806) each 300 mm x 8 mm at 30 °C with THF eluent controlled by a Malvern pump (Viscotek, VE1122) at a flow rate of 1.0 mL.min⁻¹. The SEC apparatus is equipped with a refractive index (RI) detector (Viscotek VE3580), a Wyatt Heleos II Multi Angle Laser Light Scattering detector (MALLS, 18 angles, λ₀ = 664.4 nm), an online viscometer (Wyatt Viscostar 311-V4) and a UV-visible detector (Viscotek-Malvern VE3210). Toluene was used as a flow marker. Sample concentrations were limited to the range of 1.5 – 4.5 mg mL⁻¹ and dissolved samples were filtered through polytetrafluorethylene (PTFE) membranes with a pore size of 0.45 μm prior to injection. The refractive index increments (dn/dc) of each polymer for MALLS analysis are reported in **Table S4** and **Table S5**.

The values of refractive index increment (dn/dc) of the copolymers in THF was calculated using Eq S14 as found in literature.⁴⁵ $dn/dc_{PBzMA} = 0.151 \text{ mL g}^{-1}$, $dn/dc_{PS} = 0.185 \text{ mL g}^{-1}$, and $dn/dc_{POEGA} = 0.062 \text{ mL g}^{-1}$ were respectively taken from references.⁴⁶⁻⁴⁸ The dn/dc describes how much the refractive index of a copolymer solution changes with respect to the concentration of the solute. Calculated values of dn/dc of P(S-co-BzMA) macroCTA and P(S-co-BzMA)-b-POEGA block copolymer were reported respectively in **Table S4** and **Table S5** determined by Eq S14. These values are expected to match experimental ones according to literature.⁴⁵

$$\frac{dn}{dc_{macroCTA}} = W_{BzMA,\gamma} \left(\frac{dn}{dc} \right)_{PBzMA} + W_{S,\gamma} \left(\frac{dn}{dc} \right)_{PS}$$

S14

$$\frac{dn}{dc_{BC}} = W_{macroCTA,\gamma} \left(\frac{dn}{dc} \right)_{macroCTA} + W_{POEGA,\gamma} \left(\frac{dn}{dc} \right)_{POEGA}$$

The experimentally determined molar mass ($M_{n,MALLS}$) were compared to the theoretical number-average molar mass ($M_{n,theo}$) of the macroCTA and BC calculated from Eq S15 and S16 respectively.

$$M_{n,theo} macroCTA = M_{TTC} + X_w \frac{(m_{0,S} + m_{0,BzMA})}{n_{0,TTC}} \quad S15$$

$$M_{n,theo} BCP = M_{n,MALLS,macroCTA} + \frac{x_{PEGA} \times [OEGA]_0}{[macroCTA]_0} \quad S16$$

Table S4: Summary of Initial Monomer Feed Composition, Final BzMA fraction in the copolymer calculated from different methods, values of refractive index increment and Macromolecular Features of the P(S-co-BzMA) macro-CTA Synthesized by RAFT copolymerization in bulk

macroCTA	$f_{BzMA,0}$ ¹	X_m ²	X_w ³	$F_{BzMA,\beta}$ ⁴	$F_{BzMA,\alpha}$ ⁵	$F_{BzMA,\gamma}$ ⁶	$\frac{dn}{dc Poly}$ ⁷ (mL g ⁻¹)	$M_{n,MALLS}$ ⁸ (kg·mol ⁻¹)
<i>l</i> -A _{1.0}	1	-	62	1	1	1	0.151	38
<i>l</i> -A _{0.59}	0.38	-	76	0.39	0.43	0.46	0.169	28
<i>l</i> -A ₀	0	-	52	0	0	0	0.185	22
<i>s</i> -A _{1.0}	1	65	65	1	1	1	0.151	217
<i>s</i> -A _{0.98}	0.92	60	60	0.93	0.96	0.97	0.152	123
<i>s</i> -A _{0.86}	0.74	74	73	0.73	0.75	0.78	0.155	152
<i>s</i> -A _{0.71}	0.51	77	76	0.47	0.50	0.58	0.160	134
<i>s</i> -A _{0.62}	0.38	69	68	0.36	0.44	0.49	0.163	122
<i>s</i> -A _{0.43}	0.21	59	57	0.24	0.30	0.31	0.170	80
<i>s</i> -A ₀	0	52	52	0	0	0	0.185	122

¹ BzMA molar fraction in the initial feed.

² Overall molar conversion of monomers, Eq S3.

³ Overall weight conversion of monomers, Eq S4.

⁴ $F_{BzMA,\beta}$ is the molar fraction of the monomer into the copolymer calculated from individual monomer conversion determined by NMR-CDCl₃, Eq S10.

⁵ Molar fraction of the monomer into the copolymer after purification determined by NMR-CDCl₃, Eq S11.

⁶ Mole fraction of the monomer in the copolymer after purification by NMR-CD₂Cl₂, Eq S11.

⁷ Refractive index increments of the copolymer determined from Eq S14.

⁸ M_n values obtained from the SEC analysis with a MALLS detector.

5.6 Synthesis of P(S-co-BzMA)-b-POEGA block copolymer.

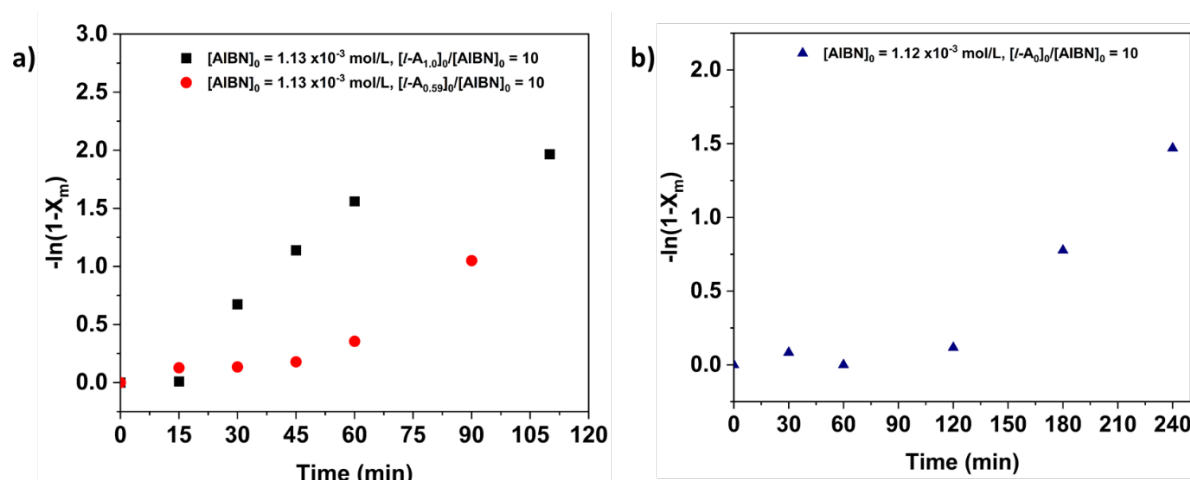


Figure S19. Chain extension of POEGA from linear macro-CTA. (a) PBzMA and P(BzMA-co-S) macroCTA in bulk polymerization. (b) PS macro-CTA in solvent polymerization (1,4-dioxane, 1:1 v/v). Polystyrene was insoluble in OEGA monomer, hence solvent polymerization was the only feasible route for block copolymerisation.

The molar conversion of OEGA monomer during block copolymerization (x_{OEGA}) was calculated from ^1H NMR in CD_2Cl_2 given by Eq S17, taking the integral of one aromatic proton (7.5 – 6.4 ppm) of P(BzMA-co-S) first block as internal standard.

$$x_{OEGA} = 1 - \frac{[I_{1H, OEGA(5.9ppm)}]_t / [I_{1H, P(S-co-BzMA)}]_t}{[I_{1H, OEGA(5.9ppm)}]_0 / [I_{1H, P(S-co-BzMA)}]_0} \quad \text{S17}$$

The molar fraction of POEGA in the block copolymer after purification (F_{OEGA}) was calculated from ^1H NMR in CD_2Cl_2 is given by Eq S18. Where $I_{1H, macroCTA+OEGA}$ is the summation of the integral of 1 aromatic proton of P(S-co-BzMA) and 1 proton of POEGA.e and 37 protons of POEGA in the final BCP. $I_{1H, OEGA(5-3ppm)}$ is obtained by subtracting peak from 5 ppm to 3 ppm corresponding to 2 protons of PBzMA in the starting macroCTA from BCP and dividing by 37 protons of POEGA.

$$F_{OEGA} = \frac{[I_{1H, OEGA(5-3ppm)}]}{[I_{1H, macroCTA+OEGA}]} \quad \text{S18}$$

The weight fraction of OEGA in the block copolymer (W_{OEGA}) was obtained from Eq S19, considering the molar fraction of the OEGA monomer (F_{OEGA}) in the purified BCP measured in CD_2Cl_2 . Where $M_{P(S-co-BzMA)} = (176 \text{ g mol}^{-1} \times F_{BzMA}) + (104 \text{ g mol}^{-1} \times F_S)$ and $M_{OEGA} = 480 \text{ g mol}^{-1}$.

$$W_{POEGA,Y} = \frac{(F_{OEGA} \times M_{OEGA})}{(F_{OEGA} \times M_{OEGA}) + ((1 - F_{OEGA}) \times M_{P(S-co-BzMA)})} \quad S19$$

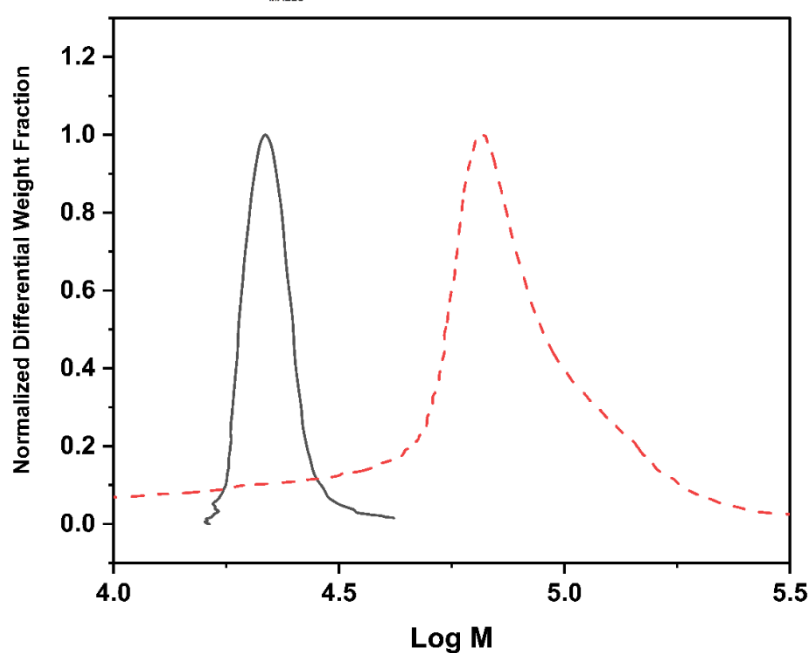


Figure S20. SEC-MALLS traces of l-A₀ macroCTA (—) and lc-(A₀)_{0.32}B_{0.68} Block copolymer (---).

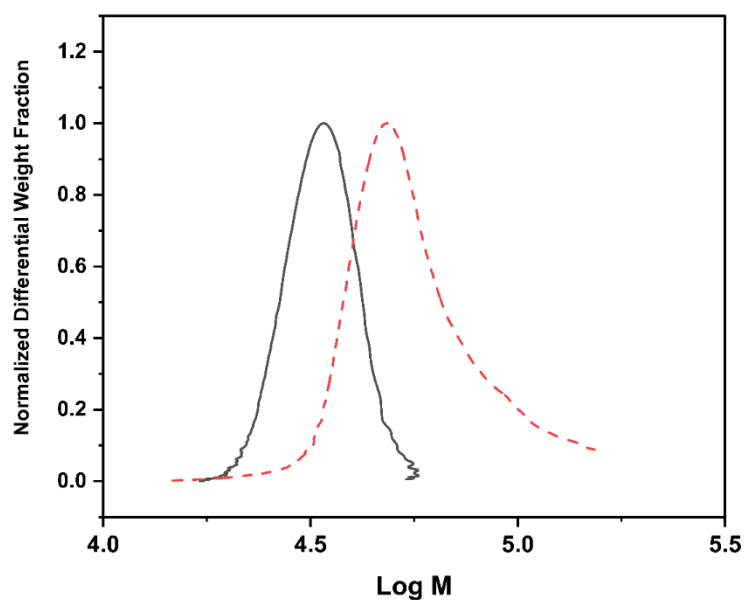


Figure S21. SEC-MALLS analysis of l-A_{0.59} macroCTA (—) and lc-(A_{0.59})_{0.71}B_{0.29} Block copolymer (---).

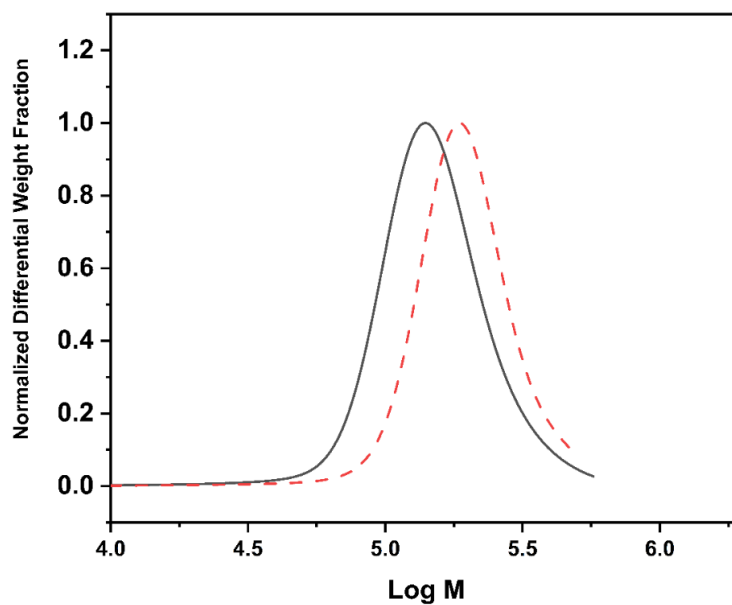


Figure S22. SEC-MALLS analysis of s-A_{0.62} macroCTA (—) and sc-(A_{0.62})_{0.80}B_{0.20} Block copolymer (- - -).

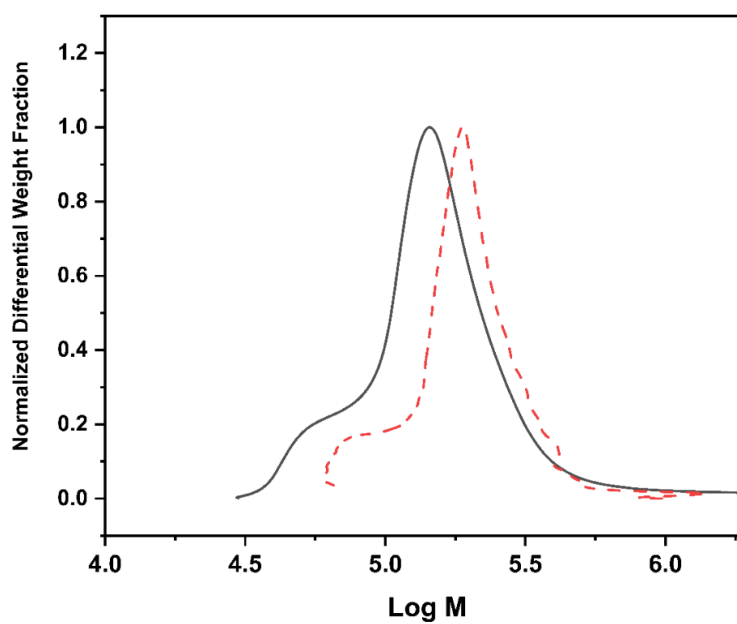


Figure S23. SEC-MALLS analysis of s-A_{0.43} macroCTA (—) and sc-(A_{0.43})_{0.84}B_{0.16} Block copolymer (- - -).

Table S5. Features of the AB Linear Comb-like and Star Comb-like Diblock Copolymers Synthesized from the macro-CTA reported in Table 1.

Macro-CTA	W_{POEGA}^a	dn/dc_{poly} $mL \cdot g^{-1}$	$M_{n,theo}^b$ $(kg \cdot mol^{-1})$	$M_{n,SEC\ MALLS}$ $(kg \cdot mol^{-1})$	$D_{SEC\ MALLS}$	BCP ^c
<i>l</i> -A ₀	0.68	0.101	59	41	1.20	<i>lc</i> -(A ₀) _{0.32} B _{0.68}
<i>l</i> -A _{0.59}	0.29	0.114	48	41	1.10	<i>lc</i> -(A _{0.59}) _{0.71} B _{0.29}
<i>s</i> -A _{0.62}	0.77	0.085	530	<i>n.a.</i> ^d	<i>n.a.</i> ^d	<i>sc</i> -(A _{0.62}) _{0.23} B _{0.77}
<i>s</i> -A _{0.62}	0.27	0.138	219	414	1.31	<i>sc</i> -(A _{0.62}) _{0.73} B _{0.27}
<i>s</i> -A _{0.62}	0.20	0.147	153	155	1.22	<i>sc</i> -(A _{0.62}) _{0.80} B _{0.20}
<i>s</i> -A _{0.43}	0.16	0.145	95	109	1.31	<i>sc</i> -(A _{0.43}) _{0.84} B _{0.16}

^a W_{POEGA} is the weight fraction of POEGA in the block copolymer after purification, as determined from the molar fraction calculated from ¹H NMR spectra (see Eq. S19).

^b Theoretical molar mass determined from Eq. S14.

^c *s*- and *l*- represents the star and linear polymers respectively.

^d The SEC analysis was not applicable as the solubility of samples was too low and refractive index signal at very low intensity to be reliable.

5.7 Preparation of Block Copolymer Electrolytes (BCPEs) films.

Electrolyte solutions were prepared by mixing as prepared BCPs with an equivalent amount of LiTFSI salt ([EO]/[Li] = 15) in THF (0.39 g/mL). Polymer electrolyte films for conductivity, TEM and X-ray scattering were made by solvent-casting the electrolyte solution onto a stainless-steel disc. Samples were allowed to dry in the vacuum oven for 24 h. Thereafter, the samples could be peeled off as free-standing films (see Figure 24) with typical thickness range, $L \approx 90 - 470 \mu m$. The volume fraction of conducting phase, ϕ_c , was estimated from Eq S21 by using the densities of POEGA homopolymer (1.54 g cm^{-3}), PS (1.05 g cm^{-3}), PBzMA (1.17 g cm^{-3}) and LiTFSI (1.33 g cm^{-3}).⁵⁰ The density of the BCP was calculated using Eq S21. The density of the POEGA homopolymer was estimated using Van Krevelen's method, and the details of this calculation are shown in Table S5.⁴⁹ The resulting values of ϕ_c are given in Table S6.



Figure 24: Exemplary pictures of self-standing transparent films (\varnothing 16 mm, $L= 100 \mu\text{m}$) derived from block copolymer electrolyte $sc\text{-(A}_{0.62}\text{)}_{0.80}\text{B}_{0.20}$.

Table S6. Volume fraction of the BCPE conducting phase calculated with Eq S21

<i>Polymer</i>	[EO]/[Li]	ϕ_c
<i>lc</i> -(A ₀) _{0.32} B _{0.68}	15	0.67
<i>lc</i> -(A _{0.59}) _{0.71} B _{0.29}	15	0.29
<i>sc</i> -(A _{0.62}) _{0.23} B _{0.77}	15	0.78
<i>sc</i> -(A _{0.62}) _{0.73} B _{0.27}	15	0.27
<i>sc</i> -(A _{0.62}) _{0.80} B _{0.20}	15	0.20
<i>sc</i> -(A _{0.43}) _{0.84} B _{0.16}	15	0.15

The volume fraction of conducting phase of BCPE was calculated from Eq S20.

$$\phi_c = 1 - \left(\frac{M_A/\rho_A}{M_{AB+LiTFSI}/\rho_{AB+LiTFSI}} \right) \quad \text{S20}$$

Where ρ is used to denote density. The density of the copolymer was calculated from Eq S21.

$$\rho_{12} = \rho_1\rho_2(M_1 + M_2)/(\rho_1M_2 + \rho_2M_1) \quad \text{S21}$$

Table S7. Van Krevelen method for estimating density of POEGA⁴⁹

	Number of groups	molar volume (cm ³ mol ⁻¹)	Total molar volume (cm ³ mol ⁻¹)
-CH ₂ -	9	16.37	147.33
(-CH<)	1	10.80	10.80
0=C<	1	21.46	21.46
-O-	10	10.67	106.70
CH ₃	1	24.58	24.58
Total	-	-	310.87
OEGA MW (g mol ⁻¹)	480		
Density (g cm ⁻³)	1.54		

5.8 Differential Scanning Calorimetry (DSC).

DSC was performed using the Q100 from TA instruments under a N₂ atmosphere. For each sample, the temperature regime was initially stabilized at -80 °C for 5 min, heating and cooling was done within -80 and 120 °C with a rate of 5 °C.min⁻¹. The heat capacity change in the second heating scan was used for the determination of the glass transition temperature (T_g).

In **Figure S25**, the DSC curves of the BCPEs show low T_g values associated to the POEGA and LiTFSI phase increasing from -51 °C to -23 °C with decreasing content of conductive phase. At the lowest conductive phase content, a T_g around 80 °C, associated to the P(S-co-BzMA) is observed.

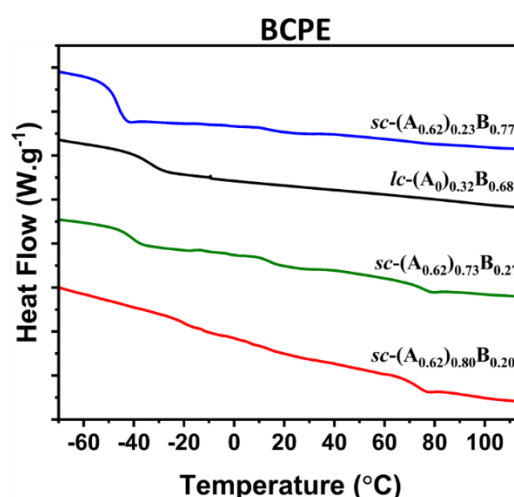


Figure S25. DSC heating curves collected on star and linear BCPEs presented in Table S8. The lower T_g values are attributed to the POEGA and LiTFSI phase and are reported in Table S3.

5.9 Electrochemical Impedance Spectroscopy (EIS).

Free-standing BCPE films were previously dried in the vacuum oven for 24 h and stored in the glove box (see Figure S16). The films (8 mm ϕ , thickness, $L \approx 90 - 470 \mu\text{m}$) were sandwiched between two blocking gold electrodes plates in CESH-e (Enhanced Controlled Environment Sample Holder) cells (ϕ 6.35 mm) and EIS measurement using Biologic Potentiostat (equipped with EC-Lab software package) at frequency from 1 Hz to 1 MHz with an oscillating voltage of 50 mV. Subsequently, these cells were preconditioned in a temperature chamber (Binder KB53, 230V 1~ 50Hz) for 2 h at 90 °C to anneal the films. After the preconditioning was finished, measurements were carried out by gradually decreasing the temperature in 20 °C steps from 90 °C to -10 °C with each temperature being maintained for 2 h to attain a thermal equilibrium. The ionic conductivity (σ ; S cm^{-1}) was determined by $\sigma = L/RA$ where R is the measured resistance, L is the film thickness and A is the area of the electrode.

Table S8. Vogel temperature, T_0 , determined from VFT fitting together with the corresponding glass transitions, T_g , of the POEGA and LiTFSI phase (B/Li⁺ block); both collected on the highest conductive star and linear BCPEs. All BCPEs featured a constant salt concentration $[\text{EO}]/[\text{Li}^+] = 15$. The associated DCS curves are displayed in Figure S25 and VFT fitting in Figure 5.

<i>Polymer</i>	T_0 (°C) ^a	T_g B/Li ⁺ block (°C)
<i>lc</i> -(A _{0.32} B _{0.68})	-86.3	-40.3
<i>sc</i> -(A _{0.62}) _{0.23} B _{0.77}	-99.0	-50.8
<i>sc</i> -(A _{0.62}) _{0.73} B _{0.27}	-91.2	-46.6
<i>sc</i> -(A _{0.62}) _{0.80} B _{0.20}	-84.0	-22.8

^aValues of T_0 are determined by fitting conductivity data with VFT model in Eq 3.

5.10 Small Angle X-ray Scattering (SAXS).

Small angle X-ray scattering SAXS measurement was performed on Xenoxs Xeuss 3.0 equipped in Cu K α radiation source ($\lambda = 1.54 \text{ \AA}$) and Eiger2 R 1M by Dectris 2D detector. The sample to detector distance was 1.1 m. Pristine samples were sealed in the heating stage between two Kapton foils. The scattering data was collected at chosen temperature points during heating/cooling cycle (25, 100, 90, 70, 50, and 30 °C) under vacuum to track any possible temperature induced changes in self-assembly. Films were heated/cooled down with rate 5 °C/min. Virtual detector mode was used, acquiring three images in horizontal plane (240 s exposure time for each). Each temperature point was measured twice after maintaining for 1

h to attain a thermal equilibrium. Data was subjected to standardized correction including background subtraction and azimuthal averaging of the 2D scattering data to obtain 1D SAXS profiles. Temperature dependent scattering curves were plotted as a function of scattering vector q ; its magnitude is given by $q = 4\pi \sin\theta/\lambda$, where 2θ is the scattering angle.

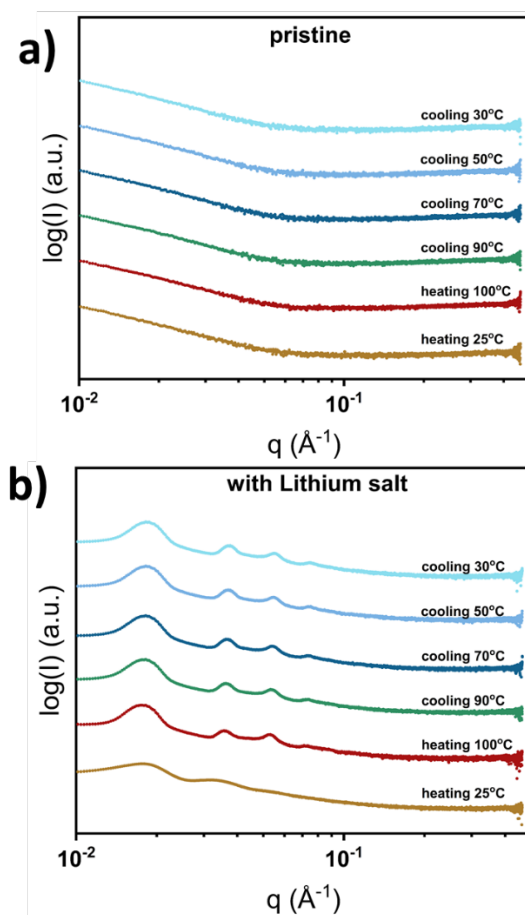


Figure S26. Representative example of SAXS of in-situ annealing for lc-(A_{0.59})_{0.71}B_{0.29} a) linear BCP b) linear BCPE. Temperature sequence: 25, 100, 90, 70, 50 and 30 °C.

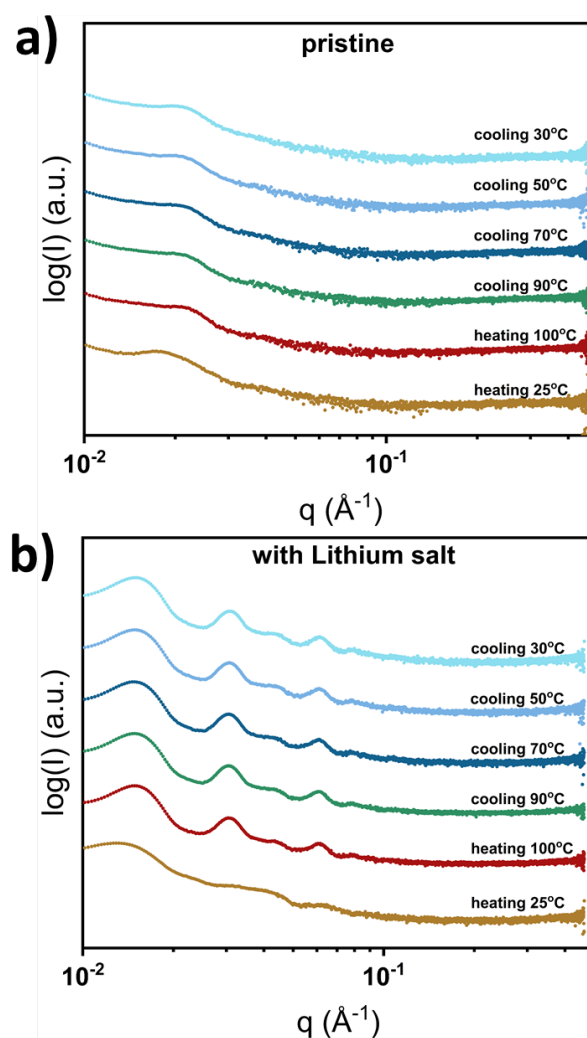


Figure S27. Representative example of SAXS of in-situ annealing for sc- $(A_{0.62})_{0.80}B_{0.20}$ a) star BCP b) star BCPE. Temperature sequence: 25, 100, 90, 70, 50 and 30 °C.

5.11 Transmission Electron Microscopy (TEM).

Ultra-thin sections (~ 70 nm) for TEM characterization was prepared from previously solvent casted BCPE films. Samples were annealed at 100 °C for approximately 1 h. Subsequently, samples were fixed to a pin and cut at -80 °C with Diatome 25 ° diamond knife on a Leica EM UC7 cryo-ultramicrotome. Sections were collected and transferred on 300 mesh copper grid coated with lacey carbon. Prepared grids were immersed in liquid nitrogen and cryo-transferred to microscope in order to prevent moisture accumulation. CryoTEM measurements were performed on Schottky field-emission cryo-electron microscope JEOL JEM-3200FSC at 300 kV accelerating voltage, while keeping the temperature of the examined specimen at -187 °C. The micrographs were acquired in bright field mode using zero energy loss omega type

filter with a slit width 20 eV and with slight under focus. Images were recorded via Gatan Ultrascan 4000 CCD camera.

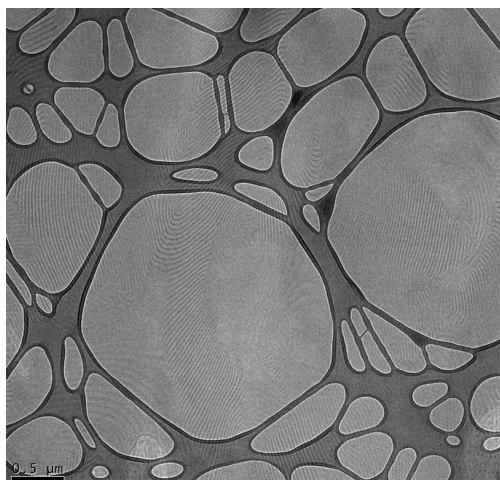


Figure S28. TEM images for annealed star comb-like BCPE: $sc-(A_{0.62})_{0.73}B_{0.27}$, $\phi_c = 0.27$

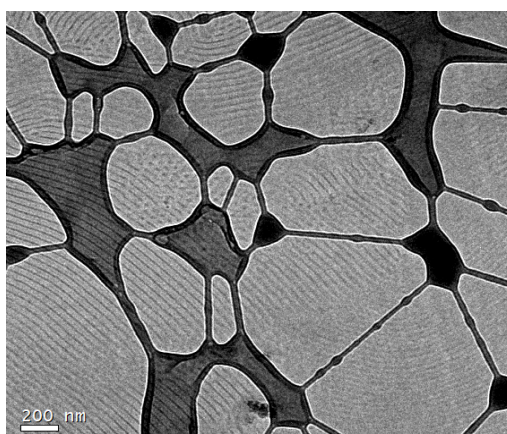


Figure S29. TEM images for annealed star comb-like BCPE: $sc-(A_{0.62})_{0.80}B_{0.20}$, $\phi_c = 0.20$



Figure S30. TEM images for annealed linear comb-like BCPE: $lc-(A_{0.59})_{0.71}B_{0.29}$, $\phi_c = 0.29$

5.12 Rheology measurements

Rheology measurements were performed on Anton Paar modular compact rheometer (MCR-302) with a torque range from 0.5 nNm to 230 mNm and integrated active thermal management system. Self-standing films (130 - 200 μm) was sandwiched between two 8 mm \varnothing parallel plate geometry at a constant shear stress of 25 Pa and a frequency of 5 Hz. The measurements were performed in temperature range 25 -100 $^{\circ}\text{C}$.

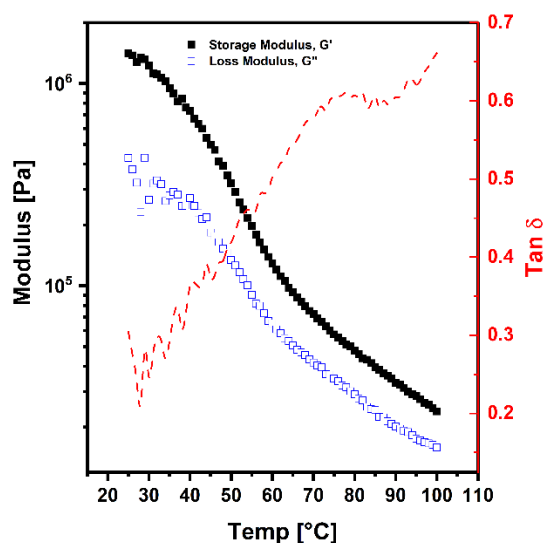


Figure S31. Rheological properties of linear comb-like BCPE with 67 vol% of conducting phase: $lc-(A_0)_{0.32}B_{0.68}$

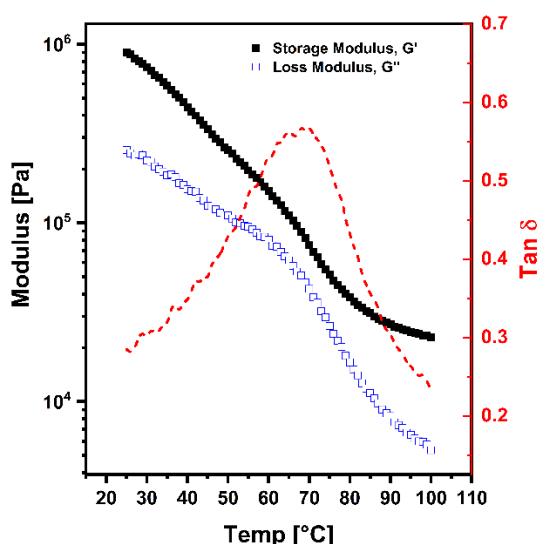


Figure S32. Rheological properties of star comb-like BCPE with 78 vol% of conducting phase: $sc-(A_{0.62})_{0.23}B_{0.77}$

6 References

1. Nair, J. R.; Imholt, L.; Brunklaus, G.; Winter, M., Lithium Metal Polymer Electrolyte Batteries: Opportunities and Challenges. *The Electrochemical Society Interface* **2019**, *28* (2), 55-61.
2. Hallinan, D. T.; Balsara, N. P., Polymer Electrolytes. *Annual Review of Materials Research* **2013**, *43*, 503-525.
3. Hallinan, D. T.; Mullin, S. A.; Stone, G. M.; Balsara, N. P., Lithium Metal Stability in Batteries with Block Copolymer Electrolytes. *Journal of The Electrochemical Society* **2013**, *160* (3), A464-A470.
4. Hashim, N. H. A. M.; Subban, R. H. Y., Studies on Conductivity, Structural and Thermal Properties of PEO-LiTFSI Polymer Electrolytes Doped with EMImTFSI Ionic Liquid. *AIP Conference Proceedings* **2018**, *2031* (1), 0200211 - 0200216.
5. Phan, T. N. T.; Issa, S.; Gimes, D., Poly(ethylene oxide)-Based Block Copolymer Electrolytes for Lithium Metal Batteries. *Polymer International* **2019**, *68* (1), 7-13.
6. Choi, Y. K.; Bae, Y. H.; Kim, S. W., Star-Shaped Poly(ether-ester) Block Copolymers: Synthesis, Characterization, and Their Physical Properties. *Macromolecules* **1998**, *31* (25), 8766-8774.
7. Croce, F.; Appetecchi, G. B.; Persi, L.; Scrosati, B., Nanocomposite Polymer Electrolytes for Lithium Batteries. *Nature* **1998**, *394* (6692), 456-458.
8. Bergman, M.; Bergfelt, A.; Sun, B.; Bowden, T.; Brandell, D.; Johansson, P., Graft Copolymer Electrolytes for High Temperature Li-battery Applications, Using Poly(methyl methacrylate) Grafted Poly(ethylene glycol)methyl Ether Methacrylate and Lithium bis(trifluoromethanesulfonimide). *Electrochimica Acta* **2015**, *175*, 96-103.
9. Tikhonov, P. A.; Vasilenko, N. G.; Muzafarov, A. A. M., Multiarm Star Polymers. Fundamental Aspects. A Review. *Doklady Chemistry* **2021**, *496* (1), 1-17.
10. Young, W.-S.; Kuan, W.-F.; Epps, I. I. I. T. H., Block copolymer electrolytes for rechargeable lithium batteries. *Journal of Polymer Science Part B: Polymer Physics* **2014**, *52* (1), 1-16.
11. Xue, Z.; He, D.; Xie, X., Poly(ethylene oxide)-Based Electrolytes for Lithium-ion Batteries. *Journal of Materials Chemistry A* **2015**, *3* (38), 19218-19253.
12. Simone, P. M.; Lodge, T. P., Phase Behavior and Ionic Conductivity of Concentrated Solutions of Polystyrene-Poly(ethylene oxide) Diblock Copolymers in an Ionic Liquid. *ACS Applied Materials & Interfaces* **2009**, *1* (12), 2812-2820.
13. Chintapalli, M.; Chen, X. C.; Thelen, J. L.; Teran, A. A.; Wang, X.; Garetz, B. A.; Balsara, N. P., Effect of Grain Size on the Ionic Conductivity of a Block Copolymer Electrolyte. *Macromolecules* **2014**, *47* (15), 5424-5431.
14. Galluzzo, M. D.; Loo, W. S.; Wang, A. A.; Walton, A.; Maslyn, J. A.; Balsara, N. P., Measurement of Three Transport Coefficients and the Thermodynamic Factor in Block Copolymer Electrolytes with Different Morphologies. *The Journal of Physical Chemistry B* **2020**, *124* (5), 921-935.
15. Loo, W. S.; Galluzzo, M. D.; Li, X.; Maslyn, J. A.; Oh, H. J.; Mongcopa, K. I.; Zhu, C.; Wang, A. A.; Wang, X.; Garetz, B. A.; Balsara, N. P., Phase Behavior of Mixtures of Block Copolymers and a Lithium Salt. *The Journal of Physical Chemistry B* **2018**, *122* (33), 8065-8074.
16. Chakraborty, S.; Jiang, X.; Hoffman, Z. J.; Sethi, G. K.; Zhu, C.; Balsara, N. P.; Villaluenga, I., Reversible Changes in the Grain Structure and Conductivity in a Block Copolymer Electrolyte. *Macromolecules* **2020**, *53* (13), 5455-5464.

17. Chintapalli, M.; Higa, K.; Chen, X. C.; Srinivasan, V.; Balsara, N. P., Simulation of Local Ion transport in Lamellar Block Copolymer Electrolytes Based on Electron Micrographs. *Journal of Polymer Science Part B: Polymer Physics* **2017**, *55* (3), 266-274.
18. Chintapalli, M.; Le, T. N. P.; Venkatesan, N. R.; Mackay, N. G.; Rojas, A. A.; Thelen, J. L.; Chen, X. C.; Devaux, D.; Balsara, N. P., Structure and Ionic Conductivity of Polystyrene-block-poly(ethylene oxide) Electrolytes in the High Salt Concentration Limit. *Macromolecules* **2016**, *49* (5), 1770-1780.
19. Devaux, D.; Glé, D.; Phan, T. N. T.; Gigmes, D.; Giroud, E.; Deschamps, M.; Denoyel, R.; Bouchet, R., Optimization of Block Copolymer Electrolytes for Lithium Metal Batteries. *Chemistry of Materials* **2015**, *27* (13), 4682-4692.
20. Butzelaar, A. J.; Liu, K. L.; Röring, P.; Brunklaus, G.; Winter, M.; Theato, P., A Systematic Study of Vinyl Ether-Based Poly(Ethylene Oxide) Side-Chain Polymer Electrolytes. *ACS Applied Polymer Materials* **2021**, *3* (3), 1573-1582.
21. Ruzette, A.-V. r. G.; Soo, P. P.; Sadoway, D. R.; Mayes, A. M., Melt-Formable Block Copolymer Electrolytes for Lithium Rechargeable Batteries. *Journal of The Electrochemical Society* **2001**, *148* (6), 537 - 543.
22. Bergfelt, A.; Rubatat, L.; Brandell, D.; Bowden, T., Poly(benzyl methacrylate)-poly(oligo ethylene glycol) Methyl Ether Methacrylate Triblock-copolymers as Solid Electrolyte for Lithium Batteries. *Solid State Ion.* **2018**, *321*, 55-61.
23. Park, J.; Jang, S.; Kon Kim, J., Morphology and Microphase Separation of Star Copolymers. *Journal of Polymer Science Part B: Polymer Physics* **2015**, *53* (1), 1-21.
24. Liffland, S.; Hillmyer, M. A., Enhanced Mechanical Properties of Aliphatic Polyester Thermoplastic Elastomers through Star Block Architectures. *Macromolecules* **2021**, *54* (20), 9327-9340.
25. Lee, D.; Jung, H. Y.; Park, M. J., Solid-State Polymer Electrolytes Based on AB₃-Type Miktoarm Star Copolymers. *ACS Macro Letters* **2018**, *7* (8), 1046-1050.
26. Wang, S.; Wang, A.; Yang, C.; Gao, R.; Liu, X.; Chen, J.; Wang, Z.; Zeng, Q.; Liu, X.; Zhou, H.; Zhang, L., Six-arm Star Polymer Based on Discotic Liquid Crystal as High Performance All-solid-state Polymer Electrolyte for Lithium-ion Batteries. *J. Power Sources* **2018**, *395*, 137-147.
27. Niitani, T.; Amaike, M.; Nakano, H.; Dokko, K.; Kanamura, K., Star-Shaped Polymer Electrolyte with Microphase Separation Structure for All-Solid-State Lithium Batteries. *Journal of The Electrochemical Society* **2009**, *156*, 577 - 583.
28. Tong, Y.; Chen, L.; He, X.; Chen, Y., Sequential effect and enhanced conductivity of star-shaped diblock liquid-crystalline copolymers for solid electrolytes. *J. Power Sources* **2014**, *247*, 786-793.
29. Xie, H.-q.; Xie, D.; Liu, J., Solid Polymer Electrolyte Complexes of Polyoxyethylene-Containing Star-Shaped Block Copolymers and Copolymers with Uniform Grafts. *Polymer-plastics Technology and Engineering* **1989**, *28*, 355-369.
30. Mueller, A. H. E.; Yan, D.; Litvinenko, G.; Zhuang, R.; Dong, H., Kinetic Analysis of "Living" Polymerization Processes Exhibiting Slow Equilibria. 2. Molecular Weight Distribution for Degenerative Transfer (Direct Activity Exchange between Active and "Dormant" Species) at Constant Monomer Concentration. *Macromolecules* **1995**, *28* (22), 7335-7338.
31. Charleux, B.; Nicolas, J.; Guerret, O., Theoretical Expression of the Average Activation-Deactivation Equilibrium Constant in Controlled/Living Free-Radical Copolymerization Operating via Reversible Termination. Application to a Strongly Improved Control in Nitroxide-Mediated Polymerization of Methyl Methacrylate. *Macromolecules* **2005**, *38* (13), 5485-5492.

32. Beuermann, S.; Harrisson, S.; Hutchinson, R. A.; Junkers, T.; Russell, G. T., Update and Critical Reanalysis of IUPAC Benchmark Propagation Rate Coefficient Data. *Polymer Chemistry* **2022**, *13* (13), 1891-1900.
33. Segall, I.; Dimonie, V. L.; El-Aasser, M. S.; Soskey, P. R.; Mylonakis, S. G., Core-shell Structured Latex Particles. I. Copolymerization of Styrene/benzyl Methacrylate as a Choice for Shell Material and Characterization of Poly(*Z* butyl acrylate) Core Latex Particles. *Journal of Applied Polymer Science* **1995**, *58*, 385-399.
34. Zhang, C.; Lessard, B.; Maric, M., Synthesis and Characterization of Benzyl Methacrylate/Styrene Random Copolymers Prepared by NMP. *Macromolecular Reaction Engineering* **2010**, *4* (6-7), 415-423.
35. Striegel, A.; Yau, W. W.; Kirkland, J. J.; Bly, D. D., Polymer Architecture and Dilute Solution Thermodynamics. *Modern Size-Exclusion Liquid Chromatography* **2009**, 292-321.
36. Bawn, C. E. H.; Grimley, T. B.; Wajid, M. A., High Polymer Solutions. Part IV.—The Intrinsic Viscosity-Molecular Weight Relationships in Mixed Solvents. *Transactions of the Faraday Society* **1950**, *46* (0), 1112-1120.
37. Stenzel-Rosenbaum, M.; Davis, T. P.; Chen, V.; Fane, A. G., Star-polymer Synthesis via Radical Reversible Addition–fragmentation Chain-transfer Polymerization. *Journal of Polymer Science Part A: Polymer Chemistry* **2001**, *39* (16), 2777-2783.
38. Diederichsen, K. M.; Buss, H. G.; McCloskey, B. D., The Compensation Effect in the Vogel–Tammann–Fulcher (VTF) Equation for Polymer-Based Electrolytes. *Macromolecules* **2017**, *50* (10), 3831-3840.
39. Kotobuki, M., Polymer Electrolytes. *Polymer Electrolytes: Characterization Techniques and Energy Applications* **2020**, 1-22.
40. Gartner, T. E.; Morris, M. A.; Shelton, C. K.; Dura, J. A.; Epps, T. H., Quantifying Lithium Salt and Polymer Density Distributions in Nanostructured Ion-Conducting Block Polymers. *Macromolecules* **2018**, *51* (5), 1917-1926.
41. Wang, J.-Y.; Chen, W.; Russell, T. P., Ion-Complexation-Induced Changes in the Interaction Parameter and the Chain Conformation of PS-*b*-PMMA Copolymers. *Macromolecules* **2008**, *41* (13), 4904-4907.
42. Nakamura, I.; Wang, Z.-G., Salt-doped Block Copolymers: Ion Distribution, Domain Spacing and Effective χ Parameter. *Soft Matter* **2012**, *8* (36), 9356-9367.
43. Hallinan, D. T.; Villaluenga, I.; Balsara, N. P., Polymer and Composite Electrolytes. *MRS Bulletin* **2018**, *43* (10), 759-767.
44. Kambe, Y.; Arges, C. G.; Patel, S.; Stoykovish, M. P.; Nealey, P. F., Ion Conduction in Microphase-Separated Block Copolymer Electrolytes. *The Electrochemical Society Interface* **2017**, *26* (1), 61-67.
45. Kowalczuk, A.; Mendrek, B.; Żymełka-Miara, I.; Libera, M.; Marcinkowski, A.; Trzebicka, B.; Smet, M.; Dworak, A., Solution behavior of star polymers with oligo(ethylene glycol) methyl ether methacrylate arms. *Polymer* **2012**, *53* (25), 5619-5631.
46. Boissé, S.; Rieger, J.; Belal, K.; Di-Cicco, A.; Beaunier, P.; Li, M.-H.; Charleux, B., Amphiphilic Block Copolymer Nano-Fibers via RAFT-mediated Polymerization in Aqueous Dispersed System. *Chemical Communications* **2010**, *46* (11), 1950-1952.
47. Aggarwal, R.; Baskaran, D., Synthesis and Dilute Solution Properties of Branched Poly(benzyl methacrylate) Using Na-clay Supported Aqueous-phase Catalysis. *Journal of Polymer Science Part a-Polymer Chemistry* **2018**, *56* (19), 2225-2237.
48. Chao, D.; Jia, X.; Tuten, B.; Wang, C.; Berda, E. B., Controlled Folding of a Novel Electroactive Polyolefin via Multiple Sequential Orthogonal Intra-chain Interactions. *Chemical Communications* **2013**, *49* (39), 4178-4180.

49. Rojas, A. A.; Inceoglu, S.; Mackay, N. G.; Thelen, J. L.; Devaux, D.; Stone, G. M.; Balsara, N. P., Effect of Lithium-Ion Concentration on Morphology and Ion Transport in Single-Ion-Conducting Block Copolymer Electrolytes. *Macromolecules* **2015**, *48* (18), 6589-6595.
50. Bouchet, R.; Phan, T. N. T.; Beaudoin, E.; Devaux, D.; Davidson, P.; Bertin, D.; Denoyel, R., Charge Transport in Nanostructured PS-PEO-PS Triblock Copolymer Electrolytes. *Macromolecules* **2014**, *47* (8), 2659-2665.

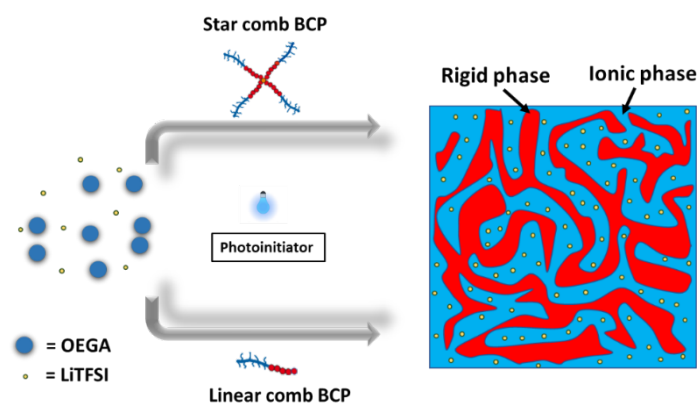
Chapter 3

Block copolymer-derived Nanostructured Solid Electrolyte based on comb-like PEO



Synopsis

In this chapter, a one-step protocol exploits the use of pre-synthesized linear and star Poly (styrene-co-benzyl methacrylate)-*b*-Poly [poly (oligo ethylene oxide methyl ether) acrylate] BCPs synthesized in chapter 2 to modulate in-situ the nanostructuring of poly(oligo (ethylene glycol) methyl ether acrylate) (POEGA) solid electrolyte synthesized by photopolymerization. The final material can be described as a nanostructured solid polymer electrolyte with kinetically arrested glassy domains in an ion conductive matrix of homopolymer. We have demonstrated that a variety of morphologies could be controlled by adjusting lithium salt content. More importantly, embedding BCP in the POEGA matrix acted as physical crosslinkers that simultaneously enhance the mechanical strength ($\sim 7\times$) while maintaining a good level of ionic conductivity.



The morphological characterization by TEM was carried out in collaboration with Monika Król and Janne Ruokolainen at Aalto University in Finland. SAXS experiments were performed at ALBA synchrotron Barcelona, Spain.

Table of Contents

1	Introduction	114
2	Results and Discussion	116
2.1	Preparation and characterization of initial formulations	116
2.2	Morphology of Solid Polymer Electrolyte	120
2.3	Mechanical Strength, Conductivity and Thermal Stability of SPEs	125
3	Conclusion	128
4	Supporting Information	129
4.1	Materials	129
4.2	Synthesis of Block Copolymer	129
4.2.1	Linear and Star macro-CTAs	129
4.2.2	Synthesis of Linear and Star Block copolymers	130
4.3	Characterization Methods	131
4.3.1	Nuclear Magnetic Resonance (NMR) Spectroscopy.	131
4.3.2	Size Exclusion Chromatography (SEC).....	133
4.3.3	UV Mold design	133
4.3.4	UV Calibration	134
4.3.5	Fourier-Transform Infrared Spectroscopy	136
4.3.6	Small Angle X-ray Scattering (SAXS)	136
4.3.7	Transmission Electron Microscopy (TEM).....	137
4.3.8	Differential Scanning Calorimetry (DSC).....	138
4.3.9	Rheological Characterization.	140
4.3.10	Electrochemical Impedance Spectroscopy (EIS).	141
5	References	142

1 Introduction

PEO is the most investigated polymer electrolyte, exhibiting good stability against Li metal and high solubility for various Li salts.¹ Nevertheless, its ionic conductivity is low compared to liquid electrolytes, and it lacks the mechanical strength required to impede the growth of Li dendrites.^{2, 3} PEO's ionic conductivity is facilitated by macromolecular segmental motion in the amorphous region of the polymer.^{4, 5} As explained in chapter 1, various strategies have been employed to increase the amorphous phase in PEO and break up the long-range macromolecular symmetry such as utilizing PEO with comb or star macromolecular architectures, cross-linking, polymer blending, copolymerization and addition of nano-fillers.⁵⁻¹⁰ Nonlinear PEO are preferred over linear ones because of their lower viscosities and reduced crystallinity.^{10, 11} Even though crosslinking PEO chains disrupts the formation of crystallite and increases mechanical strength,¹² this method restricts chain dynamics and can limit the possibilities for recycling. Discovering alternative methods to enhance the bulk strength of PEO, reduce crystallinity, improve chain dynamics, without compromising recyclability would represent a significant breakthrough in the advancement of solid-state batteries.

In chapter 2, we have demonstrated how the macromolecular architecture of star comb block copolymer electrolyte (BCPE) encompass unique self-organization that affect the structural range and connectivity of ordered grains so that the ionic pathway is less tortuous than the linear ones. BCPEs suffer from a notable drawback in which the equilibrium morphology frequently faces disruption due to network defects, such as dead ends occurring at grain boundaries. These defects interrupt the conducting pathways, consequently elevating resistance to ion transport.¹³ An approach to mitigating this limitation involves ensuring that the conductive block becomes the majority phase. Another challenge lies in the substantial time, effort, and volume of solvents required for the preparation of BCPEs. In response to this issue, significant attention is currently focused on the development of scalable, mechanically reinforced solid-state electrolytes that simultaneously offer maximized ionic conductivity.

In this chapter, we were inspired by the thesis work of Xavier Pascassio-Comte (IPREM/UPPA PhD 2016) on photopolymerized encapsulant based on block copolymer for photovoltaic panels,¹⁴ where it was demonstrated that poly(methyl methacrylate)-*b*-poly(*n*-butyl acrylate)-*b*-poly(methyl methacrylate) (PMMA-*b*-PnBA-*b*-PMMA) triblock copolymer and *n*-butyl acrylate (nBA) monomer can form complex hierarchical morphology during

photopolymerization. Therefore, we aimed to undertake fabrication of solid polymer electrolyte (SPE) using pre-synthesized block copolymers as additives in the photopolymerization of ion-conductive monomer. The appeal of this photopolymerization technique lies in its ability to expedite the fabrication process and complete non-utilization of solvent, rendering it particularly attractive.

To do that we have photo-polymerized the ion conductive oligo(ethylene oxide) methyl ether acrylate (OEGA) monomer in presence of the P(*S-co-BzMA*)-*b*-POEGA linear or star comb-like block copolymers (BCP) synthesized in chapter 2 and lithium bis(trifluoromethanesulfonyl)imide (LiTFSI) salt (refer to Figure 1). We show herein the morphological evolution of the blend before and after polymerization using small angle x-ray scattering (SAXS) techniques as well as transmission electron microscopy (TEM). Our primary objective was to uncover any underlying morphological difference that can be attributed to the different architectures of BCP used. Finally, we try to correlate the SPE structures to their mechanical and conducting properties.

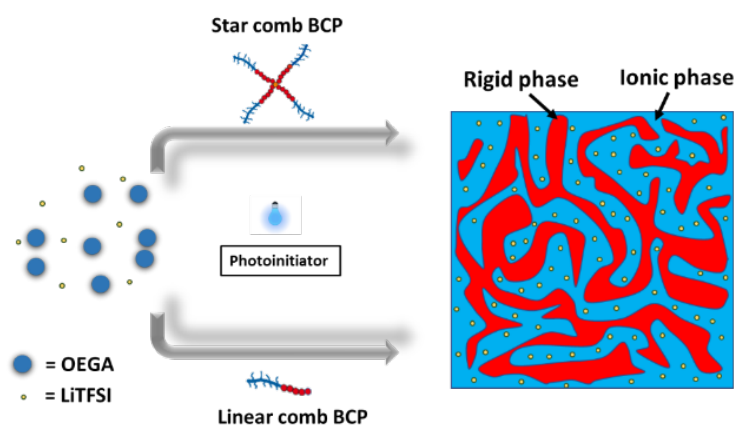


Figure 1. Schematic illustration of the polymer electrolyte membrane (SPE) fabrication, using linear or star comb-like BCP.

2 Results and Discussion

2.1 Preparation and characterization of initial formulations

We formulated the resin to be photopolymerized considering the requirements of good interplay between conductivity, low crystallinity as well as sufficient mechanical strength necessary for applications as SPE in lithium-ion batteries. Oligo (ethylene oxide) methyl ether acrylate (OEGA) was therefore carefully selected as the monomer for creating the ionic conductive matrix of poly(oligo(ethylene oxide) methyl ether acrylate) (POEGA) by photopolymerization. Preformed linear and star comb-like BCP (represented as *lc*-(A_{0.59})_{0.71}B_{0.29} and *sc*-(A_{0.62})_{0.73}B_{0.27} respectively, see Chapter 2) of poly(styrene-*co*-benzyl methacrylate)-*b*-poly[oligo(ethylene oxide) methyl ether acrylate)] were selected to be included *ab-initio* in OEGA-based resin. Synthesis of *lc*-(A_{0.59})_{0.71}B_{0.29} and *sc*-(A_{0.62})_{0.73}B_{0.27} BCPs having 29 and 27 wt.% of POEGA block respectively was achieved by RAFT polymerization and have been extensively discussed in chapter 2 (as presented in Table 1).¹⁵ For clarity, x, y and z subscripts in code (A_x)_yB_z represents the weight fraction of PBzMA in P(S-*co*-BzMA) hard block, total weight fraction of P(S-*co*-BzMA) hard block, and weight fraction of POEGA in the block copolymer, respectively. For emphasis, the SEC elution chromatograms plotted against Log M shown in Figure 2 and Figure 3 confirms the chain extension of the starting macroCTA to form block copolymers. Small fraction of residual first block is observed for star comblike BCP (Figure 3).

Table 1: Macromolecular characterization of BCPs. See Chapter 2 supporting information for more details.

BCP	P(S- <i>co</i> -BzMA) [wt%]	POEGA [wt%]	Mn, THEO [kg mol ⁻¹]	Mn, MALLS [kg mol ⁻¹]	Đ
<i>sc</i> -(A _{0.62}) _{0.73} B _{0.27}	0.73	0.27	281	414	1.31
<i>lc</i> -(A _{0.59}) _{0.71} B _{0.29}	0.71	0.29	44	41	1.10

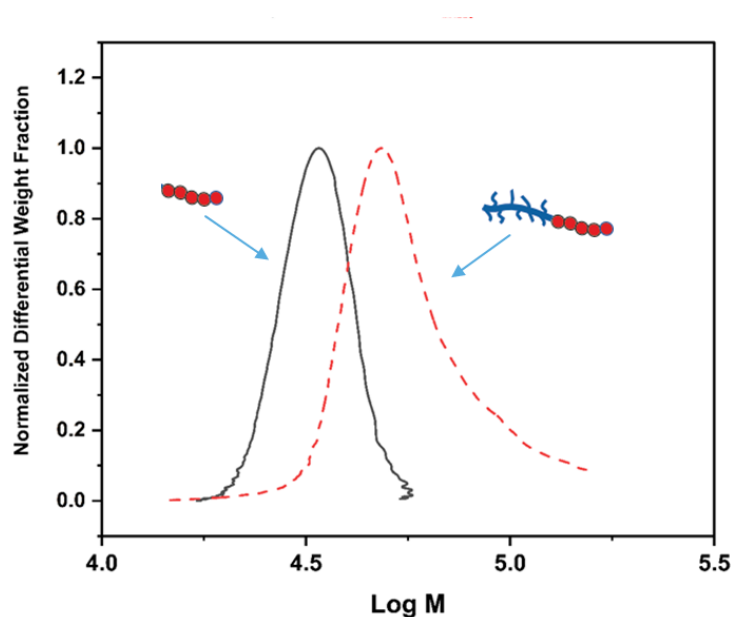


Figure 2. SEC-MALLS analysis of *l*-A_{0.59} macroCTA (—) and *lc*-(A_{0.59})_{0.71}B_{0.29} block copolymer (- - -)

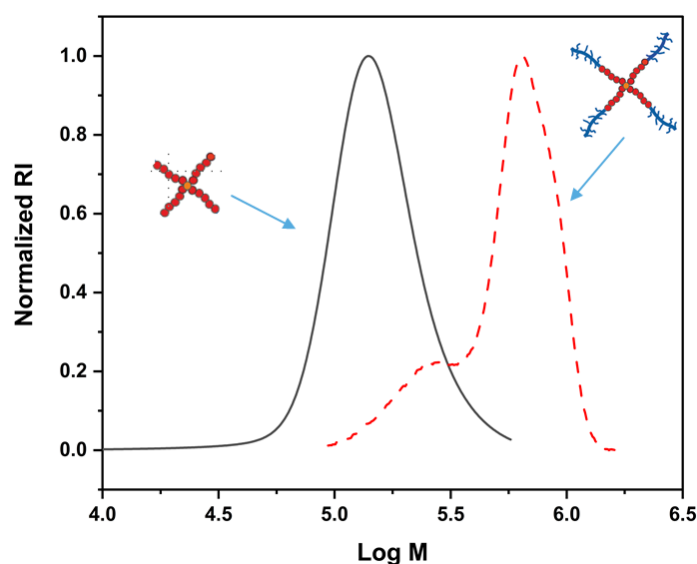


Figure 3. SEC-MALLS analysis of *s*-A_{0.62} macroCTA (—) and *sc*-(A_{0.62})_{0.73}B_{0.27} block copolymer (- - -).

Typical electrolyte formulation was composed of OEGA monomer, *lc*-(A_{0.59})_{0.71}B_{0.29} or *sc*-(A_{0.62})_{0.73}B_{0.27} BCP, lithium bis(trifluoromethanesulfonyl)imide (LiTFSI) salt, and 2,4,6-Trimethylbenzoyldi-Phenylphosphinate (TPO-L) photoinitiator. The description of formulation used in this work is presented in **Table 2**. In terms of nomenclature, electrolyte formulated with the linear or star comb-like BCP are called L-SPE-X% or S-SPE-X% respectively in this chapter. X is used to represent the weight percentage of soft phase present in the resin. Moreover, when lithium salt is added in the formulation the [EO] to [Li] molar

ratio is indicated to the name in subscript, $L\text{-SPE}_{30-92\%}$ then means electrolyte composed of the linear comb-like BCP, OEGA and a [EO] to [Li] ratio of 30. Introduction of lithium bis(trifluoromethanesulfonyl)imide (LiTFSI) salt *in-situ* in the electrolyte formulation obviates the post-polymerization salt doping steps that are compulsory for typical BCPEs, however, it disturbed the solubility of the entire system.

Table 2. Summary of the composition of the resins in terms of the volume percent of conducting phase.

Exp	Code ^a	BCP	$\frac{[\text{OEGA}]}{[\text{TPOL}]}$	$\frac{[\text{EO}]}{[\text{Li}^+]}$	Hard Phase ^b (wt%)	Soft Phase ^c (wt%)	$\Phi_{\text{cond}}^{\text{d}}$
KA115	$L\text{-SPE}_{-82\%}$	$lc\text{-}(A_{0.59})_{0.71}B_{0.29}$	330	-	18	82	-
KA112	$L\text{-SPE}_{30-92\%}$	$lc\text{-}(A_{0.59})_{0.71}B_{0.29}$	330	30	8	92	0.91
KA110	$L\text{-SPE}_{15-92\%}$	$lc\text{-}(A_{0.59})_{0.71}B_{0.29}$	330	15	8	92	0.91
KA118	$S\text{-SPE}_{-85\%}$	$sc\text{-}(A_{0.62})_{0.73}B_{0.27}$	330	-	15	85	-
KA120	$S\text{-SPE}_{30-92\%}$	$sc\text{-}(A_{0.62})_{0.73}B_{0.27}$	330	30	8	92	0.91
KA123	$S\text{-SPE}_{15-92\%}$	$sc\text{-}(A_{0.62})_{0.73}B_{0.27}$	330	15	8	92	0.91

^aThe prefix *L* and *S* represents the BCP architecture (linear and star respectively). Subscripts represents the EO/Li ratio in SPEs.

^bP(S-co-BzMA) constitutes the hard phase of the electrolyte.

^cPOEGA or POEGA+LiTFSI constitutes the soft phase of the electrolyte.

^d Φ_{cond} is the volume fraction of conducting phase in the initial resin according to equation S1. Density of POEGA, P(S-co-BzMA), LiTFSI are taken as 1.05 g cm⁻³, 1.12 1.05 g cm⁻³, and 1.33 1.05 g cm⁻³ respectively.

The formulation started by the solubilization of the block copolymers in OEGA. Although the ratio of incompatible hard block is high (P(S-co-BzMA), ~70%), the copolymer was readily solubilized. However, the addition of the lithium salt in the mixture resulted in the formation of a cloudy solution (**Figure 4a**). SAXS experiments was performed on electrolyte formulations (with and without LiTFSI) by means of a glass capillary (**Figure 4b-c**). $L\text{-SPE}_{-82\%}$ and $S\text{-SPE}_{-85\%}$ resins free of lithium salt appeared as clear solution with no scattering features indicating the good initial solubility of the BCP in OEGA monomer (**Figure 4b** and **Figure 4c**). On the other hand, formulations $L\text{-SPE}_{30-92\%}$ and $S\text{-SPE}_{30-92\%}$ appeared as opaque and the SAXS curve indicated a spherical form factor, which confirmed the assembly of the BCPs into micelles upon introduction of LiTFSI in the formulation. It is known that LiTFSI is largely immiscible with P(S-co-BzMA) and thus is excluded from the hard phase.¹⁶
¹⁷ The ethylene oxide (EO) units of OEGA monomer and POEGA block of the BCP easily coordinate with lithium-ion and therefore solvates the salt to form the ion-conducting phase. Therefore, the segregation of [OEGA/POEGA/LiTFSI] phases and P(S-co-BzMA) phases results in formation of micelles with soft corona and hard core. When the concentration of

LiTFSI is increased ($[EO]/[Li] = 15$), the formulation mixture becomes too viscous and could not be introduced into the capillary for SAXS analysis.

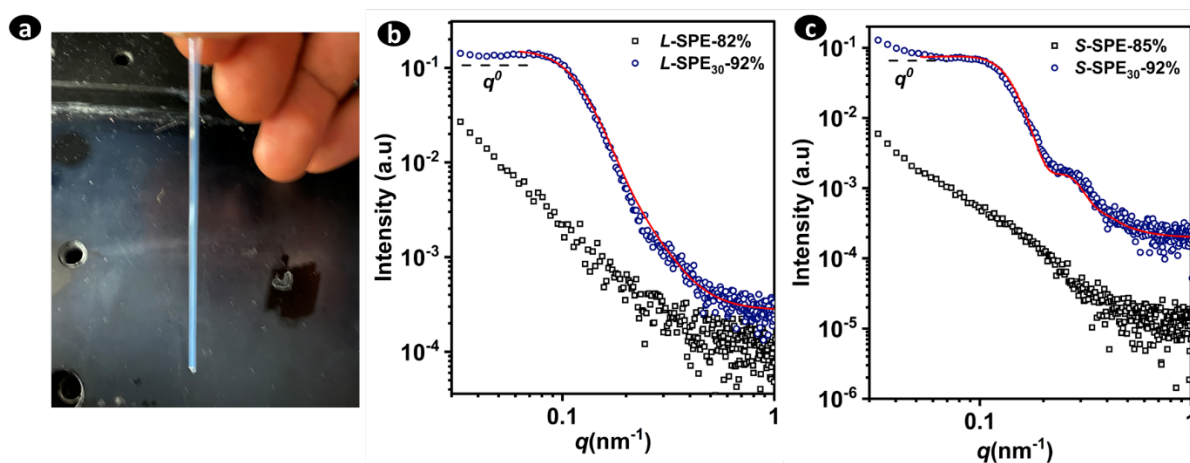


Figure 4. (a) Glass capillary ($\varnothing=1,5$ mm, length = 80 mm) filled with electrolyte formulation. SAXS profiles of the liquid reaction mixture obtained at $t = 0$ showing micellar self-assembly upon addition of LiTFSI salt. (b) SAXS of starting formulation of *L-SPE*-82% and *L-SPE*₃₀-92% (c) SAXS of starting formulation of *S-SPE*-85% and *S-SPE*₃₀-92%. SAXS data was fitted (red line) with a hard sphere model shown in the q range between 0.03 and 1 nm⁻¹.

SAXS data were analyzed in the Guinier region (lower q region), with a simple power-law model, defined in equation 1. $I(q)$ is the scattering intensity as a function of q , the wave vector and n is the power law exponent.

$$I(q) = q^n \quad 1$$

Ideally, the numerical value of n is gotten by taking the slope of the guinier regime (lower q region) in a $\text{Log } I(q)$ vs $\text{Log } q$ plot. In **Figure 4b**, scattering patterns of *L-SPE*₃₀-92% display power-law decays of $n = 0$ in intensity reflecting power-law scaling features for dispersed spheres (**Figure 4c**). On the other hand, formulations with *S-SPE*₃₀-92% show a slight deviation from $n = 0$ (refer to **Figure 4c**) which indicates perhaps the presence of aggregated spheres.

Using insights gained from the power law, we employed the hard sphere model to fit the SAXS curves (see red lines in **Figure 4b** and **Figure 4c**).¹⁸ This model is frequently employed to characterize the interparticle structure factor in systems consisting of spherical particles subject to interactions governed by hard sphere (excluded volume) principles. Doing so, we obtained the radius, r of the hard spheres in *L-SPE*₃₀-92% and *S-SPE*₃₀-92% as 15.1 nm (polydispersity = 0.30) and 19.6 nm (polydispersity = 0.18) respectively. Also, the effective radius, R_{eff} for *L-SPE*₃₀-92% and *S-SPE*₃₀-92% was determined as 28.2 nm and 21.3 nm respectively. R_{eff} describes classically the closest approach distance of the hard sphere. This

parameter give insight on the incompressible POEGA corona dimension. Ideally, in a system with dispersed hard spheres, the minimum average distance between two sphere centers can be computed as $\geq 2R_{eff}$ (refer to Figure 5). Another interesting observation is that *L-SPE*_{30-92%} contain broader distribution of hard spheres compared to *S-SPE*_{30-92%}. A direct interpretation of this may be that star comb-like BCP self-assembles into hard spheres in OEGA/LiTFSI mixture with more defined geometry.

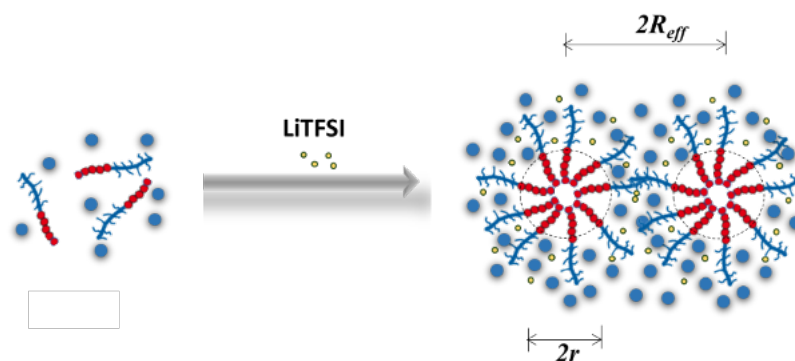


Figure 5. Schematic illustration of in-solution self-assembly for form sphere. Here, R_{eff} is the effective radius and r is the radius.

Regrettably, due to excessive viscosities of liquid formulations of *L-SPE*_{15-92%} and *S-SPE*_{15-92%} (preventing insertion in SAXS capillaries), we were unable to acquire specific information regarding the self-assembly characteristics prior to photopolymerization. Nevertheless, this lack of information does not hinder our comprehension that the introduction of lithium salt into the initial formulation results in well-defined patterns of block copolymer self-assembly in OEGA, forming hard spheres when $[EO]/[Li] = 30$. Therefore, we hypothesize that increasing salt content ($[EO]/[Li] = 15$) might enhance the segregation strength, leading to similar type of assembly of the BCP in OEGA (as in $[EO]/[Li] = 30$ formulations).

2.2 Morphology of Solid Polymer Electrolyte

Once the starting formulation were characterized, we performed the polymerization by exposure to UV light. As a preliminary experiment, kinetic studies via real-time Fourier-transform infrared (FTIR) spectrometer (see Figure 6) showed that $\sim 90\%$ OEGA conversion could be reached after 3 min by irradiating ($I_0 = 2.1 \text{ mW cm}^{-2}$) a glass capillary tube containing the OEGA and TPO-L (without BCP and LiTFSI). In a case of 90 % OEGA conversion, the theoretical degree of polymerization ($DP = [OEGA]/[TPOL]$) of POEGA matrix would be about 297 (143 kg/mol). Attempts to verify the degree of polymerization experimentally by

size exclusion chromatography (SEC) and nuclear magnetic resonance (NMR) was not successful because the final SPE was insoluble (specifically in THF).

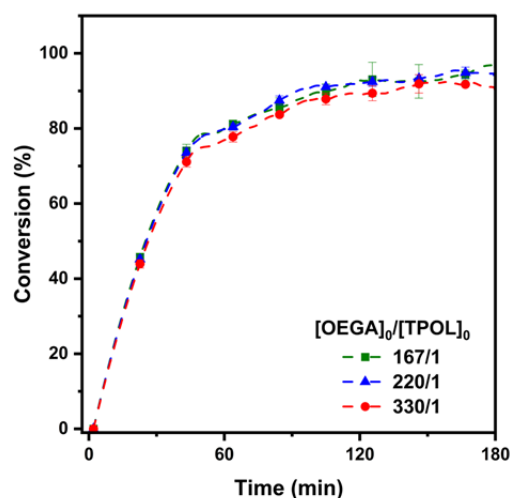


Figure 6. Graph showing effect of decreasing $[OEGA]_0/[TPOL]_0$ ratio on polymerization kinetics for the photopolymerization of oligo (ethylene glycol) methyl ether acrylate (OEGA) at $2.1 \text{ mW}\cdot\text{cm}^{-2}$ (photopolymerization in 1.5 mm capillary).

We subsequently applied this knowledge of kinetics to the photopolymerization process for the formulations detailed in Table 2, aiming to create the SPE within our custom-made PTFE molds as outlined in Figure S17. The formulation mixtures underwent irradiation using a 365 nm UV lamp (with the current set to 670 mA, corresponding to an intensity of approximately 78 mW cm^{-2}) for a duration of 30 minutes. It is important to note that we employed rigorous conditions, utilizing a higher irradiance of 78 mW cm^{-2} and allowing for a sufficient irradiation period of 30 minutes so as to achieve a higher conversion of the OEGA monomer. Recovered samples appeared opaque white as shown in Figure 7. The fabricated SPEs were then vacuum dried at $60 \text{ }^\circ\text{C}$ overnight (still white after drying) and characterized by SAXS and TEM.



Figure 7. Exemplary pictures of as-fabricated SPE before vacuum drying. In this photo, the sample is $S\text{-SPE}_{15-92\%}$ (\varnothing 30 mm, thickness $\approx 500 \mu\text{m}$).

SAXS curves and TEM images of L-SPE-82% and S-SPE-85% are shown in Figure 8. SAXS results for L-SPE-82% show the absence of particular scattering feature whereas S-SPE-85%

display a structural peak at $q = 0.16 \text{ nm}^{-1}$ (bragg distance = 39.2 nm). According to TEM images, *L*-SPE-82% show macroscopic phase separation with no defined pattern. *S*-SPE-85% features a chain-like connection of dispersed objects (refer to Figure S18 for larger scale images).

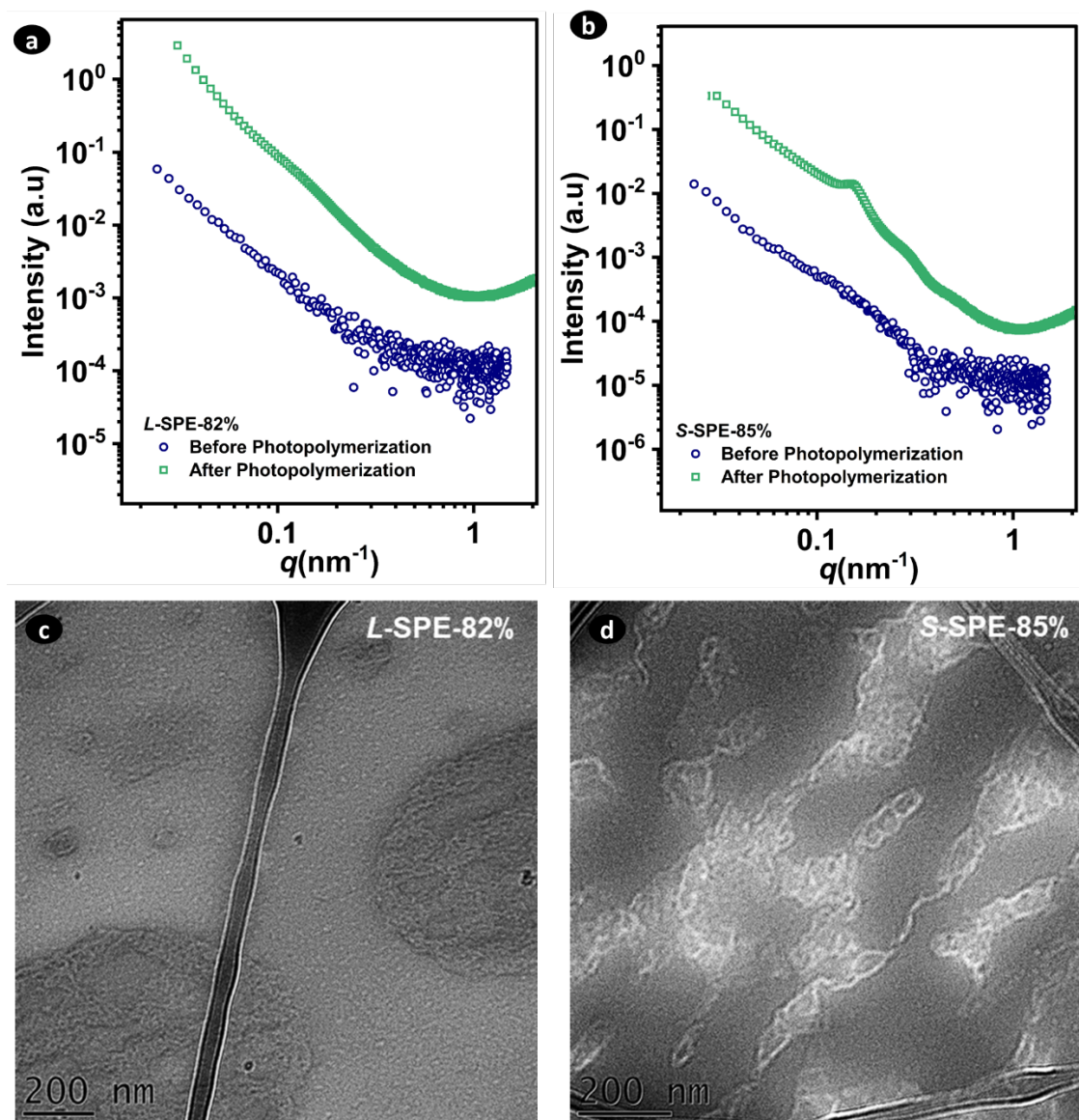


Figure 8. SAXS profile of samples derived from a) *L*-SPE-82% before and after photopolymerization b) *S*-SPE-85% before and after photopolymerization. TEM micrographs showing morphology of SPEs samples after photopolymerization c) *L*-SPE-82% d) *S*-SPE-85%.

At $[\text{EO}]/[\text{Li}] = 30$, the SAXS intensity profiles of final *L*-SPE₃₀-92% and *S*-SPE₃₀-92% revealed a stronger decay of $I(q)$ in the low q range $0.03 - 0.12 \text{ nm}^{-1}$ (see **Figure 9a** and **Figure 9b**). These are the signature of aggregated objects. The slope of this region is consistent with power law exponent of $n = -2$ (refer to equation 1) which can be ascribed to disc-like form factors.

These results were confirmed by TEM micrographs of the films (**Figure 9c** and **Figure 9d**), Specifically, $L\text{-SPE}_{30-92\%}$ displayed dispersed disc-like nano-objects within the PEOGA matrix. The $S\text{-SPE}_{30-92\%}$ showed large aggregates of apparent spherical particles. Recall that in samples without salt, a pronounced macro phase separation occurred without a defined pattern. Here, the morphology is much defined owing to increased segregation strength. Therefore, it can be concluded that increasing salt concentration causes the BCP to self-assemble into hard sphere and then aggregates together during photopolymerization of OEGA to form larger embedded objects.

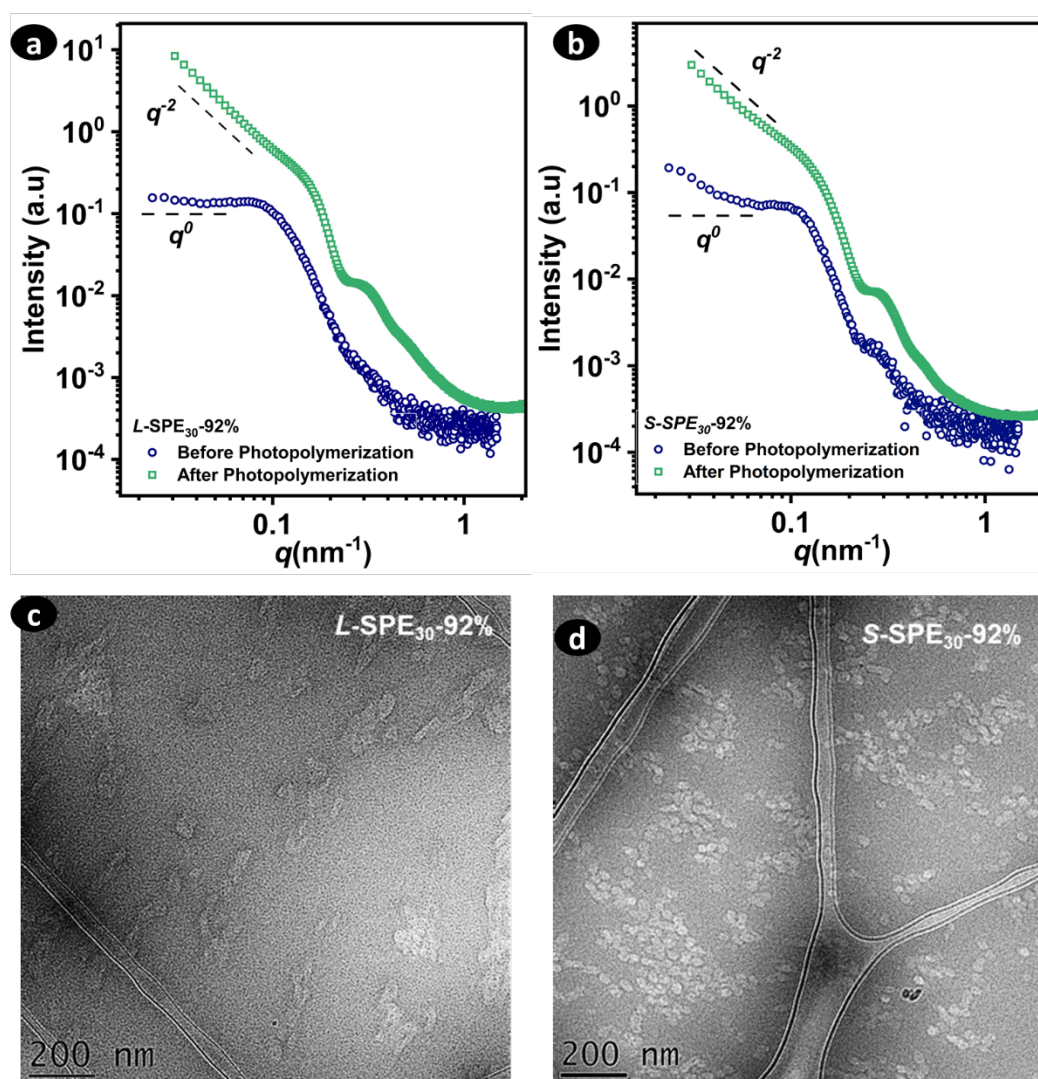


Figure 9. SAXS profile of SPE samples derived from a) $L\text{-SPE}_{30-92\%}$ before and after photopolymerization b) $S\text{-SPE}_{30-92\%}$ before and after photopolymerization. Short dash black lines represent power law with exponents $n = 0$ and $n = -2$. TEM micrographs showing morphology of SPEs samples after photopolymerization c) $L\text{-SPE}_{30-92\%}$ d) $S\text{-SPE}_{30-92\%}$.

In the case of $L\text{-SPE}_{15-92\%}$ and $S\text{-SPE}_{15-92\%}$, where $[\text{EO}]/[\text{Li}] = 15$, the SAXS patterns (refer to Figure 10a and Figure 10b) exhibit lower power low slope values (about -1) compared to

samples with $[EO]/[Li] = 30$. That power low exponents could be the signature of an elongated object form factor (cylinder-like). Furthermore, SAXS profile of $L-SPE_{15-92\%}$ exhibit a weak structure factor, implying well-dispersed and distant scattering objects.

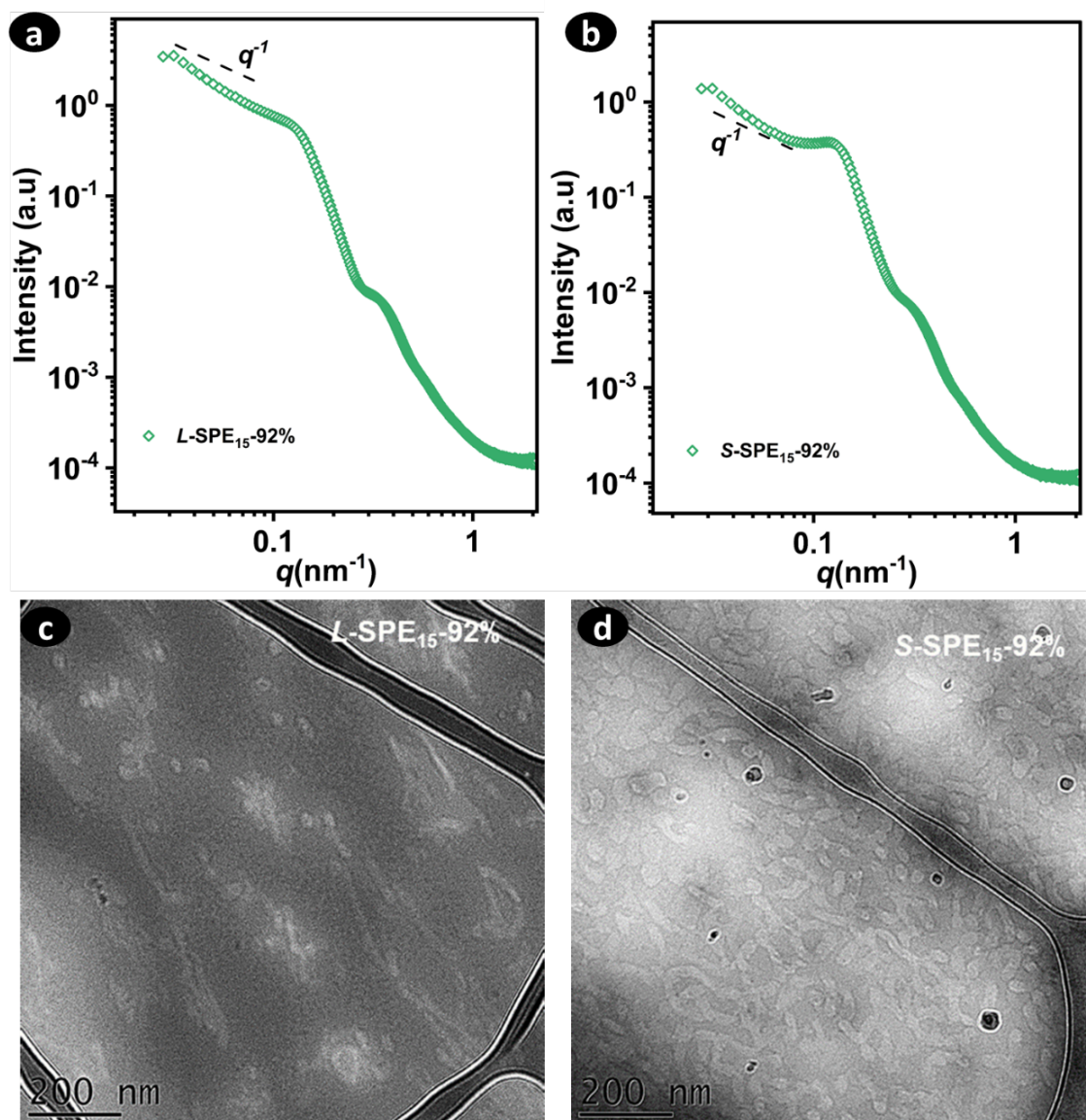


Figure 10. SAXS profile of SPE samples derived from a) $L-SPE_{15-92\%}$ before and after photopolymerization b) $S-SPE_{15-92\%}$ before and after photopolymerization. Short dash black lines represent a power law with an exponent -1. TEM micrographs showing morphology of SPEs samples after photopolymerization c) $L-SPE_{15-92\%}$ d) $S-SPE_{15-92\%}$.

On the other hand, SAXS profile of $S-SPE_{15-92\%}$ show a significant structure factor which may signify that there are macro domains with a higher concentration of scattering objects.

TEM images of the SPEs are provided in Figure 10c and Figure 10d. *L-SPE*_{15-92%} and *S-SPE*_{15-92%} displayed aggregated spherical particles and elongated objects, aligning with the trends identified through SAXS analysis.

2.3 Mechanical Strength, Conductivity and Thermal Stability of SPEs

To investigate the influence of BCP morphology on the strength of the POEGA matrix, we conducted constant shear experiments on SPEs with a [EO]/[Li] ratio of 15, specifically *L-SPE*_{15-92%} and *S-SPE*_{15-92%}. To facilitate comparison, we also synthesized a pure POEGA matrix by initiating the photopolymerization of the OEGA monomer and LiTFSI under the same conditions used for fabricating *L-SPE*_{15-92%} and *S-SPE*_{15-92%}, resulting in *POEGA*_{15-100%}. To anticipate the mechanical properties with the introduction of a crosslinker, we prepared *POEGA*_{15-100%}(crosslinked) by incorporating 1 mol% of Oligo ethylene glycol diacrylate (OEGDA). In Table 3, we present the storage (G') moduli of *L-SPE*_{15-92%}, *S-SPE*_{15-92%}, *POEGA*_{15-100%}, and *POEGA*_{15-100%}(crosslinked) as 52.9, 34.7, 7.5, and 31.7 KPa, respectively at 30 °C (**Figure 11a**). This demonstrates that embedding linear BCP in the POEGA matrix at a prevailing [EO]/[Li] = 15 can increase storage moduli by a factor of 7. In the case of embedding star BCP, the moduli increase by approximately 5-fold. Similarly, a comparable enhancement in storage moduli (approximately 4-fold) is achievable by incorporating 1 mol% of OEGDA, a crosslinker, into *POEGA*₁₅ during photopolymerization. These results suggest that BCP-derived morphologies in the SPEs act as physical-crosslinking points that strengthen the POEGA matrix.

Another interesting observation is the gradual decrease in modulus with temperature for *L-SPE*_{15-92%} and *S-SPE*_{15-92%}, indicating a gradual transition of the SPE from a hard to a viscous material. Specifically, *L-SPE*_{15-92%} exhibits a significant decline after reaching around 70 °C. This phenomenon may be connected to the T_g of the P(*S-co-BzMA*) hard phase, which was previously reported to be approximately 76 °C in **Chapter 2**. Moreover, we emphasize that embedding BCP in POEGA, rather than using a crosslinker, may allow for recycling or processing of the material when subjected to temperatures above the T_g (70 °C).

Thermogravimetric analysis was performed on samples (with [EO]/[Li] = 15) in order to assess their chemical stability (**Figure 11b**). There was a slight loss in weight (~4wt%) of the samples after 100 °C. This may be due to moisture during manipulation of TGA samples or evaporation of monomer remaining after photopolymerization. Overall, the samples exhibited thermal

stability up to 300 °C thus demonstrating the capacity to withstand operating temperature conditions (-20 °C to 60 °C) of lithium batteries.¹⁹

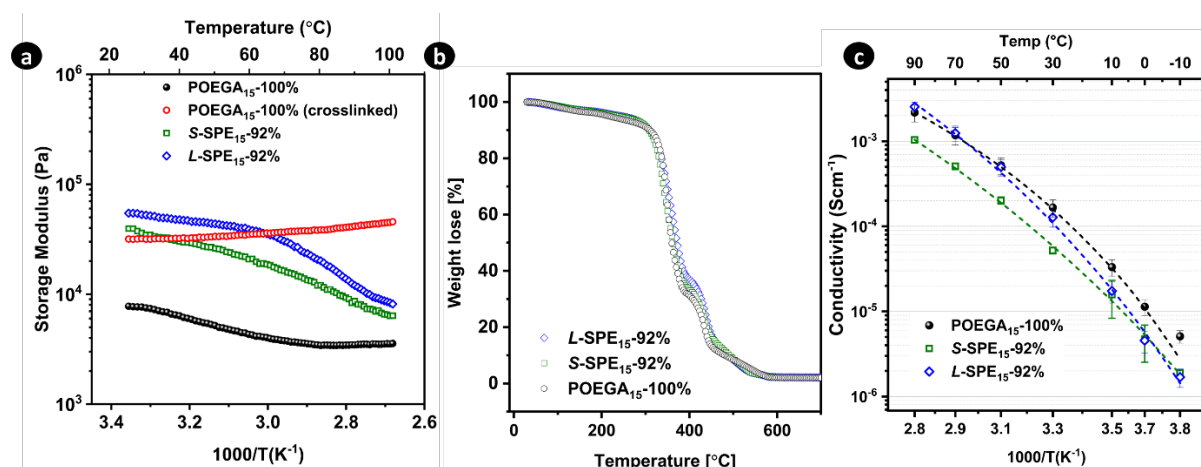


Figure 11. a) Storage (G') moduli versus frequency, b) Thermogravimetric analysis and c) Temperature-dependent ionic conductivity of $L-SPE_{15-92\%}$ (\diamond), $S-SPE_{15-92\%}$ (\square), $POEGA_{15-100\%}$ (\bullet) and $POEGA_{15-100\%}$ (crosslinked) (\circ). Short dash lines represent the VFT model fits to the conductivity data.

Table 3. Summary of the storage moduli, conductivity of SPEs.

Code ^a	$\frac{[EO]}{[Li^+]}$	Soft Phase (wt%)	Φ_{cond}	$G'(KPa)^a$	σ^a (Scm ⁻¹)	T_g (°C)	T_0 (°C)
$L-SPE_{15-92\%}$	15	92	0.91	52.9	1.30×10^{-4}	n/a	105
$S-SPE_{15-92\%}$	15	92	0.91	34.7	5.20×10^{-5}	-47.6	129
$POEGA_{15-100\%}$	15	100	1	7.5	1.66×10^{-4}	-50.3	104
$POEGA_{15-100\%}$ (crosslinked)	15	100	1	31.7	n/a	n/a	n/a

^a Values taken at 30°C.

The conductivity of vacuum-dried samples was assessed using electrochemical impedance spectroscopy (EIS). **Figure 11c** illustrates a classical decline in conductivity as the temperature decreases. This decrease in conductivity can be attributed to the reduced segmental mobility of polymer chains at lower temperatures, which limits ion transport across all the samples.^{20, 21}

At a temperature of 30 °C, the conductivity values for $POEGA_{15-100\%}$, $L-SPE_{15-92\%}$, and $S-SPE_{15-92\%}$ are 0.17, 0.13, and 0.05 mS cm⁻¹, respectively. $L-SPE_{15-92\%}$ exhibits improved conductivities beyond 50 °C comparable to $POEGA_{15-100\%}$ (as seen in **Figure 11c**). This observation suggests that the open morphology with well-dispersed non-conductive nano-domains does not impede ionic motion across the film. In contrast, $S-SPE_{15-92\%}$ displays reduced conductivity, which may be attributed to the presence of macro-domains containing

concentrated non-conductive nano-domains (refer to TEM in Figure 10c, Figure 10d and Figure S20).

Due to time limitations, extensive testing in lithium batteries could not be conducted within the duration of this thesis. Furthermore, our objective was to further enhance the mechanical properties through the exploration of a polymerization-induced microphase separation approach.

3 Conclusion

Herein, we introduced the straightforward fabrication of POEGA-based SPE featuring nanoscale structures. Two mechanisms underpinned the formation of such nanostructures. (i) The *ab initio* self-assembly of the BCPs into hard spheres upon addition of lithium salt in the initial liquid resin prior photopolymerization of OEGA monomer. An occurrence that is due to the insolubility of P(S-*co*-BzMA) in the mixture of salt and monomer and to the solubility of POEGA block in this mixture. (ii) Kinetic arrest of the already formed hard spheres during photopolymerization. This may include a subtle interplay between photopolymerization of OEGA monomer and interactions of the self-assembled hard spheres, which depends strongly on original salt concentration. This mechanism differs from the typical PIMS process, where polymerization starts from a completely soluble mixture and then phase separation occurs continuously during polymerization.

Our analysis using SAXS and TEM revealed that the hard spheres present in the resin formulations (*L*-SPE₃₀ and *S*-SPE₃₀) at EO/Li = 30 aggregate during photopolymerization to form dispersed disc-like nanostructures within the POEGA matrix. When the salt concentration is increased to a ratio of EO/Li = 15, elongated objects are observed in both *L*-SPE_{15-92%} and *S*-SPE_{15-92%}. In *L*-SPE_{15-92%}, the hard nano-domains are more uniformly dispersed, whereas in *S*-SPE_{15-92%}, localized higher concentrations of hard nano-domains are observed. We have demonstrated how this microstructure ultimately influences the strength and conductivity of the SPEs through shear tests and electrochemical impedance spectroscopy (EIS). It can be concluded that the presence of kinetically arrested nanostructures in the POEGA matrix serves as physical crosslinkers, leading to a remarkable 7-fold enhancement in mechanical properties in the case of *L*-SPE_{15-92%} and a 5-fold improvement in the case of *S*-SPE_{15-92%}. The conductivity of *L*-SPE_{15-92%} (0.13 mS cm⁻¹) was approximately twice that of *S*-SPE_{15-92%} (0.05 mS cm⁻¹), underscoring the significant influence of BCP architecture on the POEGA matrix. Furthermore, the conductivity of *L*-SPE_{15-92%} increases with temperature, eventually reaching levels comparable to that of POEGA_{15-100%} above 50 °C.

Nevertheless, there is still much to discover concerning the need for better control of morphology on larger length scales and a comprehensive understanding of the macromolecular chain dynamics within these intricate systems. This particularly pertains to understanding the extent to which block copolymer (BCP) architecture impacts these materials. However, our

study, primarily focused on elucidating the process of forming BCP-derived morphologies at the nanoscale, can serve as a foundational basis for future investigations within this class of photopolymerized polymer blends.

4 Supporting Information

4.1 Materials

Benzyl Methacrylate (BzMA, Sigma-Aldrich, 96%) was passed through a silica gel column to remove monomethyl ether hydroquinone inhibitor. Styrene (S, Sigma-Aldrich, 99%+), Azobis(isobutyronitrile) (AIBN, Sigma-Aldrich, 98%), Poly (ethylene glycol) methyl ether acrylate (OEGA, DP_n = 8-9, average M_n = 480 g.mol⁻¹, Sigma-Aldrich) were used as purchased. Pentaerythritol tetrakis[2-(dodecylthiocarbonothioylthio)-2-methylpropionate (4 arm star DDMAT RAFT agent, Sigma-Aldrich, 97%), 4-cyano 4-[(dodecylsulfanylthiocarbonyl)-sulfanyl]-pentanoic acid (monofunctional RAFT agent, Sigma-Aldrich, 97%), Ethyl (2,4,6-trimethylbenzoyl) phenylphosphinate (TPO-L) photo-initiator (316 g.mol⁻¹).

4.2 Synthesis of Block Copolymer

4.2.1 Linear and Star macro-CTAs

Synthesis of linear and star block copolymers used in this work have been extensively discussed in our previous work (Chapter 2) as depicted in Scheme S1.

First, the synthesis of P(S-*co*-BzMA) macro-CTA was achieved by RAFT polymerizations of 8 g monomer mixture of styrene (37 mol%) and benzyl methacrylate (63 mol%). tetra-functional macro-CTA (*s*-A_{0.62}), AIBN (2.1 mg, 1.29 × 10⁻² mmol, 0.1 eq), 4 arm star DDMAT RAFT agent (49.2 mg, 3.23 × 10⁻² mmol = 1.29 × 10⁻¹ mmol of trithiocarbonate TTC, 1 eq), BzMA (4.00 g, 2.27 × 10⁻² mol, 176 eq), and S (4.00 g, 3.85 × 10⁻² mol, 298 eq) were added to a 25 mL Schlenk flask and sealed with a silicone septum. The reactant mixture was degassed with nitrogen bubbling for 20 min in an ice bath. The Schlenk flask was placed into an oil bath at previously heated 75 C to start the reaction. The reaction was stopped at *t* = 31.5 h and purification was done by addition of 2 vol. equivalence of THF to solubilize the crude mixture

and precipitation in 10 vol. equivalence of EtOH. Purification was done twice to ensure complete removal of unreacted monomer and precipitates were recovered via vacuum filtration and dried in vacuum for 72 h. In the synthesis of monofunctional macro-CTA (*l*-A_{0.59}), equivalent amount of 4-cyano 4-[(dodecylsulfanylthiocarbonyl)-sulfanyl]-pentanoic acid RAFT agent was used instead while keeping other experimental conditions the same. Weight fraction of the BzMA and S units in the final copolymer was determined from ¹H NMR and molecular weight determined on SEC MALLS (refer to Table 4).

Table 4: Macromolecular characterization and properties of macro-CTAs synthesized in chapter 2.

macroCTA	S [wt%]	BzMA [wt%]	Mn, Theo [kg mol ⁻¹]	Mn, MALLS [kg mol ⁻¹]	Đ
<i>s</i> -A _{0.62}	0.40	0.60	159	133	1.50
<i>l</i> -A _{0.59}	0.44	0.56	31	30	1.04

4.2.2 Synthesis of Linear and Star Block copolymers

Previously synthesized macroCTA were extended to include POEGA block by solvent RAFT polymerization. In a typical experiment, AIBN (0.9 mg, 5.57 × 10⁻³ mmol), macroCTA: *s*-A_{0.62} (1.7 g, 1.39 × 10⁻² mmol = 5.57 × 10⁻² mmol TTC), OEGA (10.2 g, 21.3 mmol) and 1,4-dioxane (1:1 v/v) were added to a 100 mL Schlenk flask and sealed with a silicone septum. The reaction mixture was degassed with nitrogen bubbling for 30 min in an ice bath. The Schlenk flask was placed into an oil bath at previously heated 75 °C to start the reaction. The reaction was stopped after 2 h by cooling down in an ice -water bath and by introduction of oxygen in the crude mixture. Purification was done by solubilization of the crude mixture in THF and dialyzed over water using 50kDa cellulose membrane. Dialysis was done over 6-water cycles to ensure complete removal of unreacted PEGA monomer and dialyzed sample is lyophilized. Weight fraction of PEGA was determined from ¹H NMR and molecular weight determined on SEC MALLS (Table 1).

The volume fraction of conducting phase of PIMS films was calculated from equation S1.

$$\phi_c = 1 - \left(\frac{m_{0,POEGA+LiTFSI} / \rho_{POEGA+LiTFSI}}{M_{0,PIMS} / \rho_{PIMS}} \right) \quad S1$$

Where ρ is used to denote density. The density of the POEGA+LiTFSI was calculated from equation S2.

$$\rho_{POEGA+LiTFSI} = \frac{\rho_{POEGA}\rho_{LiTFSI}(m_{0,POEGA} + m_{0,LiTFSI})}{(\rho_{POEGA}m_{0,LiTFSI} + \rho_{LiTFSI}m_{0,POEGA})} \quad S2$$

The density of the PIMS was calculated from equation S3.

$$\rho_{PIMS} = \frac{\rho_{POEGA+LiTFSI}\rho_{P(S-co-BzMA)}(m_{0,POEGA+LiTFSI} + m_{0,P(S-co-BzMA)})}{(\rho_{POEGA+LiTFSI}m_{0,P(S-co-BzMA)} + \rho_{P(S-co-BzMA)}m_{0,POEGA+LiTFSI})} \quad S3$$

4.3 Characterization Methods

4.3.1 Nuclear Magnetic Resonance (NMR) Spectroscopy.

NMR spectra were recorded using a Bruker 400 MHz spectrometer at 25 °C with 32 scans and a time delay D1 of 5 seconds. ^1H NMR measurements were performed at frequencies of 400 MHz. DOSY NMR spectra were recorded at 30 °C with 6000 scans and a time delay D1 of 2 seconds. Deuterated chloroform (CDCl_3) and deuterated dichloromethane (CD_2Cl_2) were used as solvent respectively for crude and purified polymer. All products were dissolved with concentrations between 10 and 20 mg/mL.

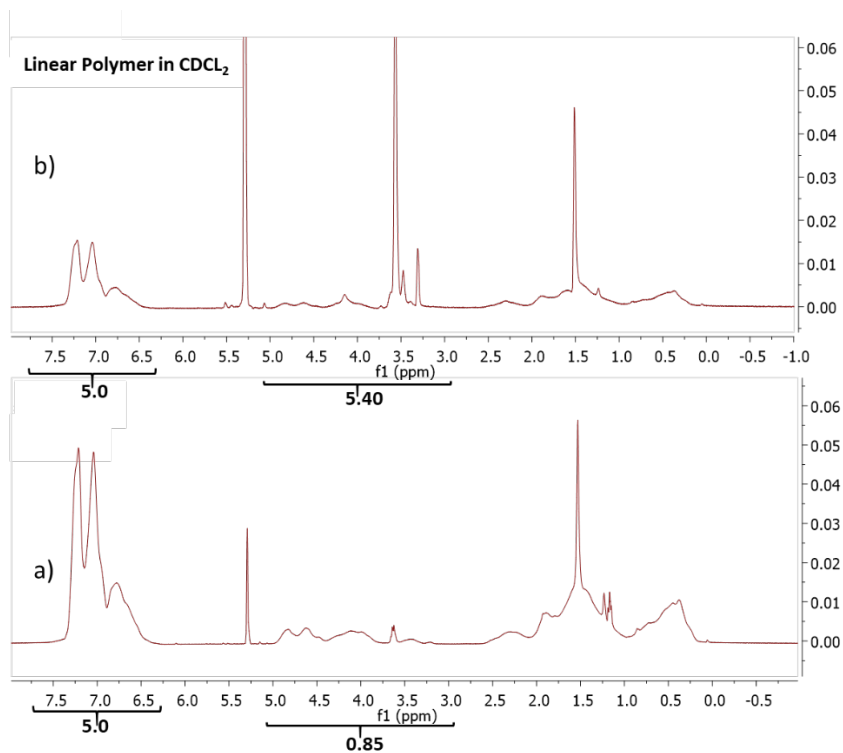


Figure S12: ^1H NMR spectrum of a) linear macro-CTA and b) linear BCP.

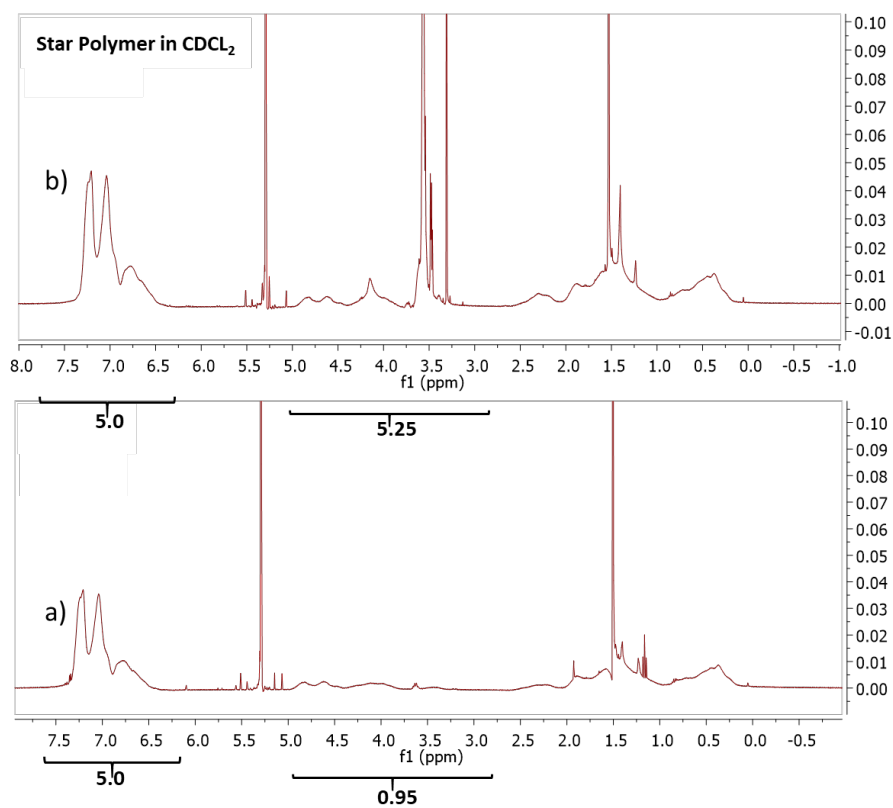


Figure S13: ^1H NMR spectrum of a) star macro-CTA and b) star BCP.

Table S5. Summary of the composition of the resins in terms of the volume percent of conducting phase.

Code ^a	BCP	BCP (g)	OEGA (g)	[OEGA] [TPOL]	LiTFSI (g)	[EO] [Li ⁺]	Hard Phase ^b (wt%)	Soft Phase ^c (wt%)	$\Phi_{\text{cond}}^{\text{d}}$
<i>L-SPE-82%</i>	<i>lc</i> -(A _{0.59}) _{0.71} B _{0.29}	0.50	1.67	330	-	-	18	82	-
<i>L-SPE</i> _{30-92%}	<i>lc</i> -(A _{0.59}) _{0.71} B _{0.29}	0.55	3.75	330	0.70	30	8	92	0.91
<i>L-SPE</i> _{15-92%}	<i>lc</i> -(A _{0.59}) _{0.71} B _{0.29}	0.45	2.65	330	0.98	15	8	92	0.91
<i>S-SPE-85%</i>	<i>sc</i> -(A _{0.62}) _{0.73} B _{0.27}	0.57	2.85	330	-	-	15	85	-
<i>S-SPE</i> _{30-92%}	<i>sc</i> -(A _{0.62}) _{0.73} B _{0.27}	0.48	3.27	330	0.61	30	8	92	0.91
<i>S-SPE</i> _{15-92%}	<i>sc</i> -(A _{0.62}) _{0.73} B _{0.27}	0.48	2.83	330	1.05	15	8	92	0.91

^aThe prefix *L* and *S* represents the BCP architecture (linear and star respectively). Subscripts represents the EO/Li ratio in SPEs.

^bP(S-co-BzMA) constitutes the hard phase of the electrolyte.

^cPOEGA or POEGA+LiTFSI constitutes the soft phase of the electrolyte.

^d Φ_{cond} is the volume fraction of conducting phase according to equation S1. Density of POEGA, P(S-co-BzMA), LiTFSI are taken as 1.05 g cm⁻³, 1.12 1.05 g cm⁻³, and 1.33 1.05 g cm⁻³ respectively.

4.3.2 Size Exclusion Chromatography (SEC).

Measurements were performed on a bank of 4 Shodex columns (KF801, KF8025, KF804 and KF806) each 300 mm x 8 mm at 30 °C with THF eluent controlled by a Malvern pump (Viscotek, VE1122) at a flow rate of 1.0 mL.min⁻¹. The SEC apparatus is equipped with a refractive index (RI) detector (Viscotek VE3580), a Wyatt Heleos II Multi Angle Laser Light Scattering detector (MALLS, 18 angles, $\lambda_0 = 664.4$ nm), an online viscometer (Wyatt Viscostar 311-V4) and a UV-visible detector (Viscotek-Malvern VE3210). Toluene was used as a flow marker. Sample concentrations were limited to the range of 1.5 – 4.5 mg mL⁻¹ and dissolved samples were filtered through polytetrafluorethylene (PTFE) membranes with a pore size of 0.45 μm prior to injection.

4.3.3 UV Mold design

The upper section of the mold is formed from PTFE, cut into the desired membrane geometry shape. The lower portion of the mold consists of a metallic base, which provides support during the assembly of the mold. An intermediate layer of PTFE sheet is positioned between the upper and lower parts to facilitate the effortless separation of the photopolymerized membrane. The three mold components were held together by means of a screw while ensuring tight sealing.

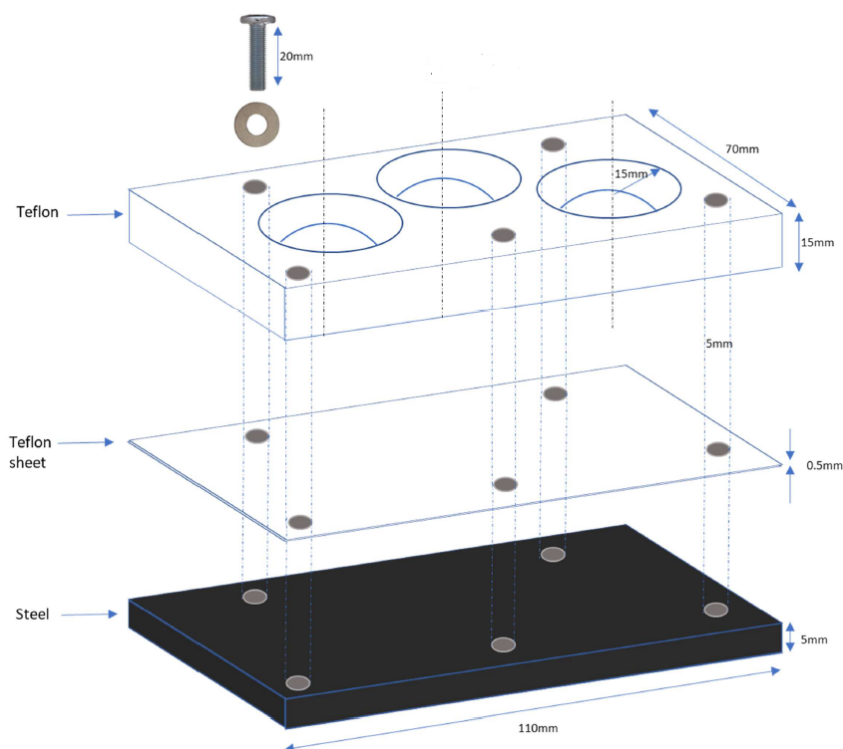


Figure S14. Mold designed to contain electrolyte formulation during photopolymerization.

4.3.4 UV Calibration

SOLIS 365 UV SOURCE (LED1)

The SOLIS 365 UV source from Thorlabs was employed for irradiation in the PTFE mold. This high-power LED source is centered at a 365 nm wavelength and delivered intense illumination (with a maximum power of 7.1 W when collimated through a $\text{\O} 48.3$ mm aperture). The emission spectrum was analyzed using a spectroradiometer, and the results of irradiance vs current were plotted in Figure S15a. For the experiment, the mold was positioned inside the UV-box (30 cm in height), as depicted in Figure S16. It is important to note that we have fitted the UV source with a convex lens diffuser for photopolymerization experiment carried out in Chapter 4. The emission spectrum with diffuser in place was analyzed using a spectroradiometer, and the results of irradiance vs current were plotted in Figure S15b.

Thorlabs mounted LED (M365L2) UV SOURCE (LED2)

To realize FTIR experiments within the capillary protocol, we use the LED 365 source equipped with an optic fiber. (\varnothing 5 mm and 1.2 m long). The results of irradiance vs current were plotted in Figure S15b.

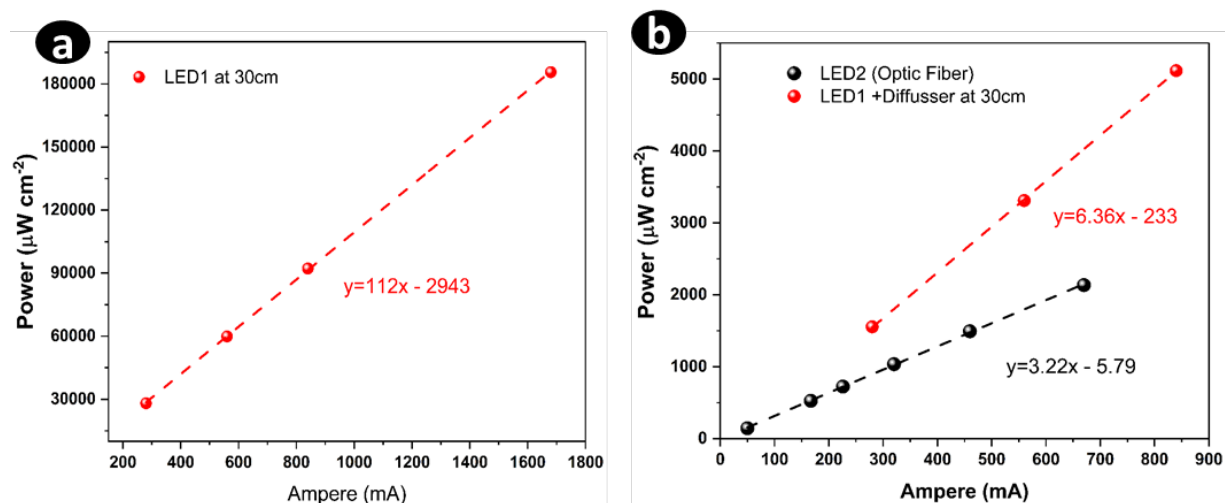


Figure S15. Irradiance vs current for a) SOLIS 365 UV source (LED1) at 30cm. b) SOLIS 365 UV source fitted convex diffuser at 30cm and LED2 (Optic fibre).

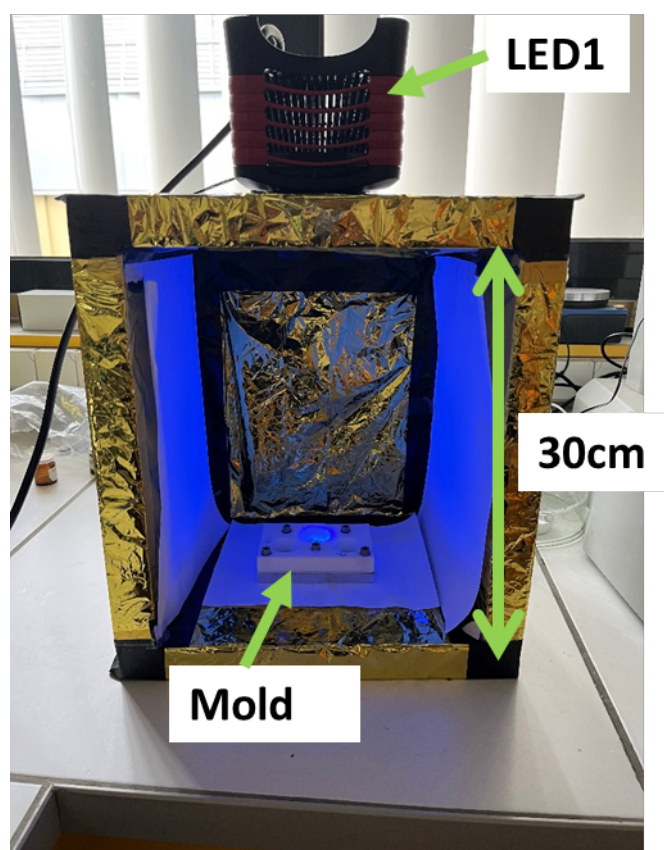


Figure S16. UV setup for photopolymerization

4.3.5 Fourier-Transform Infrared Spectroscopy

Real-time FT-IR spectroscopy was used to investigate the kinetic of photopolymerization of PPEGA in quartz capillary tube (2 mm thickness). The experiment was performed on a spectrometer (Thermo Scientific Nicolet iS50 FT-IR Spectrometer). After taking a background reading of the capillary tube, aliquot of polymerization resin was pipetted into the tube via a syringe. Polymerization was started by irradiating with a Thorlabs mounted LED (M365L2) ($\lambda_{\max} = 365$ nm, current = 659 mA, $I_0 = 2.1$ mW cm⁻²). Simultaneously, IR spectra were recorded for 400 s interval to determine the integral, $Int_{(6103 - 6245 \text{ cm}^{-1})}$ of the vinylic peak at 6103 – 6245 cm⁻¹. Each measurement included an average of 2 scans with a resolution of 8 cm⁻¹. Spectra were analysed using Omsec software. The conversion (X_{OEGA}) was calculated from equation S4.

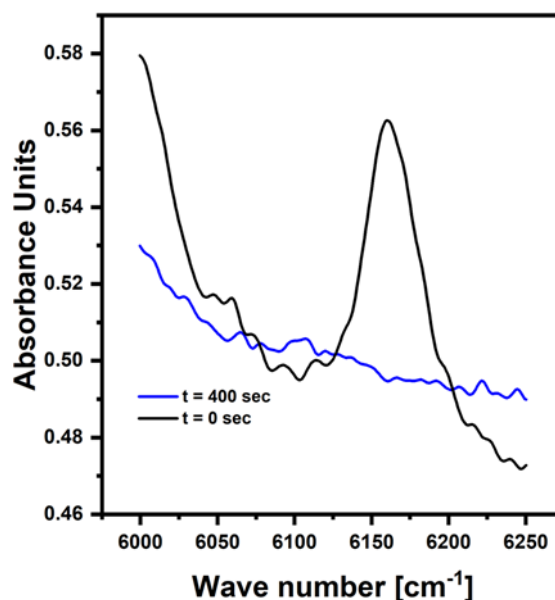


Figure S17. Representative FTIR spectra at the beginning ($t = 0$) and after 400 s of UV irradiation at 2.1 mW.cm⁻².

$$X_{OEGA} = \left[1 - \frac{Int_{(6103-6245)t}}{Int_{(6103-6245)t=0}} \right] \times 100 \quad \text{S4}$$

4.3.6 Small Angle X-ray Scattering (SAXS)

SAXS measurements were collected on the BL11 NCD-SWEET beamline at ALBA synchrotron facility using 0.99 Å X-ray wavelength, a 2.9 m sample-to-detector distance, and

standard data corrections. Scattering curves were plotted as a function of scattering vector $q = 4\pi \sin\theta/\lambda$, with measurements performed under vacuum at RT.

4.3.7 Transmission Electron Microscopy (TEM).

This experiment was performed in collaboration with Monika Król and Janne Ruokolainen at Aalto University in Finland. Samples were fixed directly to the pin without any previous heat treatment and microtomed at $-80\text{ }^{\circ}\text{C}$ on Leica EM UC7 Ultramicrotome, using Diatome 25° diamond knife. The sections were collected on 300 mesh Copper grid coated with lacey carbon. Subsequently, such prepared samples were submerged in liquid nitrogen and transferred onto Petri dish placed in the styrofoam box filled with dry ice, subsequently exposed to OsO_4 vapour for approximately 2 h. After staining, grids were cryo-transferred to the microscope. CryoTEM measurements were performed on Schottky field-emission cryo-electron microscope JEOL JEM-3200FSC at 300 kV accelerating voltage, while keeping the temperature of the examined specimen at $-187\text{ }^{\circ}\text{C}$. The micrographs were acquired in bright field mode using zero energy loss omega type filter with a slit width 20 eV and with slight under focus. Images were recorded via Gatan Ultrascan 4000 CCD camera.

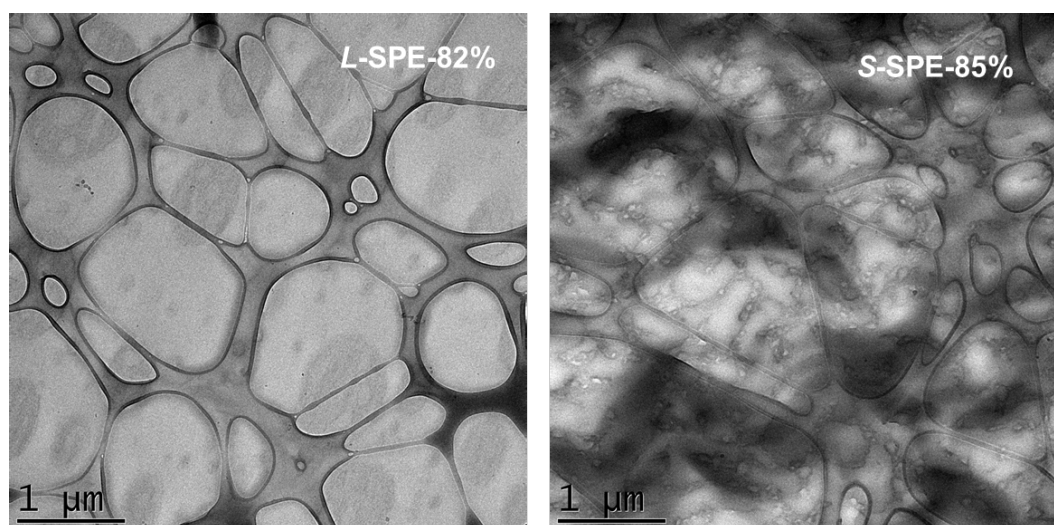


Figure S18. TEM images of L-SPE-82% and S-SPE-85%

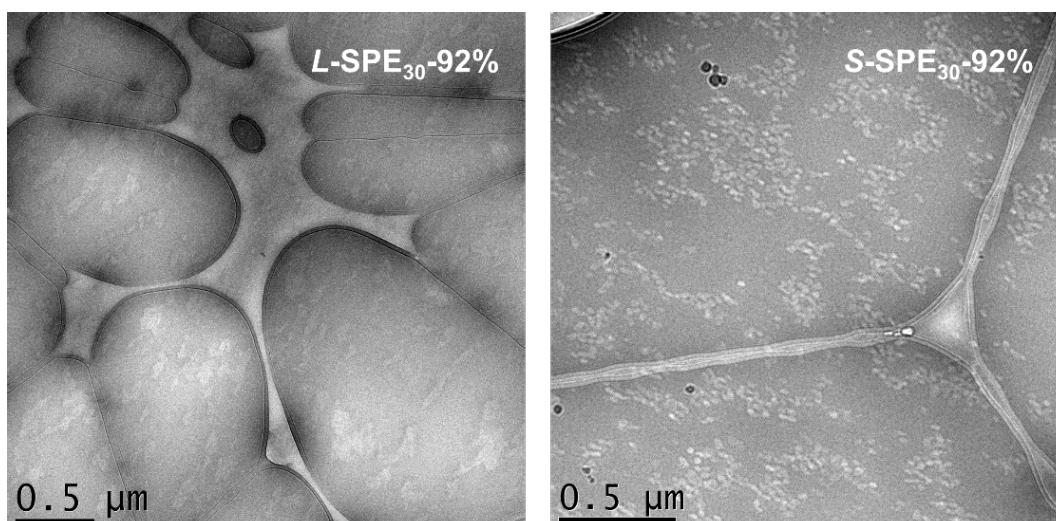


Figure S19. TEM images of L-SPE₃₀-92% and S-SPE₃₀-92%.

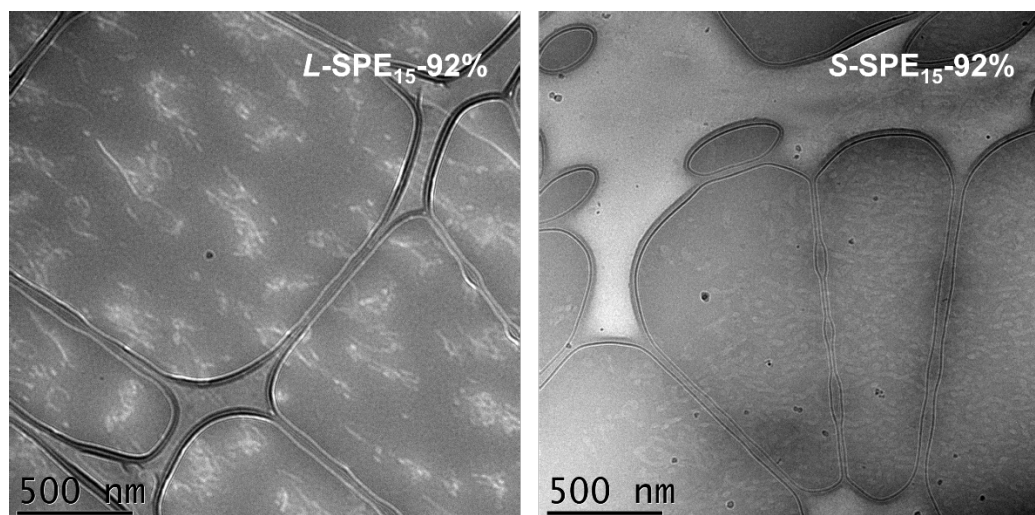


Figure S20. TEM images of L-SPE₁₅-92% and S-SPE₁₅-92%.

4.3.8 Differential Scanning Calorimetry (DSC).

DSC was performed using the Q100 from TA instruments under a N₂ atmosphere. For each sample, the temperature regime was initially stabilized at -90 °C for 5 min, heating and cooling was done within -80 and 120 °C with a rate of 5 °C min⁻¹. The heat capacity change in the second heating scan was used for the determination of the glass transition temperature (T_g).

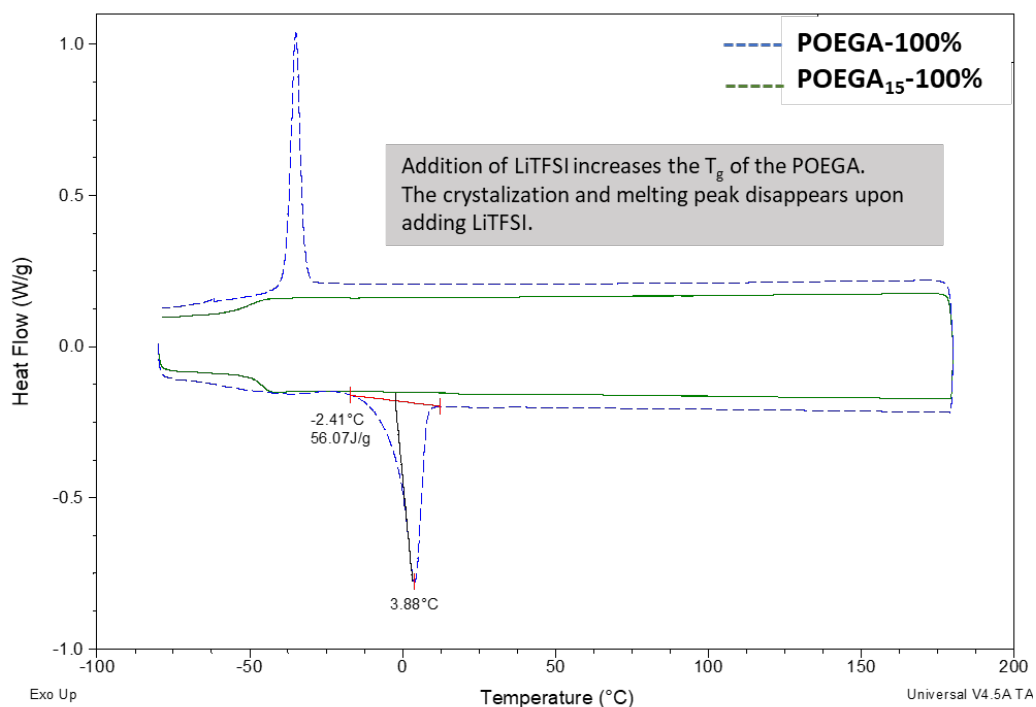


Figure S21. DSC of pristine photopolymerized POEGA polymer sample (POEGA-100%) and POEGA polymer sample with salt (POEGA₁₅-100%).

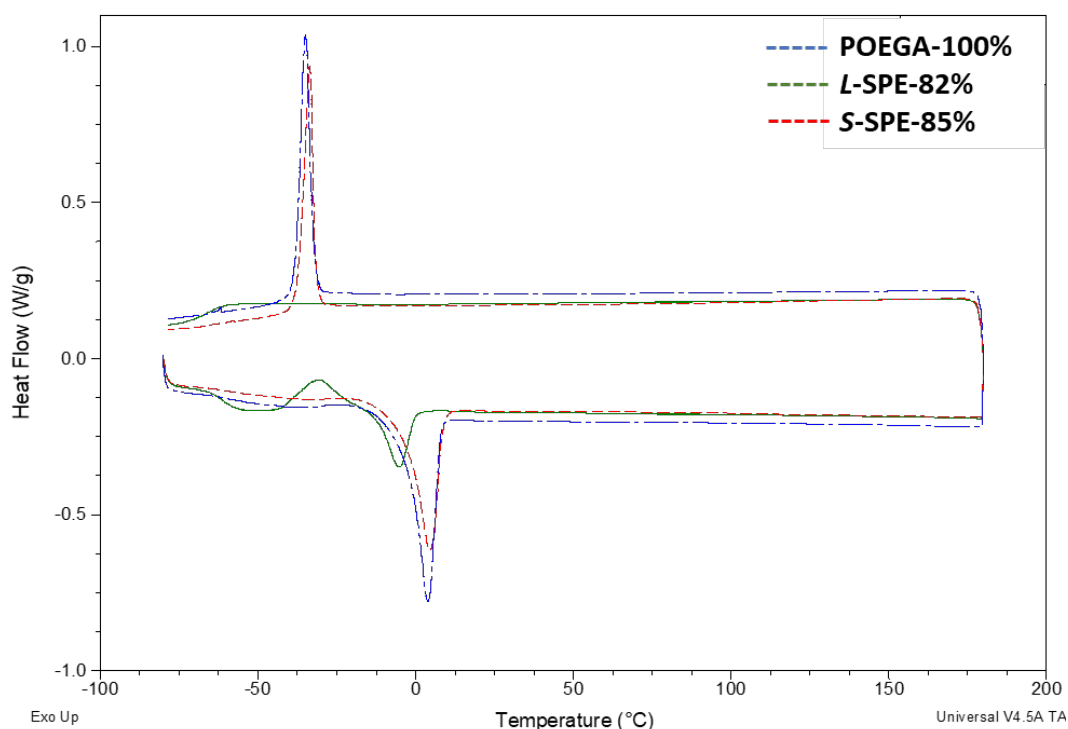


Figure S22. DSC of pristine photopolymerized POEGA polymer sample (POEGA-100%), POEGA polymer sample with linear comb BCP (L-SPE-82%) and POEGA polymer sample with star comb BCP (S-SPE-85%).

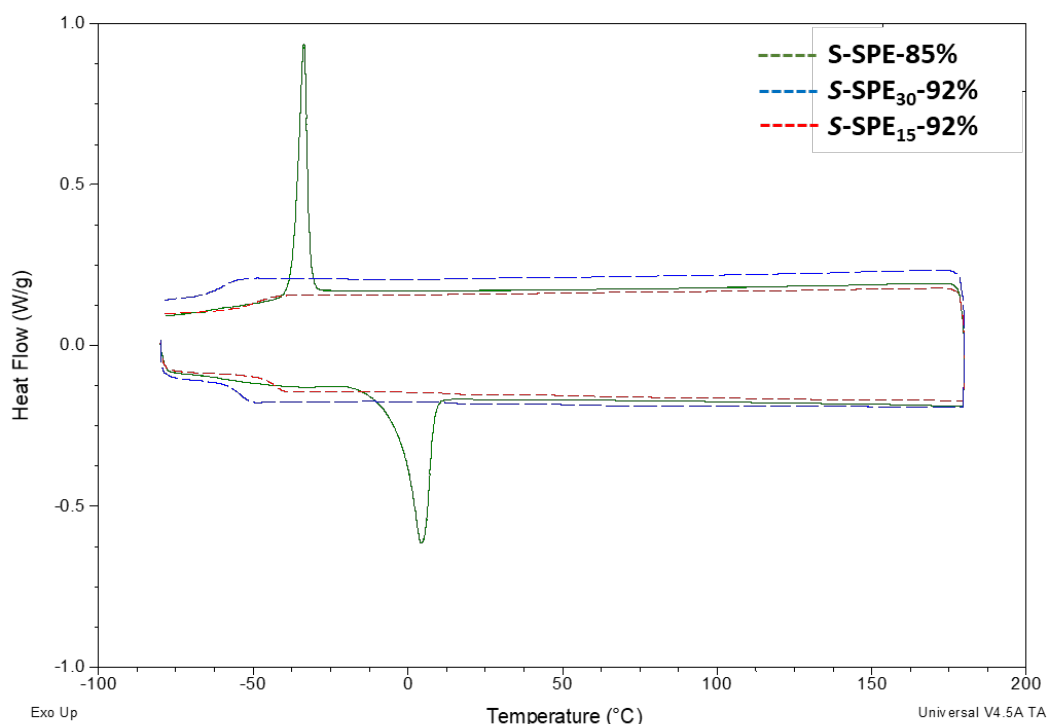


Figure S23. DSC of S-SPE-82%, S-SPE₃₀-92% and S-SPE₁₅-92%.

4.3.9 Rheological Characterization.

Rheology measurements were performed on Anton Paar modular compact rheometer (MCR-302) with a torque range from 0.5 nNm to 230 mNm and integrated active thermal management system. Sample was sandwiched between two 8 mm \varnothing parallel plate geometry at a constant shear stress of 25 Pa and a frequency of 5 Hz. The measurements were performed in temperature-controlled environment.

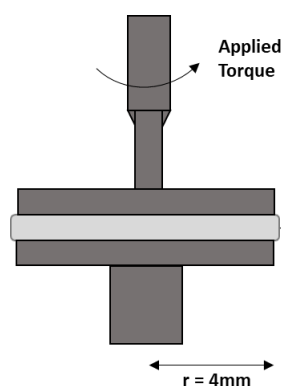


Figure S24. Setup of rheology experiment with parallel-plate geometry. The applied torque, $M = (\pi r^3 \tau)/2$ which is a function of the shear

4.3.10 Electrochemical Impedance Spectroscopy (EIS).

Free-standing BCPE films were previously dried in the vacuum oven for 24 h and stored in the glove box (see Figure S16). The films (8 mm ϕ , thickness, $L \approx 90 - 470 \mu\text{m}$) were sandwiched between two blocking gold electrodes plates in CESH-e (Enhanced Controlled Environment Sample Holder) cells (ϕ 6.35 mm) as shown in Figure S25. EIS measurement using Biologic Potentiostat (equipped with EC-Lab software package) at frequency from 1 Hz to 1 MHz with an oscillating voltage of 50 mV. Subsequently, these cells were preconditioned in a temperature chamber (Binder KB53, 230V 1~ 50Hz) for 2 h at 90 °C to anneal the films. After the preconditioning was finished, measurements were carried out by gradually decreasing the temperature in 20 °C steps from 90 °C to -10 °C with each temperature being maintained for 2 h to attain a thermal equilibrium. The ionic conductivity (σ ; S cm^{-1}) was determined by $\sigma = L/RA$ where R is the measured resistance, L is the film thickness and A is the area of the electrode.

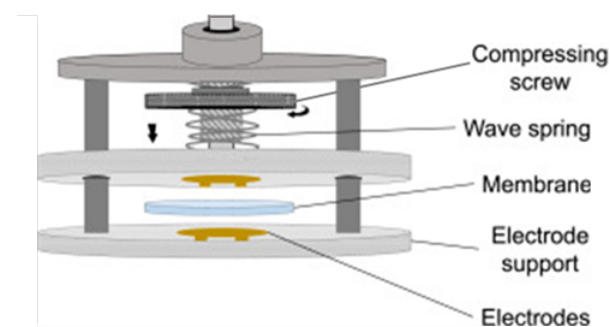


Figure S25. Typical CESH setup showing a sandwich of SPE between two blocking gold electrodes for EIS measurements of ionic resistance of the PE. The wave spring is designed to maintain a constant pressure during the experiment. Redrawn from literature.²²

5 References

1. Liu, Y.; Zhao, Y.; Lu, W.; Sun, L.; Lin, L.; Zheng, M.; Sun, X.; Xie, H., PEO based polymer in plastic crystal electrolytes for room temperature high-voltage lithium metal batteries. *Nano Energy* **2021**, *88*, 106205.
2. Mindemark, J.; Lacey, M. J.; Bowden, T.; Brandell, D., Beyond PEO—Alternative host materials for Li⁺-conducting solid polymer electrolytes. *Progress in Polymer Science* **2018**, *81*, 114-143.
3. Hallinan, D. T.; Mullin, S. A.; Stone, G. M.; Balsara, N. P., Lithium Metal Stability in Batteries with Block Copolymer Electrolytes. *Journal of The Electrochemical Society* **2013**, *160* (3), A464-A470.
4. Hashim, N. H. A. M.; Subban, R. H. Y., Studies on Conductivity, Structural and Thermal Properties of PEO-LiTFSI Polymer Electrolytes Doped with EMImTFSI Ionic Liquid. *AIP Conference Proceedings* **2018**, *2031* (1), 0200211 - 0200216.
5. Phan, T. N. T.; Issa, S.; Gignes, D., Poly(ethylene oxide)-Based Block Copolymer Electrolytes for Lithium Metal Batteries. *Polymer International* **2019**, *68* (1), 7-13.
6. Choi, Y. K.; Bae, Y. H.; Kim, S. W., Star-Shaped Poly(ether-ester) Block Copolymers: Synthesis, Characterization, and Their Physical Properties. *Macromolecules* **1998**, *31* (25), 8766-8774.
7. Croce, F.; Appetecchi, G. B.; Persi, L.; Scrosati, B., Nanocomposite Polymer Electrolytes for Lithium Batteries. *Nature* **1998**, *394* (6692), 456-458.
8. Li, Y.-J.; Fan, C.-Y.; Zhang, J.-P.; Wu, X.-L., A promising PMHS/PEO blend polymer electrolyte for all-solid-state lithium ion batteries. *Dalton Transactions* **2018**, *47* (42), 14932-14937.
9. Zhu, P.; Yan, C.; Dirican, M.; Zhu, J.; Zang, J.; Selvan, R. K.; Chung, C.-C.; Jia, H.; Li, Y.; Kiyak, Y.; Wu, N.; Zhang, X., Li_{0.33}La_{0.557}TiO₃ ceramic nanofiber-enhanced polyethylene oxide-based composite polymer electrolytes for all-solid-state lithium batteries. *Journal of Materials Chemistry A* **2018**, *6* (10), 4279-4285.
10. Butzelaar, A. J.; Liu, K. L.; Röring, P.; Brunklaus, G.; Winter, M.; Theato, P., A Systematic Study of Vinyl Ether-Based Poly(Ethylene Oxide) Side-Chain Polymer Electrolytes. *ACS Applied Polymer Materials* **2021**, *3* (3), 1573-1582.
11. Bakar, R.; Darvishi, S.; Aydemir, U.; Yahsi, U.; Tav, C.; Menciloglu, Y. Z.; Senses, E., Decoding Polymer Architecture Effect on Ion Clustering, Chain Dynamics, and Ionic Conductivity in Polymer Electrolytes. *ACS Applied Energy Materials* **2023**, *6* (7), 4053-4064.
12. Xin, C.; Wen, K.; Guan, S.; Xue, C.; Wu, X.; Li, L.; Nan, C.-W., A Cross-Linked Poly(Ethylene Oxide)-Based Electrolyte for All-Solid-State Lithium Metal Batteries With Long Cycling Stability. *Frontiers in Materials* **2022**, *9*.
13. Young, W.-S.; Epps, T. H., Ionic Conductivities of Block Copolymer Electrolytes with Various Conducting Pathways: Sample Preparation and Processing Considerations. *Macromolecules* **2012**, *45* (11), 4689-4697.
14. Pascassio-comte, X. Mise au point d'un nouvel encapsulant photo-réticulable sur base copolymère à blocs. UNIVERSITE DE PAU ET DES PAYS DE L'ADOUR, Pau, 2016.
15. Aniagbaoso, K. I.; Król, M.; Ruokolainen, J.; Bousquet, A.; Save, M.; Rubatat, L., Improved Solid Electrolyte Conductivity via Macromolecular Self-Assembly: From Linear to Star Comb-like P(S-co-BzMA)-b-POEGA Block Copolymers. *ACS Applied Materials & Interfaces* **2023**, *15* (12), 15998-16008.

16. Simone, P. M.; Lodge, T. P., Phase Behavior and Ionic Conductivity of Concentrated Solutions of Polystyrene-Poly(ethylene oxide) Diblock Copolymers in an Ionic Liquid. *ACS Applied Materials & Interfaces* **2009**, *1* (12), 2812-2820.
17. Zhang, S.; Lee, K. H.; Frisbie, C. D.; Lodge, T. P., Ionic Conductivity, Capacitance, and Viscoelastic Properties of Block Copolymer-Based Ion Gels. *Macromolecules* **2011**, *44* (4), 940-949.
18. Kotlarchyk, M.; Chen, S. H., Analysis of small angle neutron scattering spectra from polydisperse interacting colloids. *The Journal of Chemical Physics* **1983**, *79* (5), 2461-2469.
19. Ma, S.; Jiang, M.; Tao, P.; Song, C.; Wu, J.; Wang, J.; Deng, T.; Shang, W., Temperature effect and thermal impact in lithium-ion batteries: A review. *Progress in Natural Science: Materials International* **2018**, *28* (6), 653-666.
20. Gray, F.; Armand, M., Polymer Electrolytes. In *Handbook of Battery Materials*, 2011; pp 627-656.
21. Brooks, D. J.; Merinov, B. V.; Goddard, W. A., III; Kozinsky, B.; Mailoa, J., Atomistic Description of Ionic Diffusion in PEO–LiTFSI: Effect of Temperature, Molecular Weight, and Ionic Concentration. *Macromolecules* **2018**, *51* (21), 8987-8995.
22. Díaz, J. C.; Kamcev, J., Ionic conductivity of ion-exchange membranes: Measurement techniques and salt concentration dependence. *Journal of Membrane Science* **2021**, *618*, 118718.



Chapter 4

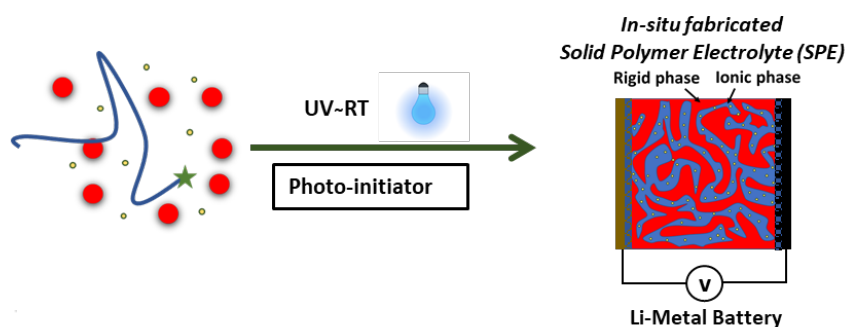
Photo-Polymerization-Induced Microphase Separation to Design Solid Polymer Electrolyte for Lithium Metal Batteries



Synopsis

In this study, we utilized photopolymerization-induced microphase separation (PIMS) process with UV-lamp to fabricate a flexible comblike poly(ethylene oxide) (PEO)-based nanostructured solid polymer electrolyte (SPE), which was applied here for all-solid-state lithium metal battery (LMB). The uniqueness of this one-pot fabrication process lies in its capacity to enhance the interfacial properties within LMBs by rendering the nanostructuring of SPE in-situ on electrodes, and the ability to customize the structural dimensions of conducting domains by tweaking macromolecular architecture and composition.

Bi-continuous nanoscale domains of soft poly(styrene-co-oligo ethylene glycol methyl methacrylate)/Propylene carbonate/Lithium bis(trifluoromethanesulfonyl)imide phase and hard P(isobornyl acrylate-stat- oligo ethylene glycol diacrylate) phase furnished the SPE with high ionic conductivity (0.34 mS cm^{-1} at $30 \text{ }^\circ\text{C}$) and enhanced mechanical strength ($10^6 - 10^7 \text{ Pa}$ at $30 \text{ }^\circ\text{C}$) respectively. The as prepared SPE showed good electrochemical properties with lithium transference number of 0.28 ± 0.03 , electrochemical stability window of about 4.2 V vs. Li^+/Li and low interfacial resistance. This electrolyte enables the $\text{Li}/\text{SPE}/\text{Li}$ symmetric cell to cycle over 350h at 0.1 mAcm^{-2} without evidence of dendrite formation. By means of galvanostatic cycling studies in $d\text{-Li}||d\text{-NMC811}$ and $d\text{-Li}||d\text{-LiFePO}_4$ cells, we further demonstrate that the SPE exhibited good cycling performance up to 50 cycles. This work shows that PIMS process could be a promising method of fabrication of advanced solid polymer electrolytes for more efficient, reliable and safer lithium metal batteries.



The majority of electrolyte testing in batteries were carried during my 2-month research secondment under the supervision of Dr. Jan Bitenc at the National Institute of Chemistry, Ljubljana in Slovenia. SAXS experiments were performed at ALBA synchrotron Barcelona, Spain.

Table of Contents

1	Introduction	150
2	Results and Discussion	153
2.1	Synthesis of ion-conductive precursor, a P(S-co-OEGMA) macroCTA.....	153
2.2	Formulation of electrolytes.....	155
2.3	Kinetics of Microphase Separation.....	160
2.4	Morphological study of solid electrolytes	167
2.5	Electrochemical and Mechanical Properties of Fabricated Solid Electrolytes	172
2.6	Cell Performance	175
3	Conclusion	184
4	Supporting Information	185
4.1.1	Materials.....	185
4.1.2	Synthesis of linear and star comb of P(S-co-OEGMA) macroCTA.	185
4.1.3	NMR analysis for monomer conversion	186
4.1.4	Size Exclusion Chromatography – Multi-Angle Laser Light Scattering (SEC-MALLS). 189	
4.1.5	UV-Visible spectrometer.....	190
4.1.6	Fabrication of Solid Polymer Films by UV Photopolymerization.....	191
4.1.7	Fourier-Transform Infrared Spectroscopy (FTIR)	191
4.1.8	Small Angle X-ray Scattering (SAXS)	193
4.1.9	Atomic Force Microscope (AFM).....	195
4.1.10	Scanning Electron Microscope (SEM)/ Energy Dispersive X-Ray spectroscopy (EDS) 195	
4.1.11	Electrochemical Impedance Spectroscopy (EIS)	195
4.1.12	Rheology measurements	196
4.1.13	Cathodes Fabrication.....	197
4.1.14	Development of cathode.....	198
4.1.15	Development of Lithium Metal anode	198
4.1.16	Transference Number Measurement	198
4.1.17	Lithium Plating and Stripping:.....	199
4.1.18	Electrochemical window	199
4.1.19	Galvanostatic Charging and Discharging:.....	200
5	References	200

1 Introduction

Lithium metal batteries (LMBs) have emerged as a highly desirable energy storage option.¹ However, the widespread use of LMBs is currently hindered by challenges such as the high chemical reactivity of Lithium metal that can cause uncontrolled parasitic side reactions with the liquid electrolytes (LEs), uneven deposition of lithium and the formation of dendrites on the lithium metal anode, which can cause short circuits.^{2, 3} To overcome these issues and harness the potential benefits of LMBs, researchers are looking to avoid the use of traditional LEs. One alternative are solid polymer electrolytes (SPEs), which offer increased safety, mechanical stability and flexibility, better resistance to dendrite growth as well as improved resistance to temperature and pressure.⁴ Moreover, dissolution of cathode active material (transition metal ions) in liquid electrolytes during cycling is another existing problem responsible for quick aging and capacity fading in LMBs, further highlighting the need of SPEs.⁵

The key challenge of designing high performing SPEs is that mechanical properties and ionic conductivity exists in a duality; efforts to optimize either one of the properties would trade off the other.^{6, 7} Therefore, it is necessary to decouple the mechanical properties of SPEs from their ionic conductivity. Standalone block copolymer electrolytes (BCPEs) have been employed as SPE in solid state batteries to leverage the synergistic effect of mechanical and conductive properties of the individual blocks.^{3, 8-11} Although, such BCPEs can self-assemble into various morphologies with well-defined domain sizes and spacing, the conductivity of these electrolytes is often compromised by network defects (e.g., dead ends at grain boundaries) which interrupts the conducting pathways.^{12, 13} Moreover, typical 2D-connected morphologies (lamellar or hexagonal) of conventional BCPEs have been reported to be more sensitive to preparation and processing effects.¹⁴ 3D double gyroids phase are less sensitive to preparation effect¹⁴ but their range of volume fraction in the phase diagram is very limited.¹⁵ To make solid-state energy storage devices practical, researchers need to find new ways to produce and fabricate scalable nanostructured solid-state electrolytes that can simultaneously provide high ionic conductivity and robust mechanical performances. In this context, polymerization induced microphase separation (PIMS) is explored to prepare SPEs with 3D bi-continuous network structure.¹⁶ The technique involves the chain extension of macro-chain transfer agent

(macroCTA) with a second chemically distinct polymer segments, through a controlled polymerization process (and in some cases crosslinking).^{17, 18}

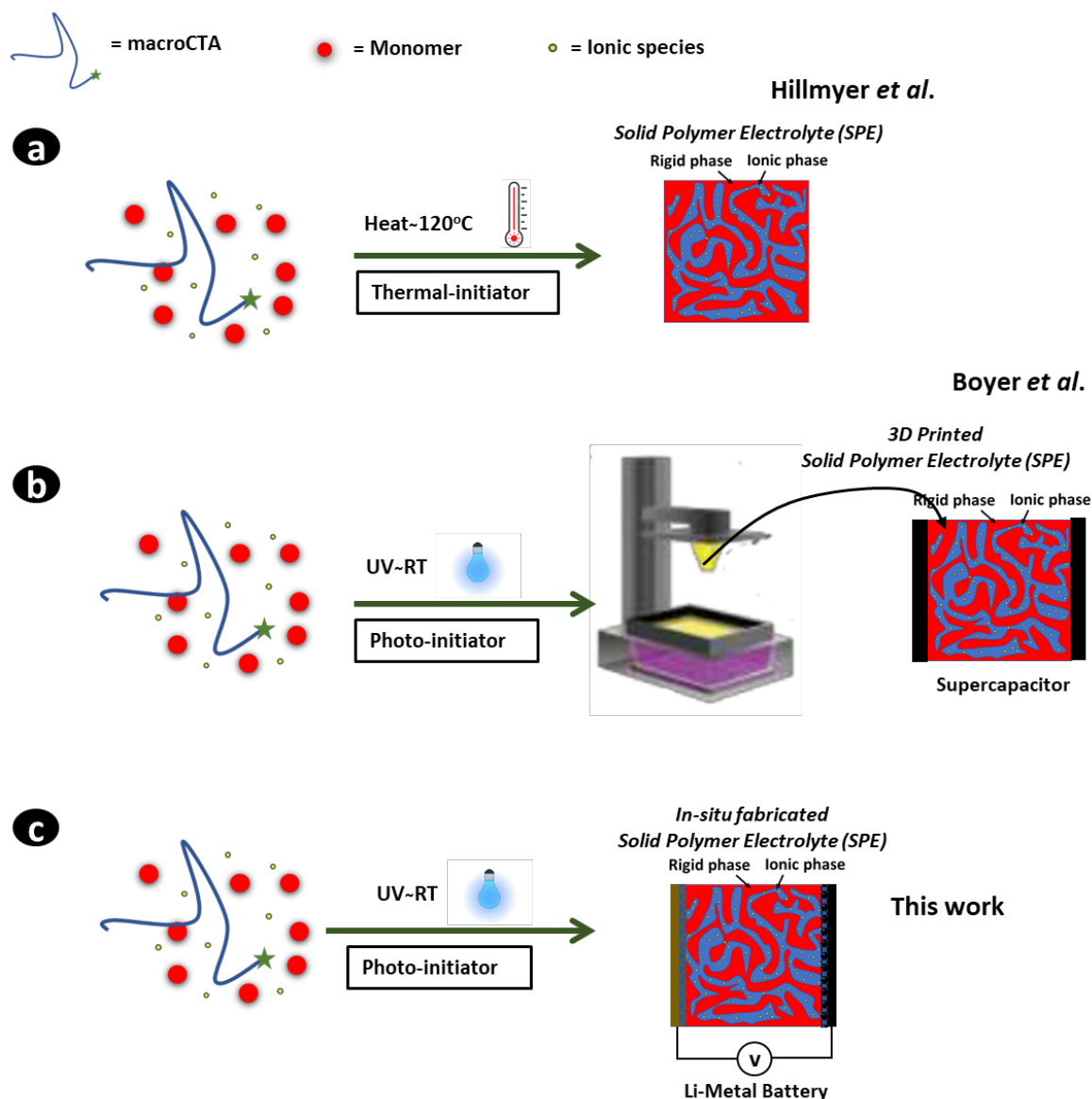


Figure 1. Schematic illustration highlighting the novelty of this work in comparison to previously reported SPEs fabricated from the PIMS process. a) Works done by Hillmyer *et al.* utilizing PEO-TTC as macroCTA, Styrene/divinyl benzene monomers and BMITFSI/LiTFSI as ionic species^{16, 19, 20} b) Works done by Boyer *et al.* utilizing PEO-TTC (star and linear) or POEGMA-TTC as macroCTA, Isobornyl Acrylate/ trimethyl propane triacrylate monomers and BMITFSI as ionic species to print solid electrolytes for supercapacitors^{21, 22} c) Present work utilizing linear and star POEGMA-TTC as macroCTA, Isobornyl Acrylate/Oligo(ethylene glycol diacrylate) monomers and LITFSI/PC as ionic species to fabricate solid electrolytes for lithium metal batteries.

A macroCTA, synthesized through reversible deactivation radical polymerization (RDRP), typically using reversible addition-fragmentation transfer polymerization (RAFT), is a reactive

block with chain end functionality capable of extending the polymerization of a second monomer through RAFT polymerization. A few studies reported on fabrication of SPE by PIMS process, employing initiators activated through either thermal dissociation of radical initiator in reversible addition fragmentation transfer (RAFT) polymerization (thermal-RAFT) or photo-initiated RAFT polymerization by using photoinitiator (photo-RAFT).^{16, 19-25}

A seminal work by Hillmyer and Lodge serves as an early example, outlining the utilization of PIMS through reversible addition-fragmentation chain transfer initiated by a thermally activated benzoyl peroxide initiator.¹⁶ Starting with a mixture of styrene/divinyl benzene monomer, 1-butyl-3-methylimidazolium bis(trifluoromethylsulfonyl)imide (BMITFSI) ionic liquid (IL), lithium bis(trifluoromethanesulfonyl)imide (LiTFSI) salt and poly(ethylene oxide) with trithiocarbonate chain end (PEO-TTC) serving as a macroCTA (refer to Figure 1a), they achieved a bi-continuous network comprising a crosslinked polystyrene rigid phase alongside an ion-conducting PEO/ionic moieties phase (IL/LiTFSI) after the PIMS protocol. Resulting SPEs showed ionic conductivities of ~ 0.6 mS/cm at room temperature, while maintaining an elastic modulus nearly 1 GPa. In a related work, they utilized protic IL as the ionic specie to underscore the potential applicability of these fabricated SPEs in fuel cells.²⁰ Subsequently, their research delved into the utilization of succinonitrile (SN) as a plasticizer and LiTFSI salt as the ionic species.¹⁹ This approach rendered the PEO-based conducting channels entirely amorphous, facilitating facile ion transport with a conductivity of around 0.35 mS/cm and an elastic modulus of ~ 0.3 GPa at 30°C.

However, the formation of this nanostructure required high temperatures (> 100 °C) and long curing time (> 12 h). Boyer *et al.* first reported the fabrication of nanostructured polymer electrolytes by 3D printing (refer to Figure 1b).²² Their work harnessed photo-RAFT for PEO-TTC (with trithiocarbonate functions) chain extension within a mixture of BMITFSI ionic liquid, Isobornyl acrylate (IBoA) monomer and trimethylpropane triacrylate (TMPTA) crosslinker. This process yielded a so-called bi-continuous phase of poly(ethylene oxide)-*block*-poly(isobornyl acrylate-*stat*-trimethyl propane triacrylate), PEO-*b*-P(IBoA-*stat*-TMPTA) characterized by ionic conductivities ($\text{BMI}^+/\text{TFSI}^-$) up to 0.3 mS/cm at room temperature and storage modulus $G' > 200$ MPa. By demonstrating the practicality of the SPEs in symmetric carbon supercapacitor, their work unveils a new paradigm for the modular on-demand design of SPEs with printed tailored dimensions. In another work, they reported on the

use of non-crystalline POEGMA-TTC as macroCTA to replace semi-crystalline PEO-TTC to improve macromolecular chain dynamics at room temperature.²¹

Despite the promising prospects of PIMS fabrication method, the resulting SPEs have not yet been practically demonstrated in solid-state lithium batteries (SSLBs). Indeed, the solubilization of the starting resin components is a difficult task, which is why the majority of resins used for SPEs designed by PIMS reported use of solvent or ionic liquids (IL). However, it is worth noting that IL-based electrolytes exhibit limited ion transport properties.²⁶ Although, increasing salt concentration in IL-based electrolytes can enhance ion transport, it also results in increased viscosity.^{27, 28} Another general challenge is the engineering issues associated with implementation of the SPEs in SSLBs such as contact loss between battery components, microstructural cracking of electrodes upon repeated cycles of lithiation/de-lithiation to mention a few.²⁹ Certain studies have shown that in-situ polymerization on electrodes is one of the strategies employed to address interfacial issues in batteries.³⁰⁻³²

The aim of this work is to design SPEs via PIMS fabrication process that can reach implementation in LMBs as shown in Figure 1c. The body of work is organized as follows. First of all, we undertook the synthesis of linear and star comb-like ion-conductive polymers which will serve as a base to our electrolyte formulation. Then the electrolyte formulation is submitted to photo-PIMS. The PIMS process is monitored by synchrotron-based scattering techniques to witness the formation of rigid and soft microphases. Effects of macroCTA architecture, molar mass as well as UV intensity on kinetics of phase separation are discussed from the viewpoint of systems with competing interactions. Inherent morphologies, mechanical properties and ion conductivity of fabricated SPEs were studied by small angle x-ray scattering (SAXS), rheology measurements and electrochemical impedance spectroscopy (EIS) respectively. Finally, the SPE was incorporated into the half-cell manufacturing, involving $Li || LiN_{0.8}M_{0.1}C_{0.1}O_2$ and $Li || LiFePO_4$ configurations, achieved through the in-situ photopolymerization of designed formulation.

2 Results and Discussion

2.1 Synthesis of ion-conductive precursor, a P(S-co-OEGMA) macroCTA

Linear comb-like (R_I) and star comb-like (R_A) P(S-co-OEGMA) polymers were synthesized from monofunctional chain transfer agent (4-cyano 4-[(dodecylsulfanylthiocarbonyl)-

sulfanyl]-pentanoic acid) and tetra functional chain transfer agent (CTA) (Pentaerythritol tetrakis[2-(dodecylthiocarbonothioylthio)-2-methylpropionate) respectively, as shown in Figure S23 (§4 Supporting Information). The different P(S-co-OEGMA) copolymers were synthesized via RAFT polymerization of oligo (ethylene glycol) methyl ether methacrylate (OEGMA, $DP_{EO} = 8-9$) using 2,2'-azobisisobutyronitrile as thermal initiator and addition of 6 mol% of styrene (S) to achieve control of OEGMA methacrylate monomer from the commercial tetra functional chain transfer agent, as previously reported for methacrylate monomers in chapter 2.³³ The weight fraction of OEGMA in copolymer was derived from the molar fraction of OEGMA calculated from the integrals of proton nuclear magnetic resonance (¹H NMR) signals (see Equation S5, Equation S6 and Figure S24 in SI). NMR results indicate that the polymers contain ~ 2 wt% of styrene. The number-average molar mass ($M_{n,SEC}$) and dispersity (D) of the synthesized polymers were determined by multi-detection size exclusion chromatography (SEC) (see Table 1 and Figure S26). With molar masses of 144 kg mol⁻¹ and 39 kg mol⁻¹ respectively for R_4 and R_1 macroCTAs, R_1 can be reasonably considered as macromolecular analogues of a single branch of R_4 . In an auxiliary experiment to understand the influence of molar mass on star comb macroCTA, a lower molar mass, R_4^* (62 kg mol⁻¹) was synthesized by solution polymerization in 50/50 w/w 1,4-dioxane. Note that D is reduced to 1.2 for polymerization in dioxane compared to the one of bulk polymerization. Synthesis of star polymer in bulk polymerization induced higher monomer conversion so a higher molar mass along with an increase of dispersity (Table 1). UV-Vis experiment (refer to Figure S27) confirmed the chain end fidelity of the linear and star comb macroCTA with average 1 TTC and at least 3 TTC group retained per chain, respectively (see Table 1). As such they are called in the rest of the document P(S-co-OEGMA) macroCTA for macromolecular chain transfer agent.

Table 1. Characterization of linear (R_1) and star (R_4 and R_4^*) comb-like P(S-co-OEGMA) macroCTA. Refer to **Table S4** for more information.

macroCTA	Exp	$F_{POEGMA}^a)$	$W_{POEGMA}^b)$	$M_{n,theo}^c)$ (kg/mol)	$M_{n,SEC}$ (kg/mol)	D	$X_n^{d)}$	$N_{TTC/chain}^e)$
R_1	KA143	0.90	0.98	24	39	1.48	79	1.3
R_4	KA149	0.91	0.98	113	144	1.37	293	3.7
$R_4^{*f)}$	KA250	0.82	0.96	44	62	1.19	128	3.3

^{a)} F_{OEGMA} is the molar fraction of OEGMA in the copolymer after purification determined from ¹H NMR (See Equation S5 in SI).

^{b)} W_{OEGMA} (See Equation S6) is the weight fraction of OEGMA in the copolymer after purification.

^{c)} $M_{n,theo}$ is calculated from Eq. S8 in SI.

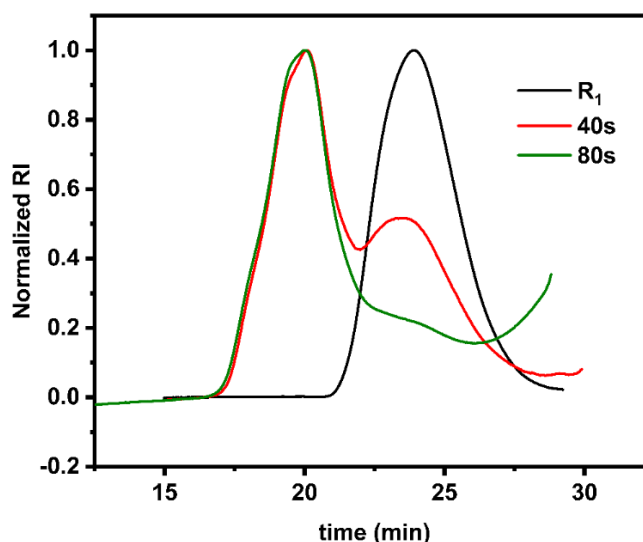
^{d)} X_n is calculated from Eq. S10 in SI.

^{e)} Number of TTC group per chain measured by UV-visible spectroscopy in cuvette (see equation S10).

^{f)} Synthesis performed by solution polymerization (50:50 wt/wt 1,4-dioxane: Styrene + OEGMA) rather than bulk polymerization.

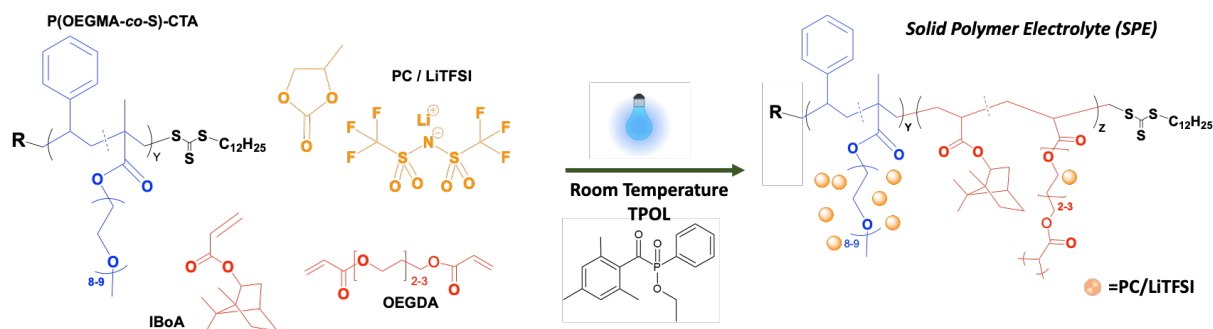
The presence of TTC end function on the chains conferred to the polymers the possibility to undergo a subsequent chain-extension by RAFT polymerization of a second monomer to form a block copolymer. This can be performed by merely photo-initiated RAFT polymerization. To demonstrate the chain extension of macroCTA, resin formulation prepared (without OEGDA crosslinker) with 34 wt% R₁, 66 wt% IBoA and [TTC]/[TPO-L] = 2. The SEC traces shown in Figure 3 are qualitatively indicative of the molecular weight increases at early times ($t = 40$ s and $t = 80$ s) due to chain extension of R₁ macroCTA. The isolated solid at $t = 40$ s contained 10% gel content already. As $t = 80$ s, the gel content increased drastically, and samples could barely be redissolved in THF for SEC analysis.

Figure 2. Time evolution of chromatogram to illustrate the utility of R₁ macroCTA in the controlled growth of linear of a P(S-*co*-OEGMA)-*b*-PIBoA diblock in the absence of cross-linker.



2.2 Formulation of electrolytes.

Photoactive electrolyte resins were formulated using the synthesized P(S-*co*-OEGMA) as macroCTA, ethyl phenyl(2,4,6-trimethylbenzoyl) phosphinate (TPO-L) as photoinitiator, isobornyl acrylate (IBoA) as monomer, oligo(ethylene glycol diacrylate) (OEGDA, DP_{EO} = 2-3, Mn = 250 g.mol⁻¹) as cross-linker, and a solution of lithium bis(trifluoromethanesulfonyl)imide (LiTFSI) salt in propylene carbonate (PC) solvent (50/50 wt/wt, 4 mol L⁻¹). For all resins, the [TTC]/[TPO-L] and [IBoA]/[OEGDA] molar ratios were kept constant as 2 and 4 respectively. The architecture and quantity of macroCTA in the resins were varied for comparison (see Table 2).



Scheme 1. Reaction scheme describing the elaboration of SPE by photo initiated PIMS.

The SPE(R_x -Y) nomenclature employed to name the different samples (Table 2) follows a specific pattern. SPE state for solid polyelectrolyte, the x subscript of R_x indicates the type of macroCCTA, either linear comb-like (R_1) or star comb-like (R_4) P(OEGMA-co-S) statistical copolymer, respectively. Y represents the weight percentage of macroCCTA ($Wt_{\text{macroCCTA}}$). As an example, SPE(R_4 -34) signifies a resin containing 34 wt% of star comb-like macroCCTA compared to the overall mass of iBoA, OEGDA and macroCCTA. Reactive resins were prepared according to recipes described in Table 2. They vary mainly from two main parameters, the weight fraction of macroCCTA ranging from 24 to 44 wt% and the topology of macroCCTA (linear comb-like versus star comb-like copolymer). It should be noted that both molar ratio of [EO]/[LiTFSi] and [PC]/[LiTFSi] were set constant at a value of 5 and 2.8 respectively. [EO] corresponds to the concentration of ethylene glycol units from OEGMA and OEGDA monomer units.

The use of OEGMA for the synthesis of the first reactive block in this chapter was preferred as polymerization of methacrylate monomers is less prone to irreversible transfer reaction and branching compared to acrylate monomers (like OEGA in Chapter 2). Indeed, control of polymerization for the synthesis of the first block is required to synthesize a reactive polymer with living trithiocarbonate chain end.

The selection of iBoA as the monomer was based on its relatively high hydrophobicity and a high glass transition temperature of PIBoA ($T_g > 70^\circ\text{C}$). This monomer is suitable for photo RAFT polymerization as acrylate monomers exhibiting higher polymerization rate constant compared to methacrylate, they are less inhibited by oxygen in fast photopolymerization process.^{22, 34} A crosslinker (OEGDA) was incorporated to provide the SPE with a decent level of rigidity. Therefore, OEGDA is herein regarded as part of the hard phase despite having 2-3 ethylene oxide (EO) units capable of ionic conduction (refer to **Scheme 1**). LiTFSi was added in the initial electrolyte formulation prior to polymerization to facilitate lithium-ion conduction.

However, it reduces solubility of the macroCTA in monomer. Therefore, PC was chosen as solvent to provide a homogeneous formulation. The choice of solvent was based on the fact that PC possesses a high ability to solubilize lithium salts, high dielectric constant, wide liquid range (melting point = -48.8 to boiling point = 242 °C).³⁵⁻³⁷

Table 2. Formulation of electrolyte resins. Conversion was determined on fabricated films using equation S15 and exceeded 94%.

CODE	Type of macroCTA	Mass of resin component (g)							DP^a	$Wt_{macroCTA}^b$ (%)	Wt_{ionic}^c (%)	Wt_{PC}^d (%)
		macroCTA	IBoA	OEGDA	LiTFSi	PC						
KA219	SPE(R_1 -24)	R_1	0.79	2.05	0.57	1.07	1.07	475	24	40	20.5	
KA224	SPE(R_1 -34)	R_1	0.74	1.13	0.32	0.89	0.89	287	34	46	23.0	
KA221	SPE(R_1 -44)	R_1	1.20	1.20	0.35	1.35	1.35	191	44	50	25.1	
KA225	SPE(R_4 -24)	R_4	0.89	2.3	0.64	1.17	1.17	2066	24	40	20.0	
KA226	SPE(R_4 -34)	R_4	1.09	1.7	0.49	1.32	1.32	1300	34	46	23.0	
KA230	SPE(R_4 -44)	R_4	0.57	0.57	0.16	0.65	0.65	829	44	50	25.1	
KA253	SPE(R_4^* -24)	R_4^*	0.55	1.50	0.43	0.80	0.80	965	24	40	20.0	
KA254	SPE(R_4^* -34)	R_4^*	0.70	1.10	0.33	0.85	0.85	578	34	44	22.0	
KA255	SPE(R_4^* -44)	R_4^*	0.65	0.59	0.186	0.73	0.74	356	44	50	25.1	

^{a)} Dp represents the ratio of IBoA and OEGDA monomer calculated as $[IBoA+OEGDA]/[macroCTA]$.

^{b)} $Wt_{macroCTA}$ represents the weight percent of macroCTA calculated from equation S11.

^{c)} Wt_{ionic} represents the weight percent of ionic solution (LiTFSI + PC) according to equation S12.

^{d)} Wt_{PC} represents the weight percent of propylene carbonate in the initial formulation calculated from equation S13.

Note: $[EO]/[LiTFSi]$ and $[PC]/[LiTFSi]$ were set constant at a value of 5 and 2.8 respectively. While $[TTC]/[TPOL] = 2$ and $[IBoA]/[OEGDA] = 4$ for all resins

Moreover, PC-based electrolytes has been reported to have better stability (less electrolyte decomposition) at a critical LiFSI–salt concentration threshold of 3 mol L^{-1} or solvent-to-salt molar ratio (MR) of 2:1, above which the electrolyte decomposition is suppressed.³⁷ Therefore, we pegged our PC:LiTFSI concentration at (50/50 wt/wt, 4 mol L^{-1} , MR 2.8:1).

Higher retardation and longer inhibition period were observed for polymerization kinetics of SPE(R_4 -34) experiment studied by real-time FTIR spectroscopy compared to the analogue photopolymerization experiment carried out in the absence of macroCTA suggests the involvement of the trithiocarbonate CTA in the polymerization process (Figure 3). Indeed, such impact of CTA on polymerization kinetics has already been reported for RAFT polymerization mediated by trithiocarbonate CTA.³⁸

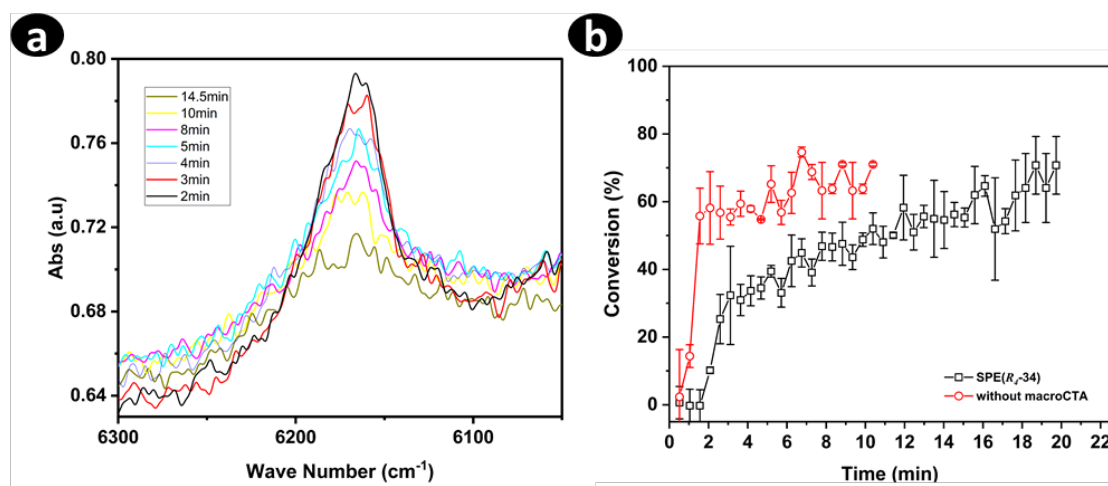


Figure 3. a) FTIR spectra in capillary of crude SPE(R_4 -34) sample at different time in the range of 6110 - 6230 cm^{-1} used to calculate conversion at various stages of polymerization while irradiated with 365 nm light b) Conversion of IBoA and OEGDA as a function of time with R_4 -34-SPE macroCTA (black squares) and without macroCTA (red circles).

2.3 Kinetics of Microphase Separation

The mode of polymerization, whether thermal or photo process, plays a crucial role in controlling the PIMS process by affecting the thermodynamic interaction of polymer chains or segments. Hillmyer and Seo¹⁷ conducted an investigation into domain formation during a PIMS process using in situ SAXS measurements. They employed a 22 kDa PLA macroCTA (32 wt %) in a blend of styrene (S) and divinylbenzene (DVB, [S]/[DVB] = 4) for a duration of 5 hours at 120°C. Notably, a conspicuous peak at $q = 0.3 \text{ nm}^{-1}$ surfaced after 35 minutes, manifesting a gradual increase in intensity until it levelled off at 80 minutes. In the early stages of the reaction, the scattering intensity displayed an exponential surge, hinting at an initial-phase transition propelled by the *in-situ* formation of block copolymers as shown in Figure 4a. The result was further elaborated by characterizing the polymers generated over the first 20 min via SEC. The apparent molar masses gradually shifted to higher values, suggesting controlled growth of P(S/DVB) from PLACTA by the RAFT process (Figure 4b). However, their work does not incorporate ionic component (or salts) in reactive mixture and therefore the kinetics of microphase separation cannot be directly compared to typical PIMS process for the SPE fabrication.

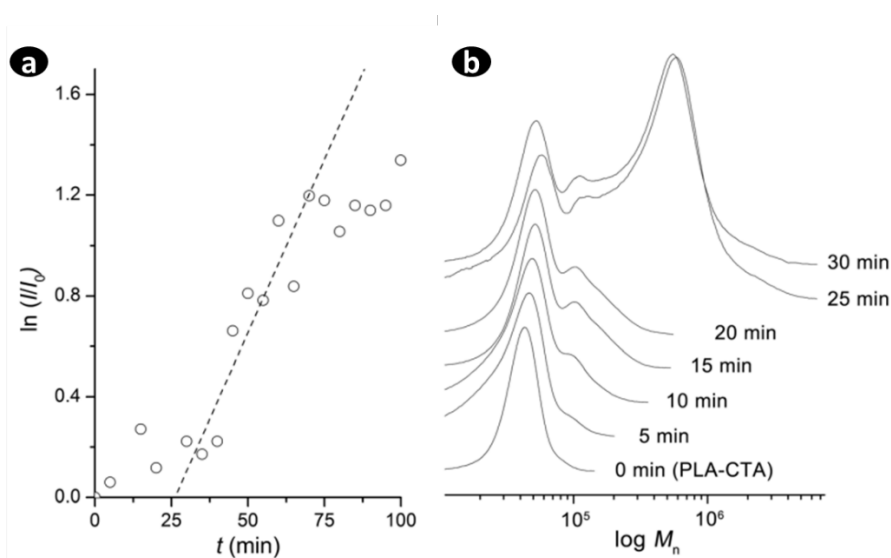


Figure 4. (a) Evolution of SAXS peak intensity (I) over polymerization time (t) during the polymerization of S and DVB (4/1) in the presence of PLA-CTA-22 (31 wt %) at 120°C. The peak intensity at $q = 0.3 \text{ nm}^{-1}$ was normalized by the intensity at $t = 0$. The dashed line indicates exponential increase of I at the onset of phase separation obtained by linear least-square fitting of data points from 35 to 70 min. (b) Evolution of SEC traces for the first 30 min of polymerization of S and DVB (4/1) in the presence of PLA-CTA-22 (32 wt %) at 120°C. Intensities were obtained by refractive index detector responses, and molar masses were relative to polystyrene standards. Taken from the work of Seo *et al.*¹⁷

To elucidate the actual kinetics of microphase separation in SPE via thermal-RAFT PIMS, McIntosh *et al.*²⁴ conducted a mechanistic study on the formation of nanoscale morphology by in-situ, time-resolved SAXS experiments, conductivity, rheology, and SEC techniques. They observed the evolution of the homogeneous electrolyte resin consisting of PEO-CTA (25 vol %) and BMITFSI (21 vol %) in a blend of styrene (S) and divinylbenzene (DVB, [S]/[DVB] = 4) for a duration of 3 hours at 120°C. The experiments showed an exponential increase in the maximum scattered intensity, I_m for the first 2 h of the PIMS reaction, during which q_m becomes progressively smaller (refer to Figure 5a). The decrease in q_m over the course of the reaction, signifying a 2 nm increase in the d-spacing, was attributed to a combination of chain growth and chain stretching as the segregation strength intensified throughout the reaction. According to SEC analysis, discrete aggregates of cross-linked polymers formed up to the 45 min (refer to Figure 4b). Simultaneously, both local viscosity and the elastic modulus (as determined by rheology) exhibited a steady rise, eventually reaching the apparent gel point at approximately 1.7 h.

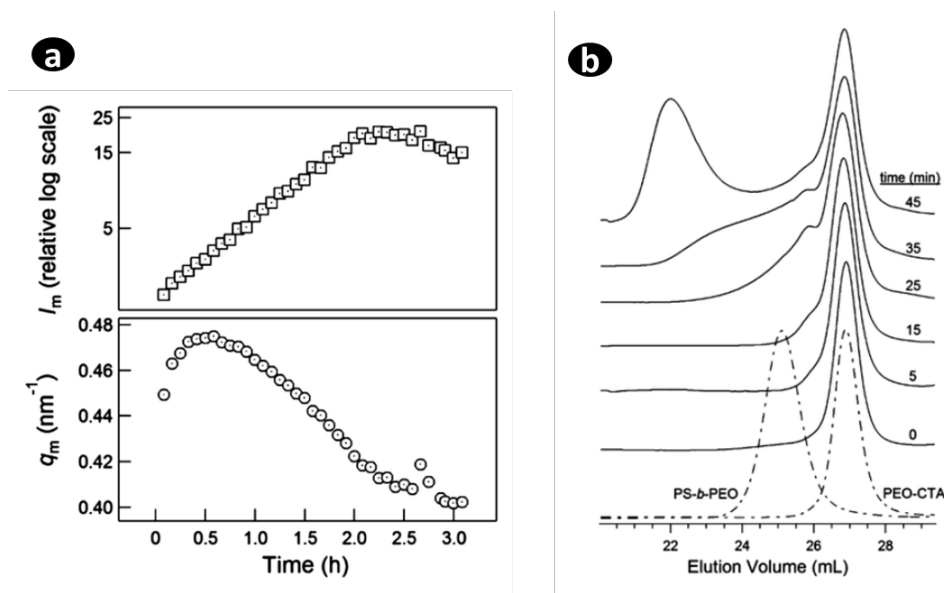


Figure 5. (a) Time-resolved evolution of the maximum scattered intensity, I_m , of the primary structure factor peak located at wave vector q_m , for a sample prepared with 21 vol % BMITFSI. (b) Progression of the size exclusion chromatograms of PEO-b-P(S-co-DVB) (solid) isolated at various times following initiation at $t = 0$ min. A separate polymerization (dash-dot) illustrates the utility of PEO-CTA in the controlled growth of linear of a PS-b-PEO diblock in the absence of cross-linker. Taken from the work of McIntosh *et al.*²⁴

In summary, a minimum of 2 h is required to reach full development of the morphology during thermal-RAFT PIMS fabrication (at 120 °C) of SPEs.

In our study, we aimed to track the time scale of nanostructure formation in the fast photo-RAFT PIMS process. By examining the scattering behaviour of the electrolyte resin during photopolymerization over a limited q range (10^{-2} - 10^2 nm^{-1}), we sought to obtain data that would provide an overarching insight to the potential effects of macroCTA architecture, macroCTA molar mass, and intensity of UV irradiation.

To carry out this experiment, liquid electrolyte resins was introduced into a glass capillary tube and placed in a home-made holder for simultaneous UV and x-ray irradiation. The shutter setting of x-ray chamber was adjusted to open every 400 ms thus allowing 100 ms exposure time for x-ray bombardment on the filled capillary tube. UV lamp was controlled by the shutter controller (in pulse mode) to irradiate at the sample during 100 ms exposure time every 400 ms. Time-stamped scattering curves for resins containing R_1 macroCTA, revealed the manifestation of structural peak with increasing intensity around $q = 0.14$ nm^{-1} (refer to Figure 6)

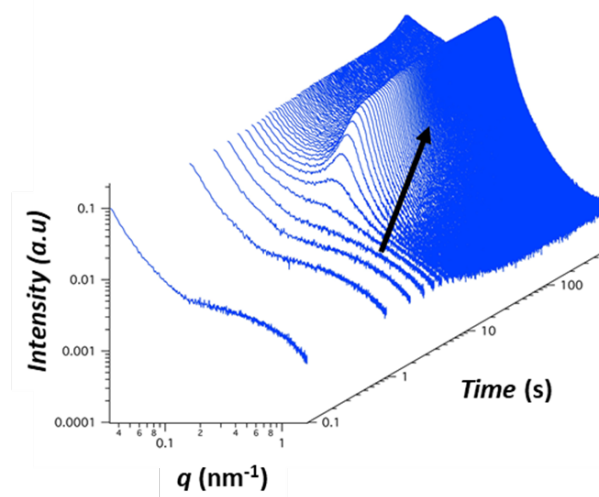


Figure 6. 3D graph of typical time-stamped scattering curves of SPE(R_1 -34) resin under simultaneous X-ray and UV irradiation (0.54 mWcm^{-2}) for 10 mins. Refer to Figure S30 for time-stamped scattering curves of other electrolyte resins.

Precise variables, such as the scattering vector value, $q_m(t)$, corresponding to the maxima of the appearing peaks and the peak intensity, $I_m(t)$, corresponding to is the maximum intensity of the appearing peaks, offer insight into subtle alterations in the nanoscale phase separation (Figure 6). Indeed variations of $q_m(t)$ directly reflects changes in domain size, $d(t) = 2\pi/q_m(t)$ and variations of $I_m(t)$ indicates on the amount of nanostructures develop over time.³⁹

From **Figure 7** (up), it can be deduced that structural formation for resins with R_1 macroCTA starts with a ~ 4 s stationary period during which normalized intensity,

$I_n(t) = I(t)/I_m$ (maximum) remained more or less constant. The absence of scattering peak at the beginning ($t = 0$) is an indication of a good initial solubility of all compounds in the initial electrolyte resin. Whatever polymer chains are formed during this time remain soluble in the resin. After the stationary period, structural peaks begin to appear and $I_n(t)$ rose sharply over ~ 40 s which can be attributed to the formation of microphase. In this second stage, discrete flocs consisting of cross-linked P(S-co-OEGMA)-*b*-P(IBoA-co-OEGDA) polymer form, undergoing continuous segregation into microphases. This segregation process optimizes thermodynamically favourable interactions between the blocks until the resulting structures become "locked in" upon gelation of the P(IBoA-co-OEGDA) microphases. By observing the slope of $I_n(t)$ vs t during this period, we can compare easily the rate of phase separation, k at different weight composition of R_1 macroCTA. It was observed that microphase separation occurs much faster with increasing content of R_1 macroCTA ($k_{44} = 1.2 \text{ s}^{-1} > k_{34} = 1.1 \text{ s}^{-1} > k_{24} = 0.7 \text{ s}^{-1}$). Once gelation occurs, the non-crosslinked block of R_1 macroCTA are unable to rearrange themselves, thus reaching a plateau where I_n remained more or less constant. Meanwhile, following the initial stationary stage, value of scattering vector at peak maximum, $q_m(t)$, remained stable without notable changes for the remaining event of the photopolymerization and crosslinking (**Figure 7**down). The $d(t)$ values for the systems with 24 wt%, 34 wt%, and 44 wt% of R_1 macroCTA saturated at 44 nm, 35 nm, and 32 nm, respectively. This implies that the domain size of the initially generated polymer flocs is maintained, and spatial connections are continuously established throughout the material during photopolymerization, resulting in a global microphase separation. It is perhaps important to note that the saturated $d(t)$ values of this *in-situ* experiment are very comparable to characteristic dimension, d_{SAXS} that are mentioned for solid films hereafter. This suggests that the time-resolved morphological transitions observed for *in-situ* experiment on glass capillary can corroborate inherent morphology of SPE films.

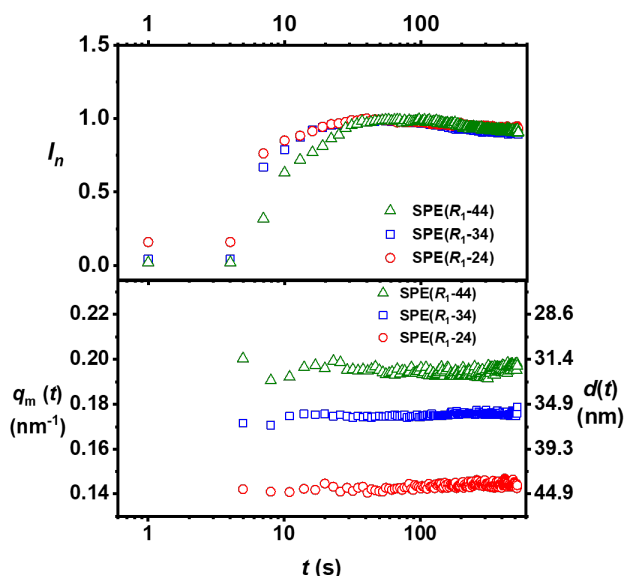


Figure 7. Time changes in the peak wavenumber $q_m(t)$ (down) and the normalized peak scattered intensity $I_n(t)$ (up) at 30 mWcm^{-2} irradiances for resins with different composition of linear comb macroCTA, R_1 .

Similar trend was observed for systems with 24 wt%, 34 wt%, and 44 wt% of low molar mass star comb macroCTA, R_4^* (Figure 8) with structural sizes of 29 nm, 25 nm and 23 nm respectively. $I_n(t)$ rose sharply after ~ 4 s which can be attributed to the formation of microphases. Like was observed previously for R_1 macroCTA, microphase separation occurs much faster with increasing content of R_4^* macroCTA ($k_{44} = 1.6 \text{ s}^{-1} > k_{34} = 1.4 \text{ s}^{-1} > k_{24} = 1.2 \text{ s}^{-1}$).

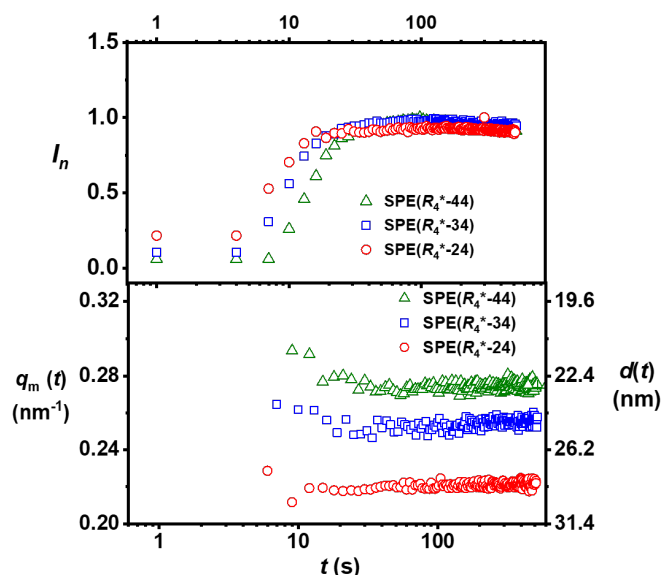


Figure 8. Time changes in the peak wavenumber $q_m(t)$ (down) and the normalized peak scattered intensity $I_n(t)$ (up) at 30 mWcm^{-2} irradiances for resins with different composition of low molar mass star comb macroCTA, R_4^* .

However, when examining the resins with 24 wt%, 34 wt%, and 44 wt% star comb macroCTA, R_4 of higher molar mass of $144 \text{ kg}\cdot\text{mol}^{-1}$, a slightly different kinetic behaviour is observed (refer to **Figure 9**).

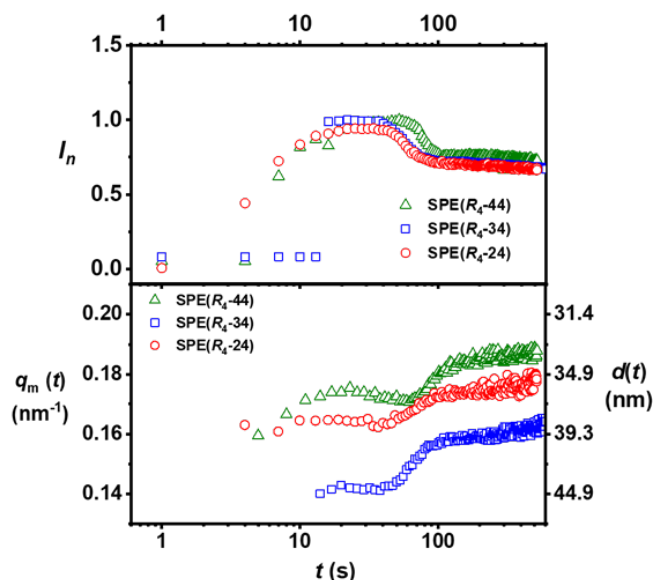


Figure 9. Time changes in the peak wavenumber $q_m(t)$ (down) and the normalized peak scattered intensity $I_n(t)$ (up) at 30 mWcm^{-2} irradiances for resins with different composition of high molar mass star comb macroCTA, R_4 .

The intensity increased sharply after a first stationary stage ($\sim 4 \text{ s}$) over 40 s , but subsequently experiences a slight decline between 50 and 100 s . After this decline, the intensity levels off into a stationary state. The structural size of the phase separating structures remained almost constant during the first stage over 40 s . Subsequently, it decreased gradually for the next 60 s indicating a constriction of the microstructures. Finally, it became almost stationary for the remaining event of the photopolymerization and crosslinking.

This analysis sheds light on the nature of the chain topology of the macroCTA within the nanostructures. While PIMS process with linear and star (low molar mass) comb macroCTA experienced a somewhat simple structural evolution characterized by two primary stage – stationary and gelation stage. Systems with the large molar mass star macroCTA displayed irregular evolution characterized by a stationary stage, gelation stage and a constriction stage. It is not fully explained at this stage what could be the particular cause of type of morphological evolution. However, we suspect that it may be as a result of the macromolecular chain organization due to the large arms of the macroCTA. This specific behaviour of the R_4 macroCTA was confirmed by a kinetic study conducted on the $\text{SPE}(R_4-34)$ resin to examine

the influence of irradiance intensity on the phase separation process. The study involved varying irradiance levels of 0.27, 0.54, 0.73, and 2.16 mW cm^{-2} . The results revealed that the overall trajectory of morphology evolution is not significantly influenced by irradiance within the investigated range (see Figure 10),

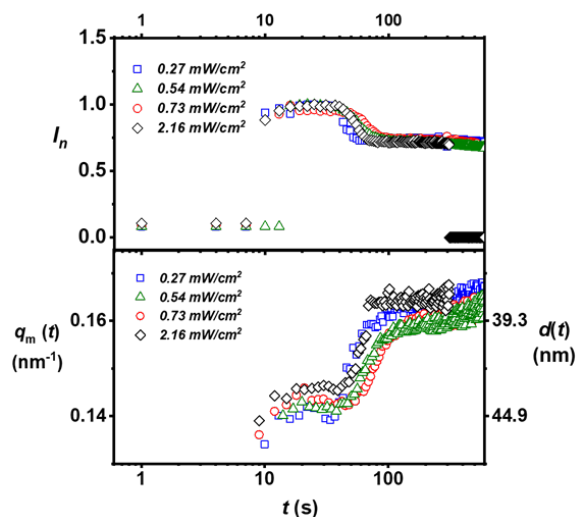


Figure 10. Time changes in the peak wavenumber $q_m(t)$ (down) and the normalized peak scattered intensity $I_n(t)$ (up) at 0.27, 0.54, 0.73, and 2.16 mW cm^{-2} irradiances for SPE(R_4 -34) resins.

Some reports have demonstrated ability to controlling morphologies at relatively low irradiance ($< 0.15 \text{ mW cm}^{-2}$) by allowing sufficient time for diffusion and phase separation of the incompatible phases prior to gelation.⁴⁰ We chose to employ higher irradiance levels in our experiments to streamline the application process, making it more efficient, rapid, and easily scalable. Consequently, we utilized an irradiance of 2.78 mW cm^{-2} to produce SPE samples intended for use in LMBs.

2.4 Morphological study of solid electrolytes

SPE films were fabricated by UV irradiation ($\lambda_{\max} = 365 \text{ nm}$, 2.78 mW cm^{-2}) of the reactive resins through a mylar sheet ($200 \mu\text{m}$, average transmittance $\sim 63\%$ at $330 - 380 \text{ nm}$) for 10 min as shown in Figure 11a. This technique allowed the preparation of free-standing flexible, smooth and transparent SPEs with scalable thickness range of $100 - 250 \mu\text{m}$. We achieved a high monomer conversion ($> 94\%$) on the film, as determined from equation S15. It's worth noting that the formulation preparation and film fabrication using UV were carried out in a glove box (Oxygen $< 2 \text{ ppm}$, H₂O $< 0.5 \text{ ppm}$). Consequently, there was no need for post-polymerization temperature/vacuum treatment to remove water-based contaminants from the solid polymer electrolytes (SPEs). In Laura's thesis work (IPREM/UPPA 2019), a brief temperature increase (reaching $115 \text{ }^\circ\text{C}$ within the first 100 seconds) was observed during the UV photopolymerization of IBoA-based formulations at an irradiance of 30 mWcm^{-2} . In our current system, we do not anticipate such a temperature increase due to the use of lower irradiance (2.78 mW cm^{-2}). Therefore, we assume that the final composition of the SPEs is similar to the starting formulation.

Figure 11b-d displays SAXS profiles of SPEs prepared from R_1 , R_4 and R_4^* macroCTA at room temperature, showing a structural peak at q^* . This peak indicates the presence of microphase separation within the sample, characterized by a lack of specific long-range periodic order in the absence of secondary diffraction peaks as previously reported for similar system by Seo *et al.*¹⁷ The characteristic dimension of the microphase separation can be computed with $d_{\text{SAXS}} = 2\pi/q^*$. For the SPEs prepared with different weight percentages of macroCTA (44 wt%, 34 wt%, and 24 wt%), the corresponding length scales of phase separation are reported in **Table 3**. As expected, a decrease in the length scale is observed when the percentage of macroCTA is increased, as this leads to the formation of a shorter second block.

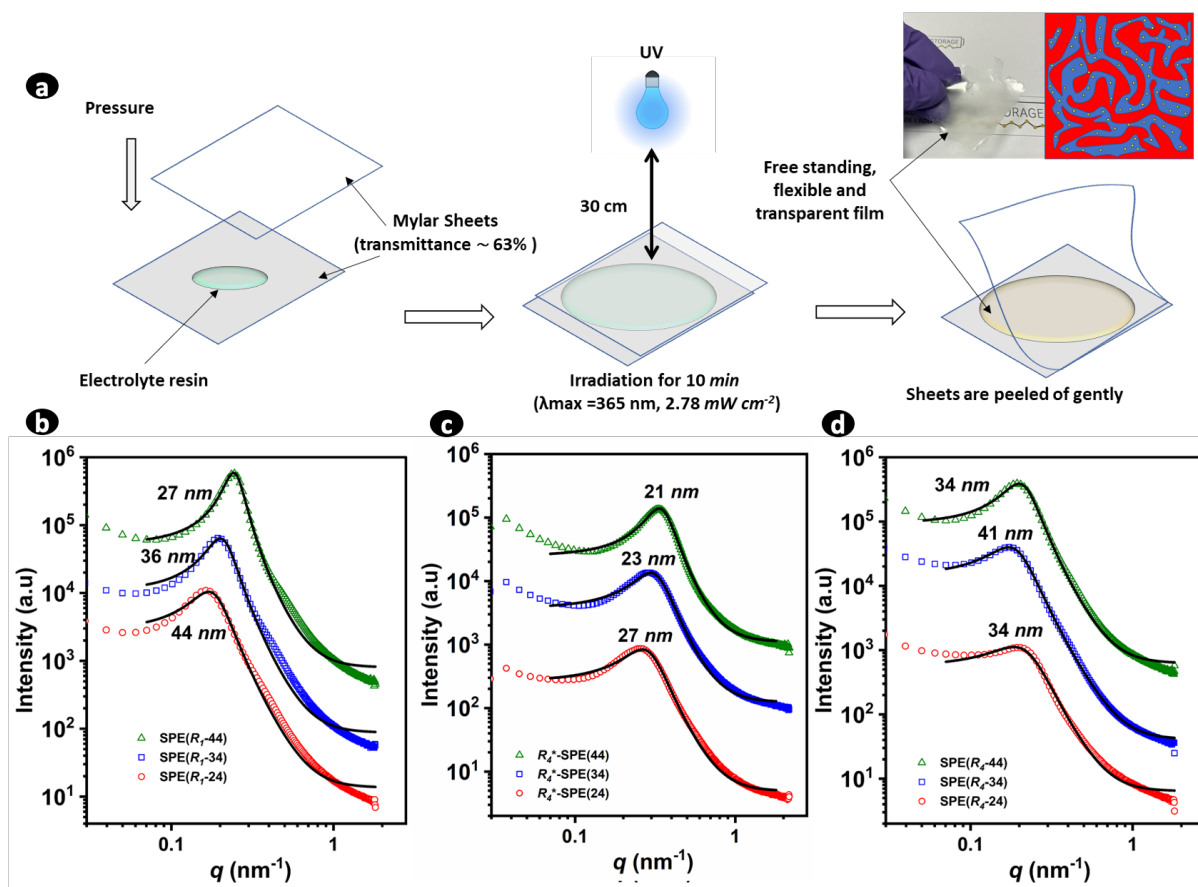


Figure 11. a) Method for preparation of free-standing SPEs. SAXS spectra of each SPE prepared from b) R_1 c) R_4^* and d) R_4 macroCTAs. The SAXS curves are shifted vertically to enable visibility. Numerical values indicate characteristic distance $d_{\text{SAXS}} = 2\pi/q^*$ calculated from the primary scattering peak q^* . Black solid curves represent the fitting with Teubner-Strey model.

This can be explained by assuming the microphase separation in the SPEs as lamellar at a local scale (see Figure 12a). Increasing the soft phase (i.e. macroCTA+PC/LiTFSI) invariably reduces molar mass of hard-rigid phase of P(IBoA-*stat*-OEGDA). Ultimately, this accounts for the reduced dimensions of domain spacing. However, this relationship deviates in the case of SPEs prepared with R_4 macroCTA (144 kg mol^{-1}), particularly with regards to SPE(R_4 -24). We suspect that this particular sample exhibits a distinct morphology, as a similar pattern was observed previously in kinetic experiments conducted within glass capillaries. We will address this anomaly in more detail at a later point in our discussion on conductivity results.

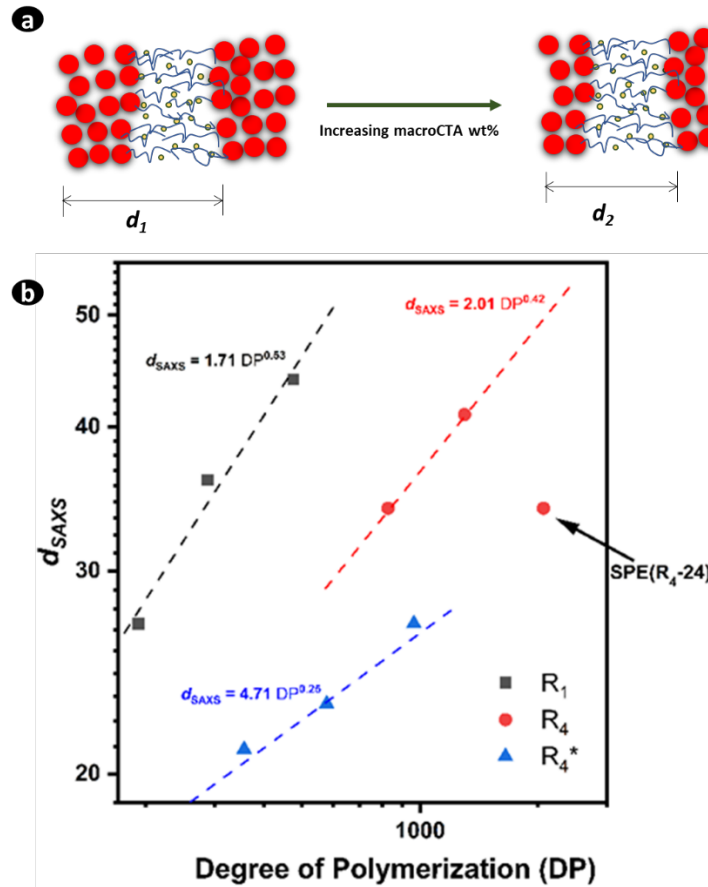


Figure 12. a) Illustration of how increasing macroCTA content affects domain size, d for SPEs. By keeping total volume constant, $d_1 > d_2$. b) Plot showing scaling of d_{SAXS} with with degree of polymerization of P(IBoA-*stat*-OEGDA).

The Teubner-Strey (T-S) model was used to fit the scattering curves (see black solid line in Figure 11), according to equation 1, in order to acquire deeper understanding of the morphology of the SPEs. The T-S model finds extensive use in characterizing two-phased materials without long range order.⁴¹ In equation 1, $I(q)$ stands for the scattered intensity after background subtraction, while a_2 , c_1 , and c_2 are the fitting parameters.

$$I(q) = \frac{1}{a_2 + c_1 q^2 + c_2 q^4}, \quad 1$$

These fitting parameters are crucial for calculating structural characteristics of the material like domain size (d_{TS}), amphiphilicity factor, f_a , and correlation length (ζ). The corresponding values are listed in **Table 3**.

$$d_{\text{TS}} = 2\pi \left[\frac{1}{2} \left(\frac{a_2}{c_2} \right)^{1/2} - \frac{1}{4} \left(\frac{c_1}{c_2} \right) \right]^{-1/2}, \quad 2$$

$$f_a = \frac{c_1}{(4a_2c_2)^{1/2}}, \quad 3$$

$$\xi = \left[\frac{1}{2} \left(\frac{a_2}{c_2} \right)^{1/2} + \frac{1}{4} \left(\frac{c_1}{c_2} \right) \right]^{-1/2}, \quad 4$$

Table 3. Overview of the T-S fitting parameters and Thermal Properties of fabricated SPEs

EXP	CODE	[EO]/[Li]	d_{SAXS} (nm)	d_{TS} ^{a)} (nm)	ξ ^{a)} (nm)	f_a ^{a)}	T_g EO ^{b)} domain (°C)	T_0 ^{c)} (°C)	G' ^{d)} (MPa)
KA219	SPE(R_1 -24)	5	44	42	17	-0.72	-56	-140	5.1
KA224	SPE(R_1 -34)	5	36	33	19	-0.86	-41	-132	5.1
KA221	SPE(R_1 -44)	5	27	27	26	-0.94	-54	-134	0.6
KA225	SPE(R_4 -24)	5	34	32	17	-0.83	-50	-100	10.0
KA226	SPE(R_4 -34)	5	41	38	16	-0.75	-42	-126	4.3
KA230	SPE(R_4 -44)	5	34	31	22	-0.90	-41	-157	0.5
KA253	SPE(R_4^* -24)	5	27	25	13	-0.83	-27	-125	4.5
KA254	SPE(R_4^* -34)	5	23	23	10	-0.77	-33	-128	5.6
KA255	SPE(R_4^* -44)	5	21	20	14	-0.90	-26	-145	1.5

^{a)}Data gotten from fitting SAXS curve with Teubner-Strey (T-S) model;

^{b)}Glass transition temperature determined from DSC experiments;

^{c)}Reference temperature determined from VFT fitting in equation 5;

^{d)}Storage moduli at 30°C

The domain size (d_{TS}) calculated from equation 2, represents a statistical average of the periodicity or repeating pattern within the material. The consistent agreement between d_{TS} and d_{SAXS} reinforces the confidence in the T-S model's capability to describe and analyse the phase separation behaviour observed in the system. The amphiphilicity factor, f_a , given in equation 3 represents the degree of segregation strength at the interface between domains. f_a value ranged from -0.72 to -0.94 regardless of the content of macroCTA (refer to **Table 3**), suggesting the strongly segregated nature of the precursors and the spontaneous formation of sharp interfaces in the SPE. Such f_a values close to -1 indicates that the system is highly structured but still globally disordered.^{42, 43}

The correlation length (ξ) given by equation 4, represents the average distance over which the phase exhibits structural coherence or order. It provides information about the spatial extent of the organization or arrangement of separated phases.^{41, 44}

The structural dispersities, d_{TS}/ξ of the SPEs are compared as illustrated in Figure S31. It is evident that dispersities reach their minimum values at 34 wt% of star comb macroCTA and

24 wt% of linear comb macroCTA. This observation suggests that this particular group of samples exhibits a higher degree of spatial order.⁴⁵

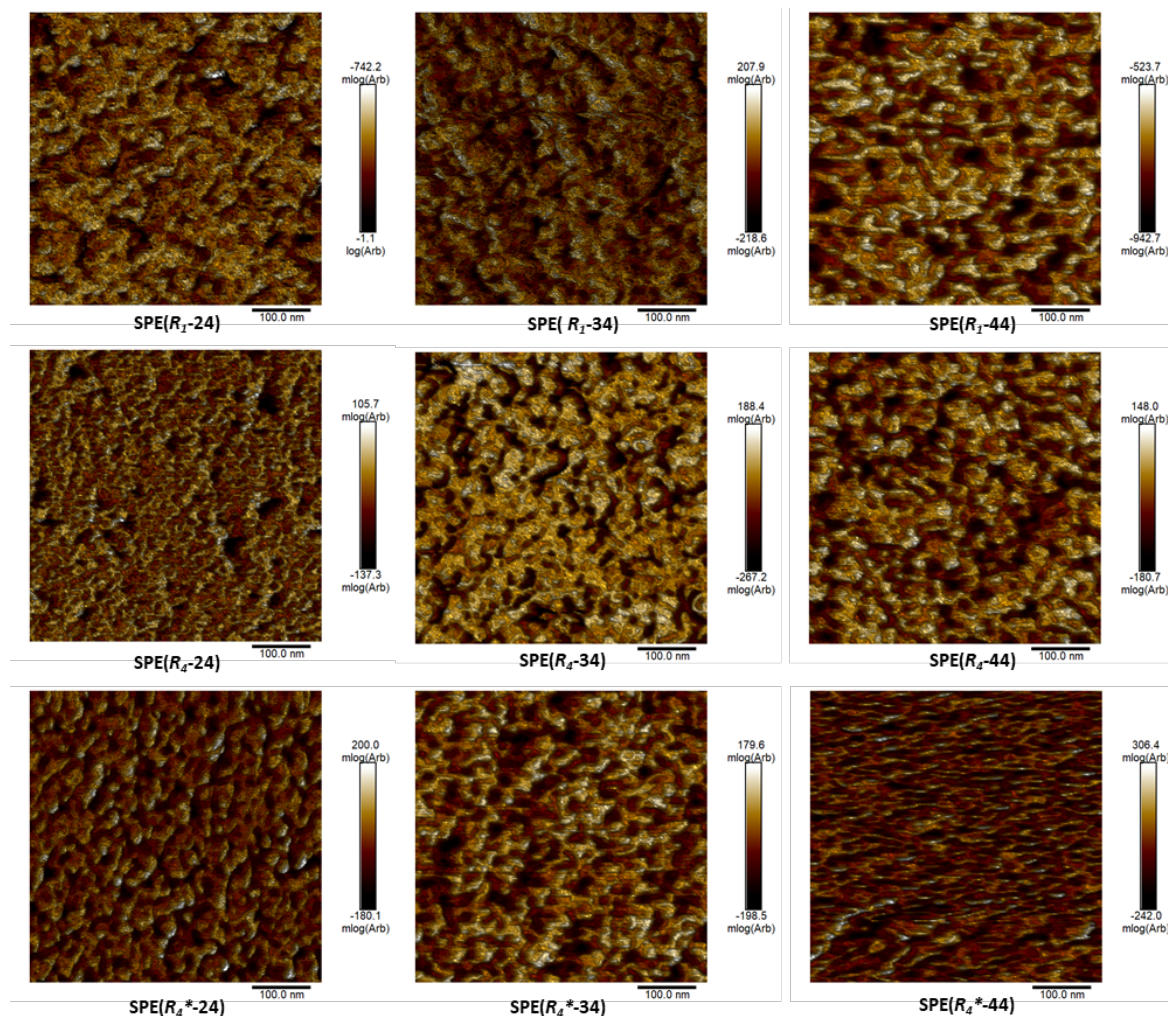


Figure 13. AFM Log DMT images of cross-section of the sample revealing bulk morphology. The dimensions of the sample are $0.5 \times 0.5 \mu\text{m}$. Negative and positive grades correlate to harder and softer domains, respectively. The Derjaguin-Muller-Toporov (DMT) model measure the reduced Young's modulus of different phase present in the sample.

To provide additional insights on morphology obtained from SAXS, a bulk cross-section of each SPE was produced by ultramicrotome and subsequently observed using atomic force microscopy (AFM). Notably, the samples were prepared by first heating the fabricated SPEs overnight at $100 \text{ }^\circ\text{C}$ under high vacuum. The observed gravimetric loss in weight of approximately 12% indicates a substantial evaporation of solvent, which could have potentially disrupted the AFM scanning process if not removed.

The AFM images shown in Figure 13 offer valuable visual information about the internal nanostructures within the SPEs. With the exception of SPE(R₄-24), all the samples exhibit a

consistent two-phase network structure, where the dark regions represent the POEGMA-based soft phase and the bright regions represent the PiBoA-based hard phase. It is important to note that making a direct comparison between the dimensions and sizes of the microphases observed in SAXS analysis and those seen in AFM images would be misleading. This is primarily because the AFM samples underwent thermal treatment to eliminate the solvent.

2.5 Electrochemical and Mechanical Properties of Fabricated Solid Electrolytes

Evaluation of the temperature-dependent lithium conductivities which is a crucial parameter for the implementation of such SPEs in solid state batteries, was achieved through EIS measurements. The plot of the ionic conductivity is presented in Figure 14a.

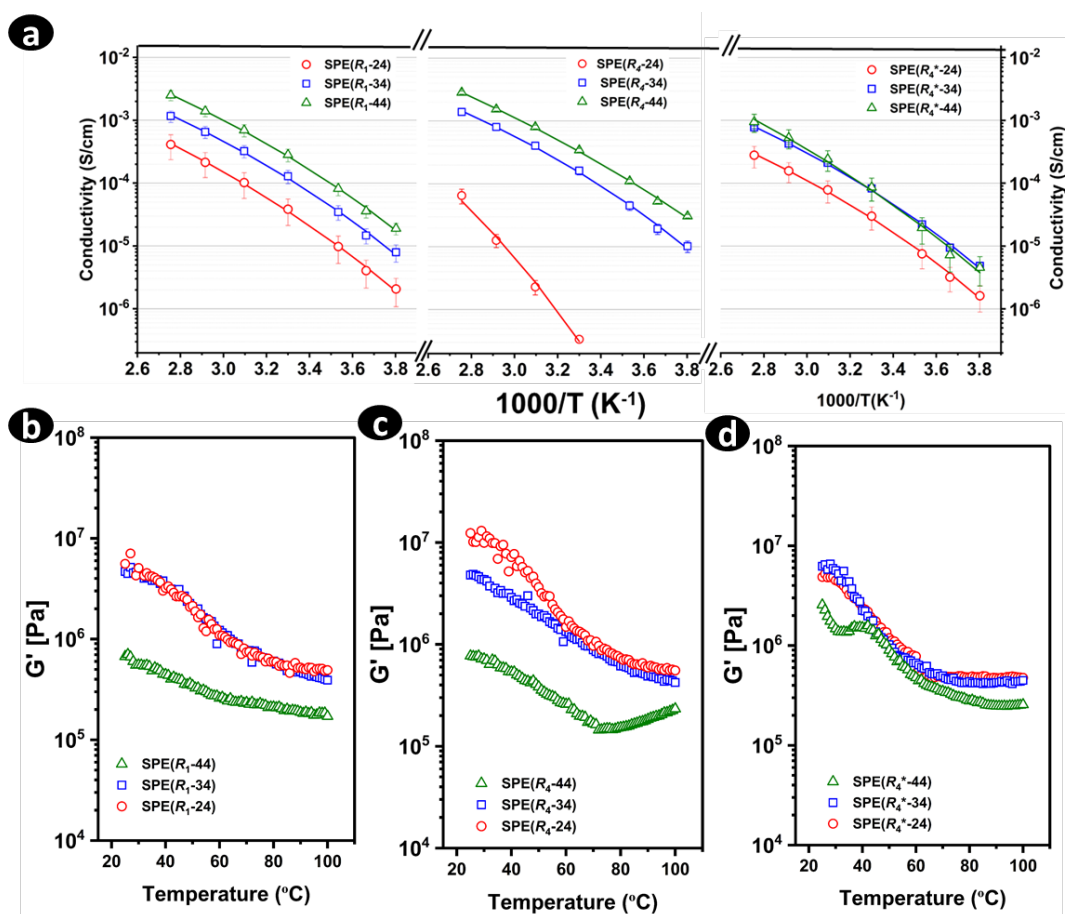


Figure 14. a) Temperature dependent conductivity of SPEs. Error bars indicate the standard deviation observed from three measurements taken at different locations on the sample. In certain cases, six measurements were conducted, including samples fabricated from duplicate formulations, to confirm the accuracy and reliability of the results. Temperature dependent storage modulus of SPEs fabricated from b) R₁ c) R₄ and d) R₄* macroCTAs.

The conductivity data has been fitted with Vogel-Tammann Fulcher (VTF) model to fully capture the temperature dependence. The VFT expression is given as;

$$\sigma = \sigma_0 \exp\left(-\frac{B}{R(T-T_0)}\right), \quad 5$$

In equation 5, B represents the pseudo activation energy for ion transport, σ_0 is a prefactor associated with the concentration of charge carriers in the electrolyte, R denotes the gas constant, and $T_0(K)$ represents the Vogel temperature. T_0 serves as a benchmark temperature, signifying the point at which the configurational entropy of the polymer matrix reaches zero. It is empirically linked to the glass transition temperature (T_g) of the conductive phase, with a relationship expressed as $T_g - T_0 \approx 50 K$.⁴⁶ The values of T_0 obtained through fitting with equation 5 (as detailed in **Table 3**) fall within the range of -100°C to -140°C . Notably, the difference between these T_0 values and the T_g values determined through dynamic scanning calorimetry (DSC) experiments is considerably greater than 50°C ($T_g - T_0 > 50 K$) for all cases except SPE(R₄-24). This observation suggests that the transport of Li^+ ions is influenced not only by the segmental motion of the flexible EO side chains but also by the solvent-assisted vehicular motion facilitated by PC coordination with Li^+ ion. It is believed that PC as a whole provides many carbonyl-groups which helps facilitate charge transport by serving as additional coordination sites. It also acts as a plasticizer thus improving chain dynamics of EO side chains.⁴⁷

At 30°C , the ionic conductivity of SPEs prepared from 44 wt%, 34 wt%, and 24 wt% of linear R_I macroCTA is 0.28, 0.13 and 0.04 mS cm^{-1} respectively. These conductivity values show a clear correlation with the composition of the POEGMA-rich Soft phase. Recall that the previously described space length of nanostructured morphology of the linear system exhibited a consistent relationship with the composition of the soft phase. Due to the simplicity of the linear system and the absence of any morphological ambiguity, it will serve as a reference for comparison with the star system.

we compared solid polymer electrolytes (SPEs) using a lower molar mass star comb macroCTA, R_4^* (62 kg mol^{-1}), as depicted in Figure 14a. At a temperature of 30°C , the conductivity of SPEs was evaluated for three different weight percentages of R_4^* macroCTA, resulting in values of 0.09, 0.08, and 0.03 mS cm^{-1} , respectively. Interestingly, we observed that SPE(R₄*-44) and SPE(R₄*-34) demonstrated nearly identical conductivity behaviours

(refer to Figure 14a). While the exact reason for this behaviour remains unknown, we suspect that the reduced conductivity of SPE(R₄*-44) may be attributed to the extremely compact nature of the conducting network structure, as previously observed through SAXS and AFM analyses.

In the case of SPEs prepared using different weight percentages of R₄ macroCTA, the measured ionic conductivity values (at 30 °C) were found to be 0.34 mS cm⁻¹, 0.16 mS cm⁻¹ and 0.34 μS cm⁻¹ respectively, for compositions of 44 wt%, 34 wt%, and 24 wt% of R₄.

Notably, when comparing SPEs with 44 wt% and 34 wt% of macroCTA, the R₄ exhibited 1.2 times higher conductivity than their linear counterparts, R₁. However, at the reduced macroCTA composition of 24 wt%, the ion conductivity of SPEs containing R₄ experienced a significant drop, over 10² times lower than that of R₁-based SPEs. This decline can be attributed to the inherent differences of their morphology, as previously described (refer to section 2.4).

In phase separated BCP electrolytes, it is commonly observed that the ion conductivity improves with increasing percolation of the POEGMA-rich soft phase.⁴⁸ When BCP electrolytes feature a low percolation of the conducting phase, such as in the case of a spherical morphology, their conductivity tends to be poor. Likewise, in the case of SPEs fabricated using PIMS method, the presence of a randomized bi-continuous network could enhance the conductive pathways for ion mobility. The movement of Li⁺ ions in this system will involve a delicate interplay among factors such as the size, shape, and connectivity of the soft phase as well as macromolecular chain dynamics of P(S-co-OEGMA) block. Therefore, it is our hypothesis that the distinct globular morphology observed in SPE(R₄-24) obstructs the percolation of the POEGMA-rich soft phase, thus resulting in decreased conductivity.

By employing OEGDA as crosslinker the PIMS process, 2-3 ethylene oxide (EO) units were effectively sequestered in the hard-rigid phase. This corresponds to 16 mol%, 23 mol%, and 32 mol% of the total EO units present in SPEs with macroCTA concentrations of 44 wt%, 34 wt%, and 24 wt%, respectively. It is reasonable to assume that EO units, regardless of their spatial distribution within the SPEs, would coordinate with Li⁺ from LiTFSI. Therefore, to assess the impact of EO units within the hard-rigid phase, we conducted a separate evaluation of the conductivity of P(IBoA-stat-OEGDA) in the absence of macroCTA. We maintained a consistent ratio of [IBoA]/[OEGDA] = 4, [EO]/[Li] = 5 and [PC]/[LiTFSI] = 2.8 to facilitate

comparison with typical SPEs. Indeed, after photopolymerization, PC was largely expelled from the solid samples, leading to the formation of droplets on the film surface. These droplets were removed using wipes, and the ionic conductivity was measured via EIS. As depicted in Figure S32, the results revealed that the crosslinked matrix displayed a conductivity of $0.16 \mu\text{S cm}^{-1}$ at 50°C , primarily attributed to the presence of PC-Li-EO coordination. Although this conductivity within the rigid matrix is relatively low, it played a critical role in reducing the overall resistance of the SPEs, as opposed to a scenario in which the rigid matrix would be entirely non-conductive.

The fabricated SPEs exhibited a decent mechanical strength (G') as demonstrated by constant shear experiments over a wide temperature window ($25 - 100^\circ\text{C}$) provided in Figure 14b-d. The SPEs prepared from R_1 , R_4 and R_4^* displayed similar viscoelastic behaviour with behaviour, characterized by a gradual reduction in modulus with increasing and temperature. At the temperature of 30°C , SPE(R_4 -24) exhibited higher storage moduli of 10 MPa, nearly double that of SPE(R_1 -24) and SPE(R_4^* -24), which registered values of 5.1 MPa and 4.5 MPa, respectively. Another noteworthy observation is that SPE(R_1 -24), SPE(R_4^* -24), SPE(R_1 -34), SPE(R_4 -34) and SPE(R_4^* -34) all recorded values near 5 MPa at 30°C with significant similarity in the temperature-dependent changes in storage moduli, except for SPE(R_4 -24), which once again stands out as an outlier. This suggests that SPE(R_1 -24), SPE(R_4^* -24), SPE(R_1 -34), SPE(R_4 -34) and SPE(R_4^* -34) may encompass similar morphologies and, consequently, similar mechanical behaviour. At 44 wt% macroCTA content, storage modulus of SPEs drops considerably to ~ 0.5 MPa (at 30°C), but not to the same extent for SPE(R_4^* -44) which had ~ 1.5 MPa.

SPE(R_4 -34) was selected as a representative example of the PIMS SPEs to showcase their suitability for use in LMBs. Indeed, SPE(R_4 -34) exhibits a favourable balance between mechanical strength, with a modulus exceeding 4.3 MPa, and ionic conductivity of 0.16 mS cm^{-1} at 30°C .

2.6 Cell Performance

Transference number was first evaluated on SPE(R_4 -34) to understand the mobility of both anion (TFSI^-) and cation (Li^+). This is crucial because the ionic conductivity of such a dual-ion conducting SPE is influenced by both TFSI^- and Li^+ mobility. As a result, Evans *et al.*⁴⁹

suggested a combined measurement involving potentiostatic polarization and complex impedance. The transference number of SPE(R_4 -34) was computed as 0.28 ± 0.03 (refer to Figure 15a) using the estimated from the Bruce-Vincent-Evans (BVE) equation S18. This value falls within the typical range observed for high molar mass PEO/LiTFSI electrolytes, as reported in the literature.⁵⁰ Consequently, this suggests that the PEOGMA/LiTFSI-PC domains within fabricated SPEs expresses comparable ion transport efficiency to that of pure PEO/LiTFSI electrolytes, despite being surrounded by the rigorous network of higher modulus block of P(IBoA-co-OEGDA). The enhanced ion transport can arguably be credited to the incorporation of PC within the conductive phase which brings a plasticizing effect on the PEOGMA chains.⁵¹

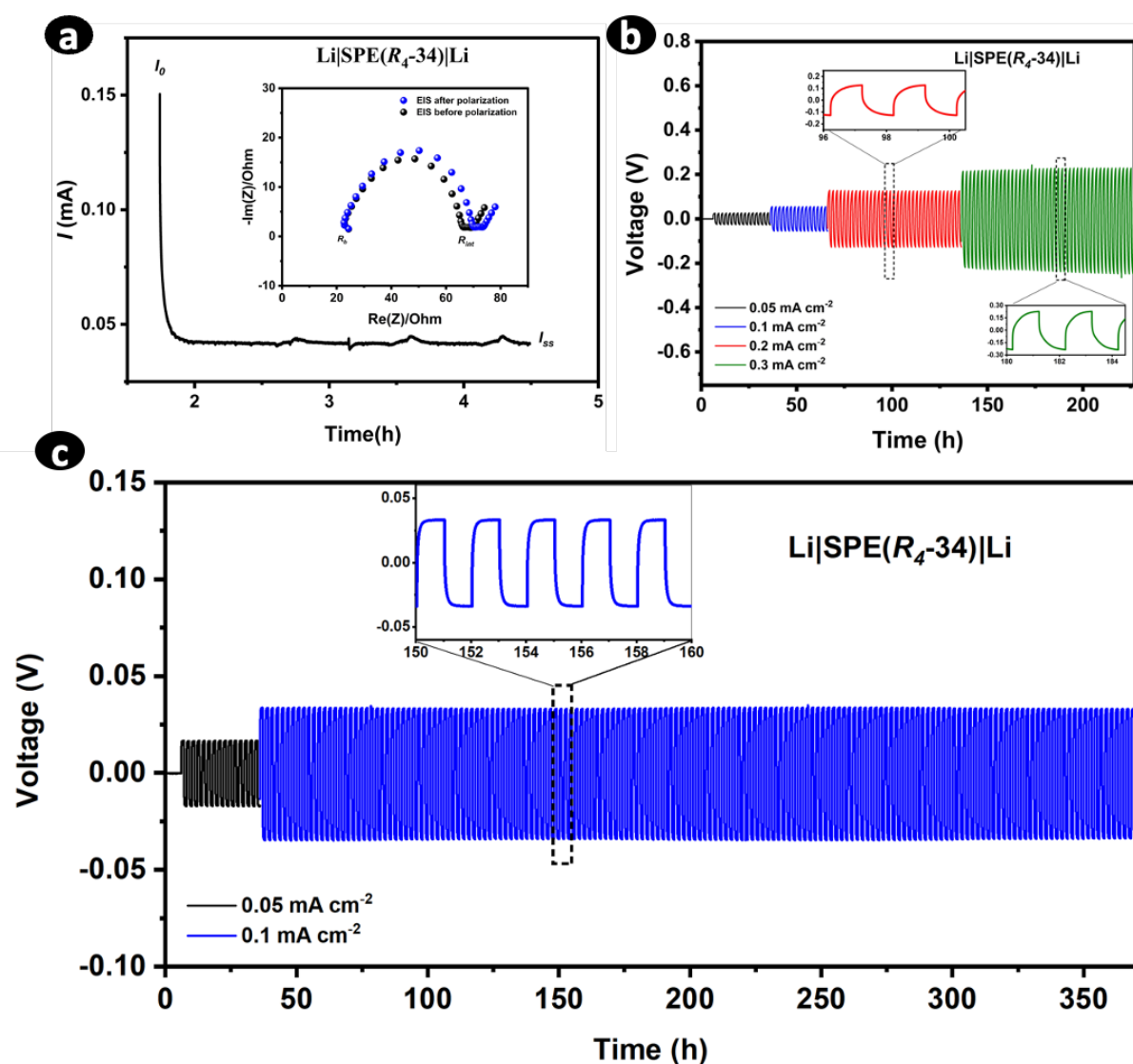


Figure 15. a) Chronoamperometry and EIS of SPE(R_4 -34) determining the transference number at 50 °C b) Lithium stripping and plating with symmetric cell (Li||SPE(R_4 -34)||Li) at 50 °C and

0.05, 0.1, 0.2, 0.3 mA cm⁻² current densities c) Long-term lithium stripping and plating with symmetric cell (Li|SPE(R₄-34)|Li) at 50 °C 0.1 mA cm⁻² (157 cycles) after 15 cycles of 0.05 mA cm⁻².

Also, achieving a high modulus in SPEs is crucial to mitigate dendrite growth and thus enhance the critical current density. The limiting current density refers to the maximum current density that Li|Li non-blocking symmetric cells can withstand without failure arising from dendrite short circuiting or a significant increase in overpotential.⁵² In situations where electrolytes are incompatible with Li-metal or where the distribution of current isn't uniform due to uneven surface contact, the undesired formation of uneven solid electrolyte interphase (SEI) in Li|Li symmetric cell can consume some amount of active Li⁺ ions and trigger the growth of lithium dendrites.⁵³ Lithium plating and stripping experiments performed on SPE(R₄-34) ($\varnothing = 16$ mm, thickness, $L \approx 170$ μ m) in symmetrical Li|Li cell showed that the fabricated SPEs can reach limiting current density of 0.3 mA cm⁻² (Figure 15b) with uniform overpotential, whereas typical PEO/LiTFSI electrolytes has been reported to short circuit at a current density of 0.2 mA cm⁻².⁵⁴ Long-term plating/stripping experiments performed at 0.1 mA cm⁻² for over 350 h (Figure 15c) similarly revealed a uniform overpotential of about ~ 0.035 V over 150 cycles, implying a stable lithium plating/stripping behaviour (see Figure 16). Such a performance in lithium plating/stripping experiments suggest that the rigorous two-phase morphology played a key role in preventing dendrite growth.

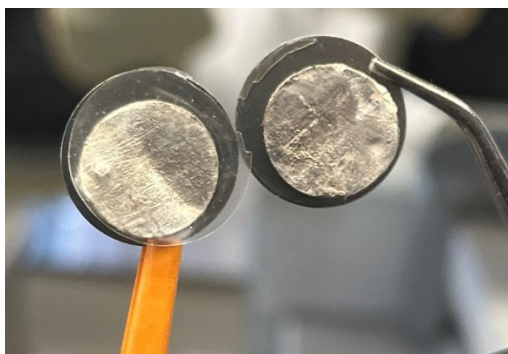


Figure 16. Photo of dismantled Li|SPE(R₄-34)|Li showing uniform lithium stripping/plating. Lithium stripping/plating was performed at 0.1 mA cm⁻² for over 350 h at 50 °C (rate of 2 h per cycle).

In a further step, the electrochemical stability window of SPE(R₄-34) was assessed according to method described in literature.¹⁰ Linear sweep voltammetry (LSV) was performed at 50°C, using copper and Pt electrodes for reductive and oxidative stability evaluations, respectively. As shown in Figure 17, there were no obvious oxidation or reduction peaks in the voltage range 0 – 4.0 V. This underscores the exceptional interfacial stability of SPE(R₄-34) against Li metal,

with an intrinsic oxidative stability extending up to 4.2 V. Notably, this oxidative limit surpasses the typical range reported for PEO-based electrolytes, which is usually ≤ 4.0 V.⁵⁵

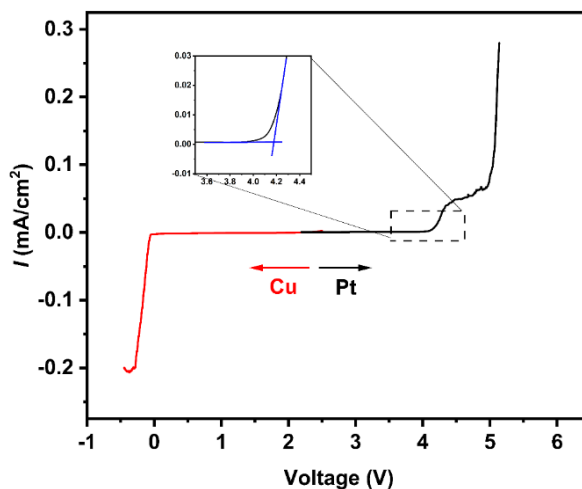


Figure 17. Determination of the electrochemical stability of R₄-34-SPE by linear sweep voltammetry (LSV) in a range from -0.5 to 6.0 V (0.1 mV s⁻¹).

Cycling performance of SPEs in LMBs was demonstrated by sandwiching SPE(R₄-34) between Li metal anode and LiN_{0.8}M_{0.1}C_{0.1}O₂ (NMC811) cathode in Li/SPE(R₄-34)/NMC811 coin cells. The cathodes were prepared using the doctor-blade technique, incorporating 90 wt% NMC811, 5 wt% PVDF, and 5 wt% carbon black on carbon-coated aluminum current collectors, resulting in an active mass loading of 4.5 mg cm⁻².

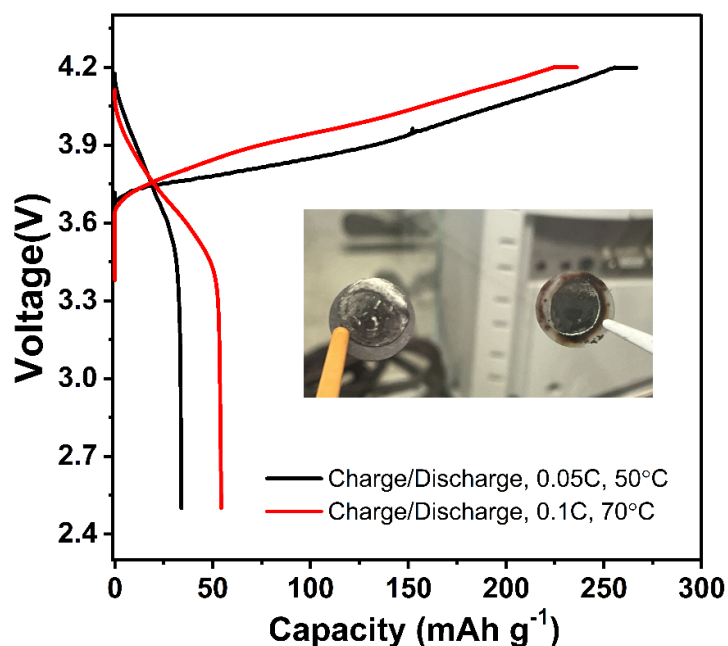


Figure 18. Galvanostatic Cycling of two battery cells prepared with free standing film, Li||R₄-34-SPE||NMC811 at 0.05C (50 °C) and 0.1C (70 °C). Inset image is a photo of dismantled cell.

Galvanostatic charging/discharging of the half-cells was performed in the range of 2.5 – 4.2 V at a rate of 0.05 C (where 0.05 C means completion of charge/discharge within 20 h) and a temperature of 50 °C. Initially, the cell exhibited a specific charge capacity of 266 mAh g⁻¹, but the discharge capacity was relatively low at 34 mAh g⁻¹, resulting in an irreversible capacity loss of over 87%, as illustrated in Figure 18. similar outcome was observed in a duplicate experiment conducted at a rate of 0.1 C and a temperature of 70°C, where the initial specific charge capacity was 235 mAh g⁻¹, and the discharge capacity was 52 mAh g⁻¹ (78% irreversible capacity loss).

It is been reported that the major cause of irreversible capacity loss at the first cycle in lithium batteries is the formation and continuous growth of the solid electrolyte interphase (SEI).⁵⁶ The three-dimensional porous microstructure of cathode material makes it difficult to achieve good contact with free-standing SPEs. Consequently, unfilled pores serve as additional resistive component at the SPE/Cathode interface, thus reducing the electrochemical active surface area.⁵⁷ It is not the case for liquid-state lithium batteries where the porous electrode structure is filled by the LE.⁵⁸ Therefore, to ensure the best interfacial contact between the electrode (anode and cathode) and the polymer electrolyte, we got inspired by the work of Duan *et al.* where they demonstrated with gel polymer electrolyte (GPE) reduced interfacial resistance of the in-situ half-cell of Li/GPE/LFP (49.0 Ohms) compared to the ex-situ prepared

ones (916.1 Ohms).³⁰ We developed a method to photopolymerize the electrolyte resin *in-situ* on the electrodes depicted in *Figure 19a* and *Figure 19b*. 20 μL of SPE(R4-34) electrolyte resin was drop casted on NMC811 cathode substrate ($\text{Ø} = 13 \text{ mm}$) and left under vacuum for 5 *min* to allow the cathode pores to become saturated with resin deposit. UV Irradiation ($I_0 = 2.78 \text{ mW cm}^{-2}$, $\lambda_{\text{max}} = 365 \text{ nm}$) was carried out for 10 *min* to generate in-situ microphase separated SPE as coating on the on the cathode with a typical SPE thickness $\sim 160 \mu\text{m}$.

In order to facilitate the comparison with alternative battery setups, LiFePO_4 (LFP) cathodes were prepared with 90% LiFePO_4 , 5% PVDF, and 5% carbon black using the doctor-blade technique. The active mass loading of the LFP cathode is 2.5 mg cm^{-2} . So-prepared NMC811 and LFP cathodes had a typical porosity in the range 60-70%. LFP cathodes ($\text{Ø} = 13 \text{ mm}$) and lithium metal anode ($\text{Ø} = 12 \text{ mm}$) were successfully developed by photopolymerizing SPE(R4-34) resin under UV with similar conditions. For ease of reference, NMC, LFP and lithium metal electrodes developed using this technique are referred as *d*-NMC811, *d*-LFP and *d*-Li respectively.

Cross-sectional samples of *d*-NMC811 and *d*-LFP examined using SEM combined with EDX analysis, are presented in *Figure 19c* and *Figure 19d*, respectively. The presence of sulphur traces in the bulk of the cathodes clearly indicates that the electrolyte resin effectively permeates the pores of the cathodes and therefore would offer larger active area for lithium de/-insertion.

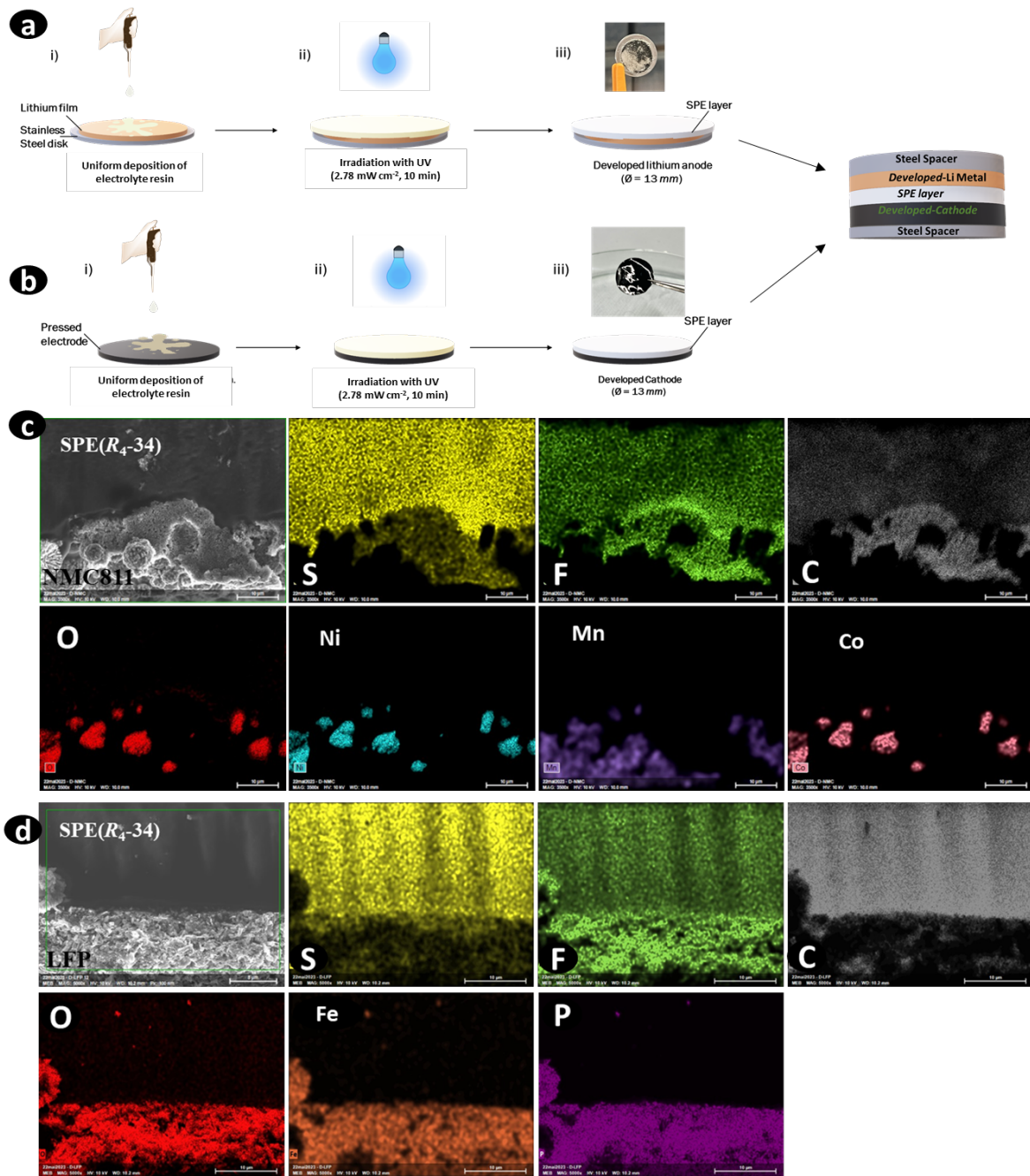


Figure 19. Procedure for developing a) lithium metal anodes and b) cathodes. EDS mapping of composition of c) d-NMC811 cathode and d) d-LFP cathode. Scale bar represents $10 \mu\text{m}$.

Cyclic voltammetry performed on $\text{Li}||\text{d-NMC}$ between 2.4 – 4.2 V at rate of 0.1 mV s^{-1} revealed the presence of cathodic and anodic activation peak even after 10 cycles (refer to Figure S35). These peaks weren't observed when *d*-NMC is replaced with plain carbon-coated aluminium foil developed with the same electrolyte resin (*d*-C-Al). This a good indication that utilizing *d*-NMC in half-cell configuration supports lithium de/-insertion during cycling.

To demonstrate further the promising prospects of these developed electrodes as safe and reliable for battery application, long-term galvanostatic charge–discharge test was performed on *d-Li||d-NMC* and *d-Li||d-LFP* at 0.1C (Figure 20a and Figure 20c respectively). The representative charge/discharge profiles are provided in Figure 21. *d-Li||d-NMC* cell delivered an initial specific discharge capacity of 206 mAh g⁻¹ with an initial CE of 93.3%. The capacity gradually fades to 133 mAh g⁻¹ (35% capacity loss) after 50 cycles with a CE of 99.4%. Capacity fading of NMC811 cathodes is an existing problem and have been reported previously.^{59, 60} Mechanistic studies have attributed the severe fading observed in NMC811 cathodes to the mixing of Li⁺/Ni²⁺ cation and poor structural stability.^{61, 62} Nevertheless, rate capability testing of *d-Li||d-NMC* exhibited decent electrochemical performance with specific discharge capacities of ~244 and ~52 mAh g⁻¹ at 0.05C and 0.5C rate, respectively (Figure 20b).

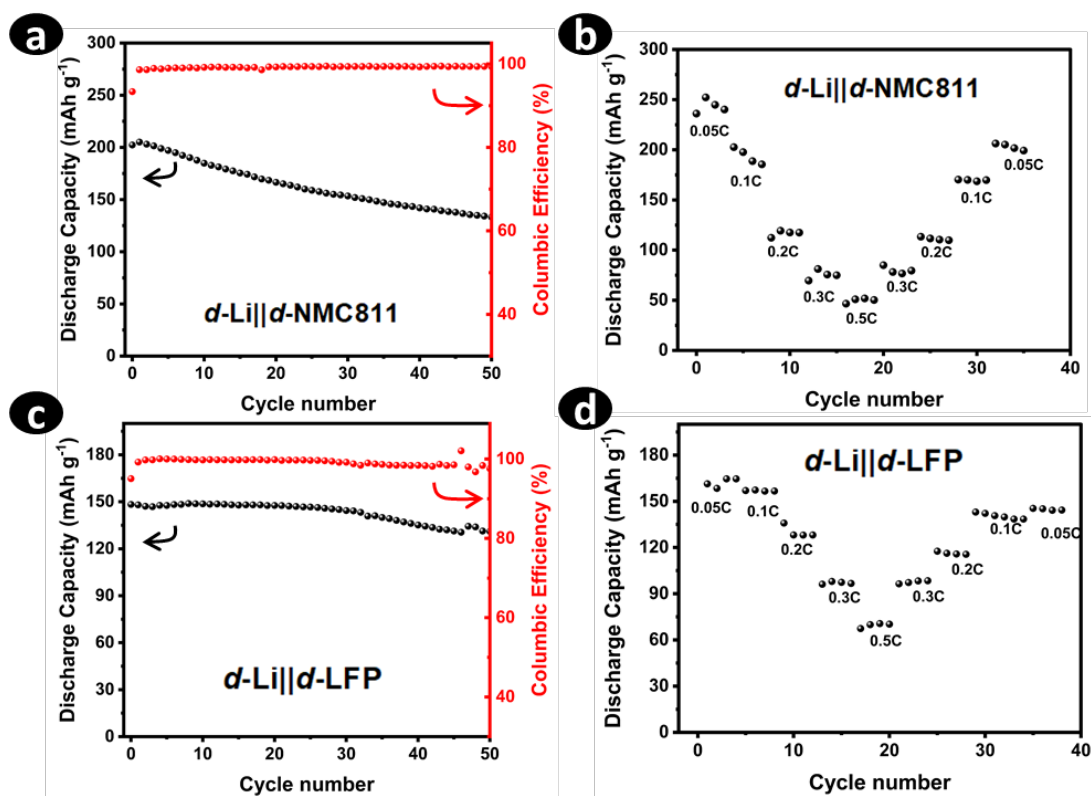


Figure 20. a) Long-term galvanostatic charge/discharge at constant rate of 0.1 C after three formation cycles at 0.05 C at 50 °C and b) at varying charge/discharge rates within a voltage window of 2.5 – 4.2 V. c) Long-term galvanostatic charge/discharge at constant rate of 0.1 C after three formation cycles at 0.05 C and e) corresponding voltage profiles for *d-Li||d-LFP* cells at 50 °C within a voltage window of 2.5 – 4.1 V f) at varying charge/discharge rate.

On the other hand, capacity fade was very minimal for battery cell with $d\text{-Li}||d\text{-LFP}$ configuration. For the first 50 cycles of charge/discharge at similar C-rate at 0.1C. The initial specific discharge capacity was 149 mAh g^{-1} at 0.1C, corresponding to 88% of the theoretical capacity of LiFePO_4 . After 50 cycles, 131 mAh g^{-1} was achieved (corresponding to 12 % capacity loss) and a CE of 98.3 %. For rate capability testing, the specific discharge capacity declined from ~ 165 at 0.05C to $\sim 70 \text{ mAh g}^{-1}$ at 0.5C.

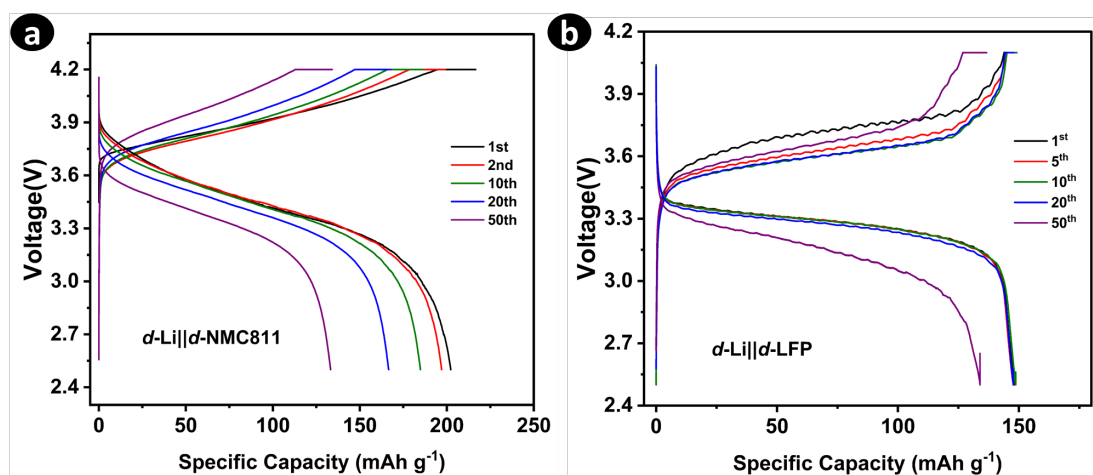


Figure 21. Representative charge/discharge profiles of a) $d\text{-Li}||d\text{-NMC}$ and b) $d\text{-Li}||d\text{-LFP}$.

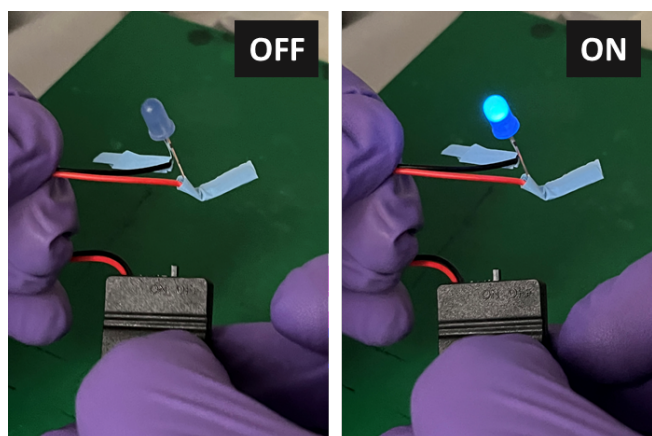


Figure 22. Photographs for the $d\text{-Li}||d\text{-NMC811}$ half-cell that powers a blue LED.

In this study, all the half-cell lithium metal batteries that have been described were evaluated for their ability to power a blue LED bulb continuously for several hours, as depicted in Figure 22. This serves to underscore the efficiency and viability of the in-situ PIMS fabrication method for solid-state batteries.

3 Conclusion

We used a novel controlled radical photo-polymerization induced microphase separation (photo-RAFT PIMS) process to prepare a flexible SPEs with disordered bi-continuous morphology at nanoscale consisting soft P(S-*co*-OEGMA)/PC/LiTFSI phase and a hard P(IBoA-*stat*-OEGDA) phase. By means of *in-situ* SAXS techniques, we studied structural development during the PIMS process for samples prepared with varying composition of either linear or star comb macroCTA. It appears that the network morphology is a direct result of concentration and molar mass of macroCTA in the electrolyte resin.

Full structural development in thermal-PIMS process, previously published, has been documented to occur within 2 *h*. In contrast, photo-PIMS process exhibits rapid microphase separation kinetics, with stable structures forming in approximately 50 to 100 *s*, representing a time requirement that is about 70 times shorter. The star comb macroCTA, regardless of its composition, exhibited an irregular evolution with a molar mass of 144 kg mol⁻¹, characterized by distinct stages including a stationary stage, gelation stage, and a constriction stage. In contrast, the linear and lower molar mass star comb counterparts displayed only a stationary and gelation stage.

SPEs prepared from 24 wt% star comb macroCTA (144 kg mol⁻¹) exhibited poor conductive properties owing to the sparsely connected conducting domains, however this effect is not observed for low molar mass star comb (62 kg mol⁻¹) or linear comb (39 kg mol⁻¹) macroCTA.

In terms of cell performance, the *in-situ* photopolymerization of SPE(*R*₄-34) resin directly on electrodes greatly improves the interfacial contact between the electrolyte and electrodes. Cycling was done using *d*-Li||*d*-NMC811 and *d*-Li||*d*-LFP cell configuration at 50 °C. Specific discharge capacities reached values of ~206 mAh g⁻¹ and ~131 mAh g⁻¹ for *d*-Li||*d*-NMC811 and *d*-Li||*d*-LFP respectively at 0.1C, over 50 cycles.

In this regard, the SPEs produced using this method avoid the unfavourable post-processing effects associated with typical BCPE and enables the independent tuning of the mechanical properties and the conductivity of polymer electrolytes. These findings would contribute to the development of advanced solid polymer electrolytes for more efficient and reliable lithium metal batteries.

4 Supporting Information

4.1.1 Materials

Styrene (S, Sigma-Aldrich, 99%⁺), Oligo(ethylene glycol) methyl ether methacrylate (OEGMA, average degree of polymerization= 8-9, average $M_n = 500 \text{ g}\cdot\text{mol}^{-1}$ Sigma-Aldrich), Azobis(isobutyronitrile) (AIBN, Sigma-Aldrich, 98%), ethylene glycol diacrylate (OEGDA, $DP_{EO} = 2-3$, average $M_n = 250 \text{ g}\cdot\text{mol}^{-1}$ Sigma Aldrich), Pentaerythritol tetrakis[2-(dodecylthiocarbonothioylthio)-2-methylpropionate (tetrafunctional chain transfer agent code-named TTC-4, Sigma-Aldrich, 97%), 4-cyano 4-[(dodecylsulfanylthiocarbonyl)-sulfanyl]-pentanoic acid (monofunctional chain transfer agent code-named TTC-1, Sigma-Aldrich, 97%), Isobornyl acrylate (IBoA, TCI chemicals, 90%), Ethyl phenyl(2,4,6-trimethylbenzoyl)phosphinate (TPO-L, Arkema), Lithium bis(trifluoromethanesulfonyl)imide (LiTFSI, Solvionic, 99.9% extra dry), Propylene Carbonate (PC, Sigma-Aldrich, anhydrous, 99.7%), N-Methyl-2-Pyrrolidone (NMP, Sigma Aldrich), Lithium Nickel Manganese Cobalt Oxide powder (NMC811, MSE), Lithium Iron Phosphate (LiFePO_4 , Targray) Super C65 Carbon (C65, Umicore), Poly(vinylidene fluoride) (PVDF, Sigma-Aldrich), Lithium Metal (Blue solutions, thickness of $65 \mu\text{m}$), Tetrahydrofuran (THF, Sigma-Aldrich, 99%⁺), Ethanol (EtOH, VWR, 96%⁺).

4.1.2 Synthesis of linear and star comb of P(S-co-OEGMA) macroCTA.

In the synthesis of R_I macroCTA, OEGMA (6.20 g, 1.24×10^{-2} mol, 100 eq), S (80 mg, 7.69×10^{-4} mol, 6 eq), TTC-1 (50 mg, 1.24×10^{-4} mol, 1 eq), and AIBN (2.0 mg, 1.24×10^{-5} mol, 0.1 eq) were mixed and sealed in a round bottom flask A. For the synthesis of R_4 macroCTA, OEGMA (6.20 g, 1.24×10^{-3} mol, 377 eq), S (80 mg, 7.69×10^{-4} mol, 23 eq), TTC-4 (50 mg, 3.29×10^{-5} mol, 1 eq), and AIBN (2.2 mg, 1.31×10^{-5} mol, 0.1 eq) were mixed and sealed in a round bottom flask B. For the synthesis of R_4^* macroCTA, OEGMA (4.0 g, 8.0×10^{-2} mol, 205 eq), S (76 mg, 7.69×10^{-4} mol, 20 eq), TTC-4 (59.4 mg, 3.90×10^{-5} mol), 1 eq), AIBN (2.6 mg, 1.56×10^{-5} mol, 0.1 eq) and 1,4-dioxane (4.08 g, 4.63×10^{-1} mol) were mixed and sealed in a round bottom flask C. Flask A, B and C were separately degassed with nitrogen in ice bath, and polymerization reaction was carried out at $75 \text{ }^\circ\text{C}$. Samples were collected for NMR analysis to determine individual monomer conversion. The reaction was stopped after 2 hours and purified by solubilizing the crude mixture in 50:50 v/v THF and

MeOH, dialyzing against water in regenerated cellulose membrane, and lyophilizing it. Purified macroCTAs were characterized using NMR and SEC. The monomer conversions were calculated using ^1H NMR spectra. The overall molar and weight conversions, the mole fractions of each unit in the copolymer, were calculated using equations given in supporting information.

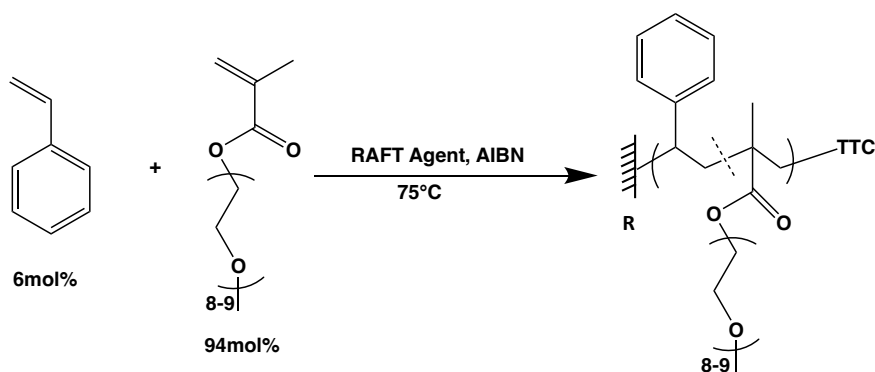


Figure S23. Schematic for synthesis of P(S-co-OEGMA)-CTA from either a tetra functional or monofunctional RAFT agent.

Table S4. Characterization of linear (R_1) and star (R_4) comb-like P(S-co-OEGMA) macroCTA.

macroCTA	Exp	$f_{\text{OEGMA}}^{\text{a)}}$	$[M]_0/[TTC]_0^{\text{b)}}$	t (h)	$X_w^{\text{c)}}$	$X_m^{\text{d)}}$	$M_n, \text{theo}^{\text{f)}}$ (kg/mol)	$dn/dc^{\text{g)}}$	M_n, SEC (kg/mol)	D
R_1	KA143	0.94	106	2	0.47	0.48	24	0.066	39	1.48
R_4	KA149	0.94	100	2	0.58	0.59	113	0.066	144	1.37
$R_4^{*e)}$	KA250	0.92	56	2	0.41	0.43	44	0.067	62	1.19

^{a)} $f_{\text{OEGMA},0}$ is the molar fraction of OEGMA in the initial monomer feed.

^{b)} $[TTC]_0$ is the concentration in trithiocarbonate functions, $[TTC]_0 = [TTC-1]_0 = 4 \square [TTC-4]_0$ and $[M]_0 = [S+OEGMA]_0$. $[TTC]_0/[AIBN]_0 = 10$.

^{c)} Overall weight conversion of both S and OEGMA monomers (Eq S4 in SI).

^{d)} Overall molar conversion of both S and OEGMA monomers (Eq S3 in SI).

^{e)} Synthesis performed by solution polymerization (50:50 wt/wt 1,4-dioxane: Styrene + OEGMA) rather than bulk polymerization.

^{f)} M_n, theo is calculated from Eq. S8 in SI.

^{g)} dn/dc is calculated from Eq. S7 in SI.

4.1.3 NMR analysis for monomer conversion

NMR spectra were recorded using a Bruker 400 MHz spectrometer at 25 °C with 32 scans and a time delay D1 of 5 s. ^1H NMR measurements were performed at frequencies of 400 MHz. Deuterated chloroform (CDCl_3) and deuterated methanol (MeOD) were used as solvent for crude and purified polymer respectively. All products were dissolved with concentrations between 10 and 20 mg mL^{-1} .

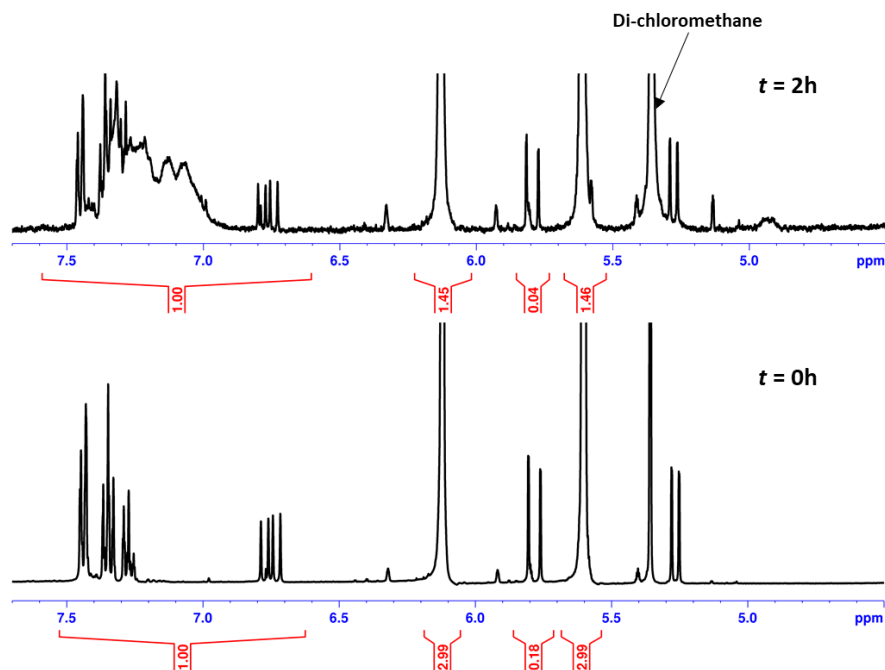


Figure S24. ^1H NMR spectra of initial ($t = 0\text{h}$) and crude ($t = 2\text{h}$) sample during synthesis of star (R_4) comb macroCTA. Deuterated dichloromethane was used as solvent for the analysis.

The conversions of the monomers X_{OEGMA} and X_S were calculated using ^1H NMR spectra according to equation S1 and equation S2. It should be noted the

$$X_{OEGMA} = 1 - \frac{\left(\frac{[I_{1H, OEGMA} (5.6\text{ppm})]_t}{[I_{1H, IS} (7.5 - 6.4\text{ppm}) - I_{1H, S} (5.8\text{ppm})]_t} \right)}{\left(\frac{[I_{1H, OEGMA} (5.6\text{ppm})]_0}{[I_{1H, IS} (7.5 - 6.4\text{ppm}) - I_{1H, S} (5.8\text{ppm})]_0} \right)} \quad \text{S1}$$

$$X_S = 1 - \frac{\left(\frac{[I_{1H, S} (5.8\text{ppm})]_t}{[I_{1H, IS} (7.5 - 6.4\text{ppm}) - I_{1H, S} (5.8\text{ppm})]_t} \right)}{\left(\frac{[I_{1H, BzMA} (5.6\text{ppm})]_0}{[I_{1H, IS} (7.5 - 6.4\text{ppm}) - I_{1H, S} (5.8\text{ppm})]_0} \right)} \quad \text{S2}$$

The equations used to calculate the overall molar (X_m) and weight (X_w) conversion of both S and methacrylate monomers is given in Equation S3 and Equation S4 (n_0 and m_0 respectively corresponds to the initial number of moles and the initial mass of each monomer).

$$X_m = \frac{(x_{OEGMA} \times n_{0,OEGMA}) + (x_S \times n_{0,S})}{(n_{0,OEGMA} + n_{0,S})} \quad \text{S3}$$

$$X_w = \frac{(x_{OEGMA} \times m_{0,OEGMA}) + (x_S \times m_{0,S})}{(m_{0,OEGMA} + m_{0,S})} \quad \text{S4}$$

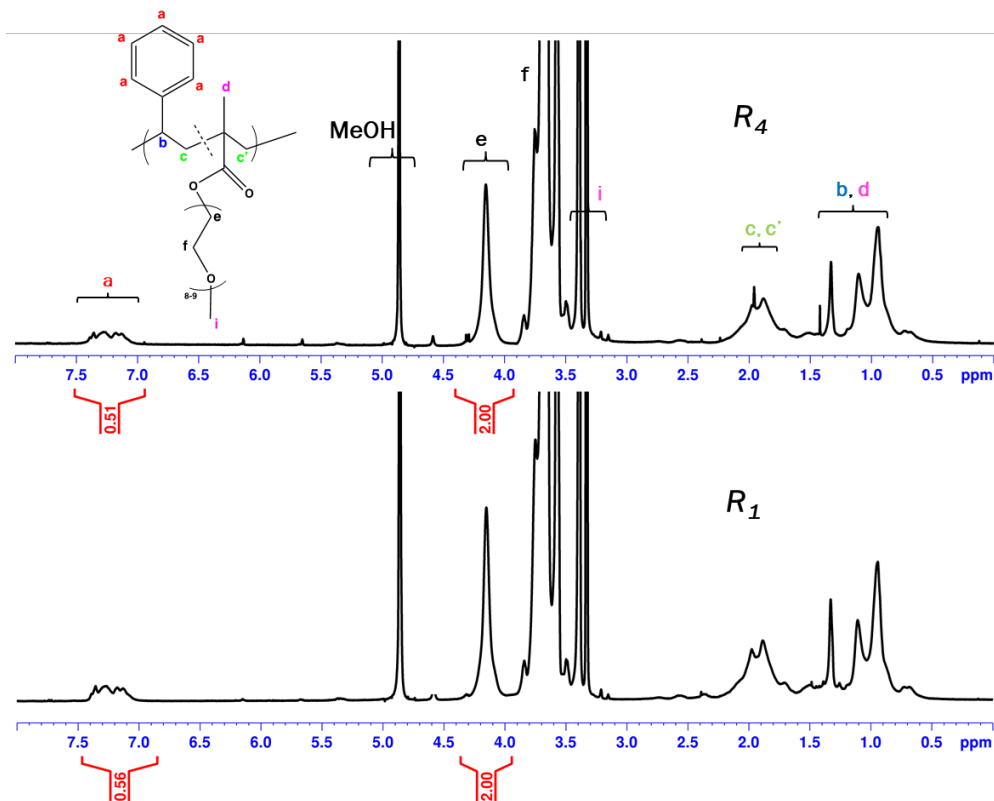


Figure S25. FTIR of purified linear (R_1) and star (R_4) comb macroCTA.

$$F_{POEGMA} = \frac{I_{1H, S(4.2ppm)}}{(I_{1H, IS(7.5 - 6.4ppm)} + I_{1H, S(4.2ppm)})} \quad \text{S5}$$

$$W_{POEGMA} = \frac{(m_{OEGMA} \times I_{1H, S(4.2ppm)})}{[(m_S \times I_{1H, IS(7.5 - 6.4ppm)}) + (m_{OEGMA} \times I_{1H, S(4.2ppm)})]} \quad \text{S6}$$

The dn/dc was calculated accordingly in Equation S7.

$$dn/dc_{P(S-co-OEGMA)} = (W_S \times dn/dc_S) + (W_{OEGMA} \times dn/dc_{POEGMA}) \quad S7$$

$$M_{n,theo} \text{ macroCTA} = M_{TTC} + X_w \frac{(m_{0,S} + m_{0,OEGMA})}{n_{0,TTC}} \quad S8$$

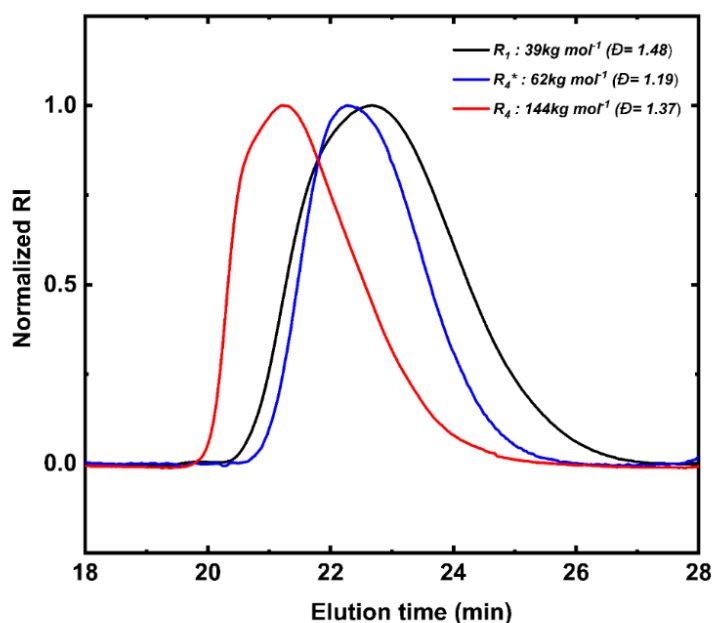
The degree of polymerization X_n of the macroCTA was determined according to equation S10. M_{OEGMA} and M_S represent the molar mass of OEGMA and Styrene respectively.

$$X_n = \frac{M_{n,SEC}}{(M_{OEGMA} * W_{POEGMA}) + (1 - W_{POEGMA}) * M_S} \quad S9$$

4.1.4 Size Exclusion Chromatography – Multi-Angle Laser Light Scattering (SEC-MALLS).

Measurements were performed on a bank of 4 Shodex columns (KF801, KF8025, KF804 and KF806) each 300 mm x 8 mm at 30 °C with THF eluent controlled by a Malvern pump (Viscotek, VE1122) at a flow rate of 1.0 mL.min⁻¹. The SEC apparatus is equipped with a refractive index (RI) detector (Viscotek VE3580), a Wyatt Heleos II Multi Angle Laser Light Scattering detector (MALLS, 18 angles, $\lambda_0 = 664.4$ nm), an online viscometer (Wyatt Viscostar 311-V4) and a UV-visible detector (Viscotek-Malvern VE3210). Toluene was used as a flow marker. Sample concentrations were limited to the range of 1.5 – 4.5 mg mL⁻¹ and dissolved samples were filtered through polytetrafluorethylene (PTFE) membranes with a pore size of 0.45 μ m prior to injection.

Figure S26. Size Exclusion Chromatography of linear (R_1) and star (R_4 and R_4^*) macroCTAs showing RI (solid).



4.1.5 UV-Visible spectrometer

Mono and tetra functional macro-CTA were characterized by UV-Visible spectrometer (PerkinElmer Lambda 850 spectrometer) to ascertain the chain end fidelity (**Figure S27**). The Absorption spectra for TTC group was observed at the range of 280-330 nm for a solution of 2 g/L of the macro-CTAs in EtOH. Molecular weight of macroCTA, $M_{n,UV-Vis}$ was calculated from equation S10 by chain-end analysis of each TTC function present in the polymer solution. In equation S10, Abs_{TTC} , $\epsilon_{TTC, EtOH} = 11,306 \text{ L.mol}^{-1}.\text{cm}^{-1}$, $l = 1 \text{ cm}$, $m_{n,SEC}$ and $C_{wt,polymer}$ represents the absorption at 310 nm, molar absorption coefficient of the TTC group, thickness of quartz cuvette, number average molar mass of macroCTA determined from the SEC, and concentration in g/L of macroCTA respectively.

$$\frac{Abs_{TTC} \times m_{n,SEC}}{\epsilon_{TTC} \times l \times C_{wt,polymer}} = N_{TTC/chain} \quad \text{S10}$$

Note, it is assumed that the molar absorption coefficient of the TTC chain end in the macroCTA is similar to the one of the molecular TTC group measured in ethanol.⁶³

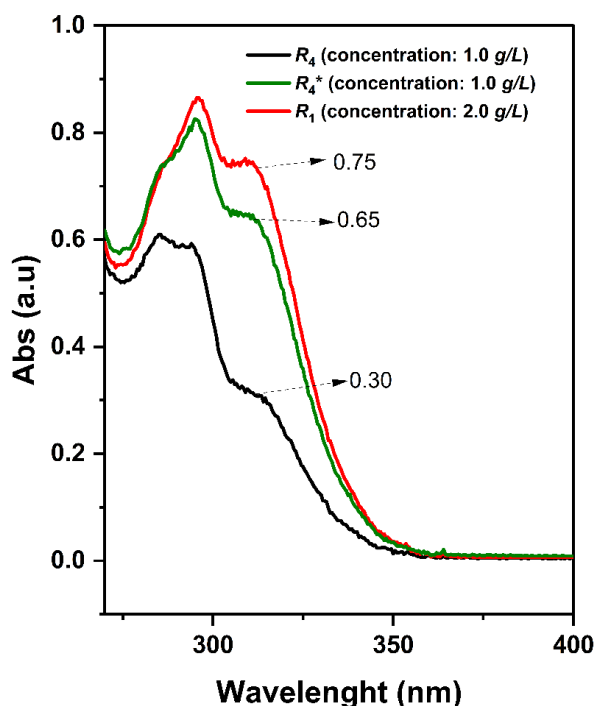


Figure S27. UV absorbance of TTC functional handle on P(S-co-OEGMA) macroCTA in ethanol. Value of absorbance are taken at 310 nm.

4.1.6 Fabrication of Solid Polymer Films by UV Photopolymerization

To prepare typical electrolyte film [R_4 -(34,65)], the following steps were taken: 0.88 g of tetra functional macro-CTA (R_4), 0.49 g of OEDGA, 1.40 g of IBoA, 59 mg of a 0.21 mmol g⁻¹ TPO-L stock solution in IBoA, and 2.15 g of 3.48 mmol g⁻¹ LiTFSI stock solution in PC were added to a 10 mL glass vial whilst in an argon (Ar)-filled glove box (O₂ < 0.1 ppm, H₂O < 0.1 ppm). The vial was covered with aluminium foil and allowed to stir at 40 °C for several hours until a homogenous solution was obtained. A thin layer of electrolyte resin was formed by placing 45 μL of the resin between two mylar sheets (200 μm thick, transmittance ~ 63%) to furnish the final films with homogenous and smooth surface. The resin-sandwiched mylar sheets were exposed to SOLIS 365 UV source (fitted with coated plano convex lens) from Thorlabs (Current = 670 mA, $I_0 = 2.78 \text{ mW cm}^{-2}$, $\lambda_{max} = 365 \text{ nm}$) at 30 cm distance away from the sandwiched resin. The irradiation lasted for 10 min and the resulting electrolyte film with a thickness ranging from ~100–250 μm was easily removed.

Composition of electrolyte resin used in this work are presented in Table 2.

$$Wt_{macroCTA} = \frac{m_{macroCTA}}{m_{macroCTA} + m_{IBoA} + m_{OEGDA}}, \quad S11$$

$$Wt_{cond-\phi} = \frac{m_{PC} + m_{LiTFSI}}{m_{macroCTA} + m_{IBoA} + m_{OEGDA} + m_{PC} + m_{LiTFSI}}, \quad S12$$

$$Wt_{PC} = \frac{m_{PC}}{m_{macroCTA} + m_{IBoA} + m_{OEGDA} + m_{PC} + m_{LiTFSI}}, \quad S13$$

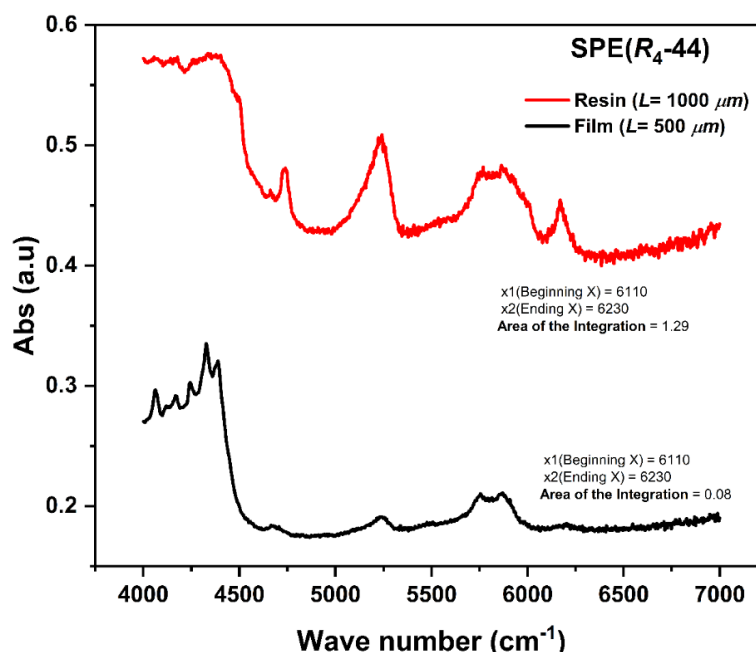
4.1.7 Fourier-Transform Infrared Spectroscopy (FTIR)

Real-time FT-IR spectroscopy was used to investigate the kinetic of photopolymerization of formulation with and without macro-CTAs. Experiment was performed in quartz capillary tube (1.5 mm thickness) in transmission mode of Thermo Scientific Nicolet iS50 FT-IR Spectrometer. An aliquot of resin was pipetted into the tube via a syringe held in place adjacent to the laser by an in-house designed sample holder. Prior to each experiment, empty capillary tube was used to furnish as background, IR spectra were recorded at 30 s time interval in the

IR range of $7000 - 4000 \text{ cm}^{-1}$ to capture the vinylic peak IBoA/OEGDA at $6110 - 6230 \text{ cm}^{-1}$. Each measurement included an average of 32 scans with a resolution of 4 cm^{-1} . Polymerization was started after 120 s by irradiating with a Thorlabs mounted LED (M365L2) with a collimation adapter (Current = 167 mA , $I_0 = 0.54 \text{ mW cm}^{-2}$, $\lambda_{\text{max}} = 365 \text{ nm}$) and allowed to last for an entire 600 s . The integral, $I_{(6103 - 6245 \text{ cm}^{-1})}$ of the vinylic peak were analyzed using Omsec software and the conversion ($X_{\text{IBoA/OEGDA}}$) was thus calculated from Eq S14.

$$X_{\text{IBoA/OEGDA}} (\%) = \left[1 - \frac{I_{(6110-6230)t}}{I_{(6110-6230)t=0}} \right] \times 100 \quad \text{S14}$$

Figure S28. FTIR spectra of SPE(R₄-44) used to calculate conversion of fabricated films. Integral peak at $6110 - 6230 \text{ cm}^{-1}$ was used to calculate conversion.



To determine final conversion in fabricated films, the starting resins were pipetted in capillary tube, and an IR spectrum was obtained by scanning from $7000-4000 \text{ cm}^{-1}$. Fabricated solid electrolyte films ($100 - 200 \mu\text{m}$) was held in place adjacent to the laser and IR spectrum was recorded. The final conversion was determined from Eq S15. Where int_{film} is the integral of the peak from $61030-6230 \text{ cm}^{-1}$ for the fabricated SPE film, int_{resin} is the integral of the peak from $6110-6230 \text{ cm}^{-1}$ for the unpolymerized resin, L_{film} is the thickness of the fabricated SPE film, and $L_{\text{capillary}}$ is the path length of the cuvette. Integrals were calculated using OPUS software 7.5.

$$X_{\text{film}} (\%) = \left[1 - \frac{Int_{\text{film},(6110-6230)}}{Int_{\text{resin},(6110-6230)}} \times \frac{L_{\text{capillary}}}{L_{\text{film}}} \right] \times 100 \quad \text{S15}$$

Fourier Transform Near-Infrared (FTNIR) spectroscopy was performed on solid samples and pristine components of the formulation by attenuated total reflection (ATR) between 4000-400 cm^{-1} to ascertain the characteristics bonds attributed to presence of each component in the final solid electrolytes.

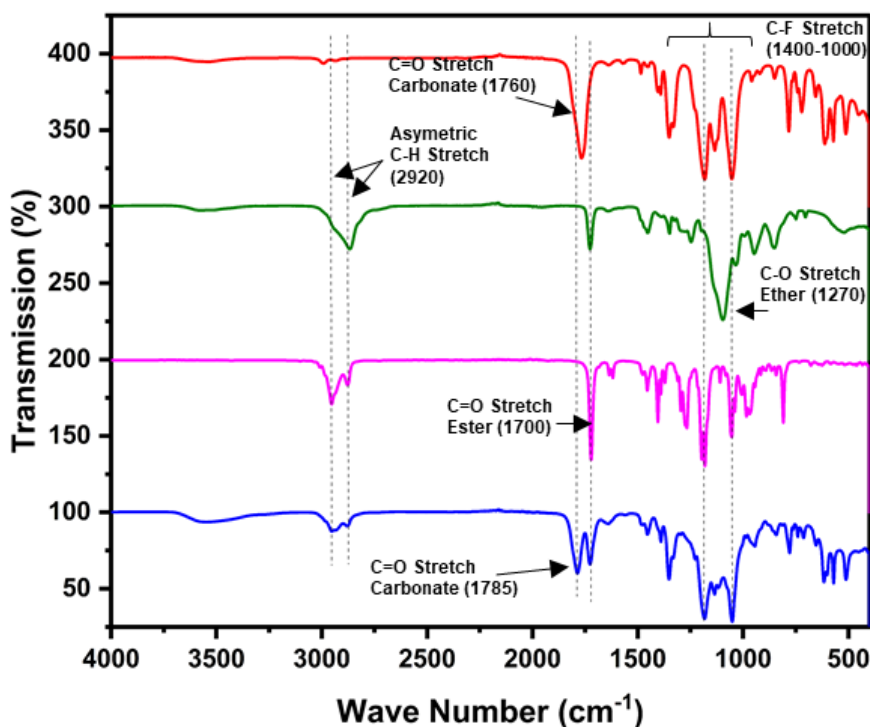


Figure S29. An analysis of FTIR spectra was conducted to compare LiTFSI/PC solution (red), IBoA (green), R₄ macroCTA (pink) and a SPE(R₄-34) (blue).

The FTIR results indicated that the C=O:Li coordination peak (1760 cm^{-1}) associated with LiTFSI/PC were present in the solid films but shifted slightly to higher wave number (1785 cm^{-1}), suggesting that LiTFSI/PC was retained in the SPEs after photopolymerized and the initial C=O:Li coordination is complimented by new EO:Li coordination. Additionally, the aliphatic ether C-O stretching mode peaks (1270 cm^{-1}) from P(S-co-OEGMA)-CTA and ester C=O stretching mode peaks (1700 cm^{-1}) from IBoA were also found to be present in the solid film.

4.1.8 Small Angle X-ray Scattering (SAXS)

SAXS measurements were collected on the BL11 NCD-SWEET beamline at ALBA synchrotron facility using 0.99 \AA X-ray wavelength, a 2.9 m sample-to-detector distance, and

standard data corrections. Scattering curves were plotted as a function of scattering vector $q = 4\pi \sin\theta/\lambda$, with measurements performed under vacuum at RT.

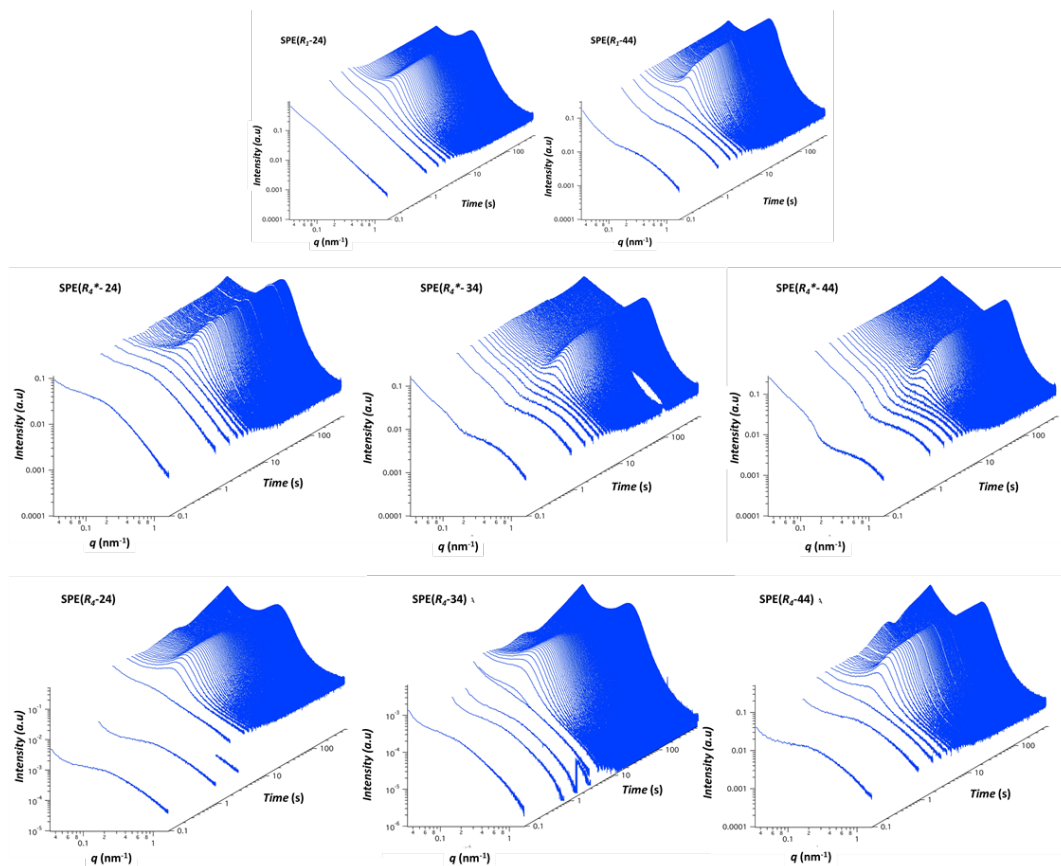


Figure S30. Time resolved scattering curve during photopolymerization of electrolyte resins at 0.54 mW cm^{-2} .

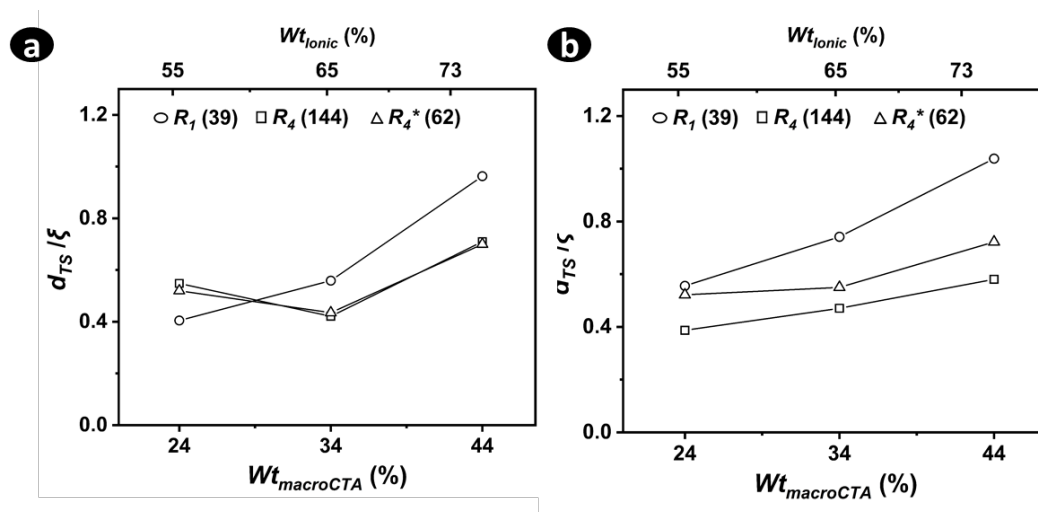


Figure S31. The ratio of length scale with varied composition of a) as-fabricated SPEs and b) SPEs tempered at $100 \text{ }^\circ\text{C}$ for 24 h. Numbers in bracket represent the molar mass of the macroCTA in g mol^{-1} .

4.1.9 Atomic Force Microscope (AFM)

Ultra-thin bulk cross-sections (~ 70 nm) was prepared by microtome from tempered (100 °C) SPE films. All the samples were analyzed on a Bruker Multimode AFM using the PeakForce QNM (r) mode. PeakForce QNM mode is an intermittent contact mode (frequency at 2 kHz) and ScanAsyst-Air tips of very low stiffness (0.4 N·m⁻¹) were used. The data were processed by Nanoscope Analysis software.

4.1.10 Scanning Electron Microscope (SEM)/ Energy Dispersive X-Ray spectroscopy (EDS)

All samples were imaged in an Apreo 2S HiVac SEM from ThermoFisher Scientific (US) coupled to a PP3010T cryo-preparation system from Quorum (GB) and EDS XFlash 61100 from Bruker (US). The observations of the SPE film were carried out at -140 °C at low voltage (2 keV) after a cryo-fracture and platinum metallization (5 mA, 30 s).

Designed NMC and LFP cathodes were prepared by cryo-fracture and SEM images were acquired using the secondary electron detector in the lens under high vacuum at low voltage (2 keV) and EDS analysis at 10 keV, with a 10 mm working distance.

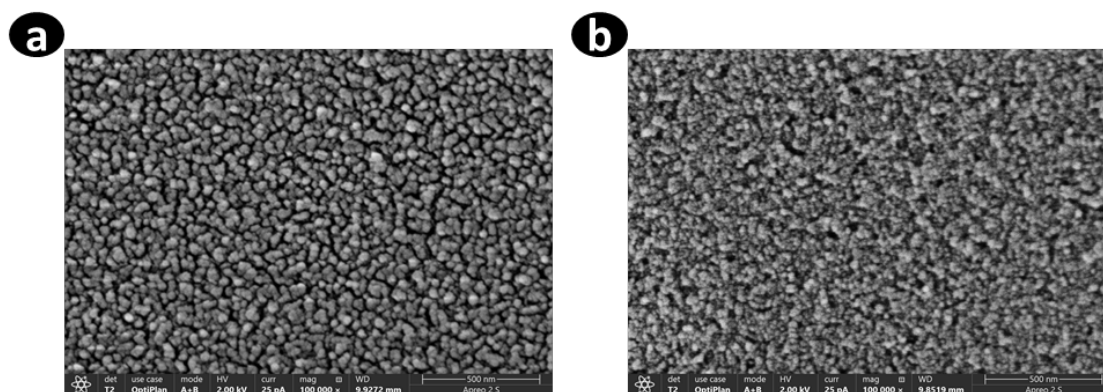


Figure S32. Scanning electron micrographs of a) SPE(R₁-24) and b) SPE(R₄-24).

4.1.11 Electrochemical Impedance Spectroscopy (EIS)

As prepared self-standing SPE films ($\varnothing = 8$ mm, thickness, $L \approx 150$ μ m) were sandwiched between two blocking gold electrodes plates in CESH-e (Enhanced Controlled Environment Sample Holder) cells ($\varnothing = 6.35$ mm) and EIS measurement using Biologic Potentiostat (equipped with EC-Lab software package) at frequency from 1 Hz to 1 MHz with an oscillating

voltage of 50 mV. Subsequently, these cells were preconditioned in a temperature chamber (Binder KB53, 230V 1~ 50 Hz) for 2 h at 90 °C to ensure the sandwiched films reach thermal equilibrium. After the preconditioning was finished, measurements were carried out by gradually decreasing the temperature in 20 °C steps from 90 °C to -10 °C with each temperature being maintained for 2 h to attain a thermal equilibrium. The ionic conductivity (σ ; $S\ cm^{-1}$) was determined by $\sigma = L/RA$ where R is the measured resistance, L is the film thickness and A is the area of the electrode.

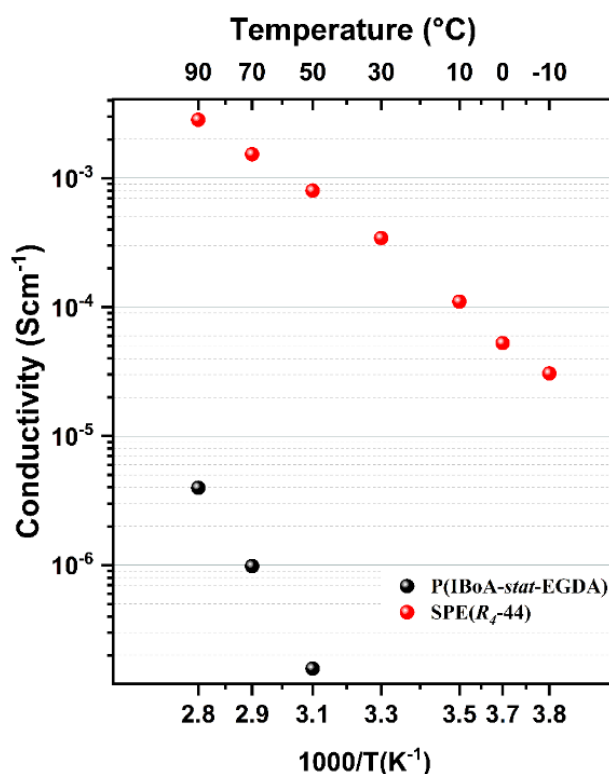


Figure S33. Conductivity of P(IBoA-stat-OEGDA) matrix overlaid with SPE(R_4 -44).

4.1.12 Rheology measurements

Rheology measurements were performed on Anton Paar modular compact rheometer (MCR-302) with a torque range from 0.5 nNm to 230 mNm and integrated active thermal management system. Self-standing films (150 - 300 μm) was sandwiched between two 8 mm \varnothing parallel plate geometry at a constant shear stress of 25 Pa and a frequency of 5 Hz. The measurements were performed in temperature range 25 -100 °C.

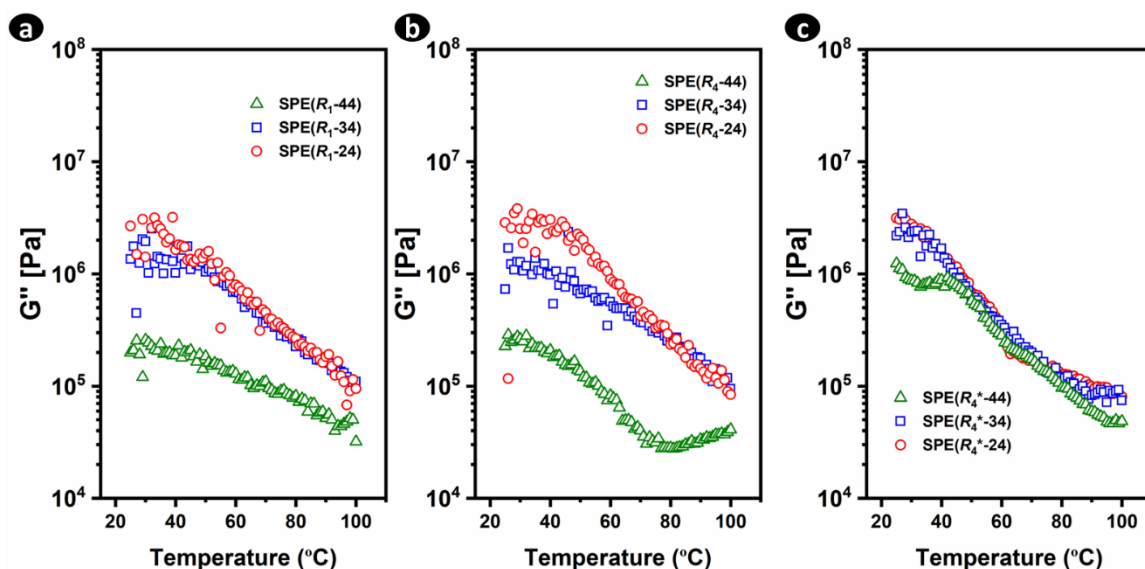


Figure S34: Temperature dependent storage modulus of SPEs fabricated from a) R_1 b) R_4 and c) R_4^* macroCTAs.

4.1.13 Cathodes Fabrication

720.00 mg NMC811 or 720.00 mg LFP, 40.00 mg PVDF, 40.00 mg C65 and 1300 μL NMP was added to a container and sealed tightly. The container was agitated for 60 min to make a homogenous slurry. The slurry is applied to a carbon coated aluminum film ($\sim 10 \mu\text{m}$) using a doctor blade technique with a gap width of $100 \mu\text{m}$ and dried overnight at 90°C under vacuum. 13 mm diameter round disks were punched out and pressed with 1-ton weight. The electrode thickness of for NMC811 cathode is $\sim 80 \mu\text{m}$ ($\sim 10 \mu\text{m}$ current collector, $\sim 70 \mu\text{m}$ coating) and the active mass loading of $\sim 4.5 \text{ mg cm}^{-2}$. The electrode thickness for LFP cathode is $\sim 60 \mu\text{m}$ ($\sim 10 \mu\text{m}$ current collector, $\sim 50 \mu\text{m}$ coating) and the active mass loading of $\sim 2.5 \text{ mg cm}^{-2}$.

Porosity Calculation:

Porosity of the casted electrode was determined from the mass loading, S divided by the density of the dry cathode, D_{cathode} and the dry electrode thickness, T according to the following equation S13.¹

$$\text{Porosity} = 1 - [S / (D_{\text{cathode}} * T)], \quad \text{S16}$$

D_{cathode} was calculated using equation S14 with the mass fractions in the dry electrode (W_{AM} , W_{PVDF} , and W_{C65}) and the densities (D_{AM} , D_{PVDF} , and D_{C65}) of the active material, PVDF and C65 components.

$$D_{cathode} = \left(\left(\frac{W_{AM}}{D_{AM}} \right) + \left(\frac{W_{PVDF}}{D_{PVDF}} \right) + \left(\frac{W_{C65}}{D_{C65}} \right) \right)^{-1}, \quad S17$$

The densities, D for NMC811 active material, LFP active material, PVDF and C65 are 5.5, 3.4, 1.78, and 2.25 g cm⁻³, respectively.² All the porosities were calculated by assuming that the weight fractions and density of each material were not changed by the fabrication process.

4.1.14 Development of cathode

First, the surface of the as-prepared NMC 811 or LFP Cathode ($\varnothing = 13$ mm) was casted with 20 μ L of SPE(R₄-34) electrolyte resin and left under vacuum for 5 min to allow the electrode pores to become saturated with resin deposit. SOLIS 365 UV source from Thorlabs (fitted with coated plano convex lens) was employed for irradiation (Current = 400 mA, $I_0 = 2.78$ mW cm⁻², $\lambda_{max} = 365$ nm) of electrolyte resin deposited on the cathode. Irradiation was carried out for 10 min to generate in-situ microphase separated SPE as coating on the on the cathode with a typical coating thickness ~ 160 μ m.

4.1.15 Development of Lithium Metal anode

Lithium metal anode ($\varnothing = 12$ mm, thickness = ~ 65 μ m) was smoothly affixed to the centre surface stainless steel spacer ($\varnothing = 18$ mm, thickness = 0.5 mm). 20 μ L of SPE(R₄-34) was spread evenly onto the entire anode surface (lithium metal + stainless steel spacer base). SOLIS 365 UV source from Thorlabs (fitted with coated plano convex lens) was employed for the irradiation (Current = 400 mA, $I_0 = 2.78$ mW cm⁻², $\lambda_{max} = 365$ nm) of electrolyte resin deposited on Lithium metal substrate. Irradiation was carried out for 10 min to generate in-situ microphase separated electrolyte as coating on the lithium metal with a thickness ~ 120 μ m.

4.1.16 Transference Number Measurement

Self-standing films (~ 150 μ m) were used to prepare three symmetrical Li|SPE(R₄-34)|Li cells. The cells were precondition at 50 °C in a temperature chamber before commencement of the measurements. Impedance measurements (frequency = 1 MHz - 100 mHz, amplitude = 50 mV) were recorded over 5 cycles before and after polarization. Direct current polarization was applied with a polarization voltage of $\Delta V = 10$ mV for 3 hours, till the system reached a steady state (ss).

$$t_+ = \frac{I_s(\Delta V - I_0 R_0)}{I_0(\Delta V - I_{ss} R_{ss})} \quad \text{S18}$$

Three measurements were performed to get an average transference number computed using equation S18,⁴⁹ where I_s is the steady-state current, ΔV is the polarization voltage, and R_0 and R_{ss} are the electrode resistance before and after the polarization, respectively.

4.1.17 Lithium Plating and Stripping:

A SPE(R4-34) film ($\varnothing = 16 \text{ mm}$, thickness, $L \approx 170 \mu\text{m}$) was used to prepare symmetrical Li||SPE(R4-34)||Li cell. The cells were preconditioned at $50 \text{ }^\circ\text{C}$ in a temperature chamber for 10 h prior to measurement. Plating and stripping protocol was performed at $50 \text{ }^\circ\text{C}$ at current densities of 0.05 mA cm^{-2} (15 cycles), 0.1 mA cm^{-2} (15 cycles), 0.2 mA cm^{-2} (35 cycles), and 0.3 mA cm^{-2} (50 cycles), with each cycle lasting for 2 h until a short circuit was observed or the 2V safety limits were reached. Long-term plating/stripping of lithium at 0.1 mA cm^{-2} (157 cycles) was also performed starting with 15 cycles (2 h each) at current density of 0.05 mA cm^{-2} .

4.1.18 Electrochemical window

Self-standing films $\varnothing = 16 \text{ mm}$, thickness, $L \approx 150 \mu\text{m}$) were used to prepare Li||SPE(R4-34)||Cu and Li||SPE(R4-34)||Pt coin cells for reductive and oxidative stability tests respectively. Prior to the measurement, the cells were preconditioned at $50 \text{ }^\circ\text{C}$ in a temperature chamber for 10 h . Linear sweep voltammetry (LSV, Bio-Logic VMP3) was performed at $50 \text{ }^\circ\text{C}$ with a sweep rate of 0.1 mV s^{-1} within a potential range of -0.5 and 6.0 V vs Li|Li⁺.

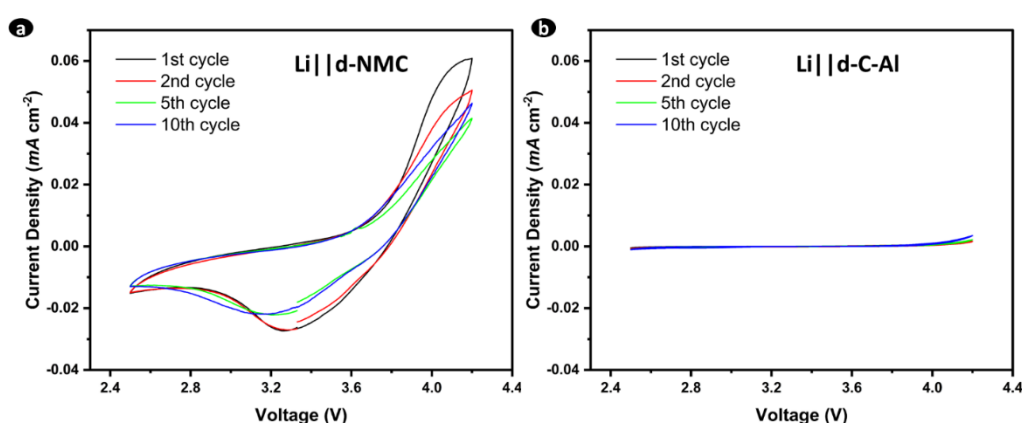


Figure S35. CV of a) d-NMC811 and b) developed carbon coated aluminium foil (d-C-Al) at a rate of 0.1 mV s^{-1} .

4.1.19 Galvanostatic Charging and Discharging:

Half-cell was assembled using coated Lithium metal as the anode in contact with either *d*-NMC811 [as in *d*-Li||*d*-NMC811] or bare NMC811 with a 150 μm intervening layer of free-standing SPE [as in Li|| SPE(R₄-34)||NMC811]. Prior to each experiment, the assembled cells were preconditioned at 50 °C in a temperature chamber for 10 *h*. Rate performance discharging/charging experiments were performed between 2.5 and 4.2 V vs Li|Li⁺ at C-rate of 0.05C, 0.1C, 0.2C, 0.3C, 0.5C and 1C. A 1 *h* and 0.02 mA limit hold was set at constant voltage of 4.2 V during discharge. For long-term cycling performance, two new cells were cycled between 2.5 and 4.2 V vs Li|Li⁺ at a C-rate of 0.1C for 100 cycles with 4 formation cycles at 0.05C. In *d*-Li||*d*-LFP battery configuration, discharging/charging experiments were performed between 2.5 and 4.1 V vs Li|Li⁺ while the other cycling parameter stays the same.

5 References

1. Armand, M.; Tarascon, J. M., Building better batteries. *Nature* **2008**, *451* (7179), 652-657.
2. Phan, T. N. T.; Issa, S.; Gignes, D., Poly(ethylene oxide)-Based Block Copolymer Electrolytes for Lithium Metal Batteries. *Polymer International* **2019**, *68* (1), 7-13.
3. Hallinan, D. T.; Mullin, S. A.; Stone, G. M.; Balsara, N. P., Lithium Metal Stability in Batteries with Block Copolymer Electrolytes. *Journal of The Electrochemical Society* **2013**, *160* (3), A464-A470.
4. Monroe, C.; Newman, J., The Impact of Elastic Deformation on Deposition Kinetics at Lithium/Polymer Interfaces. *Journal of The Electrochemical Society* **2005**, *152* (2), A396.
5. Wohlfahrt-Mehrens, M.; Vogler, C.; Garche, J., Aging mechanisms of lithium cathode materials. *J. Power Sources* **2004**, *127* (1), 58-64.
6. Snyder, J. F.; Carter, R. H.; Wetzel, E. D., Electrochemical and Mechanical Behavior in Mechanically Robust Solid Polymer Electrolytes for Use in Multifunctional Structural Batteries. *Chemistry of Materials* **2007**, *19* (15), 3793-3801.
7. Willgert, M.; Kjell, M. H.; Jacques, E.; Behm, M.; Lindbergh, G.; Johansson, M., Photoinduced free radical polymerization of thermoset lithium battery electrolytes. *European Polymer Journal* **2011**, *47* (12), 2372-2378.
8. Bates, F. S.; Fredrickson, G. H., Block Copolymers—Designer Soft Materials. In *Physics Today*, American Institute of Physics: 1999; Vol. 52.
9. Bouchet, R.; Phan, T. N. T.; Beaudoin, E.; Devaux, D.; Davidson, P.; Bertin, D.; Denoyel, R., Charge Transport in Nanostructured PS-PEO-PS Triblock Copolymer Electrolytes. *Macromolecules* **2014**, *47* (8), 2659-2665.
10. Butzelaar, A. J.; Röring, P.; Mach, T. P.; Hoffmann, M.; Jeschull, F.; Wilhelm, M.; Winter, M.; Brunklau, G.; Théato, P., Styrene-Based Poly(ethylene oxide) Side-Chain Block Copolymers as Solid Polymer Electrolytes for High-Voltage Lithium-Metal Batteries. *ACS Applied Materials & Interfaces* **2021**, *13* (33), 39257-39270.

11. Colombani, O.; Ruppel, M.; Schubert, F.; Zettl, H.; Pergushov, D. V.; Müller, A. H. E., Synthesis of Poly(n-butyl acrylate)-block-poly(acrylic acid) Diblock Copolymers by ATRP and Their Micellization in Water. *Macromolecules* **2007**, *40* (12), 4338-4350.
12. Young, W.-S.; Epps, T. H., Ionic Conductivities of Block Copolymer Electrolytes with Various Conducting Pathways: Sample Preparation and Processing Considerations. *Macromolecules* **2012**, *45* (11), 4689-4697.
13. Weber, R. L.; Ye, Y.; Schmitt, A. L.; Banik, S. M.; Elabd, Y. A.; Mahanthappa, M. K., Effect of Nanoscale Morphology on the Conductivity of Polymerized Ionic Liquid Block Copolymers. *Macromolecules* **2011**, *44* (14), 5727-5735.
14. Ketkar, P. M.; Epps, T. H., Nanostructured Block Polymer Electrolytes: Tailoring Self-Assembly to Unlock the Potential in Lithium-Ion Batteries. *Accounts of Chemical Research* **2021**, *54* (23), 4342-4353.
15. Bates, F. S., Network Phases in Block Copolymer Melts. *MRS Bulletin* **2005**, *30* (7), 525-532.
16. Schulze, M. W.; McIntosh, L. D.; Hillmyer, M. A.; Lodge, T. P., High-modulus, High-conductivity Nanostructured Polymer Electrolyte Membranes via Polymerization-induced Phase Separation. *Nano Lett* **2014**, *14* (1), 122-6.
17. Seo, M.; Hillmyer, M. A., Reticulated nanoporous polymers by controlled polymerization-induced microphase separation. *Science* **2012**, *336* (6087), 1422-5.
18. Lequieu, J.; Magenau, A. J. D., Reaction-induced Phase Transitions with Block Copolymers in Solution and Bulk. *Polymer Chemistry* **2021**, *12* (1), 12-28.
19. Chopade, S. A.; Au, J. G.; Li, Z.; Schmidt, P. W.; Hillmyer, M. A.; Lodge, T. P., Robust Polymer Electrolyte Membranes with High Ambient-Temperature Lithium-Ion Conductivity via Polymerization-Induced Microphase Separation. *ACS Applied Materials & Interfaces* **2017**, *9* (17), 14561-14565.
20. Chopade, S. A.; So, S.; Hillmyer, M. A.; Lodge, T. P., Anhydrous Proton Conducting Polymer Electrolyte Membranes via Polymerization-Induced Microphase Separation. *ACS Applied Materials & Interfaces* **2016**, *8* (9), 6200-6210.
21. Melodia, D.; Bhadra, A.; Lee, K.; Kuchel, R.; Kundu, D.; Corrigan, N.; Boyer, C., 3D Printed Solid Polymer Electrolytes with Bicontinuous Nanoscopic Domains for Ionic Liquid Conduction and Energy Storage. *Small* **2023**, *n/a* (n/a), 2206639.
22. Lee, K.; Shang, Y.; Bobrin, V.; Kuchel, R.; Kundu, D.; Corrigan, N.; Boyer, C., 3D Printing Nanostructured Solid Polymer Electrolytes with High Modulus and Conductivity. *Advanced Materials* **2022**, *n/a* (n/a), 2204816.
23. Khurana, R.; Schaefer, J. L.; Archer, L. A.; Coates, G. W., Suppression of Lithium Dendrite Growth Using Cross-Linked Polyethylene/Poly(ethylene oxide) Electrolytes: A New Approach for Practical Lithium-Metal Polymer Batteries. *Journal of the American Chemical Society* **2014**, *136* (20), 7395-7402.
24. McIntosh, L. D.; Schulze, M. W.; Irwin, M. T.; Hillmyer, M. A.; Lodge, T. P., Evolution of Morphology, Modulus, and Conductivity in Polymer Electrolytes Prepared via Polymerization-Induced Phase Separation. *Macromolecules* **2015**, *48* (5), 1418-1428.
25. Liu, L.; Wu, Z.; Zheng, Z.; Zhou, Q.; Chen, K.; Yin, P., Polymerization-induced microphase separation of polymer-polyoxometalate nanocomposites for anhydrous solid state electrolytes. *Chinese Chemical Letters* **2022**, *33* (9), 4326-4330.
26. Lewandowski, A.; Świdarska-Mocek, A., Ionic liquids as electrolytes for Li-ion batteries—An overview of electrochemical studies. *J. Power Sources* **2009**, *194* (2), 601-609.

27. Tong, J.; Wu, S.; von Solms, N.; Liang, X.; Huo, F.; Zhou, Q.; He, H.; Zhang, S., The Effect of Concentration of Lithium Salt on the Structural and Transport Properties of Ionic Liquid-Based Electrolytes. *Frontiers in Chemistry* **2020**, *7*.
28. Roy, B.; Pal, U.; Kar, M.; MacFarlane, D. R., Recent strategies for improving the performance of ionic liquids as battery electrolytes. *Curr. Opin. Green Sustain. Chem.* **2022**, *37*, 10.
29. Krauskopf, T.; Richter, F. H.; Zeier, W. G.; Janek, J., Physicochemical Concepts of the Lithium Metal Anode in Solid-State Batteries. *Chemical Reviews* **2020**, *120* (15), 7745-7794.
30. Wu, S.; Zheng, H.; Tian, R.; Hei, Z.; Liu, H.; Duan, H., In-situ preparation of gel polymer electrolyte with glass fiber membrane for lithium batteries. *J. Power Sources* **2020**, *472*, 228627.
31. Ding, P.; Lin, Z.; Guo, X.; Wu, L.; Wang, Y.; Guo, H.; Li, L.; Yu, H., Polymer electrolytes and interfaces in solid-state lithium metal batteries. *Materials Today* **2021**, *51*, 449-474.
32. Zhao, Y.; Bai, Y.; Li, W.; Liu, A.; An, M.; Bai, Y.; Chen, G., Semi closed coordination structure polymer electrolyte combined in situ interface engineering for lithium batteries. *Chemical Engineering Journal* **2020**, *394*, 124847.
33. Aniagbaoso, K. I.; Król, M.; Ruokolainen, J.; Bousquet, A.; Save, M.; Rubatat, L., Improved Solid Electrolyte Conductivity via Macromolecular Self-Assembly: From Linear to Star Comb-like P(S-co-BzMA)-b-POEGA Block Copolymers. *ACS Applied Materials & Interfaces* **2023**, *15* (12), 15998-16008.
34. Bobrin, V. A.; Lee, K.; Zhang, J.; Corrigan, N.; Boyer, C., Nanostructure Control in 3D Printed Materials. *Advanced Materials* **2022**, *34* (4), 2107643.
35. Xu, K., Electrolytes and Interphases in Li-Ion Batteries and Beyond. *Chemical Reviews* **2014**, *114* (23), 11503-11618.
36. Doi, T.; Shimizu, Y.; Matsumoto, R.; Hashinokuchi, M.; Inaba, M., Suppression of Mn-Ion-Dissolution of LiNi_{0.5}Mn_{1.5}O₄ Electrodes in a Highly Concentrated Electrolyte Solution at Elevated Temperatures. *ChemistrySelect* **2017**, *2* (28), 8824-8827.
37. Zeng, Z.; Murugesan, V.; Han, K. S.; Jiang, X.; Cao, Y.; Xiao, L.; Ai, X.; Yang, H.; Zhang, J.-G.; Sushko, M. L.; Liu, J., Non-flammable electrolytes with high salt-to-solvent ratios for Li-ion and Li-metal batteries. *Nature Energy* **2018**, *3* (8), 674-681.
38. Moad, G., Trithiocarbonates in RAFT Polymerization. In *RAFT Polymerization*, 2021; pp 359-492.
39. Saranathan, V.; Forster, J. D.; Noh, H.; Liew, S.-F.; Mochrie, S. G. J.; Cao, H.; Dufresne, E. R.; Prum, R. O., Structure and optical function of amorphous photonic nanostructures from avian feather barbs: a comparative small angle X-ray scattering (SAXS) analysis of 230 bird species. *Journal of The Royal Society Interface* **2012**, *9* (75), 2563-2580.
40. Hirose, A.; Shimada, K.; Hayashi, C.; Nakanishi, H.; Norisuye, T.; Tran-Cong-Miyata, Q., Polymer networks with bicontinuous gradient morphologies resulting from the competition between phase separation and photopolymerization. *Soft Matter* **2016**, *12* (6), 1820-9.
41. Teubner, M.; Strey, R., Origin of the scattering peak in microemulsions. *The Journal of Chemical Physics* **1987**, *87* (5), 3195-3200.
42. Irwin, M. T.; Hickey, R. J.; Xie, S.; Bates, F. S.; Lodge, T. P., Lithium Salt-Induced Microstructure and Ordering in Diblock Copolymer/Homopolymer Blends. *Macromolecules* **2016**, *49* (13), 4839-4849.

43. Washburn, N. R.; Lodge, T. P.; Bates, F. S., Ternary Polymer Blends as Model Surfactant Systems. *The Journal of Physical Chemistry B* **2000**, *104* (30), 6987-6997.
44. Zhao, Y.; Wang, G.-C.; Lu, T.-M., Two-Dimensional Fractal Surfaces. In *Experimental Methods in the Physical Sciences*, Zhao, Y.; Wang, G.-C.; Lu, T.-M., Eds. Academic Press: 2001; Vol. 37, pp 255-272.
45. Endo, H.; Mihailescu, M.; Monkenbusch, M.; Allgaier, J.; Gompper, G.; Richter, D.; Jakobs, B.; Sottmann, T.; Strey, R.; Grillo, I., Effect of amphiphilic block copolymers on the structure and phase behavior of oil–water-surfactant mixtures. *The Journal of Chemical Physics* **2001**, *115* (1), 580-600.
46. Diederichsen, K. M.; Buss, H. G.; McCloskey, B. D., The Compensation Effect in the Vogel–Tammann–Fulcher (VTF) Equation for Polymer-Based Electrolytes. *Macromolecules* **2017**, *50* (10), 3831-3840.
47. Frech, R.; Chintapalli, S., Effect of propylene carbonate as a plasticizer in high molecular weight PEO□LiCF₃SO₃ electrolytes. *Solid State Ion.* **1996**, *85* (1), 61-66.
48. Hallinan, D. T.; Villaluenga, I.; Balsara, N. P., Polymer and Composite Electrolytes. *MRS Bulletin* **2018**, *43* (10), 759-767.
49. Evans, J.; Vincent, C. A.; Bruce, P. G., Electrochemical measurement of transference numbers in polymer electrolytes. *Polymer* **1987**, *28* (13), 2324-2328.
50. Devaux, D.; Bouchet, R.; Glé, D.; Denoyel, R., Mechanism of ion transport in PEO/LiTFSI complexes: Effect of temperature, molecular weight and end groups. *Solid State Ion.* **2012**, *227*, 119-127.
51. Pitawala, H. M. J. C.; Dissanayake, M. A. K. L.; Seneviratne, V. A.; Mellander, B. E.; Albinson, I., Effect of plasticizers (EC or PC) on the ionic conductivity and thermal properties of the (PEO)₉LiTf: Al₂O₃ nanocomposite polymer electrolyte system. *Journal of Solid State Electrochemistry* **2008**, *12* (7), 783-789.
52. Wang, C.; Fu, K.; Kammampata, S. P.; McOwen, D. W.; Samson, A. J.; Zhang, L.; Hitz, G. T.; Nolan, A. M.; Wachsman, E. D.; Mo, Y.; Thangadurai, V.; Hu, L., Garnet-Type Solid-State Electrolytes: Materials, Interfaces, and Batteries. *Chemical Reviews* **2020**, *120* (10), 4257-4300.
53. Chi, S.-S.; Liu, Y.; Zhao, N.; Guo, X.; Nan, C.-W.; Fan, L.-Z., Solid polymer electrolyte soft interface layer with 3D lithium anode for all-solid-state lithium batteries. *Energy Storage Materials* **2019**, *17*, 309-316.
54. Colombo, F.; Bonizzoni, S.; Ferrara, C.; Simonutti, R.; Mauri, M.; Falco, M.; Gerbaldi, C.; Mustarelli, P.; Ruffo, R., Polymer-in-Ceramic Nanocomposite Solid Electrolyte for Lithium Metal Batteries Encompassing PEO-Grafted TiO₂ Nanocrystals. *Journal of The Electrochemical Society* **2020**, *167* (7), 070535.
55. Wang, Y.; Zhong, W. H., Development of Electrolytes towards Achieving Safe and High-Performance Energy-Storage Devices: A Review. *CHEMELECTROCHEM* **2015**, *2* (1), 22-36.
56. Lin, Y.-X.; Liu, Z.; Leung, K.; Chen, L.-Q.; Lu, P.; Qi, Y., Connecting the irreversible capacity loss in Li-ion batteries with the electronic insulating properties of solid electrolyte interphase (SEI) components. *J. Power Sources* **2016**, *309*, 221-230.
57. Eckhardt, J. K.; Klar, P. J.; Janek, J.; Heiliger, C., Interplay of Dynamic Constriction and Interface Morphology between Reversible Metal Anode and Solid Electrolyte in Solid State Batteries. *ACS Applied Materials & Interfaces* **2022**, *14* (31), 35545-35554.
58. Taleghani, S. T.; Marcos, B.; Zaghbi, K.; Lantagne, G., A Study on the Effect of Porosity and Particles Size Distribution on Li-Ion Battery Performance. *Journal of The Electrochemical Society* **2017**, *164* (11), E3179.

59. Xia, Y.; Zheng, J.; Wang, C.; Gu, M., Designing principle for Ni-rich cathode materials with high energy density for practical applications. *Nano Energy* **2018**, *49*, 434-452.
60. Liu, W.; Oh, P.; Liu, X.; Lee, M.-J.; Cho, W.; Chae, S.; Kim, Y.; Cho, J., Nickel-Rich Layered Lithium Transition-Metal Oxide for High-Energy Lithium-Ion Batteries. *Angewandte Chemie International Edition* **2015**, *54* (15), 4440-4457.
61. Shang, M.; Chen, X.; Niu, J., Nickel-rich layered $\text{LiNi}_{0.8}\text{Mn}_{0.1}\text{Co}_{0.1}\text{O}_2$ with dual gradients on both primary and secondary particles in lithium-ion batteries. *Cell Reports Physical Science* **2022**, *3* (2), 100767.
62. Xu, X.; Huo, H.; Jian, J.; Wang, L.; Zhu, H.; Xu, S.; He, X.; Yin, G.; Du, C.; Sun, X., Radially Oriented Single-Crystal Primary Nanosheets Enable Ultrahigh Rate and Cycling Properties of $\text{LiNi}_{0.8}\text{Co}_{0.1}\text{Mn}_{0.1}\text{O}_2$ Cathode Material for Lithium-Ion Batteries. *Advanced Energy Materials* **2019**, *9* (15), 1803963.
63. Boussiron, C.; Le Behec, M.; Petrizza, L.; Sabalot, J.; Lacombe, S.; Save, M., Synthesis of Film-Forming Photoactive Latex Particles by Emulsion Polymerization-Induced Self-Assembly to Produce Singlet Oxygen. *Macromolecular Rapid Communications* **2019**, *40* (2), 1800329.
64. Vidal Laveda, J.; Low, J. E.; Pagani, F.; Stilp, E.; Dilger, S.; Baran, V.; Heere, M.; Battaglia, C., Stabilizing Capacity Retention in NMC811/Graphite Full Cells via TMSPi Electrolyte Additives. *ACS Applied Energy Materials* **2019**, *2* (10), 7036-7044.

GENERAL CONCLUSION (ENGLISH)

This thesis focused on controlling self-assembly in poly(oligo(ethylene glycol) (meth)acrylate) (POEG(M)A)-based block copolymers (BCPs) as solid polymer electrolytes (SPEs) in lithium metal batteries (LMBs). Three unique approaches have been investigated namely; tweaking the polymer architectures, embedding pre-synthesized BCPs in POEGA-based matrix, and *in-situ* chain extension of pre-synthesized POEGMA-based macromolecular chain transfer agent (macroCTA). The thesis aimed to provide insights into the complex relation between morphology and properties within the field of polymer electrolytes.

Firstly, the successful synthesis of two sets of BCPs with comb-like star and linear architectures using RAFT polymerization was covered. The BCPs consisted of P(S-*co*-BzMA) hard block and POEGA soft block. To synthesize P(S-*co*-BzMA), it was necessary to incorporate a small quantity of styrene (a minimum of 6%) to effectively control the polymerization of BzMA, especially for the tetrafunctional chain transfer agent. The star-like architecture of the polystyrene macroCTA was verified through Mark-Houwink-Sakurada plots and the determination of the *g* contraction factor involving comparison with benchmark linear polystyrene. The introduction of lithium salt induced phase separation of POEGA blocks, leading to the observation of lamellar, hexagonal cylinder, and spherical phases using TEM and SAXS. As expected, the conductivity increased with the volume fraction of the POEGA/LiTFSI conducting phase, but a significant reliance on the self-assembled morphologies was evident. In the context of the quality of the lamellar morphology produced by star and linear BCPEs, we established a correlation between the generated tortuosity and ionic conductivity. Specifically, the comb-like star BCPs containing approximately 30 wt-% of the POEGA/LiTFSI conductive phase exhibited highly organized lamellar structures compared to the more disordered lamellae in the linear counterparts. Consequently, the reduced tortuosity of the lamellae in the self-assembled star comb-like BCPs resulted in an over 8-fold improvement in lithium conductivity at 30°C. Nevertheless, questions regarding the impact of the positional arrangements of the conductive block persist, as our research only compared linear and star BCPs with an outer block comprising the conducting phase.

Recognizing the difficulties posed by grain disorientation in post-processing stages, the second project had the objective of leveraging non-equilibrium structures derived from BCPs to improve conductivity and mechanical properties of SPEs, all while shortening the fabrication time. To

achieve this goal, we employed pre-synthesized comb-like star or linear BCPs containing approximately 30 wt-% of the POEGA soft block in the photopolymerization of OEGA, both with and without the addition of LiTFSI salt. Through SAXS analysis, we observed the formation of self-assembled hard spheres with P(BzMA-co-S) core in the formulation prior to polymerization, primarily due to the introduction of LiTFSI. These hard spheres subsequently aggregated to create larger dispersed objects, the size and geometry of which were highly influenced by the concentration of the LiTFSI salt. At a [EO]/[Li] ratio of 15, SPEs incorporating linear BCPs exhibited a more uniform dispersion of elongated objects compared to those with star BCPs. This resulted in higher mechanical strength and enhanced ion conductivity, approaching levels similar to those of the pristine POEGA matrix at a similar salt concentration. In this context, the embedded BCP can be considered as physical crosslinkers to potentially replace the chemical crosslinkers, thus opening up the possibility of recycling the SPEs. Nonetheless, there were significant limitations inherent to this system. The amount of BCP that could be dissolved in the OEGA monomer was severely constrained by LiTFSI. Consequently, we could only attain 8wt% hard phase in the SPEs, resulting in an overall subpar mechanical property for the material when compared to the star and linear comb-like BCPEs described in chapter 2.

In the final strategy, P(S-co-OEGMA) synthesized by RAFT polymerization was used as macroCTA for photo-PIMS process to generate phase separated SPEs comprising of P(S-co-OEGMA) soft phase and P(IBoA-*stat*-OEGDA) hard phase. The structural development of SPEs in photo-PIMS occurred on a timescale of 100 seconds, as opposed to thermal-PIMS systems, which typically take hours, indicating a shorter duration. The influence of architecture of the reactive P(S-co-OEGMA) first block is strongly witnessed at lower content of macroCTA. Systems with star comblike macroCTA of high molar mass (SPE(*R*₄-24)) featured sparsely connected conducting domains resulting in poor conductive property compared to the linear system (SPE(*R*₁-24)). At higher content of macroCTA, both SPE(*R*₄-34) and SPE(*R*₁-34)) represent a huge improvement of combined mechanical strength ($10^6 - 10^7$ Pa at 30 °C) and lithium conductivity (0.34 mS cm^{-1} at 30 °C) compared to previous strategies explored in this thesis (refer to **Figure 1**). Technical challenges like poor interface of the SPEs with battery electrodes was resolved by in-situ photopolymerization of electrolytes resin on lithium metal anode, $\text{LiN}_{0.8}\text{M}_{0.1}\text{C}_{0.1}\text{O}_2$ and LiFePO_4 cathode. Assembled half cells of exhibited good cycling performance up to 50 cycles.

In the future, it will be helpful to explore how to render homogenous layer of SPEs in-situ on electrodes using photo printing techniques methods that improve uniformity of the thickness, as there is a huge potential for practical application of PIMS process in the fabrication of SPEs for batteries.

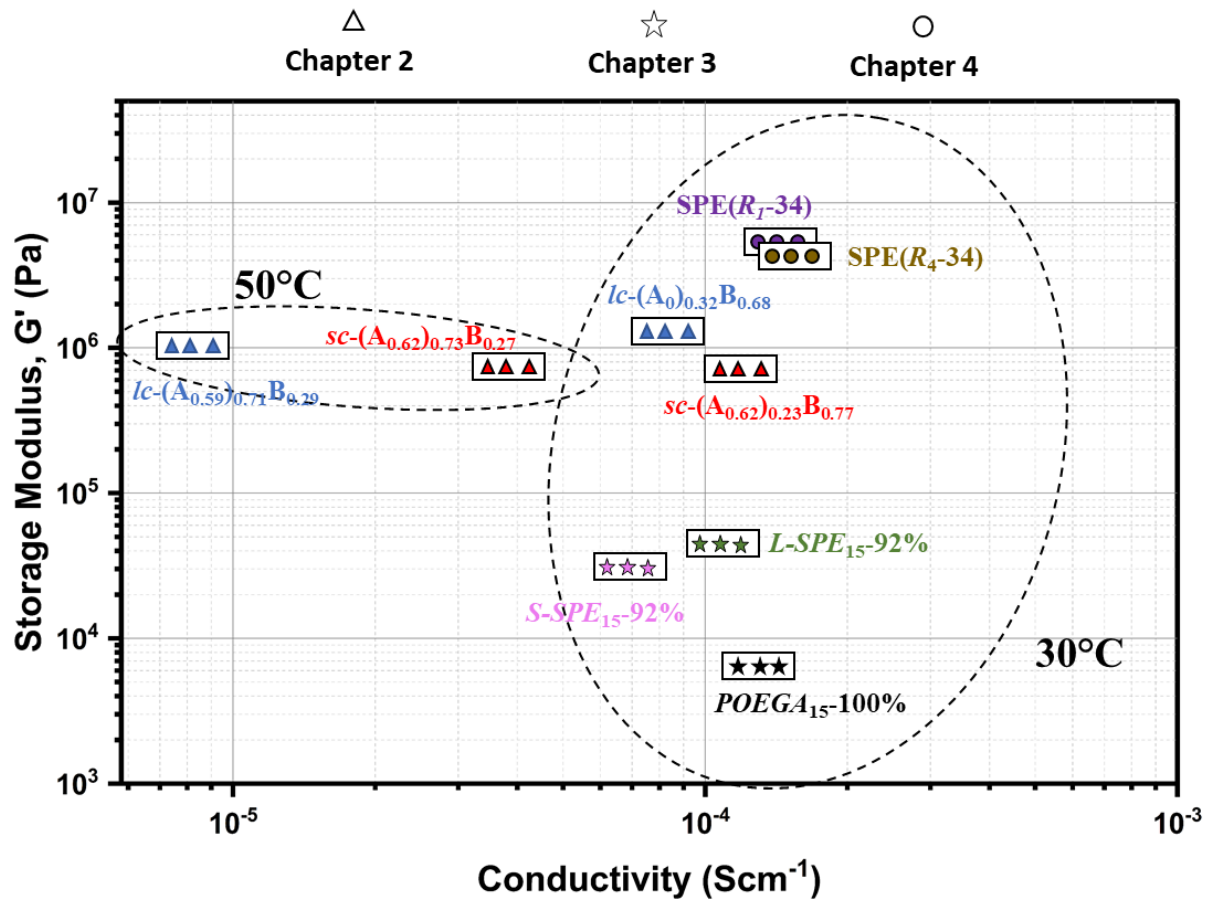


Figure 1. Overview of storage moduli and lithium ion conductivity of the three systems. Bx in the code of Chapter 2 represents wt% of POEGA+LiTFSI ([EO]/[Li]=15). For Chapter 3, X% in the code L-SPE-X% represents wt% of POEGA+LiTFSI ([EO]/[Li]=15). For Chapter 4, Y in SPE(R_x -Y) represents wt% of macroCTA ([EO]/[Li]=5).

ECOLE DOCTORALE :
Sciences Exactes et leurs Applications
ED SEA 211

LABORATOIRE :
Institut des Sciences Analytiques et de Physico-Chimie pour l'Environnement et les
Matériaux (IPREM)

CONTACT

Université de Pau et des Pays de l'Adour
Avenue de l'Université
BP 576
64012 Pau Cedex
Tél. : 05 59 40 70 00



This project has received funding from the European Union's Horizon 2020 research and innovation programme under the Marie Skłodowska-Curie grant agreement No 860403.